TRANSDERMAL DELIVERY OF THERAPEUTIC COMPOUNDS
BY IONTOPHORESIS

By

MICHAEL A. MEMBRINO

A DISSERTATION PRESENTED TO THE GRADUATE SCHOOL
OF THE UNIVERSITY OF FLORIDA IN PARTIAL FULFILLMENT
OF THE REQUIREMENTS FOR THE DEGREE OF
DOCTOR OF PHILOSOPHY

UNIVERSITY OF FLORIDA

2002

TABLE OF CONTENTS

CHAPTERS

LIST OF TABLES

LIST OF FIGURES

KEY TO SYMBOLS

i = Current density

F = Faraday's constant

R = Universal gas constant

T = Absolute temperature

k = Kinetic rate constant

Φ = Electrostatic potential

V_{OC} = Open-circuit potential

κ = Conductivity

c_i = Concentration of species i

t = Time

$\mathbf{N}_i$ = Net flux of species i

R_i = Rate of generation of species i

D_i = Diffusion coefficient for species i

z_i = Ionic charge of species i

u_i = Mobility of species i

I = Ionic strength

v_x = Bulk solution velocity in the x-direction

EIS = Electrochemical Impedance Spectroscopy

VAG = Variable-Amplitude Galvanostatic (modulation)

Abstract of Dissertation Presented to the Graduate School
of the University of Florida in Partial Fulfillment of the
Requirements for the Degree of Doctor of Philosophy

TRANSDERMAL DELIVERY OF THERAPEUTIC COMPOUNDS
BY IONTOPHORESIS

By

Michael A. Membrino

May 2002

Chair: Dr. Mark E. Orazem
Major Department: Chemical Engineering

Therapeutic administration of pharmaceuticals requires that safe and controlled delivery rates be achieved. Iontophoresis is a promising technique for delivering ionic drugs across the skin. Topical delivery of therapeutic agents by iontophoresis is attractive because the large surface area of skin provides for easy access. The top-most skin layer, the stratum corneum, does not favor the transport of most therapeutically active compounds under normal physiological conditions. Iontophoresis takes advantage of the negative background charge of skin which favors delivery of positively charged species. During iontophoresis a driving force for enhanced transport across skin is provided by an applied electric field. A limitation of the approach is that skin may be altered during the process.

The object of this work was to identify the influence of electric fields on the physicochemical properties of skin. The effect of electrolyte solution composition on these properties was also studied. Electrochemical impedance spectroscopy was applied to monitor the properties of skin before, during and after iontophor-

esis. Statistical models were regressed to the data to identify nonstationary and nonlinear behavior. Results indicated that skin properties began to change as the potential across the skin exceeded a critical value. An adaptive modulation strategy was developed to prevent alterations to membrane properties during the impedance experiment.

The delivery rate of lidocaine across the skin was studied by UV-vis absorption spectroscopy. A customized dual-beam diffusion cell was developed to account for the mildly nonstationary behavior of the spectroscopy system. The work indicated that applied current enhanced the transdermal flux of lidocaine.

An additional goal of this work was to identify the influence of controlled variables on concentration and flux profiles within the skin. A one-dimensional steady-state mathematical model was developed to provide insight into the coupled phenomena that occur in the stratum corneum. The governing equations for the model account for diffusion and migration, homogeneous reactions in the electrolyte and the negative background charge of skin. Sample calculations are provided to demonstrate the complex nature of the interactions among the species in the system during iontophoresis.

CHAPTER 1
INTRODUCTION

The object of this work was to provide insight into the important factors that influence administration of therapeutic agents by transdermal iontophoresis. Transdermal iontophoresis is a technique for delivering ionic compounds across the skin with an applied electric current. The motivation for using the applied current is to provide an additional driving force for transport, by way of the induced electric field, to overcome the low permeability of skin. An attractive feature of transdermal iontophoresis is that the drug delivery rate is directly proportional to current. Therapeutic levels of drug concentration may be achieved by adjusting the magnitude of the applied current. This relationship, in principle, makes the electrical and mechanical design of clinical devices relatively straight-forward.

The development of iontophoretic devices requires an understanding of skin transport properties under applied-current conditions. A major focus of this work was to determine the influence of the applied current on skin transport properties. In accordance with this goal, a variety of experimental techniques were applied. As part of the design process, experimental techniques were refined to minimize the influence of the experiment on skin properties.

The structure and chemical composition of skin under normal physiological conditions are described in Chapter 2. An emphasis was placed on skin properties which affect the drug delivery process. A literature review of the influence of applied electric fields on skin properties is presented in Section 2.6. The object of the review was to establish a foundation for the development of experimental tech-

niques to investigate transdermal iontophoresis. The information was also used to interpret results and to develop theoretical models for transdermal iontophoresis.

A literature review of mathematical models for transdermal iontophoresis was also performed. The important features of the transport models are summarized in Chapter 3. The limitations and underlying assumptions associated with the various models are described.

The experimental efforts were directed along two general themes. The first was to identify the influence of electric fields on the physicochemical properties of skin. The second was to evaluate the enhancement of transdermal delivery rates of the model drug lidocaine by an applied electric field. The literature indicates that skin properties may be altered by the applied electric fields.[1−3] The potential impact of this behavior on the design of iontophoretic devices is significant should the alterations be shown to be irreversible or associated with adverse reactions. Therefore, a strong emphasis was placed on identifying the magnitude of potential or current where the properties of skin begin to change. The reversibility of the changes in skin properties was also assessed. Heat-separated human cadaver skin was selected as the model for skin; therefore, all of the experiments were conducted *in vitro*.

Electrochemical Impedance Spectroscopy and current and potential step-change experiments were conducted to achieve this goal. The implementation of these techniques is discussed in Chapter 4. Preliminary studies of skin by impedance spectroscopy indicated that the traditional modulation method can alter membrane properties. An adaptive modulation strategy was developed to prevent changes in skin properties. The results from the preliminary studies and the implementation of the adaptive modulation method are discussed in Chapter 5.

Chapter 6 provides a discussion of the skin impedance studies conducted under a wide range of experimental conditions. For example, the dynamics of skin hydration were studied performing periodic impedance experiments in the absence of an applied current. This investigation provided an estimate of the baseline properties of skin. Iontophoretic conditions were simulated by applying a current bias across the skin. A comparison of the results provided an estimate for the influence of current on skin properties.

A large database of skin impedance spectra was collected in this work. The skin samples were obtained from the dorsal and abdominal regions of 18 human cadavers. Multiple pieces of skin from each macroscopic skin sample were studied by Electrochemical Impedance Spectroscopy. Visual inspection of the spectra revealed a large variation in the impedance response of skin. The statistical procedure used to assess the relative contributions to the overall variation in skin properties is described in Chapter 7. For example, the variation was assumed to be caused by differences among the donors (inter-individual differences), differences within a given donor (intra-individual differences) or stochastic measurement errors. Estimates for the contributions to the overall variation were obtained by regressing a nested statistical model to the impedance data. The polarization resistance and critical frequency were selected as the independent variables for the regressions to reduce computational effort.

The results for the step-change experiments are presented in Chapter 8. The objective was to identify the response of skin to prolonged exposure to electric fields. Two studies were performed where the applied step-change was either current or potential. The work was designed to supplement the impedance work.

The application of UV-vis absorption spectroscopy for *in vitro* monitoring of transdermal lidocaine fluxes is described in Chapter 9. The technique was used

in conjunction with electrochemical impedance spectroscopy to simultaneously measure drug delivery rates and monitor skin transport properties during transdermal iontophoresis. The combined methodology provided for a more accurate assessment of the important factors affecting transdermal iontophoresis.

A steady-state mathematical model was developed to provide insight into the experimental results. The model was derived from macroscopic transport theory and was designed to simulate the conditions of the experimental system. Contributions to the total flux from diffusion, migration and convection were included. A unique feature of the model was that the migration contribution was evaluated without assuming a constant field within the skin. Furthermore, multiple homogeneous reactions, such as the dissociation of water, were included. The development of the mathematical model is discussed in Chapter 10 and the results from the simulations are presented in Chapter 11.

Conclusions from the work presented in this report are discussed in Chapter 12. Suggestions for future research of transdermal iontophoresis are provided in Chapter 13. Proposals for supplemental experimental studies are described here. Recommendations for refinements to the mathematical model for transdermal iontophoresis are also included.

CHAPTER 2
PHYSICOCHEMICAL PROPERTIES OF SKIN

An extensive body of research related to transdermal iontophoresis is available in the literature. This chapter of the report is a description of the structure and chemical composition of the skin under normal physiological conditions. Particular focus is given to the top-most layer of the skin, the stratum corneum, since it is considered to be the dominant barrier to percutaneous absorption. The physical behavior of the stratum corneum during iontophoresis is described in Section 2.6.

2.1 Structure and Function of Skin

Development of efficient clinical devices for transdermal iontophoresis requires knowledge of the chemical composition and physical structure of the skin. The commonly accepted view of these properties under normal physiological conditions is summarized in this section. The physicochemical properties that influence transport of species through the skin are emphasized. Unless otherwise noted, the material presented here is limited to the properties of skin under normal physiological conditions. More extensive discussions describing the anatomy and physiology of skin are available elsewhere.[4−9]

The skin, also known as the integument, is the largest organ of the human body. The total surface area of skin for an average adult is approximately 2 m^2.[10] Skin is a very dynamic organ that functions to accommodate mechanical stresses, prevent excessive water loss, facilitate transpirational cooling, protect against the harmful radiation of the sun, provide for skin cell renewal and prevent absorption of foreign bodies.[11,12]

5

In order to perform such a wide variety of tasks, human skin has evolved into a highly specialized heterogeneous membrane possessing a complex morphological structure and chemical composition. Physiological properties such as thickness, sweat production and barrier function exhibit considerable variability for different anatomical sites of the body. Variations in these properties are directly linked to differences in the chemical composition and structural organization of the skin.[4,13−18]

The skin is composed of two distinct macroscopic regions which are referred to as the epidermis and the dermis.[19,20] This anatomical division becomes obvious upon closer inspection of the unique morphological structure and physiological function of each of these regions. For example, the vascular dermis is a physiologically active region that makes up the majority of skin.[21] The second macroscopic region of the skin, the epidermis, is located directly on top of the dermis and comprises only a small fraction of the overall skin mass. A schematic of the thickness and structures contained within each skin region is presented in Figure 2-1. The important features of the dermis and epidermis are discussed separately below.
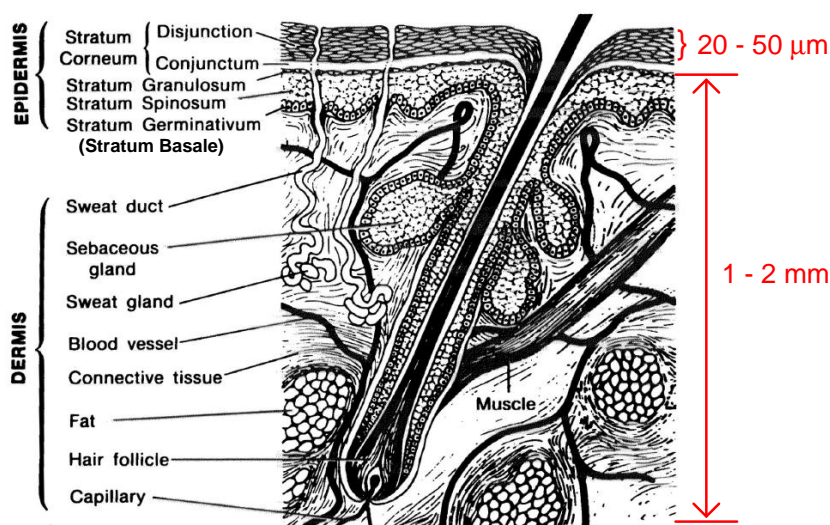
Figure 2-1: Relative thickness and structure of the dermis and epidermis. Figure reproduced from Goldsmith.[7]

2.2 Dermis

The dermis is a composite network of fibrous and elastic tissue sparsely populated with cells.[22] Fibrous proteins of the dermis include collagen, elastin and reticulin.[23] The organization of these tissues provide skin with its ability to withstand a variety of mechanical stresses.[24] There is considerable variation in dermal thickness with location on the body. The typical thickness of the dermis is on the order of 1-2 mm where the maximum thickness of 4 mm is found on the back.[25]

Embedded in the dermis is a dense network of blood vessels, nerve endings, and lymphatic vessels. The capillaries located in the dermis provide for nutrient and heat exchange.[4] The capillaries are also believed to act as a sink for molecules diffusing through the skin.[26,27] Appendages such as sebaceous glands, sweat glands and hair follicles originate in the dermis. These structures have been implicated as routes of transport during iontophoresis.[28−31] Discussion of the important characteristics of skin appendages is provided in Section 2.5.

2.3 Epidermis

The epidermis is a dynamic multi-layered structure that performs a broad range of physiological functions. The epidermis is avascular in comparison to the dermis and has a thickness of approximately 100 microns.[20] The epidermis is normally subdivided into four anatomical regions. The innermost layer is the stratum basale, which is also referred to as the stratum germinativum. The next three regions are the overlying stratum spinosum, the intermediate stratum granulosum, and the outermost layer known as the stratum corneum.[11] The unique features of each of these regions are discussed in the subsequent sections of this chapter.

Corneocytes, also known as keratinocytes, compose the majority of epidermal cells. There is a constant turnover of corneocytes in all regions of the epidermis. Migration of cells occurs in an upward direction from the innermost layers of the

epidermis to the surface of the skin. As the corneocytes travel through the epidermis a variety of enzymatic processes change the chemical composition and structural organization of the cells.[32] Upon reaching the surface, the corneocytes are eventually shed from the body. The turnover rate through the complete epidermis is approximately 28-42 days.[21]

Although blood vessels are absent from the epidermis, nutrient exchange occurs via passive diffusion through the interstitial space.[4] The structure, composition, and organization of the corneocytes and lipids in each of the regions of the epidermis correlate with the state of differentiation and physiological function. The cellular structure and relative thickness in each of the respective layers of the epidermis are illustrated in Figure 2-2.
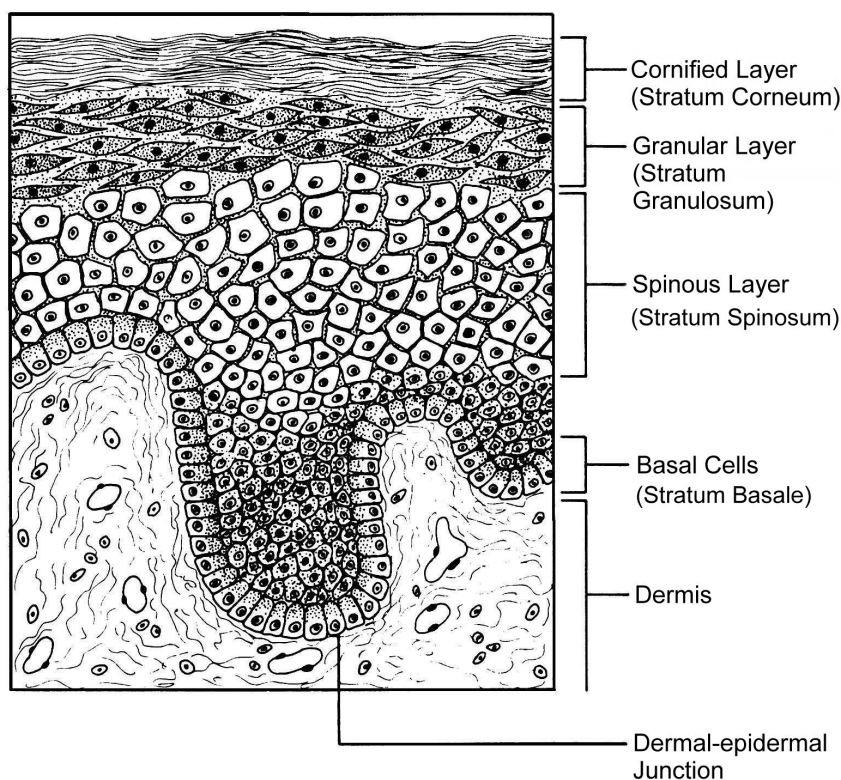
Figure 2-2: Relative thickness and structure of corneocytes in the various layers of the epidermis. Figure reproduced from Schaefer and Redelmeier.[4]

2.3.1 Stratum Basale

The stratum basale, also known as the basal layer, consists of a band of columnar cells located directly above the dermis. The cells in this region are physiologically active and possess intact cell membranes, functional nuclei and typical cellular organelles such as mitochondria and Golgi apparatus.[21] The stratum basale is the source of all corneocytes found in the epidermis. Upon mitosis the corneocytes gradually migrate upward. After leaving the stratum basale, the corneocytes lose the ability to perform cellular division.

The lipids present in the stratum basale primarily consist of phospholipids. The phospholipids make up the cell membranes of the corneocytes in this region of the epidermis.[4] The interior of the corneocytes contain bundles of the fibrous protein keratin. Keratin exhibits a high affinity for water,[24] although it is extremely insoluble in water.[33] An additional property of keratin is that it has a high sulfur content due to the cysteine residues of the protein.[24]

Connection between adjacent corneocytes is made by fibrous proteinaceous units called desmosomes. The desmosomes maintain connection between the corneocytes as they migrate toward the surface of the epidermis. The desmosomal connections are believed to degrade in the uppermost layers of the stratum corneum to facilitate corneocyte exfoliation.[22] The corneocyte production rate in the stratum basale leads to the formation of approximately one new cell layer per day. As the cells mature they migrate into the stratum spinosum at approximately the same rate to maintain constant basal layer thickness.[34]

2.3.2 Stratum Spinosum

The stratum spinosum lies directly on top of the basal layer. The corneocyte cells of this region are shaped like ovoids. The surface of the corneocytes possess spinous extensions that help to maintain adhesion between adjacent cells.

The interior of the cells contain larger bundles of keratin filaments. The concentration of keratin bundles in the stratum spinosum corneocytes is higher than in the basal layer corneocytes. The corneocytes in the upper layers of the stratum spinosum contain newly developed organelles known as lamellar granules.[11] Enclosed within the lamellar granules is an abundance of phospholipids, glycolipids and cholesterol organized into lamellar sheets.[35,36] The lamellar granules also contain enzymes that begin to synthesize the lipids that eventually fill the intercellular space of the stratum corneum.[37]

2.3.3 Stratum Granulosum

The corneocytes of the stratum granulosum exhibit a gradual transition in chemical composition and structural organization as they migrate toward the surface of the skin. As the corneocytes move upward through successive layers of the stratum granulosum they gradually begin to lose their ovoid shape as they become more elongated and flattened. The concentration of proteins continues to increase and highly cross-linked proteins begin to aggregate around the outer periphery of the corneocytes. The number of lamellar granules also increases in the stratum granulosum. The lamellar granules begin to organize near the corneocyte borders to facilitate the extrusion of the internal lipids and enzymes into the intercellular space.[36−38] The lipid composition of the granular layers also exhibits a gradual increase in the relative concentration of ceramides, cholesterol and fatty acids.[4,6,39]

2.4 Stratum Corneum

The outermost layer of the skin is the stratum corneum. The stratum corneum is described in detail in this section of the report because it is generally regarded as the dominant barrier to transport in the epidermis.[20,23,24,40−42] The excellent barrier properties of the stratum corneum are mostly provided by the chemical and

structural changes that occur in the corneocytes in the underlying layers of the epidermis. Barrier functions of the stratum corneum include the retention of water within the body and protection from the invasion of external species such as toxins and microorganisms.[19,43]

The stratum corneum is a relatively thin tissue structure that ranges in thickness from 10 microns on the underside of the forearm[20] to a few millimeters on the soles of the feet.[44] The macroscopic structure of stratum corneum consists of a network of anucleate proteinaceous cells known as corneocytes embedded in a lamellar lipid matrix. The structure is often idealized as a two-compartment brick-and-mortar network where the corneocytes are represented by the bricks and the intercellular lipid is represented by the mortar.[45,46]

The assignment of the skin transport barrier to the stratum corneum was first based on tape-stripping experiments.[47] For example, the stratum corneum layers were removed by repeated application and removal of adhesive tape. A dramatic increase in drug influx and water efflux was observed upon removal of the stratum corneum.[48,49] Many studies have been conducted that support this assignment.[35,50−53] An amazing property of the stratum corneum is that the highly efficient transport barrier resides within such a narrow domain.[54] Increased water loss in severely burned patients, often leading to dehydration, provides a striking example of the importance of the stratum corneum in restricting transdermal diffusion.

Until recently,[24] many researchers studying transdermal diffusion have described the stratum corneum as being a dead membrane with relatively invariant properties. This conclusion was partly based on the fact that the corneocytes of the stratum corneum lack the organelles required for cellular division. The conclusion was also supported by the observation that the stratum corneum has a much lower

water content than most of the other soft tissues in the body. Despite this anecdotal evidence, much of the recent literature suggests that the stratum corneum is a highly functionalized membrane with considerable enzymatic activity.[55]

2.4.1 Corneocytes

As mentioned earlier, the source of corneocytes in the stratum corneum is the underlying granular layer. The corneocytes comprise 70-90% of the total volume of the stratum corneum[17] with the remainder consisting primarily of lamellar sheets of lipids.[56] Corneocytes are approximately disk shaped with an average diameter of 30 microns and a thickness of approximately one micron.[11,57,58] There are approximately 15 to 20 layers of corneocytes stacked on top of each other in the stratum corneum.[22,59,60]

The corneocytes are filled with keratin filaments surrounded by a dense band of interwoven fibrous proteins located at the outer edges of the cell. A monolayer of covalently bound lipids is attached to the proteins located on the outermost surface of the corneocytes.[61] The lipid monolayer consists of hydroxyceramides with attached ω-hydroxyacids possessing chain lengths of 30-34 carbons.[22] The integrated protein-lipid monolayer envelope enclosing the corneocytes provides the cells with excellent structural integrity and may serve as a scaffolding for the intercellular lipid bilayers.[35] The structure and composition of the proteinaceous envelope is dramatically different than the typical phospholipid bilayer membrane of other cells in the body.

2.4.2 Stratum Corneum Lipids

The source of the stratum corneum's permeability barrier characteristics are generally attributed to the unique composition and structural organization of the intercellular lipids.[29,41,62−64] Support for this assignment was provided by experiments where removal of stratum corneum lipids by organic solvent extraction led

to a dramatic increase in water loss from the skin.[65,66] Furthermore, the lipid composition of skin from patients with pathologically compromised barrier function was found to be different than the skin of healthy patients.[63]

Considerable effort has been directed toward identifying the exact composition and structural organization of the stratum corneum lipids. Despite the progress made in this work, the relationship between lipid properties and corresponding anatomical function is not completely understood. An overview of the important chemical and physical characteristics of stratum corneum lipids is presented in this section. The currently accepted views of the relationship between lipid structure and anatomical function is also discussed. The intent was to develop a physical basis for interpretation of the transdermal iontophoretic studies conducted in this work. Manuscripts providing detailed discussions of stratum corneum lipids are available elsewhere.[14,17,22,35,56,67]

Lipids compose approximately 8 to 10% of the dry stratum corneum weight,[68] which corresponds to 5 to 30% of the total stratum corneum volume.[17] The types and relative composition of stratum corneum lipids is unique to this region of the epidermis. For example, stratum corneum lipids primarily consist of ceramides, cholesterol and fatty acids.[69,70] The fraction of these types of lipids is much smaller in the underlying stratum granulosum.

Another example of unique composition of stratum corneum lipids is provided by the relatively low weight fraction of phospholipids. In the stratum corneum, phospholipids comprise less than 5% of the total lipid weight fraction, as compared to 25% in the stratum granulosum.[64,66,71] Furthermore, phospholipids are usually found in great abundance as part of the cellular membranes present in other regions of the body.[72−74] The difference in lipid composition is significant because the bilayer phospholipids of cellular membranes are much more amenable

to aqueous transport. This provides a partial explanation as to why the unique composition of stratum corneum lipids is considered as the primary source of the membrane's low permeability characteristics.

Fatty acids and cholesterol. Fatty acids make up approximately 10 to 20 weight percent of stratum corneum lipids.[12,35,75] The fatty acids contain long hydrocarbon chains that are predominantly saturated (consisting of 20 to 28 carbons,[22] with most possessing 22 or 24 carbons).[35] The hydrocarbon tails of stratum corneum fatty acids are longer than fatty acids found elsewhere in the body. The longer tail lengths decrease the stiffness and rigidity of stratum corneum intercellular bilayers as compared to cellular membranes.[76]

Cholesterol, along with smaller amounts of cholesterol sulfate and the fatty acids of cholesterol esters, compose approximately 20 to 25 weight percent of the total lipids in dry stratum corneum.[12,35,75] Cholesterol is a common component of most lipid bilayer membranes.[73] Cholesterol is a relatively rigid molecule that influences packing of the lamellar bilayers. Depending on the composition of the other components in the lipid bilayers, cholesterol can either condense the lipids into more structured states[77] or fluidize the membrane as a whole.[4,71,78] The influence of cholesterol on the phase behavior of stratum corneum lipids is also dependent on temperature.[77]

Ceramides. Ceramides compose approximately 35 to 50% of stratum corneum lipids by weight.[12,14,35,75] Ceramides also make up the majority of polar lipids present in the stratum corneum, although they are generally much less polar than the phospholipids found in cellular membranes.[12] Ceramides are a heterogeneous family of lipids that possess a common backbone of sphingosine with lesser amounts of sphinganine and phytosphingosine. The head groups are linked to long-chained fatty acids. The sphingosine component of the ceramides provides the lipids with

a polar region. The fatty acids attached to the ceramides possess characteristically long hydrocarbon tails (22-34 carbons) that are predominantly saturated or mononounsaturated.[35] In general, lipids with extra unsaturation decrease the stiffness and rigidity of the intercellular bilayers.[76]

Ceramides are generally grouped into six or seven classes according to head group composition, hydrocarbon tail length and degree of unsaturation.[35,63,79,80] A schematic of the chemical structures of typical stratum corneum ceramides is presented in Figure 2-3. The sphingosine and phytosphingosine head groups are indicated by the bounding boxes in Figure 2-3. Ceramides 1, 2, 4, 5 and 6a possess sphingosine head groups whereas the fatty acids of Ceramides 3 and 6b are attached to phytosphingosine.[67]

The classification scheme shown in Figure 2-3 was developed to help identify the ceramide or combination of ceramides that provides the greatest contribution to the permeability barrier of the stratum corneum. Partial validation of this approach was provided by lipid extraction studies where patients with pathologically compromised barrier function exhibited lower proportions of Ceramide 1 in comparison to healthy patients.[63]

Ceramide 1 is also found in lower concentrations in healthy, nonkeratinizing oral stratum corneum, *i.e.,* the epithelial lining of the mouth, as compared to healthy epidermal stratum corneum.[35] Furthermore, the permeability of oral stratum corneum is generally higher than for epidermal stratum corneum.[48,81−83] These two observations strongly suggest that Ceramide 1 is the dominant contributor to the stratum corneum transport barrier.

The chemical structure of Ceramide 1 also suggests the compound can provide excellent diffusion limiting properties.[84] For example, Ceramide 1 consists of a sphingosine head group ester linked to a hydroxyacid with a hydrocarbon tail
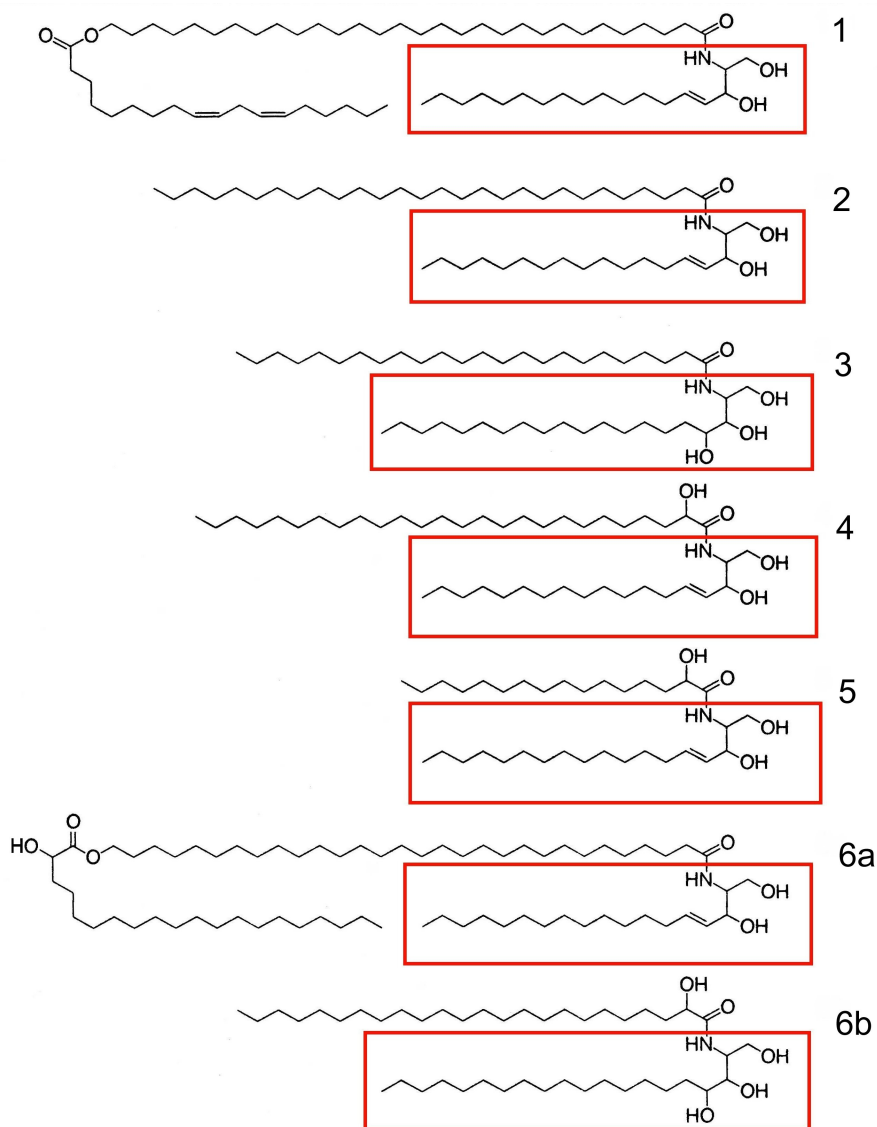
Figure 2-3: Classification scheme of stratum corneum ceramides based on chemical structure and composition. Figure adapted from Schürer.[17]

of much longer length than tails of the other ceramides present in the stratum corneum.[22] The longer hydrocarbon tail was used to develop a structural model for the organization of the intercellular stratum corneum lipids.[22,38] The model is discussed further in Section 2.4.4 The long hydrocarbon tail also provides the intercellular bilayer with a more rigid structure. The rigid organization of the bilayers provides for an enhanced transport resistance to diffusing compounds.[85]

2.4.3 Model Membrane Systems

The diverse number of lipids present in the bilayers makes it difficult to isolate contributions to overall barrier function from specific components. Determination of the relationship between lipid composition and barrier function *in vivo* is further complicated by the presence of sebaceous lipids on the surface of the skin. In order to study the relationship between relative lipid composition and membrane structure/permeability, a variety of model membrane systems have been developed.[64,69,71,84−89]

The model membrane approach has been successful in relating structure and composition to cellular function in bilayer membranes.[90] Model membranes for transdermal studies are typically constructed from the major classes of lipids found in this stratum corneum such as ceramides, cholesterol and fatty acids. The general approach involves adjusting the relative concentration of individual lipid species and observing the phase behavior and permeability. The studies were designed to isolate a specific lipid or combination of lipids that provides the dominant contribution to the overall permeability barrier. In addition, the influence of pH and temperature on the molecular organization of the model lipids has been investigated. For example, an increase in pH can promote the long range ordering of the bilayers.[84]

The development of model membranes has helped to identify many of the physical processes governing the interactions between stratum corneum lipids. Specifically, insight regarding the physical interactions between select classes of stratum corneum lipids has been obtained using this approach. For example, an increase in the relative concentration of cholesterol resulted in an increase in the permeability of a model lipid membrane. The observed increase in permeabil-

ity of the cholesterol rich membrane was only slightly higher than the membrane composed of lipids in proportions similar to normal stratum corneum bilayers.[75]

Although standard procedures are available, it is generally difficult to construct bilayers with compositions and structural organizations similar to those of anatomical stratum corneum lipids. Despite this experimental limitation, many of the important features of stratum corneum lipids that affect transdermal diffusion have been identified. A more complete understanding of the physical interactions that occur between stratum corneum lipids and the corneocytes is required to characterize transdermal diffusion completely. A general description of the molecular forces governing organization of stratum corneum lipids is presented in the next section.

2.4.4   Intercellular Lamellar Lipid Organization

The intercellular lipids of the stratum corneum form broad, sheet-like structures that are parallel to the surface of the skin.[79] The bilayers are vertically stacked into repeating units that results in an overall lamellar arrangement. Ruthenium tetroxide fixation studies have revealed that the relative thickness of the repeating lipid units exhibits alternating bands of broad and narrow regions.[38,91−93] The unit cell for the repeating lamellar structure was identified as being broad:narrow:broad. The thickness of the broad and narrow regions was estimated to be 13 μm and 6 μm. The alternating layer structure has been confirmed by X-ray diffraction studies.[94−96] It was proposed that the broad regions corresponded to the hydrocarbon tails of lipid bilayers. In contrast, the narrow regions were believed to be hydrocarbon tails of monolayers. The macroscopic organization of the lamellar lipids provides for a continuous hydrophobic phase around the corneocytes.

A structural model was developed to explain the alternating regions of broad and narrow lipid layers. It was proposed that the lipid regions of the fatty acids

and sphingosine were arranged on opposite sides of the polar head group. The broad regions corresponded to the long hydrocarbon tails of the fatty acids or the tail of a small fatty acid in line with the relatively short sphingosine tail. For example, the 30-34 carbon tail of Ceramide 1 could form a broad region and the lipophilic portion of the sphingosine would correspond to the narrow region. The alternating broad:narrow:broad lipid structure is illustrated in Figure 2-4. A single unit cell is presented where the broad:narrow:broad structure is covalently bound between two corneocytes. In the stratum corneum, the intercellular space between the corneocytes is filled with multiple unit cells stacked on top of each other. A polar region is provided to the layered lipid structure by the oxygen atoms of the fatty acids and sphingosine.
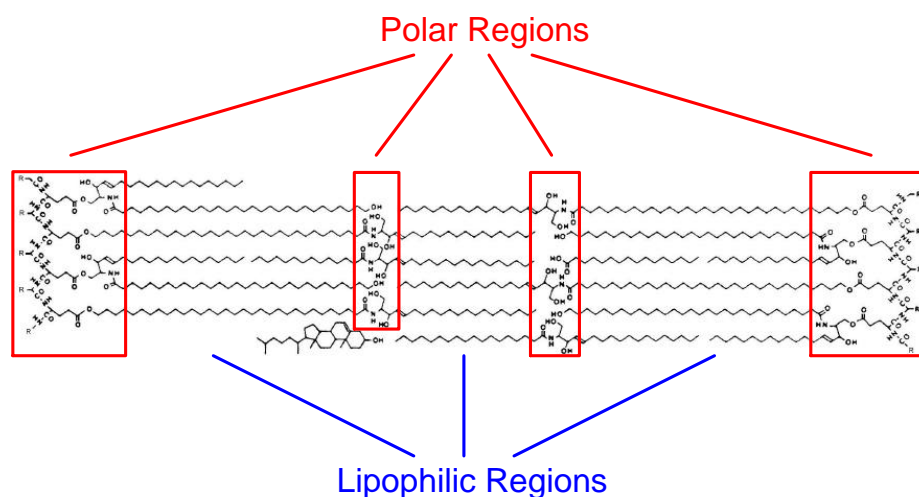
Figure 2-4: Alternating-width layered structure of stratum corneum lamellar lipids. The bounding boxes correspond to the polar regions of the stratum corneum lipids. Figure adapted from Swartzendruber.[38]

The segregation of the lipophilic and hydrophilic regions is caused by a trade-off between competing forces. For example, electrostatic interactions dominate near the surface of polar head groups and van der Waals forces and hydrogen bonding are responsible for the closely packed arrangements of the lipid hydrocarbon tails.[17]

It is generally accepted in the literature that the long hydrocarbon tails of the ceramides and fatty acids are ideally suited to form highly organized, densely packed membrane structures.[12] As mentioned earlier, extensive research has been conducted to characterize the interactions between diffusing molecules and the stratum corneum lipids. Particular emphasis has been placed on identifying the relationship between lipid microstructure and the diffusion rate of compounds. The biophysical properties of stratum corneum lipids, such as phase behavior and structural organization, have been studied by a variety of experimental techniques including ^{2}H nuclear magnetic resonance,[31,64,71] Raman spectroscopy,[88,97,98] infrared spectroscopy,[54,99−104] differential scanning calorimetry,[88,99,103,105,106] freeze-fracture electron microscopy,[36,59,71,94,107] ruthenium staining analysis[37,38,91] and x-ray diffraction studies.[12,94,96,108,109]

An important characteristic of stratum corneum lipids identified in these studies is that order-disorder phase transition temperatures are generally higher than the normal physiological temperature of 37 °C.[70,99] In contrast, the lipids present in the cellular membranes in other regions of the body have transition temperatures which are usually lower than 37°C.[20] The high transition temperature of stratum corneum lipids is consistent with more ordered packing arrangements at normal physiological temperature.

The relatively high phase transition temperatures of stratum corneum lipids are due to the large thermal energy required to fluidize the long hydrocarbon tails. For example, a two carbon increase in the length of hydrocarbon tail of phospholipids is accompanied by a 20°C increase in the gel to liquid crystalline transition temperature.[4] The densely packed arrangements of stratum corneum lipid bilayers typically observed at physiological temperatures greatly restricts the diffusion of water and ionic species directly through the membrane.

Lipid polymorphism. The mixture of lipids in the stratum corneum bilayers exhibit complex phase behavior. For example, the lipids demonstrate considerable lateral anisotropy in chemical composition and structural organization. Instead of assembling into a single phase with uniform composition, the bilayers are organized into clustered domains which are arranged in different packing states.[24,100] Within a given bilayer, stratum corneum lipids are predominantly assembled in either a lamellar gel or lamellar liquid-crystalline state.[69,97] Both of these phases correspond to highly ordered structures; however, in the liquid-crystalline phase the hydrocarbon tails are less tightly packed.[73,85]

The comparatively looser packing arrangement of liquid-crystalline lipids provides for a two order of magnitude increase in membrane fluidity upon transition from the gel state.[73] At higher temperatures ($> 80°C$) hexagonal packing of the lipids has been observed. The hexagonal packed structure is much more fluid and porous than the gel or liquid-crystalline phase which are associated with lower temperatures. A schematic of the structural organization of the various phases observed in stratum corneum lipids is presented in Figure 2-5.
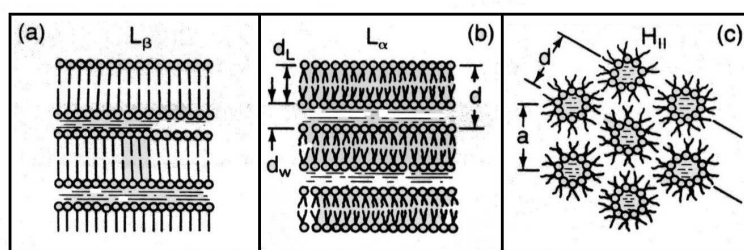
Figure 2-5: Structural organization of stratum corneum lipid phases. The lamellar gel phase, liquid-crystalline phase and hexagonal close-packed phase are denoted by the keys (a), (b) and (c), respectively. Figure adapted from Gennis.[73]

The observation of multiple phases within a given bilayer is a defining characteristic of lipid polymorphism.[78,110] Polymorphism is a well-documented property of lipids which has been used to provide a causal relationship between molecular structure and the regulation function of cellular membranes. Polymorphism is ob-

served in bilayers with uniform lipid composition as well as in more chemically diverse systems.[73,110] Temperature, water content, pH, protein content and local composition of lipids influence the structure of the localized phase domains of the bilayers.[24,73,78,84]

An important biophysical property associated with polymorphism is that lipids are able to diffuse laterally within a given bilayer.[73,77] The relatively high mobility of cellular lipid bilayers observed at physiological temperatures is consistent with the flexible and fluid packing arrangements seen in the liquid-crystalline phase. As the hydrocarbon tails of stratum corneum lipids are generally longer than in cellular membrane lipids, it is likely that there is less lateral diffusion in the skin.

Intercellular water. Water is an important contributor to the overall lipid organization of the stratum corneum bilayers. The weight percentage of water in the stratum corneum is approximately 20% as opposed to 70-80% in the stratum granulosum.[111,112] There is also a water concentration gradient across the stratum corneum. The concentration of water is highest in the innermost layers of the stratum corneum and gradually decreases toward the surface of the skin.[113] Most of the water is bound to the corneocyte proteins; however, results from x-ray scattering experiments suggested that small amounts of water were present in the intercellular lipid matrix.[95] The water was believed to reside along the polar head groups of the lipid bilayers.[95,114]

The stratum corneum possesses an amazing ability to absorb large quantities of water. It has been reported that water is absorbed in quantities equal to three to four times the dry weight of the stratum corneum.[59] The hydration process is not instantaneous. As the water content of the stratum corneum increases over time the corneocytes begin to swell. Experiments with fully hydrated skin revealed that

corneocyte expansion does not lead to significant structural alteration of individual lipid bilayers.[59,91,95,96,115,116]

The studies indicated that water was generally aggregated into small pools located near the jagged interfaces of lipid regions. The pools of water were believed to have been caused by phase separation between the hydrophobic regions of the lipid bilayers and the water.[59] Although not directly observed, the authors proposed that the pools were interconnected. Such a scheme could result in a continuous network of aqueous pathways for diffusion of ionic substances.

2.4.5 Domain Mosaic Model

A complete framework establishing the link between the morphological structure and chemical composition of stratum corneum lipids and the corresponding physiological function is not yet complete. The Domain Mosaic Model developed by Forslind incorporates the physicochemical properties of stratum corneum lipids with many of the observed anatomical features and physiological functions of the skin.[24] This model is an extension of the brick-and-mortar network model proposed by Michaels *et al.*[45] An inherent assumption of the brick-and-mortar model was that transport of molecules occurred through the lipid matrix and around the corneocytes. The corneocytes were assumed to be impermeable; however, absorption of compounds along the outside surface of the cells was considered.

The Domain Mosaic model was developed where the interactions between diffusing compounds and stratum corneum lipids were emphasized. The Domain Mosaic model considered the absorption of water into the corneocytes. For example, it was argued that the corneocytes require a small flux of water to prevent cell embrittlement. The model included a mechanism for diffusion of water through

the lipid bilayers. The proposed transport pathway was consistent with the composition and structure of the lipid matrix was incorporated into the model.

Forslind's Domain Mosaic model is an adaptation of the Fluid Mosaic model of phospholipid bilayers developed by Singer and Nicolson.[117] Lipid polymorphism was used extensively in both of these models to establish the relationship between membrane structure and transport properties. Forslind applied thermodynamic arguments to propose that stratum corneum lipids aggregate into crystalline sub-domains. The composition of each sub-domain would in turn consist of lipids with hydrocarbon tails of similar lengths. The high-energy grain boundaries at the interface between the crystalline sub domains could provide routes of aqueous transport across the lamellar lipids.

Once water diffused across a given bilayer it could then travel laterally in the aqueous regions located between the polar head groups of the lamellar bilayers. Transport would continue parallel to the surface of the skin direction until another lipid-phase grain boundary was encountered. The alternating process of lateral and transverse diffusion could provide for transport across the entire stratum corneum. An implication of this model is that aqueous transport occurs along a tortuous route. A tortuous pathway would require a longer diffusion path length in comparison to transport directly through the stratum corneum.

The relatively low observed transport rates of water across the skin is consistent with extended diffusion pathway.[75,81,114] For example, diffusion coefficients obtained from experiments with fully hydrated skin were 20-30% of their corresponding free solution values.[59,118] The lateral diffusion of water along the polar regions has been shown to be relatively fast.[119] Therefore, the rate limiting step in the overall transport process will likely be movement from one bilayer to another.

Although the Domain Mosaic model is fairly successful in relating the complex structure of stratum corneum lipids to the barrier properties of skin, unresolved issues remain. For example, the model cannot be directly applied for prediction of transport rates across the skin. It should be emphasized that the model was developed to account for the transport properties of the stratum corneum under normal physiological conditions. It is likely that the bilayers will be significantly disturbed by the presence of an electric field during iontophoresis. A variety of predictive models have been developed to account for the influence of the electric field on the transport of species through the skin.[120-124] Most of the predictive models are based on macroscopic transport theory and do not account for the range of interactions considered in the Domain Mosaic model. Additional discussion of predictive transdermal transport models is provided in Chapter 3.

2.5   Intercellular Appendages

Interspersed throughout the skin is a variety of appendageal structures which provide passageways for water and metabolites from the dermis to the surface of the skin.[10,125] The three types of appendages in human skin are hair follicles, sebaceous glands and sweat glands. The structure of these dermal appendages is illustrated in Figure 2-6.

Appendages account for only 0.1% to 1% of the total surface area of skin.[6,126] Although appendages make up such a small fraction of the overall skin surface, these macroscopic structures may serve as potential routes of transport for transdermal drug delivery. The proposal is based on the observation that appendages bypass the diffusion barrier of the stratum corneum and provide direct access to the dermis.[4] A brief discussion of the anatomical structure and physiological activity of these appendages is provided here. The objective was to describe the types
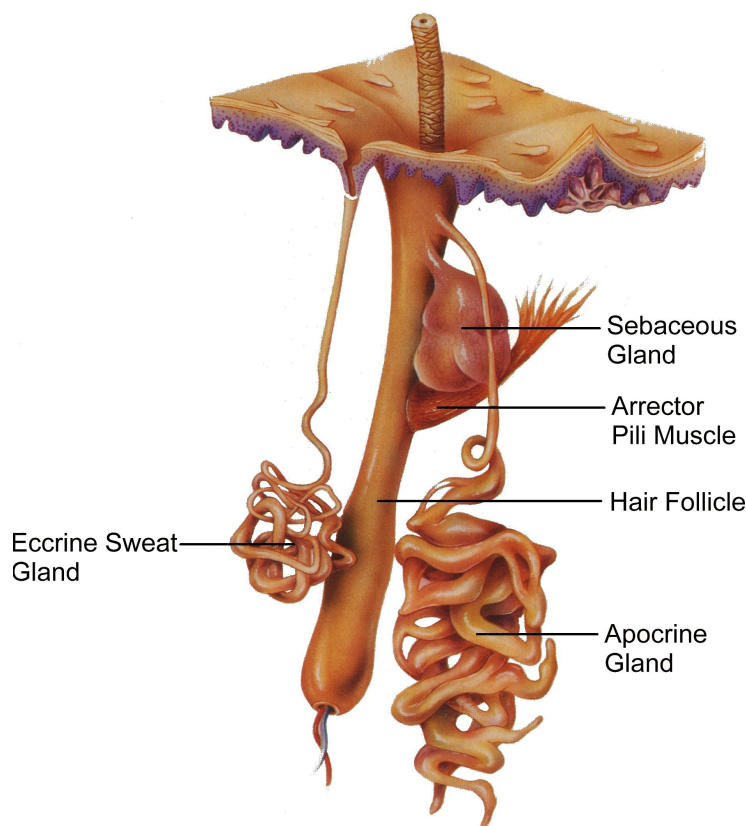
Figure 2-6: Structure of skin appendages that penetrate the stratum corneum. Figure reproduced from Orkin.[5]

of interactions that diffusing molecules might encounter as they pass through the appendages.

2.5.1 Hair Follicles

Hair follicles are composed of closely packed, proteinaceous cells assembled into a long, fibrous cylindrical shaft. Hair proteins are predominantly arranged in filaments that are cross-linked by sulfur bonds.[6] Similar to the proteins in the corneocytes, hair proteins are also made of keratin. In the lower regions of the skin the hair follicle is completely surrounded by cells. The cells help to anchor the follicle in the skin and promote growth of the shaft. In the upper regions of the dermis the hair follicle is located in the annular space of the follicular canal. The density of hair follicles varies throughout the body. A follicular density of 300-500/cm^2 is found on the scalp. The scalp has the highest density of follicles which

is in stark contrast to the soles of the feet where these structures are essentially absent.[4]

Associated with hair follicles are sebaceous glands. Sebaceous glands are pouch shaped structures that are connected via ducts to the hair follicle canals. Similar to hair follicles, the density of sebaceous glands also varies over the surface of the body. The highest density of sebaceous glands is found on the forehead and upper regions of the body. This maximum glandular density corresponds to 400 to 900 glands/cm^2. The remainder of the body has approximately 100 sebaceous glands/cm^2.[19]

Sebaceous glands excrete an amorphous mixture of lipids, known as sebum. Sebum is released into the hair follicle canals and deposited on the surface of the skin. The types of lipids present in sebum are primarily composed of triglycerides, wax esters and small amounts of cholesterol esters.[127] The triglycerides are partially hydrolyzed which maintains the acidic pH ($\sim$ 5) of sebum.[7,128] The acidic nature of sebum helps to provide skin with its antimicrobial character.[35,129] The thickness and content of sebum present on the surface of the skin varies greatly with anatomical location.[127] The high lipid content of sebum will likely prevent the passage of drug salts through the hair follicles.

2.5.2 Sweat Glands

Sweat glands form the majority of appendages present on the surface of the body. Sweat glands are classified as being either apocrine sweat glands or eccrine sweat glands. Apocrine sweat glands are predominantly found in the genital and underarm regions and therefore will not likely be subjected to iontophoresis. Eccrine glands comprise approximately 80% of the total sweat glands. They are distributed over the entire body with an average density of approximately 400 glands/cm^2.[4]

The main function of eccrine sweat glands is to facilitate thermoregulation via sweating. The structure of sweat glands consists of coiled tubular bundles located in the dermis which are attached to cylindrical ducts with openings on top of the stratum corneum (see, for example, Figure 2-6). The secretions from sweat glands are 99% water and have a pH of approximately 5 under rest conditions and 7 under maximum sweating.[130] The efflux of the aqueous secretions from the sweat glands may prevent the influx of material from the surface of the skin into the body. It could also be argued that the aqueous nature of the secretions might be favorable for the transport of ionic compounds.

2.6 Influence of Electric Fields on Skin Properties

The material presented in Sections 2-2.5 described the properties of skin under homeostatic conditions. During iontophoresis the application of current will induce a nonequilibrium electric field in the skin. Although an imposed current can increase the transdermal flux of charged compounds, skin properties may be altered during the process. The object of this section was to describe the behavior of skin during iontophoresis.

2.6.1 Electrical Properties of the Stratum Corneum

The electrical properties of the stratum corneum are directly linked to the chemical composition and structural arrangement of the membrane's constituent molecules. It is generally accepted that the stratum corneum possesses a net negative background charge.[114, 120, 131−135] The negative background charge favors the transport of cations over anions through the skin. The transport of anions is restricted in order to maintain electroneutrality within the membrane. Transference number experiments with monovalent cations of chloride salts provided the first evidence for this conclusion.[131, 133]

Although the negative background charge of skin is generally accepted in the literature, the exact source of the charge is still unclear. For example, it has been proposed that the protein residues in the corneocytes provide the negative background charge.[120,131] This would require an excess of amino acid residues with negative charges (such as carboxylic acid groups) as opposed to positive moieties such as amine groups.[131] It has also been proposed that a small fraction of the negative charge resides with the polar head groups of the lipid bilayers.[114] The overall charge is probably concentrated in the interior of the corneocytes with a minor component distributed throughout the lamellar lipid matrix.

Electroosmotic flow of water through skin lipids. In addition to supporting the preferential transport of cations, the negative background charge of skin can also facilitate the bulk flow of water during iontophoresis. The mechanism for the solvent transport is based on the assumption that the negative charge is localized along the surface of approximately cylindrical pores. The negative charge along the pore walls will introduce a diffuse region of positive charge in the adjacent electrolyte solution to maintain system electroneutrality.

The thickness of the diffuse region of charge is inversely related to ionic strength of the electrolyte and the charge density on the surface of the pore walls. When a voltage difference is applied across the skin during iontophoresis an electrical body force will be exerted on the thin layer of positively charged fluid. The electric force on the positively charged electrolyte will cause bulk fluid flow through the system. This type of electrically induced flow is referred to as electroosmosis which is a subset of the more general class of behavior known as electrokinetic phenomena.[136,137]

The mechanism for the flow of bulk water through skin was first proposed by Grimnes.[138] Evidence for electroosmosis during transdermal iontophoresis

was provided by experiments where neutral species were delivered through the skin.[121,131,135,139−146] Sophisticated mathematical models have been developed to account for electroosmotic flow through skin. The models are described in more detail in Section 3.2.

Macroscopic electrical properties of the stratum corneum. Skin has an isoelectric point at pH values between 3 and 4.[23,112,147] This implies that skin will be negatively charged when the pH of the surrounding solution is above this value and positively charged at more acidic pH. The isoelectric point must be considered when compiling drug formulations. Improper selection of solution pH could lead to neutralization of the background charge which would produce a reversal of the cation selectivity of the membrane. As a result, the iontophoretic delivery of the target molecule would become more difficult.[148]

Excised stratum corneum exhibits characteristically high polarization resistance values which are generally on the order of 100 kΩ/cm^2.[1,111] The electrical resistance of whole skin, as measured *in vivo*, is generally one to two orders of magnitude higher.[1,149] The cause for the difference in the *in vitro* and *in vivo* values of skin resistance remains unresolved. However, it is likely that the procedure used to extract the stratum corneum from the underlying layers of the skin is largely responsible for the lower electrical resistance of excised epidermal tissue.

The relatively high percentage of lipids and low percentage of water in the stratum corneum is responsible for the high electrical resistance of the membrane. Experiments have shown that the electrical resistance is inversely proportional to the water content of the stratum corneum.[112,150,151] Another interesting feature of skin is that the impedance can vary dramatically depending on anatomical location.[16,44] The *in vivo* impedance values from adjacent skin sites in the same anatomical region have been shown to differ by several orders of magnitude.[152]

Skin also exhibits a nonlinear response to large applied-current signals.[2,3,153,154] The nonlinear properties of skin correspond to decreased values of skin impedance with increased values of current density. The range of applied-current densities for the onset of nonlinear behavior lies between $0.1 \mu A/cm^2$ and $75 \mu A/cm^2$. The potential difference across the membrane at these applied-current densities falls between 0.1 V and 2 V.[3] The alterations to the skin may or may not be reversible. The degree of reversibility depends on the skin hydration, the amplitude of the imposed current and the duration of the applied current.[153]

The decrease in skin resistance to large electrical signals strongly suggests that the internal structure of the stratum corneum has been modified. Such structural modifications may introduce additional pathways for enhanced transport. A variety of mechanisms have been proposed for the formation of new pathways during iontophoresis. For example, it has been proposed that electrical burns on the skin are caused by localized regions of high current density.[3] The high current density pathways would likely experience Joule heating. If the increase in thermal energy was large enough, stratum corneum lipids could undergo phase transitions to more fluid and permeable configurations.[3] This hypothesis is supported by the observation of increased skin permeability at temperatures above the glass transition temperature of stratum corneum lipids.[155]

Influence of electrical field on skin lipids. The effect of electric fields on biological membranes is a well studied phenomenon. For example, the coupling of concentration polarization and potential gradients across cell membranes can produce short-duration current pulses. This type of mechanism is responsible for the conduction of nerve impulses and the contraction of muscle fibers.[156,157] The structures and mechanisms responsible for physiological and metabolic processes are diverse. For example, electrochemically coupled transmembrane exchange of

calcium in cardiac muscles occurs in hydrophilic protein channels that span across the lipid bilayers which enclose the muscle cells.[156] In the stratum corneum, the lamellar lipids lack these type of protein channels which helps to explain the low permeability of skin.

Another mechanism responsible for exchange of species across membranes requires an additional carrier molecule to complex with the physiologically active compound. The carrier molecule serves as an escort through the membrane in order to overcome the otherwise unfavorable interactions in the cellular lipid bilayers. This type of transport is responsible for the exchange of glucose across erythrocyte membranes.[73] The concept of carrier molecules was used to develop liposomes for topical delivery of therapeutic compounds.[158,159]

Typically for liposomal transport the ionic drug is encapsulated in the aqueous inner core of micelles. The outer lipophilic region of the micelles provides for energetically favorable interactions between the liposomes and the lamellar bilayers of the stratum corneum. The reduction of hydrophilic-hydrophobic interactions between the ionic drug and the lipid bilayers provides for enhanced transport rates.

A dramatic example of the therapeutic use of applied electric fields for manipulating biological bilayers is provided by electroporation. Electroporation consists of the application of high-voltage pulses in short duration to reversibly open pores in lipid bilayer systems. The technique was developed to introduce genetic material across the lipid bilayers of cellular membranes.[160−162] The electric fields applied during transdermal iontophoresis might also be expected to cause the formation of new channels for aqueous transport. However, the mechanism for structural changes will likely be different in iontophoresis as the electric fields are applied at much lower amplitudes for longer periods of time.

Indirect support for electrically induced alterations to the stratum corneum was provided by constant-current iontophoresis experiments where an increase in species flux was accompanied by decreased skin impedance.[112, 131, 163] There is also considerable evidence that a reduction in skin impedance has no effect on the magnitude of transdermal flux.[133, 164] It is possible that current may disrupt the lamellar lipids but the magnitude of the alterations may not be large enough to promote enhanced transport.

2.6.2 Iontophoretic Transport Pathways

There is considerable discussion in the literature pertaining to the route that diffusing molecules travel as they pass through the skin during iontophoresis. Transport through the stratum corneum can be envisioned to occur along the following pathways; intercellular, transcellular and appendageal. A schematic of the proposed pathways for transdermal drug delivery is presented in Figure 2-7. The
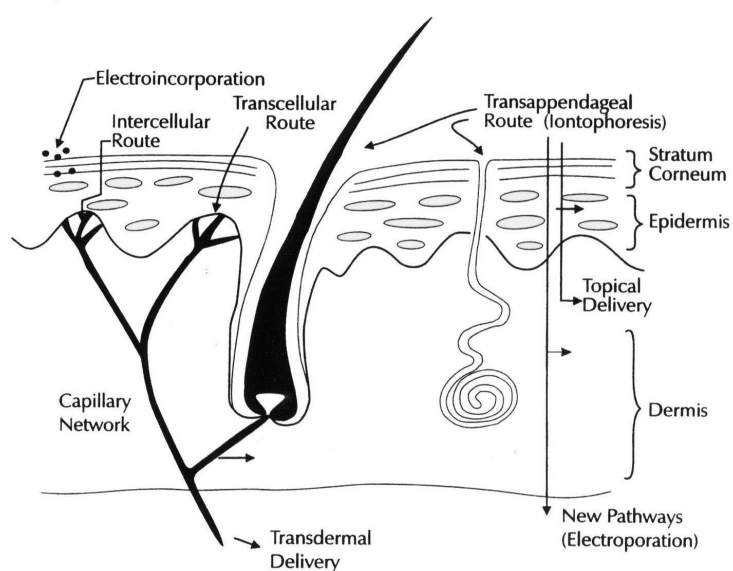
Figure 2-7: Potential routes for transport of therapeutic compounds during transdermal iontophoresis. Figure reproduced from Banga.[10]

intercellular pathway corresponds to diffusion through the lipid matrix of the stratum corneum. The intercellular pathway also includes the possibility of induced

pores or pathways caused by the alteration of the lipid bilayers during the passage of current. The transcellular route refers to transport which alternates between the lipid region and directly through the corneocytes. The appendageal pathway is described by transport through the macroscopic shunts in the stratum corneum such as hair follicle canals and sweat glands. Relatively little experimental evidence is available for the transcellular route; however, there is significant experimental support for both the intercellular[54,58,62,120,165] and the appendageal pathways.[28−31,166−168] During transdermal iontophoresis, it is likely that both intercellular and appendageal pathways contribute to the overall flux of molecules across the skin.

The physicochemical properties of the diffusing species will strongly influence the transport route during iontophoresis. For example, lipophilic compounds will most likely travel through the intercellular lipid matrix whereas sterically hindered, high molecular weight species might be expected to pass through the appendageal shunt pathways. Target molecule properties for predicting the magnitude and location of iontophoretic transport include charge, molecular weight, molecular size, pK_a and lipid-water partition coefficient.[23,81,120,139,145,169,170]

2.7   Summary of Skin Properties Affecting Iontophoretic Transport

In Sections 2.1-2.5 the structure and composition of human skin under normal physiological conditions was described. A dominant of those sections was that the physicochemical properties of skin are extremely complex. Although the anatomy and physiology of skin is complicated, some important generalizations related to percutaneous transport can be made. For example, the dominant barrier to transdermal drug delivery is the top-most layer of the skin, the stratum corneum. The thickness across the heterogeneous membrane is only 10 to 20 microns over most

of the body. The stratum corneum is comprised of disk shaped cells surrounded by a lamellar lipid matrix.

The unique composition and relatively high percentage of lipids in the stratum corneum is generally considered to provide a major contribution to the low permeability characteristics of the membrane. Although the cells of the stratum corneum, the corneocytes, are not capable of mitotic division there is considerable, physiological and enzymatic activity in this region.[55] Important characteristics of the stratum corneum include a low permeability to hydrophilic compounds and a relatively low percentage of water.

Section 2.6 describes the electrical properties of the stratum corneum. Major features of the stratum corneum under homeostatic conditions include a negative background charge and a high electrical resistance. Another important characteristic of stratum corneum is that the electrical resistance drops dramatically when the applied voltage is greater than the 0.1 to 2 V. It is imperative that these properties be considered for the development of transdermal drug delivery modalities such as iontophoresis. Although a comprehensive description of the interactions and mechanisms involved in iontophoresis remains unresolved, it is clear that an imposed electric field can enhance transdermal delivery rates of both ionic[120,142,171−179] and uncharged[121,131,135,139−146,178] compounds.

CHAPTER 3
MODELS FOR TRANSDERMAL IONTOPHORESIS

A variety of mathematical models have been developed to provide insight into the important factors affecting transdermal iontophoresis. These models have been used for the prediction of transdermal drug delivery rates for given values of applied current and as a tool for the identification of the mechanisms involved in the transport process. The approaches used to formulate these models are diverse, however most are based on continuum, hindered transport, nonequilibrium thermodynamic, or kinetic rate concepts.

The final sections of this chapter (see, for example, Sections 3.6.1 - 3.6.3) provide a discussion of ideal electric circuit models developed for the prediction of the impedance response of skin. Electrochemical Impedance Spectroscopy (EIS) is commonly used to study skin transport properties during iontophoresis. The formulation of the overall circuit network involves the semi-empirical addition of circuit elements until the model provides an accurate description of the skin impedance response. Upon the establishment of an appropriate network, a deductive process is then used to relate the properties of the skin to the individual circuit elements that comprise the overall network. A summary of the assumptions and limitations associated with each of the modeling frameworks is provided.

3.1   Nernst-Planck Continuum Models

One of the most common approaches for modeling transdermal iontophoresis is based on the Nernst-Planck definition of species flux through homogeneous media. Dilute-solution theory is also applied in these derivations. Several au-

thors have implemented the Nernst-Planck formalism to develop predictive expressions of species flux in steady-state[122,132,140,144,145,180−182] and time varying systems.[27,121,140,183,184]

The overall flux is driven by the electrochemical potential gradient and by the net flow of the bulk solution. The flux resulting from the electrochemical potential gradient is typically decoupled into an electromigration term that accounts for the force of the electric field on charged molecules and a diffusion term corresponding to activity or concentration gradient driven flow. The Nernst-Planck flux, that account for these driving forces, is presented by

$$N_i = -\frac{D_i z_i \text{F}}{\text{RT}} c_i \nabla \Phi - D_i \nabla c_i + v c_i \qquad (3\text{-}1)$$

where N_i is the flux density, D_i is the diffusion coefficient, z_i is the charge number of the species i, F is Faraday's constant, R is the universal gas constant, T corresponds to the absolute temperature, c_i is the concentration of species i, $\nabla \Phi$ is electrostatic potential gradient and v is the net velocity of the solution. The terms on the right hand side of Equation (3-1) correspond to the contributions to the overall flux from electromigration, diffusion and convection, respectively. Transport throughout the entire system domain is generally characterized by integrating the flux equations with appropriate boundary conditions. The approach leads to expressions for potential and concentration profiles within the membrane.

The nonlinear electromigration term in the flux expression makes direct analysis intractable except for in a few restricted cases. As a result, simplifying assumptions are usually invoked to obtain an analytical solution to the flux equation. For most of the models available in the literature it is assumed that the electric field through the skin is constant or that the system is everywhere electrically neutral.

The constant field assumption removes the nonlinearity in the electromigration term. The simplification allows for direct solution for the species flux under the

additional assumption of a time invariant system.[180] An alternative approach is to relax the constant field condition and assume the system is electrically neutral everywhere. In the restricted case where the electrolyte solution is composed of a single binary 1:1 salt, such as NaCl, application of the electroneutrality assumption will also lead to a system of equations that is amenable to analytical solution.

In clinical iontophoretic delivery systems, drug formulations are usually be composed of drug salts, buffers and supporting electrolytes. The electroneutrality condition is insufficient to provide for direct solution of the flux expressions corresponding to these more complex mixtures. Numerical methods must be implemented to obtain transdermal profiles of species flux, concentration and potential from mathematical models based on the Nernst-Planck definition of flux. A goal of the work presented here was to investigate the effect of solution composition on the drug delivery rate and the concentration, pH and potential profiles. In accordance with this objective, iterative numerical techniques were applied in the development of the model for transdermal iontophoresis. The details of the approach are described in Chapter 10.

3.2   Hindered Transport Models

As demonstrated in Chapter 1, skin cannot be described as being a homogeneous membrane. In order to account for the complex structure of the skin many authors have utilized hindered transport theory to develop mathematical models for transdermal iontophoresis.[120−124] Hindered transport theory is an extension of the Nernst-Planck description of flux where the effects of constrained flow geometries and electrostatic interactions on the fluid are considered. An inherent assumption made in the development of models for transdermal iontophoresis based on hindered transport theory is that transport occurs through aqueous pores in the stratum corneum. The hypothesized pores could be considered to be inte-

gral structures of the skin or temporary channels induced upon the application of current during iontophoresis.

The hindered transport or pore restriction model framework was originally developed to characterize flow through long, narrow passages such as capillaries and straight channeled porous membranes.[185−189] The diffusing particles are assumed to be of the same dimensions as the flow channels. Under these conditions, interparticle interactions and particle-wall interactions constitute a significant fraction of the overall resistance to flow through the membrane. The same types of interactions are also present in larger channels; however, in this situation, the relative influence on the hydrodynamic flow profile can usually be neglected. The approach has provided for successful prediction of species flux through capillary systems. In contrast, direct application of the standard Nernst-Planck flux expressions to similar constrained networks overpredicts transport rates as compared to experiment.

The general form for species flux based on hindered transport theory is directly analogous to the standard Nernst-Planck expression. However, the correction terms, H and W are introduced to account for the additional transport resistance through narrow channels. The flux expression for hindered transport theory is presented by

$$N_i = \epsilon \left[-HD_i \left(\frac{z_i \mathrm{Fc_i}}{\mathrm{RT}} \frac{d\Phi}{dx} + \frac{dc_i}{dx} \right) \pm W v_x c_i \right] \tag{3-2}$$

where the void fraction of the membrane is lumped together with the tortuosity factor in the parameter ϵ. H represents the hindrance factor for diffusion and migration and W represents the hindrance factor for convection. On a molecular scale, the term, H, accounts for steric and long-range electrostatic interactions. The term, W, accounts for the enhanced hydrodynamic drag on particles caused by the presence of the pore wall.

Predicted values for the hindrance factors, H and W, are usually obtained from correlations based on the ratio of the radii of the fluid particles to the radii of the pore walls. In general, the correction factors H and W increase as the size of the diffusing particles approaches the size of the pore openings. The standard expressions for the hindrance factors, H and W, developed by Anderson and Quinn[185] for spherical particles are given by

$$H(\lambda_*) = (1 - \lambda_*)^2(1 - 2.144\lambda_* + 2.089\lambda_*{}^3 - 0.0948\lambda_*{}^5) \tag{3-3}$$

$$W(\lambda_*) = (1 - \lambda_*)^2(2 - (1 - \lambda_*)^2)(1 - \frac{2}{3}\lambda_*{}^2 - 0.163\lambda_*{}^3) \tag{3-4}$$

where the independent variable λ_*, is defined by

$$\lambda_* = \frac{r_{particle}}{r_{pore}} \tag{3-5}$$

where $r_{particle}$ is the particle radius and r_{pore} is the pore radius.

3.3 Refined Hindered Transport Models: Solute Interactions with Pore Walls

An attractive feature of the hindered transport formalism is that the negative background charge of skin can be considered. It is typically assumed that the charge is located on the surface of cylindrical pores with large aspect ratios. The negative charge on the pore wall causes a diffuse region of positive charge to develop in the electrolyte solution adjacent to the pore surface. The function of the positively charged region is to maintain system electroneutrality

The Debye screening length provides an estimate for thickness of the diffuse charge region.[136] The expression for calculating the Debye length is given by

$$\lambda = \left[\frac{\epsilon RT}{F^2 \sum z_i{}^2 c_{i,bulk}} \right] \tag{3-6}$$

where ϵ, R, T and F are the solution permittivity, which is also referred to as the dielectric constant, universal gas constant, absolute temperature and Faraday's

constant. The bulk solution concentration and charge number of an ion are signified by z_i and $c_{i,bulk}$. The expression for the Debye length states that the thickness of the diffuse region is inversely proportional to ionic strength.

When an electric field is applied across a charged, porous membrane, an electrical body force will be exerted on the volume of ionic solution located in the diffuse charge region adjacent to the pore walls.[136] If the electric field is the oriented perpendicularly to the pore walls, bulk fluid flow can occur. The phenomenon of electrically induced fluid flow is known as electroosmosis. A schematic of flow through charged capillaries is presented in Figure 3-1. The fluid streamlines converge at the mouth of the pore which decrease the probability that a fluid particle will enter the channel.
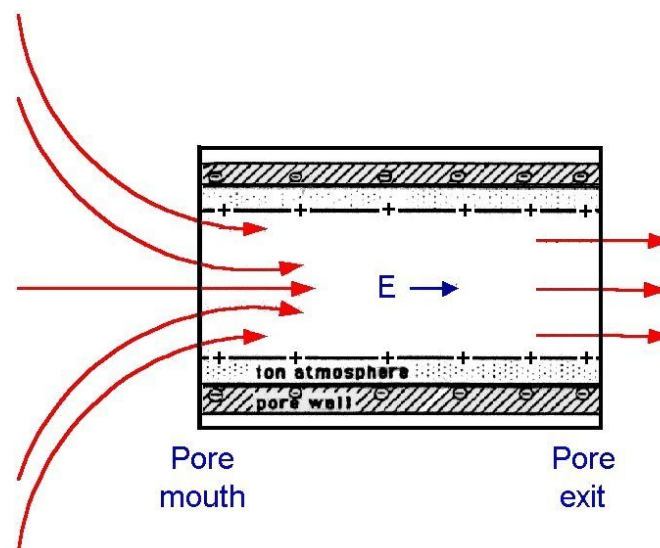
Figure 3-1: Schematic representation of fluid flow through constrained pores. Flow trajectories of the fluid particles are denoted by arrows.

The situation within the skin during iontophoresis is generally consistent with the conditions required for electroosmotic flow. For example, it can be envisioned that the negative background charge of the stratum corneum is located on the surface of the straight cylindrical aqueous pores. Although there is considerable experimental evidence suggesting the presence of aqueous pores during ionto-

phoresis, the exact structure of these pores has not been completely characterized.[30,31,54,58,62,118,122,165] The assumption that transport occurs through straight channeled pores seems unrealistic given the complex morphological structure of skin. Even if transport does occur through cylindrical pores it is likely that there is a distribution of pore sizes in skin. Despite these limitations the types of molecular interactions considered in hindered transport theory can explain the observation of electroosmotic flow during iontophoresis.

Many authors have applied models of transdermal iontophoresis based on hindered transport theory to estimate an equivalent pore size based on measured flux values.[120,123] As part of the calculation process, the electric field through the skin was considered to be uniform. Calculated values of the pore radii were in the range of 8-30 Å. The estimates for the pore sizes provided in the literature could be used with the corresponding models to predict upper and lower bounds of drug delivery rates for a given current.

The predicted dimensions of the cylindrical pathways are much smaller than those associated with the appendageal pathways. This could imply that transport is occurring intercellularly or that the effective pore sizes present in the appendages are smaller than their structural dimensions. Models based on hindered transport theory have provided insight into potential routes of transport through the skin during iontophoresis. Although application of the hindered transport models suggest mechanisms that affect transdermal iontophoresis, the approach cannot be applied directly to estimate species fluxes.

Roberts *et al.* developed a refined model of transdermal iontophoresis based on the hindered transport formalism where the effects of partially ionized solutes and irregularly shaped particles were considered.[124] The model also accounted for electrostatic interactions between the solution ions and a charged pore wall.

The general objective of the model was to develop an expression for relating the molecular volume of a drug to the iontophoretic transport rate. The species flux corresponding to the refined model was presented by

$$N_i = PC_{ionto,i}c_i \tag{3-7}$$

where $PC_{ionto,i}$ is the overall iontophoretic permeability coefficient and c_i is the solute concentration. The iontophoretic permeability coefficient is defined by

$$PC_{ionto,i} = \frac{2u_i z_i \widehat{f_i} F I_T (\Omega PRT_i)}{(k_{s,c} + k_{s,a})\left[1 + \widehat{fu_i}\theta_i^u + (1 - \widehat{fu_i})\theta_i^i\right]} \pm (1 - \sigma_i)v_{sol} \tag{3-8}$$

where the first and second terms on the right hand side correspond to the contributions to the overall flux from electromigration and convection, respectively. The parameters contributing to the permeability coefficient, Equation (3-8), included the solute mobility, u_i, species charge number, z_i, Faraday's constant, F, total current through the skin, I_T and the permselectivity of skin, Ω. The other variables required for calculation of the iontophoretic permeability coefficient included the pore restriction term, PRT_i, the donor and receptor solution conductivities, $k_{s,d}$ and $k_{s,r}$, the fractions of ionized and unionized solute, θ_i^i and θ_i^u, the pore reflection coefficient, σ_i and the solvent velocity, v_{sol}.

All of the parameters for the permeability coefficient were known or could be calculated by standard correlations with the exception of the pore restriction term, PRT_i, and the corrected convection coefficient, $(1 - \sigma_i)$. For example, the fraction of ionized and unionized solute were calculated from published pK_a values and measured solution pH. The pore restriction term and corrected convection coefficient were calculated according to Equations (3-3) and (3-5) which are implicit functions of the pore radius. The pore size was determined iteratively such that difference between the iontophoretic flux predicted from the model and the flux determined by experiment was minimized.

A limitation of the refined hindered transport model is that *a priori* estimation of iontophoretic drug fluxes is not possible. This is because the relationship between pore size and drug physicochemical properties of the drug must determined experimentally. Bulk solution values of physicochemical properties, such as solute mobility and pH, were used for the regression of Equation (3-7) to the flux data. It is likely that these parameters will be different in the constrained environment of the narrow pore. Although these types of errors will lead to inaccurate estimates of pore sizes, the model accounts for the interactions which are expected to be important for transdermal iontophoresis.

3.4   Nonequilibrium Thermodynamic Models

Numerous mathematical models based on nonequilibrium thermodynamics have been developed for molecular transport across biological membranes.[156,190] Models of transdermal iontophoresis based on nonequilibrium thermodynamics are attractive because skin subjected to constant current will not be under equilibrium conditions. Although many models for the exchange of metabolic species across cellular membranes have been developed from nonequilibrium thermodynamics only a limited number of attempts have been made to apply the infrastructure to transdermal iontophoresis.[172,175,191−193]The goal here is to provide a summary of the application of nonequilibrium thermodynamics for biological membrane transport. An outline of the governing equations and limitations of the theoretical infrastructure is provided.

The application of nonequilibrium thermodynamics for modeling biological membrane transport was pioneered by Kedem and Katchalsky.[194−196] The objective of their work was to account for specific interactions between the membrane and the electrolyte solution components. In this work, the solvent was considered as a diffusing species. Therefore, bulk fluid flow, which has been observed

in biological membrane transport, was considered explicitly.[194] The treatment represented a point of departure from the classical Nernst-Planck formalism for diffusion processes. The governing equations for membrane transport developed in this work are still widely accepted by the biological community. The derivation of the equations for membrane transport based on nonequilibrium thermodynamics presented here loosely follows the explanation presented by Friedman.[156]

An underlying assumption of nonequilibrium thermodynamics, also known as irreversible thermodynamics, is that the forces and fluxes of a given system are directly related. This assumption also holds for equilibrium thermodynamics, however, the approach for defining the flux equations is different. For example, the electrochemical potential gradient is considered to be the driving force for the flux in the Nernst-Planck formalism.

The forces and fluxes for nonequilibrium thermodynamics are constrained by the dissipation function. The integrated form of the dissipation function anticipation function is defined according to

$$\Phi = T \int_0^a \frac{d_i S}{dt} dx \tag{3-9}$$

where Φ is the integrated form of the dissipation function, $\frac{d_i S}{dt}$ corresponds to the rate of entropy generation per unit volume of the membrane and the absolute temperature, T, is placed outside the integral because biological systems are essentially isothermal. The integrated form of the dissipation function is usually applied for membrane transport because it is difficult to assess the local forces within the interior of the membrane.

The fluxes are related to the dissipation function according to

$$\Phi = \sum_i J_i X_i \tag{3-10}$$

where the J_i's are the fluxes and the X_i's are the driving forces for the fluxes. Equation (3-10) states that the fluxes contribute to the entropy of the system at a rate that is proportional to the driving force. The general form of species flux for irreversible thermodynamics, subject to the constraint defined by Equation (3-10), is described by

$$J_i = \sum_i L_{ij} X_i \qquad (3\text{-}11)$$

where the only new variable, L_{ij}, is the phenomenological coefficient. The phenomenological coefficients are proportionality constants that represent the contribution to the species fluxes from a given force. The subscript j, is included to account for the interaction of species i, with all other components in the solution. The approach accounts for interactions between the solvent and the various solute molecules. Interactions with molecules of the same type are also considered (i.e. when $i = j$).

Since explicit consideration of all of the possible interactions between the various components in the system is provided by this framework, the number of phenomenological coefficients increases dramatically as the number of species in a given system increases. Upon inspection of Equation (3-11) the number of phenomenological coefficients necessary to characterize the system should equal n^2, where n is the number of unique components in the system. However, the Onsager reciprocal relation states that $L_{ij} = L_{ji}$, which reduces the number of unique phenomenological coefficients to $\frac{n^2+n}{2}$. For multicomponent solutions it is usually assumed that the interactions between a given solute and the remaining solutes do not affect the flux of the selected species. The assumption implies $L_{ij} = 0$ for $i \neq j$ which reduces the number of independent coefficients to 2n-1.

A difficulty with this modeling approach is that the phenomenological constants must be determined experimentally. Any modification to the solution com-

position requires additional experimentation to determine a new set of phenomeno-logical coefficients. The manner in which the flux equations for irreversible thermodynamics are defined provides no information regarding the transport mechanisms.[156] Furthermore, the structure of the physical system cannot be assessed by nonequilibrium thermodynamics. The approach instead yields expressions for relating mass transport across membranes to measurable quantities such as solution compositions. The large number of parameters required to characterize the system coupled with lack of mechanistic insight of the transport process may explain the limited application of irreversible thermodynamics for mathematical models of transdermal iontophoresis.[193,197]

3.5   Kinetic Rate Theory Based Models

The multilaminate structure of the stratum corneum has prompted the development of mathematical models for transdermal drug delivery which assume that the overall transport process is composed of a series of discrete transport events.[60,154,198] The approach has also been applied successfully to model transport through cellular membranes.[199] It is assumed that drug compounds must overcome a series of potential energy barriers in order to pass through the skin. The spatial distribution of the potential energy barriers is generally considered to be located at the interfacial region between the various layers of the stratum corneum. Formal relationships between the transport rate across each of the energy barriers and the local concentration is established by the application of kinetic rate theory, also referred to as the theory of activated rate processes.[60] The general approach for modeling transdermal transport by this formalism is outlined here; however, the methodology was not applied for interpreting the experiments presented in this report.

An expression for species flux can be developed by assuming that particles move across a given energy barrier in both the forward and backward directions. Generally a unique amount of energy is required for particle movement from each side of the barrier. The probability for a transport event to occur is inversely proportional to the energy required to overcome the barrier. In addition, the probability for transport across an energy barrier is directly proportional to the local concentration of a species. The velocity of particles, or transport rate, over the barrier is directly related to the probability associated with movement from the respective direction. The expressions for the forward and backward velocities based on the local concentration are

$$v_{f_{i,j}} = K_{i,j}c_{i,j} \tag{3-12}$$

$$v_{b_{i,j}} = K_{i,j+1}c_{i,j+1} \tag{3-13}$$

where $v_{f_{i,j}}$ and $v_{b_{i,j}}$ are the velocities of species i crossing barrier j in the forward and backward direction, respectively. The forward and backward rate constants are signified by $K_{i,j}$ and $K_{i,j+1}$. The concentrations of species i to the left and right of barrier j are indicated by $c_{i,j}$ and $c_{i,j+1}$.

The net flux across a given energy barrier, defined in terms of the velocities associated with each direction of transport, is

$$J_{i,j} = v_{f_{i,j}} - v_{b_{i,j}} = K_{i,j}c_{i,j} - K_{i,j+1}c_{i,j+1} \tag{3-14}$$

where $J_{i,j}$ is the flux of species i across barrier j and the remaining terms are defined according to Equations (3-12) and (3-13). The rate constants $K_{i,j}$ and $K_{i,j+1}$ are typically functions of energy barrier length, temperature, and electrical state of the system. The general approach for calculating flux through a system is to include expressions of the form presented in Equation (3-14) for each energy barrier.

The expressions are used in combination with the mass conservation principle to determined the overall flux.

An Arrhenius form can be assigned to the rate constants to reflect the dependence on the state of the system. For example, the rate constants are commonly presented by

$$K_{ij} = k_{i,j} e^{\left(\frac{-\Delta G_{i,j}}{RT}\right)} \tag{3-15}$$

where $k_{i,j}$ is the proportionality constant, $\Delta G_{i,j}$ is the Gibbs free energy and RT is the system thermal energy. The exponential term corresponds to the activation energy required to cross an energy barrier. It should be noted that proportionality constant, $k_{i,j}$, has an implicit dependence on the width of the energy barrier.

The Gibbs free energy term can be deconvoluted to include a driving force based on the electrical potential and a term corresponding to the chemical potential. With this type of separation it is possible to examine the effect of electrical potential on the transport rate of charged compounds.

A schematic representing the sequence of transport events which are assumed to occur within the skin is shown in Figure 3-2. Transport through the skin is envisioned as occurring from left to right. The skin surface is located at the left-hand side of the figure and entrance into the circulatory system is assumed to occur at the right hand side. The vertical dashed lines correspond to the locations of the potential energy barriers.

An advantage of models for transdermal iontophoresis developed from the activated rate formalism is that fluxes can be predicted in the absence of a direct mechanism for the transport process. The difficulty lies in identifying correct values for each of the proportionality constants, $k_{i,j}$. Furthermore, selection of the number and spatial locations of the energy barriers present in the stratum corneum is completely arbitrary. Most authors have assumed that there are 15-20
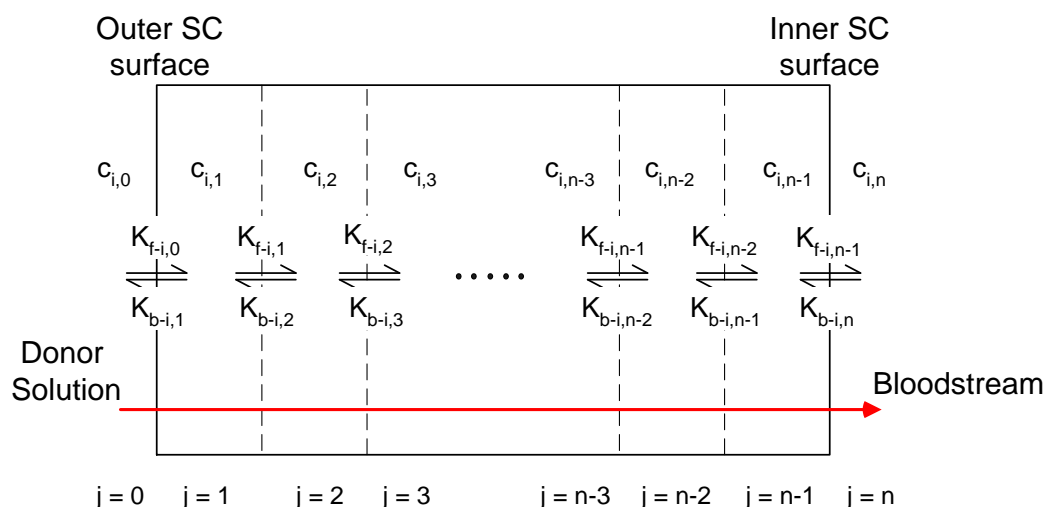
Figure 3-2: Proposed scheme for step-wise transport of dissolved species through the stratum corneum. The dashed lines represent the locations of the potential controlled transport events.

energy barriers, which is consistent with the number of corneocyte layers in the stratum corneum. Although this choice seems logical it is possible that there is an alternative distribution of transport events within the skin.

3.6 Electrochemical Impedance Spectroscopy

All of the mathematical models discussed up to this point were developed to characterize drug delivery rates during transdermal iontophoresis. For many of these models careful consideration was given to the physicochemical properties of the skin. An implicit assumption of the transport models was that the properties of skin remained constant during iontophoresis. There is considerable evidence that the transport properties of skin change during iontophoresis (see, for example Section 2.6). A variety of techniques including Transepidermal Water Loss Measurements (TEWL)[150,152,200−202] and Electrochemical Impedance Spectroscopy (EIS)[44,150−152,163,200−207] have been applied to study the influence of applied current on skin transport properties. Both of these techniques have been used to investigate skin properties in the absence of applied currents.[16,50,65,102,153,208−210] The ma-

terial presented here describes the application of ideal electric circuit networks for modeling the impedance response of skin.

3.6.1 Electrical Circuit Models of Skin Impedance Response

Electrochemical Impedance Spectroscopy (EIS) has been applied extensively for the investigation of skin transport properties. The widespread use of EIS is motivated, in part, by the technique's ease of application combined with the relatively short time required to collect a spectrum. For example, an impedance spectrum of skin with the frequency range of 65 kHz to 0.1 Hz with 12 measuring points per logarithmic decade can be collected in less than 10 minutes. A more detailed description of the theoretical and practical aspects of Electrochemical Impedance Spectroscopy is provided in Section 4.1. This section provides a discussion of the models presented in the literature for the interpretation of skin impedance data. The advantages and limitations of the various models are described.

Despite the extensive application of Electrochemical Impedance Spectroscopy for transdermal drug delivery research, unambiguous interpretation of the data is not yet available. Since EIS is a small-signal, frequency domain technique it is amenable to analysis with equivalent electric circuits. The general approach is to combine individual circuit elements, such as resistors in capacitors, in an iterative fashion until the network produces an impedance response that is consistent with the skin spectrum.[57,133,149,152,155,208,211,212] Upon formulation of an appropriate equivalent circuit, the important features of skin are deduced from the individual elements of the network.

A simple circuit network commonly used to represent the impedance response of stratum corneum[50,133,155,213] consists of a resistor in series with a parallel combination of a resistor and a capacitor. A schematic representation of the circuit is presented in Figure 3-3. For the system shown in Figure 3-3, the leading resistor R_e

represents the electrolyte solution resistance, the parallel resistor R_{skin} is the Ohmic resistance of skin, and C_{skin}, corresponds to the bulk capacitance of skin.
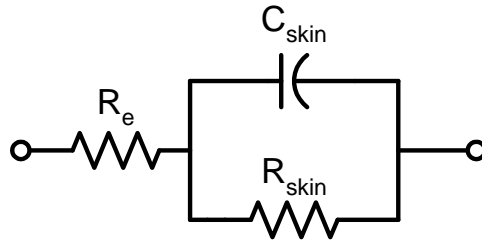
Figure 3-3: Equivalent circuit model for stratum corneum impedance. R_e, R_{skin} and C_{skin} represent the electrolyte solution resistance, the resistance of skin and the capacitance of skin, respectively.

More than one explanation has been offered as a physical justification for the capacitor C_{skin} in the equivalent circuit model of skin. For example, the macroscopic structure of the stratum corneum is roughly analogous to the configuration of a parallel plate capacitor. The high concentration of stratum corneum lipids serves as the dielectric material which provides for the separation of charge.[133,155] For a typical impedance experiment 1-5 cm^2 of stratum corneum is probed. The relatively large surface area of the stratum corneum in comparison to the membrane thickness (~ 20 μm) is also similar to the geometrical configuration of a parallel capacitor. An alternative interpretation for the capacitor is that it represents the double layer charging capacitance of the transport pathways through skin. The charging process is believed to be associated with absorption reactions between the ions in solution and the permanently charged sites of the stratum corneum.[211]

The frequency-dependent impedance response of the simple three-element circuit, in terms of the individual circuit elements, is established according to

$$Z_{R-CPE} = R_e + \frac{R_{skin}}{1 + (j\omega\tau)^{\alpha}} \tag{3-16}$$

where ω is the angular frequency of the AC signal and τ is the characteristic time constant for the system. The time constant is related to the individual circuit ele-

ments according to $\tau = R_{skin}C_{skin}$. The characteristic frequency, ω_c, is equal to the inverse of the time constant, τ. The exponent α, is equal to one for the simple circuit shown in circuit shown in Figure 3-3. When α is between 0 and 1 the circuit is referred to as a constant phase element. The significance of the constant phase element discussed in more detail in Section 3.6.2. In general, parameter values for the circuit elements are determined by regressing the model to skin impedance data. Complex nonlinear least squares (CNLR) regression routines are usually implemented with a computer to provide for rapid determination of the circuit parameters.

A typical plot of skin impedance data presented in the impedance-plane is shown in Figure 3-4. An impedance-plane plot displays the imaginary component of the impedance, Z_j, on the positive y-axis and the real part of the impedance, Z_r on the x-axis. This type of plot is sometimes referred to as a Nyquist plot. The impedance response of the three-element circuit with the same characteristic frequency and the same polarization impedance of skin, as determined by experiment, is displayed as the top curve of Figure 3-4. Visual inspection of the impedance-plane plot shows that the three-element circuit is insufficient to model the skin impedance response.

3.6.2   Refined Circuit Models

In general, CNLR regression of the three-element circuit shown in Figure 3-3 to most skin impedance spectra will not provide statistically adequate fits. A typical impedance-plane plot of skin impedance data, as shown in Figure 3-4, exhibits a depressed semicircle where the locus of the semicircle lies below the real axis. This type of impedance response is characteristic of a system with a distribution of relaxation processes. For example, impedance-plane plots of metallic electrodes often exhibit a similar depression. It is generally accepted that morphological in-
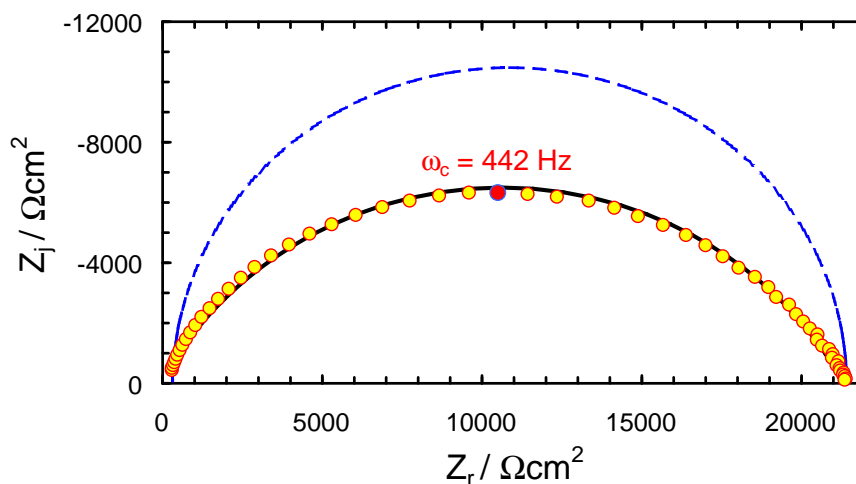
Figure 3-4: Impedance-plane plot of skin immersed in 50 mM CaCl$_2$. Experimental data is signified by open circles. The dashed line represents the three-element circuit model fit to the data. The solid line corresponds to constant phase element representation of data, where α = 0.695 and the characteristic frequency, ω_c, was 442 Hz.

homogeneities on the metallic surface cause a distribution of residual stresses at electrode/electrolyte interface. This morphological variability results in a distribution of activation energies associated with the interfacial charge transfer reactions and, hence, a distribution of time constants.[214]

As the simple three-element circuit is insufficient to model most distributed systems, more sophisticated circuit networks have been developed to describe the impedance response of skin. The refined circuit models of skin generally fall into two categories; 1) Transmission line models and 2) Constant phase element models. The circuit corresponding to transmission lines consists of RC (resistive-capacitive) elements combined with inductors and resistors in a "ladder" network arrangement. The circuit diagram for the general transmission line model is presented in Figure 3.5(a). The transmission line circuit was originally developed to model power losses that occur over long distances in high-voltage cables.[215]

The transmission line circuit has been adapted for use with heterogeneous systems, such as ionic conduction through porous electrodes and membranes with

interconnected pores.[216,217] In practice, the inductors are omitted from the transmission line model for skin impedance.[212] As a result the transmission line circuit of the skin reduces to the network shown in Figure 3.5(b). The parallel network of interconnected RC elements can be interpreted as a spatial distribution of the physicochemical properties of the skin. Superposition of the time constants associated with the circuit elements leads to an impedance response can provide statistically valid representations of skin impedance spectra.[212]

(a)

(b)
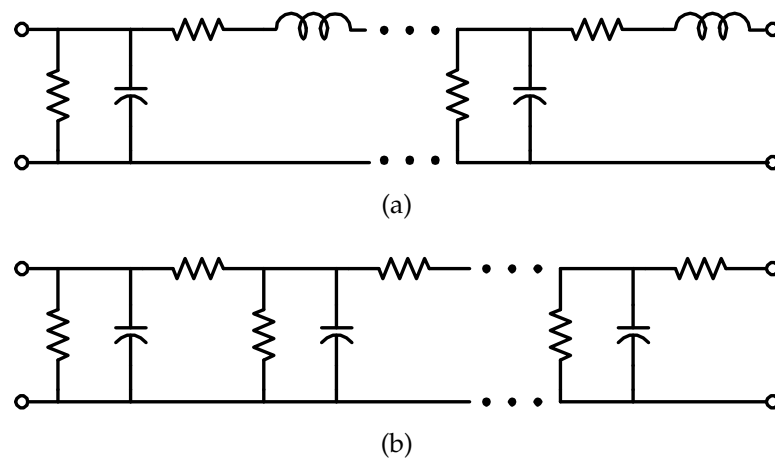
Figure 3-5: Equivalent circuit models of transmission lines. (a) General transmission line circuit. (b) Transmission line circuit for stratum corneum. The inductors are omitted as there is no obvious physical basis for incorporating the elements into the model for skin.

The second class of circuit models for the impedance of skin are constructed by replacing the capacitor, C_{skin}, in the three-element circuit shown in Figure 3-3 with a constant phase element. The constant phase element circuit for skin is presented by Figure 3-6. As described in Section 3.6.1, the complex impedance expression for the constant phase element network is presented by Equation (3-16). The impedance response of skin can generally be described by this expression when the exponential parameter, α, is in the range of $0.65 < \tau < 1.0$.[151,208,211,212] The magnitude of α reflects the relative displacement of the semicircle locus from the real axis in
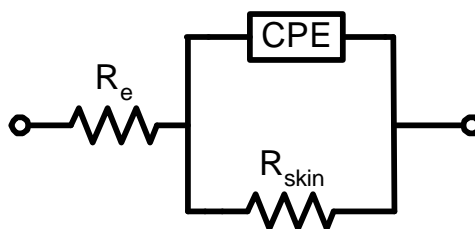
Figure 3-6: Constant phase element network representation of stratum corneum impedance. Similar to the circuit shown in Figure 3-3, R_e, and R_{skin} represent the electrolyte solution resistance and the resistance of skin, however, CPE represents a constant phase element.

the impedance-plane where smaller values of α correspond to greater degrees of semicircle depression.

Similar to the transmission line, the constant phase element network can model systems with a depressed semicircular impedance response. The major difference is that the constant phase element circuit provides for a continuous distribution of time constants, whereas the transmission line model leads to a discrete distribution. Furthermore, the time constants for the constant phase element are symmetrically distributed about the critical frequency. It has been proposed that the constant phase element is representative of a size or charge distribution of the aqueous pores which provide the transport pathways through skin.[211]

3.6.3 Limitations of Ideal Circuit Models

A limitation of electric circuit models is that multiple circuit networks can be constructed to provide statistically valid fits for a given impedance spectrum. The individual elements of the competing networks are likely to be configured differently. Therefore, assignment of physical properties to the elements of each network can lead to very different interpretations for skin impedance.

Knowledge of skin physicochemical properties can be used to justify the acceptance of an appropriate model. For example, Konturri *et al.* found that transmission lines and constant phase element networks provided satisfactory representa-

tions of skin impedance.[211,212] The authors selected the constant phase network as the better model because they could not find a physical justification for the inclusion of the inductor.[212] Although this type of deductive process seemed reasonable, a better approach would be to apply complementary experimental and modeling techniques to select the most appropriate circuit network. A methodology for modeling skin impedance is described briefly at the end of this section.

A constraint of ideal circuit models is that the elements which compose the overall circuit network, *i.e.*, the resistors, the capacitors and the inductors, etc., are assumed to behave linearly with respect to potential.[218] This implies that the proportionality between the input and output signals for a given element is independent of the potential across the element. For real systems, there is a limited range of potential where the design equations for ideal circuits are applicable. For skin, this range corresponds to 0.1-2 V,[3] (for further discussion see Section 2.6).

It should be noted that the properties associated with a given circuit element, such as resistance, capacitance and inductance are established without close regard to the internal structure of the element. This "lumped-sum" description of ideal circuit element properties greatly limits the utility of circuit networks for interpretation of the physical properties and the kinetic processes of the skin. A more rigorous methodology for interpreting impedance data is to develop deterministic models based on the governing equations which describe the physics and chemistry of skin. The model can then be regressed to skin impedance spectra to obtain parameter estimates for the physical properties of the system. This approach has been applied successfully for a limited number of systems such as the electrodissolution of copper; however, the methodology has not yet been applied to complex systems such as human skin. More detailed descriptions of the general procedure are provided in the literature.[219−223]

3.7 Summary

The literature provides a wide array of mathematical models of transdermal iontophoresis with varying degrees of sophistication. The models were developed from the traditional Nernst-Planck equilibrium description of transport, the formalism for hindered transport through constrained geometries, nonequilibrium thermodynamics and kinetic rate theory. The number of unique chemical species included in the models reviewed here was usually limited to two or three ions. Results from these models must be viewed cautiously because the body contains a complex mixture of ionic compounds. Predictions of the concentration and potential profiles within the skin cannot be obtained from these models with the exception of the simplest models based on Nernst-Planck theory.

A common feature of most of these developments is that the electric field across the skin is assumed to be uniform. Although this assumption greatly simplifies the mathematical analysis of the governing equations, the physical basis for this assumption is questionable due to the heterogeneous structure of the skin. Despite these limitations, the mathematical models discussed here have provided a method to predict drug delivery rates for given applied potentials and external electrolyte solution compositions.

In addition to the large number of models developed to predict transdermal drug delivery rates, a variety of ideal circuit networks have been developed to model the transport properties of skin. Electrochemical Impedance Spectroscopy is a commonly used technique to study the transport properties of skin and the circuit networks were developed to model the impedance response of skin. It is important to point out that although the various circuit models described in this review can adequately represent skin impedance data, the approach is severely limited in that there is not necessarily a direct connection between the individ-

ual elements of the circuit network and the physicochemical properties of the skin. Despite these limitations, the work reviewed here serves as a good starting point for the development of clinical systems and/or more sophisticated models of transdermal drug delivery.

CHAPTER 4
EXPERIMENTAL METHODOLOGY

The development of iontophoretic transdermal drug delivery devices requires a fundamental understanding of the influence of current on transdermal drug delivery rates and skin transport properties. Electrochemical Impedance Spectroscopy (EIS) was applied in this work to study the macroscopic transport properties of heat-separated cadaver skin. The modulation protocol for the EIS studies was modified to prevent large potential differences from occurring across the skin. The EIS work was supplemented by monitoring the response of skin when subjected to applied DC potential and current biases. An array of potential and current bias amplitudes were applied to determine the effect of these control variables on skin transport properties.

The influence of current on transdermal drug delivery rates was investigated with UV-vis absorption spectroscopy. The absorption spectroscopy technique allowed for concentration changes, and hence drug fluxes, to be inferred from changes in the light intensity passing through the system. A custom dual-beam spectrometer system was developed to account for drift in the baseline response of the experimental apparatus. The absorption spectroscopy system was designed for concurrent use of EIS during the transdermal delivery studies. The combined methodology was selected because skin transport properties and drug delivery rates could be measured simultaneously. The impedance data were analyzed to identify the stationary and linear portions of the impedance spectra. The key features of the experimental techniques are described in this chapter.

4.1 Electrochemical Impedance Spectroscopy

Electrochemical Impedance Spectroscopy (EIS) has been applied for the investigation of a wide variety of electroactive systems including ceramic, polymeric and biological membranes.[222,224−231] The negative background charge of skin makes EIS an attractive methodology for studying skin because it can be applied easily and in a noninvasive manner. A brief overview of electrochemical impedance spectroscopy is provided because the technique was used extensively in this work. Detailed discussions of the technical and theoretical issues associated with electrochemical impedance spectroscopy are available elsewhere.[219,220,232,233]

4.1.1 Principles of Electrochemical Impedance Spectroscopy

Electrochemical impedance spectroscopy is a small-signal technique where a sinusoidal current or potential perturbation is imposed on the system of interest and the corresponding potential or current response is measured. Comparison of the input and output signals provides for the measurement of the impedance at a given perturbation frequency. An appealing feature of EIS is that systems with characteristic time constants distributed over a wide-range of time scales can be studied. For example, transient phenomena, such as diffusion, double layer charging and charge transfer reactions, typically occur over periods of $1\text{-}10^{-1}$ s, $10^{-2}\text{-}10^{-3}$ s and 10^{-4} s, respectively.[234] Investigation of the various processes is accomplished in a typical experiment by incrementally adjusting the frequency of the incident waveform over a wide range and measuring the impedance at each frequency.

Electrochemical impedance spectroscopy has been applied extensively for studying interfacial electrochemical reactions such as in the corrosion of metals. The technique is also suitable for the investigation of solid-state and membrane systems. A short discussion of electrochemical reactions is provided to introduce
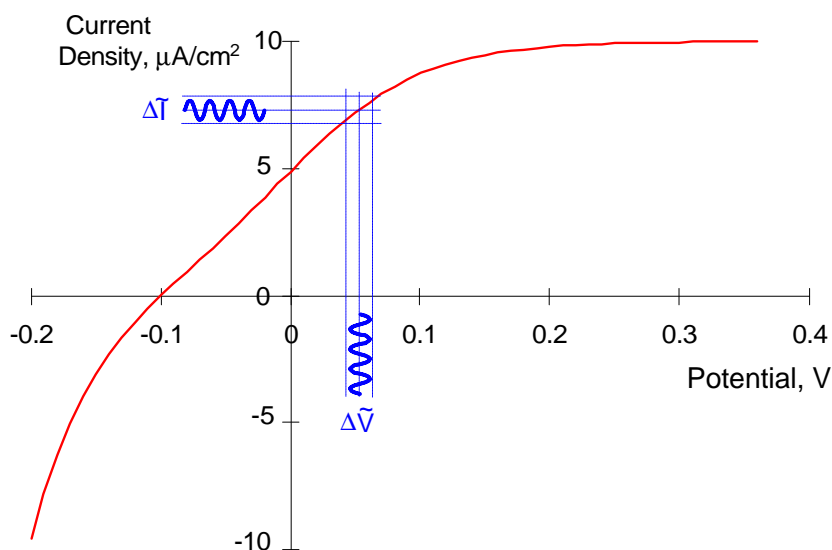
Figure 4-1: Polarization plot for a typical electrochemical system.

the theoretical foundation for impedance spectroscopy. The driving force for a typical electrochemical reaction is provided by the electrostatic potential. A measure of the reaction rate is provided by the current. The rate of a typical electrochemical reaction displays an exponential dependence on potential as described by the classical Butler-Volmer equation.[137]

The relationship between reaction rate and potential is commonly displayed graphically with polarization plots. A typical polarization curve, as shown in Figure 4-1, is constructed by plotting current density on the ordinate and potential on the abscissa. During an impedance experiment the sinusoidal potential or current perturbation is applied about a set point on the polarization curve. Ideally, the sinusoidal perturbation is small enough to maintain linearity in the system. Displacement of the system from the steady-state condition allows the current-potential relationship to be probed in a noninvasive manner.

The theoretical framework of impedance spectroscopy is derived from linear systems theory.[220] The governing equations for electrochemical impedance microscopy are based on the assumption that linearity is maintained in the system

over the course of the experiment. The instantaneous response, $y(t)$, of a linear system is related to the forcing function, $x(t)$, according to

$$b_0 \frac{d^n y(t)}{dt^n} + b_1 \frac{d^{n-1} y(t)}{dt^{n-1}} + \ldots + b_n y(t) = a_0 \frac{d^m x(t)}{dt^m} + a_1 \frac{d^{m-1} x(t)}{dt^{m-1}} + \ldots + a_m x(t) \quad \text{(4-1)}$$

where the right side of Equation (4-1) is a linear combination of the terms associated with the input function. The terms on the left side of Equation (4-1) correspond to the contributions to the system response.

In an electrochemical impedance spectroscopy experiment, the forcing function, $x(t)$, corresponds to either the sinusoidal potential or current input signal and the response, $y(t)$, is the current or potential output signal. For an experiment conducted under galvanostatic control, the current is the input signal and the potential is the response signal. The instantaneous value of the input current waveform can be expressed in polar and Cartesian coordinates, respectively, according to

$$\tilde{I}(t) = I_0 \sin(\omega t) \quad \text{(4-2)}$$

and the response signal corresponding to the potential at time, t, is

$$\tilde{V}(t) = V_0 \sin(\omega t + \phi) \quad \text{(4-3)}$$

where I_0 and V_0 are the amplitudes of the current and potential signals, respectively. The frequency of the perturbation is denoted by ω, j is $\sqrt{-1}$ and ϕ is the phase lag of the output response. Replacement of I_0 with V_0 in Equation (4-2), the expression for the input signal, and V_0 with I_0 in Equation (4-3), the expression for the response signal, provides the appropriate relationship for experiments conducted under potentiostatic modulation.

The complex impedance of the system is obtained from the input and output signals by way of a transfer function which is analogous to Ohm's law. In Carte-

sian and polar coordinates the impedance, Z, is calculated by

$$Z = \frac{\tilde{V}}{\tilde{I}} = \frac{V_0 \sin(\omega t + \phi)}{I_0 \sin(\omega t)} = \frac{V_0 e^{\phi}}{I_0} = |Z| e^{\phi} \tag{4-4}$$

The complex impedance can be converted from polar to Cartesian coordinates and vice versa by applying Euler's identity. The relationship is expressed according to

$$|Z| e^{j\phi} = |Z| (\cos\phi + j \sin\phi) \tag{4-5}$$

The real part of the impedance is described by

$$Z_r = |Z| \cos\phi \tag{4-6}$$

and the imaginary part as

$$Z_j = |Z| \sin\phi \tag{4-7}$$

The modulus of the impedance is related to the real and the imaginary components according to

$$|Z| = \sqrt{Z_r{}^2 + Z_j{}^2} \tag{4-8}$$

and the phase angle, or phase lag, of the system is

$$\phi = \arctan\frac{Z_j}{Z_r} \tag{4-9}$$

A variety of analytical and graphical approaches have been developed to interpret impedance responses. The techniques generally rely upon the impedance quantities defined in Equations (4-6) through (4-9). A few of the commonly applied presentation formats for impedance data include Bode, impedance-plane and admittance plots. The Bode representation displays the modulus of the impedance and the phase angle versus frequency. An impedance-plane plot, also known as a Nyquist plot, displays the imaginary part of the impedance, Z_j, versus the real part of the impedance, Z_r. A typical impedance-plane plot of human skin is shown
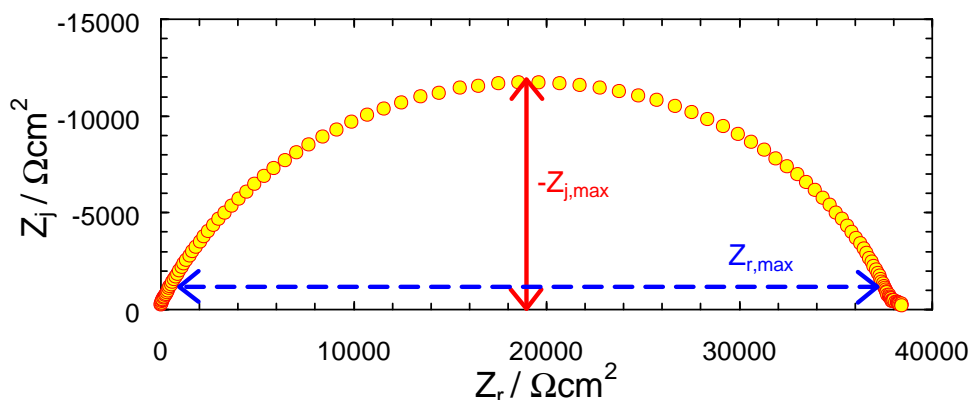
Figure 4-2: Impedance-plane plot of skin immersed in 100 mM NaCl. The maximum magnitudes of the real and imaginary components of the complex impedance are presented by the dashed horizontal and solid vertical lines, respectively.

in Figure 4-2. The shape of the impedance response of skin, as presented in the impedance-plane, is often described as being a "depressed" semicircle.

The terminology "depressed" semicircle has been adopted because the maximum magnitude of the imaginary component of the impedance, $-Z_{j,\max}$ response is less than one half of the maximum of the real part, $Z_{r,\max}$. The depressed semicircular response can usually be modeled by the constant phase element circuit presented in Section 3.6.2 which suggests that skin possesses a distribution of characteristic time constants. A depressed semicircular shaped impedance response is generally consistent with a linear system with constant properties. A combination of impedance-plane plots and ideal circuit models can provide estimates for the polarization impedance, capacitance and characteristic frequency of skin. The procedure to extract the circuit parameters is described in Section 3.6.1.

The inverse of impedance, known as the admittance, is frequently presented as an alternative method for displaying impedance data. The general form of admittance plots is similar to the Bode display format or the impedance-plane plot presentation of impedance data. Admittance plots are appealing because the admittance quantity is sensitive to changes at high frequencies.
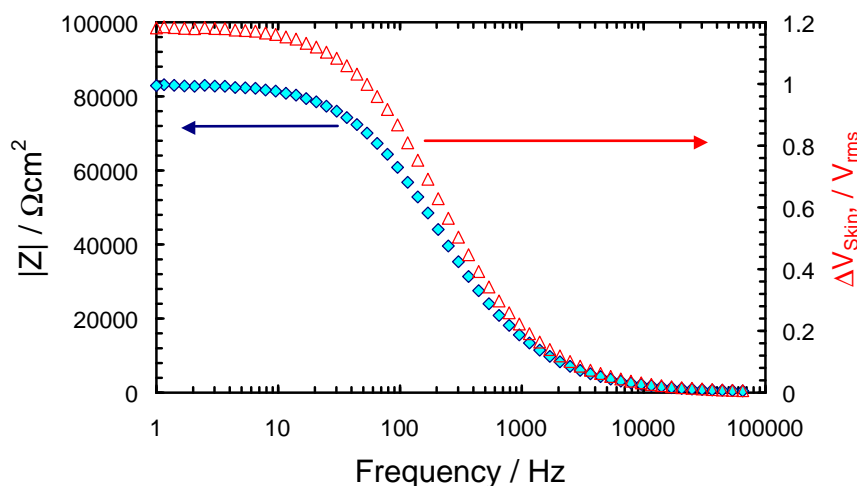
Figure 4-3: Bode magnitude plot of a typical impedance response of skin. The diamonds represent the measured values for the modulus of the impedance. The triangles represent the complex potential difference across the skin induced by the 10 μA current perturbation.

4.1.2 Modulation Procedure for EIS Experiments

The delivery of therapeutic drugs by iontophoresis is proportional to current; therefore, galvanostatic modulation of EIS is required in order to keep the baseline current at the desired value.[148] Traditional galvanostatically modulated EIS measurements, which maintain the current perturbation amplitude at a fixed level, will cause the voltage response to reach its greatest value at the low frequencies where skin exhibits its maximum impedance value (see, for example Figure 4-3).[153] The large induced potentials can alter the properties of the skin.

To prevent large potential swings during the experiment, a predictive algorithm was developed to adjust the current at each frequency such that the potential would not exceed a predetermined value.[235] The algorithm for variable-amplitude galvanostatic modulation of impedance experiments was based on a Taylor's series expansion about a given point on the polarization curve. Customized subroutines were written in the LabVIEW G® for Windows programming environment to incorporate the algorithm into the experimental control software. A summary of the design equations developed for the algorithm is provided in Appendix B.

4.1.3   Methodology

A preliminary study was conducted to determine the efficacy of the traditional constant-amplitude galvanostatic modulation method for measuring skin properties by impedance spectroscopy. Ideally, skin properties should not be altered by the experiment as impedance spectroscopy was developed to be a noninvasive technique. The approach here was to collect multiple impedance spectra by constant-amplitude modulation. The amplitude of the current perturbation was adjusted before each spectrum was collected. The perturbation amplitudes for the impedance scans were between 10 μA and 100 μA. The objective was to determine whether the skin impedance response was independent of the current perturbation amplitude. The results from these experiments are presented in Section 5.1.

For the next portion of this work, two types of galvanostatically modulated EIS experiments were conducted. The first experiment maintained the amplitudes of perturbation at values of 1 μA and 10 μA. For the second type of experiment, the current amplitude was adjusted at each frequency to maintain the voltage response of the skin below a predetermined value chosen at the beginning of the experiment.[235] In accordance with the variable-amplitude galvanostatic modulation algorithm, previously measured impedance values were used to predict the impedance at the frequency of the measurement being conducted.

A series of variable-amplitude impedance experiments were conducted on each sample of skin, where, periodically, a series of constant-current galvanostatic impedance measurements were performed. To compare the difference between the two techniques, a series of replicate variable-amplitude experiments was performed subsequent to the constant-amplitude studies. The idea was to determine the most appropriate modulation strategy for conducting skin impedance experiments.

Both modulation techniques were applied to skin samples immersed in NaCl solution and in $CaCl_2$ solution, respectively. The AC current perturbation was superimposed about a DC current bias of 0 Amperes/cm^2. The skin impedance spectra collected from both modulation techniques are discussed in Section 5.2. In general, 12 measurements were taken for logarithmic decade for frequencies between 65 kHz and 1 Hz. For some of the impedance experiments, the low-frequency portion of the spectra was extended to 0.1 Hz

The methodology described up to this point was designed to identify an experimental approach for collecting skin impedance spectra in a noninvasive manner. For the next phase of this study, impedance experiments were performed to determine the influence of prolonged electrolyte exposure on skin transport properties. The approach was to collect skin impedance spectra intermittently over a period of 24 hours. The variable-amplitude galvanostatic modulation strategy was applied for the hydration study. The sinusoidal current perturbations were modulated about a DC bias of 0 μA/cm^2. The target amplitude of the potential drop across the skin was set to $\pm$ 10 mV. The study provided a baseline to estimate the changes in skin transport properties caused by the addition of water into the membrane. The results from this investigation are presented in Section 6.2.

It has been proposed that the recovery of skin properties to large electrical perturbations is more rapid in divalent cation solutions than in monovalent cation solutions.[152] The influence of solution composition on the recovery of skin properties is described in Section 6.3. A detailed discussion of the experimental approach for the study is provided there. If it is shown that the recovery of skin properties is enhanced in the presence of divalent cations, the information could be used to develop transdermal iontophoretic protocols. For example, supporting electrolytes

with divalent cations could be included in drug formulations to enhance the recovery rate of skin properties after iontophoresis.

The influence of large potential swings on skin properties was also studied by electrochemical impedance spectroscopy. The approach was to collect a series of skin impedance spectra by variable-amplitude galvanostatic modulation. The amplitude of the target potential was adjusted incrementally from 50 mV to 1 V at the beginning of each experiment. Four spectra were collected for each set of experimental conditions. The results from the studies are described in Section 6.4.

During transdermal iontophoresis a DC current bias is applied to enhance the flux of ionic drug compounds into the body. The objective of the next investigation was to characterize the impedance response of skin under applied DC current conditions. For this work, a sinusoidal current signal was superimposed about the applied-current bias. The amplitudes of the current biases were between 0 μA/cm^2 and 855 μA/cm^2. This range was consistent with the currents applied by clinical iontophoretic systems.[177,201,236] The results of the impedance studies on the influence of DC current on skin properties are discussed in Section 6.5.

The literature indicates there is a regional variation in skin properties for any given person. Furthermore, skin properties also vary from person-to-person. A limited number of studies have been performed to characterize the variation in the electrical and transport properties of skin. A demonstration of the large regional variation in skin transport properties is provided in Section 6.6. The methodology used for the investigation is described there. Although visual inspection of the spectra from the various pieces of skin revealed a large variation in epidermal properties, rigorous statistical assessment of the sources contributing to the overall variation was performed. The approach for the statistical analysis of the variation in the impedance response of skin is described in Chapter 7.

4.1.4 Statistical Analysis of Impedance Spectra

A major portion of this work was focused on the development of in experimental techniques for monitoring skin properties during transdermal iontophoresis. Biological membranes, such as skin, often exhibit nonlinear and/or nonstationary behavior when subjected to large electric fields. This situation is likely to occur during transdermal iontophoresis because of the characteristically high resistance of the stratum corneum. The transport properties of skin may also change as the ionic solution penetrates the membrane. It is possible that these changes occur during the time period required to complete a transdermal iontophoresis experiment. The evolution of the system was monitored by impedance spectroscopy for all of the experiments conducted here.

Statistical analysis of the impedance data was performed to determine the Kramers-Kronig consistent portions of the spectra. The Kramers-Kronig relations are a set of integral equations that can be used to convert between the real and the imaginary components of the complex impedance. Impedance spectra that are stationary, linear, causal and stable conform to the Kramers-Kronig relations.

The Measurement Model approach developed by Agarwal *et al.*[237−239] was applied in this work to assess Kramers-Kronig consistent portions of the impedance spectra. The Measurement Model selected for that development was the Voigt circuit model.[237] The Voigt model is similar to the ideal circuit network presented in Figure 3-3 with additional RC elements connected in series. The complex impedance expression for the Voigt circuit is defined according to

$$Z(\omega) = Z_0 + \sum_{k}^{n} \frac{R_k}{(1 + j\tau_k \omega)} \tag{4-10}$$

where Z_0 is the electrolyte solution resistance, τ_k and R_k are the time constant and resistance for the kth RC element and n is the maximum number of line shapes that

can be justified according to the noise in the measurement. Equation (4-10) is consistent with the Kramers-Kronig relations. Therefore, a statistically significant fit of the Voigt model to an impedance spectrum implies that the data are consistent with the Kramers-Kronig relations.

The Measurement Model for each impedance spectrum was built iteratively by the successive addition of RC line shapes. The Measurement Model Tools software developed by Orazem *et al.*[240] was used to regress the measurement model to the impedance spectra. Complex nonlinear least squares (CNLS) regression was applied at each step of the model building procedure to obtain parameter estimates. The confidence intervals for the parameter estimates were calculated from Monte Carlo simulations.[239] The total number of parameters for the model was constrained such that the 95.4% confidence intervals must not include zero for each of the parameter estimates.

The Measurement Model approach was used to determine the nature of experimental errors. The residual errors from the regression procedure consist of deterministic and stochastic errors. For example, deterministic errors may be caused by an insufficient or incomplete model, nonstationary system behavior and/or instrumental bias. The stochastic errors were assumed to be randomly distributed with a mean value of 0 and a standard deviation σ. The contributions to the total error from the regression are defined by

$$Z - \widehat{Z} = \epsilon_{lof} + \epsilon_{ns} + \epsilon_{instr} + \epsilon_{stoch} \tag{4-11}$$

where Z and $\widehat{Z}$ are the complex impedance values from the experiment and the model, ϵ_{lof} is the lack of fit error due to model inadequacy, ϵ_{ns} is the error from nonstationary effects, ϵ_{instr} is the error from instrumental artifacts and ϵ_{stoch} is the stochastic error.

In accordance with the Measurement Model technique, replicate impedance spectra were collected for each set of experimental conditions. A Measurement Model was regressed to each impedance spectra separately. The regressions were weighted by the modulus of the impedance. Each of the models was selected to have the same number of line shapes and the regression parameters were adjusted for each replicate. Under the assumption that the system was evolving slowly, this approach served as a filter for the nonstationary component of the regression error. The lack of fit errors were assumed to be constant for all of the regressions since all of the Measurement Models possessed the same number of line shapes. Instrumental errors were also assumed to be constant because the control parameters for the impedance apparatus were kept constant. The general approach of regressing a measurement model to each replicate spectra resulted in the extraction of the stochastic component of the total error.

The stochastic component of the regression error typically exhibits a strong dependence on frequency for impedance data. As a unique Measurement Model with an equal number of parameters was regressed to each of the impedance spectra separately, a family of frequency-dependent residual errors was produced for each replicate. The variance and the mean of the real and imaginary residual errors were calculated according to

$$\widehat{\sigma}_r^2 = \sum_k \frac{\epsilon_{res,r,k} - \overline{\epsilon}_{res,r}^2}{N-1} \tag{4-12}$$

$$\widehat{\sigma}_j^2 = \sum_k \frac{\epsilon_{res,j,k} - \overline{\epsilon}_{res,j}^2}{N-1} \tag{4-13}$$

where $\widehat{\sigma}^2$ is the variance, N is the number of data points collected at each frequency, ϵ is the regression error and $\overline{\epsilon}$ is the mean fitting error. The mean fitting can be further decoupled to

$$\overline{\epsilon} = mean(\epsilon_{lof} + \epsilon_{instr}) \tag{4-14}$$

where ϵ_{lof} is the contribution to the fitting error from model inadequacies and ϵ_{instr} is the contribution from systematic errors in the measuring equipment.

Agarwal *et al.* developed a model for the frequency-dependent, stochastic component of the error.[238] For the development of the error structure model it was assumed that the standard deviation of the real and imaginary components were equal. This assumption was subsequently validated by Durbha *et al.* for Kramers-Kronig consistent data where the real and imaginary components of the impedance are collected simultaneously.[241] The error structure model accounts for the method by which impedance data is collected and is described according to

$$\sigma_j = \sigma_r = \sigma = \alpha|Z_j| + \beta|Z_r| + \gamma\frac{|Z|^2}{R_m} + \delta \tag{4-15}$$

where R_m is the resistance of the potentiostat measuring resistor, and α, β, γ and δ are the model constants. Parameter estimates are obtained by the regression of the error structure model to the residual errors obtained from the Measurement Model regression procedure.

Impedance spectra were assessed for consistency with the Kramers-Kronig relationship by weighting the Measurement Model regression with the experimentally determined error structure. This approach is generally superior to modulus weighting as an emphasis is placed on data with less noise content in comparison to data with more noise content. Measurement Model parameters were obtained from the complex nonlinear least squares regression by minimizing the objective function

$$J = \sum_k \frac{\left(Z_{r,k} - \widehat{Z}_{r,k}\right)^2}{\sigma_{r,k}^2} + \sum_k \frac{\left(Z_{j,k} - \widehat{Z}_{j,k}\right)^2}{\sigma_{j,k}^2} \tag{4-16}$$

where $Z_{r,k}$ and $Z_{j,k}$ are the real and imaginary components of the impedance, whereas $\sigma_{r,k}^2$ and $\sigma_{j,k}^2$ are the error structure variances of the real and imaginary parts of impedance at each frequency.

The quality of information obtained from impedance data was increased by regressing the Measurement Model according to the noise in the measurement. The regression scheme described here provided for statistically rigorous evaluation of the Kramers-Kronig consistent parts of impedance data. This information was used to identify measuring frequencies where the impedance response of skin was not causal, stable, linear or stationary. For example, data that did not conform to the Kramers-Kronig relations was associated with changes in skin properties. All of the impedance spectra presented in this work were assessed for consistency with the Kramers-Kronig relations.

4.2   Potential and Current Step-Change Studies

The transient response of skin to constant-amplitude DC potential and current signals was monitored to supplement the impedance results. The objective was to identify the response of skin to the prolonged application of electrical signals. Two types of experiments were performed for the study. For the first set of experiments a constant amplitude DC potential bias was applied across the skin and the current response was monitored for a period of 20 minutes. The current response was sampled at a rate of 52.9 mHz, which corresponds to the collection of one measurement every 20 seconds. The skin was then allowed to relax for at least 15 minutes after the potential bias was terminated.

The influence of the potential bias amplitude on skin properties was assessed by incrementally increasing the potential bias over a range of values. The magnitude of the applied biases were 10, 50, 100, 250, 500 and 1,000 mV, respectively. For this study, the smallest bias amplitude was applied at the beginning of the experiment. The experimental protocol was repeated four times, twice with samples of skin immersed in NaCl solution and twice with samples of skin immersed in $CaCl_2$ solution. The objective was to determine whether the effects of solution

cation charge and applied potential magnitude on the transport properties of skin were coupled. The results from the potential step-change studies are presented in Section 8.1.

For the second type of experiment, skin was subjected to a series of step-changes in current and the potential response was monitored. The amplitudes of the DC current signals were 1.4 μA/cm^2, 14 μA/cm^2 and 140 μA/cm^2. In general, the current step-change was held at the elevated condition for 40 minutes. Four 10 mV variable-amplitude galvanostatically modulated impedance spectra were collected before and after skin was subjected to the elevated DC current. The results from the current step-changes studies are discussed in Section 8.2.

4.3   Materials

Heat-separated excised human skin was the model membrane studied in all of the experiments. The separation procedure involved physical and mechanical manipulations to extract the stratum corneum and the adjoining layers of the epidermis from the underlying dermis. In compliance with the standard protocol, deionized water was the only solvent added during the process.[242] A complete description of the heat-separation procedure is presented in Appendix A. The thickness of the epidermal membranes was approximately 100 μm. The excised skin was obtained from the abdomen or the back. The samples were pliable and semi-translucent to visible light. A micrograph of a skin specimen is shown in Figure 4-4. The out of focus regions of the picture were caused by water bubbles trapped between the slide glass and the membrane.

The skin samples were mounted between glass diffusion cells prior to each impedance study and replaced upon changing the ionic solution. The skin and the solution were maintained at constant temperature with a water-jacketed diffusion cell. The diffusion cell provided separation between the ionic solutions and the
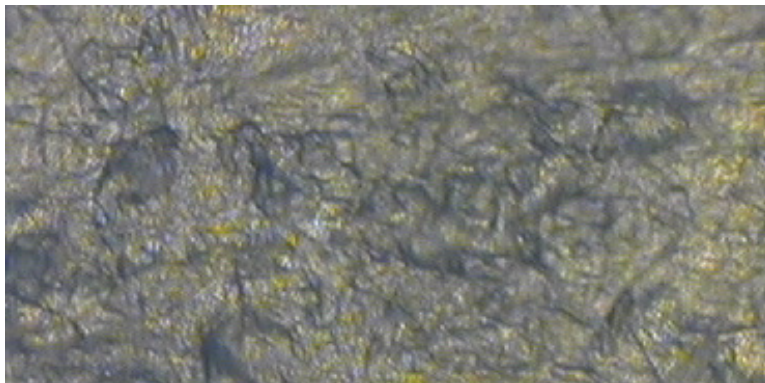
Figure 4-4: Micrograph of heat-separated cadaver skin. Picture taken at a magnification of 92x.

exterior heating bath. Magnetic stir bars were added to the diffusion cell to keep the solution well mixed.

The applied bias signals for the step-change experiments were provided by a Schlumberger 1286 potentiostat. The electrochemical impedance measurements were conducted with a Schlumberger 1286/1250 impedance couple. In order to monitor conditions across the skin a four-electrode configuration was used for all of the studies. The Ag/AgCl counter and working electrodes were produced by In Vivo Metric. The Ag/AgCl reference electrodes were fabricated by Micro Electrodes, Inc.

The electrochemical impedance spectroscopy experiments designed to demonstrate the efficacy of variable-amplitude galvanostatic modulation were conducted in solutions of 100 mM NaCl at a pH of 5.23 and 100 mM $CaCl_2$ solution at a pH of 4.92. The ionic strength of the $CaCl_2$ solution was a factor 1.8 greater than the NaCl solution. Since activity coefficient corrections are proportional to the square root of ionic strength this difference was considered negligible.[136] The water bath for these experiments was maintained at room temperature.

The ionic solutions used for the other experiments in this work were either 150 mM NaCl / 20 mM HEPES, 150 mM KCl / 20 mM HEPES, 50 mM $CaCl_2$ / 20 mM HEPES or 50 mM $MgCl_2$ / 20 mM HEPES. The pH of the solutions was approxi-

mately 7. The temperature of the heating bath was maintained at 32° C. The water bath temperature was consistent with the surface temperature of skin. To ensure that activity coefficient corrections were roughly equivalent for experiments conducted in the two electrolytes, the electrolyte concentrations were chosen to yield the same ionic strength.

4.4   UV-vis Absorption Spectroscopy

Transdermal drug delivery rates under applied-current conditions were calculated with UV-vis absorption spectroscopy. The anesthetic, lidocaine, was the model drug molecule studied in this work. The aromatic group of lidocaine provides the molecule with light absorbance properties in the UV portion of the electromagnetic spectrum. The typical absorption peak for aromatic molecules occurs between 200 and 300 nm, where the addition of functional groups shifts the absorption peak to longer wavelengths.[243]

A fundamental assumption of absorption spectroscopy is that the absorption intensity is proportional to the chromophore (light absorbing molecule) concentration and the length of the light path through the sample. The formal expression for relating light absorbance to chromophore concentration consistent with the Beer-Lambert law is presented by[243]

$$A = \log \frac{P_0}{P} = \epsilon b c_i \qquad (4\text{-}17)$$

where A is the absorbance of species, P_0 is the energy of electromagnetic radiation reaching the detector in the absence of the chromophore and P is the energy of radiation reaching the detector for a chromophore concentration of c_i. The pathlength through the sample is, b and ϵ is the molar extinction coefficient.

According to the Beer-Lambert law, the molar extinction coefficient should theoretically be independent of concentration. For real systems, this criteria is satis-

fied only over a limited range of concentrations and must be determined experimentally. In general, the absorbance response is consistent with Beer-Lambert theory when the concentration of the light absorbing molecule is less than 10 mM. Above this critical threshold, nonlinear behavior is observed because of specific interactions between the light absorbing species.[244]

Philbrick[164] successfully applied UV-vis absorption spectroscopy for measurement of lidocaine drug delivery rates. The magnitude of applied DC currents used for the study was 1 μA and 100 μA. The calibration study performed for that work provided accurate measurement of lidocaine concentration in the range of 0.5 μM to 30 μM. Drug delivery rates were estimated from the time rate of change of lidocaine concentration. Results from the study demonstrated that the transdermal delivery rate of lidocaine increased in response to applied current. Elevated lidocaine flux values were observed after the current was terminated. This result suggested that the skin serves as a reservoir for the temporary storage of lidocaine. A possible explanation for the source of the reservoir capacity was that absorption reactions were occurring between the negative background charge of the skin and the positively charged lidocaine ions.

4.4.1 Instrumentation and Data Collection

Considerable emphasis was placed on developing accurate and reliable methodologies for measuring drug delivery rates during transdermal iontophoresis. The absorption spectroscopy apparatus was designed in compliance with the general principle of a dual-beam spectrophotometers.[245] The advantage of the dual-beam system over a single beam unit is that fluctuations in the light source output as well as drift in the photodiode array of the spectrometer can be monitored.

The main components of the absorption spectroscopy apparatus consisted of a light source, a customized dual-beam absorption spectroscopy cell, a parallel com-

bination of multi-wavelength spectrophotometers, fiber optic cables and a computer interface to control the experiment. A block diagram of the dual spectrometer system is presented in Figure 4-5.
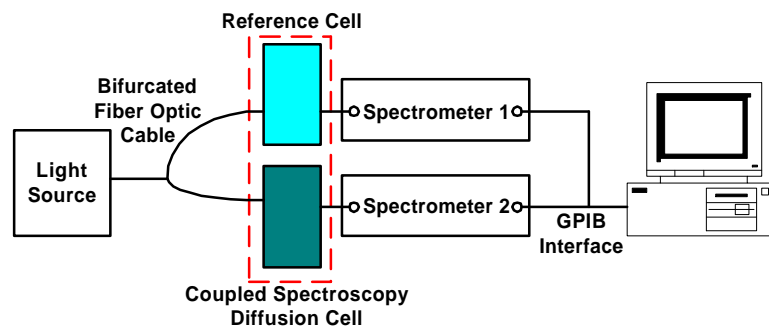
Figure 4-5: Dual spectrometer system configuration. The custom coupled spectroscopy diffusion cell is represented by the region enclosed by the dashed lines and is shown in detail in Figures 4-6 and 4-7.

A deuterium lamp served as the UV-vis light emission source for the absorption spectroscopy experiments (Model Number: AIS-UV-2, Analytical Instruments Systems, Inc., Flemington, NJ). In compliance with the recommendations of the manufacturer, the lamp was turned on 30 minutes prior to the start of all absorption spectroscopy experiments. The radiation exiting the lamp passed through a 200 μm diameter bifurcated fiber-optic cable to the dual-beam spectroscopic cell. Approximately half of the light source output intensity entered the receptor compartment of the coupled spectroscopy diffusion cell and the remainder went to the reference cell.

The major components of the dual-beam spectroscopy apparatus consisted of the cell housing enclosure and the coupled spectroscopy diffusion cell. The cell housing was designed by Riemer and Membrino as part of an independent study project. The unit was fabricated from an aluminum block and subsequently anodized to prevent atmospheric and/or environmental oxidation (TMR Engineering, Micanopy, FL). The mounting surfaces for the inlet and outlet optical lenses were made parallel to maximize light throughput. Annular channels were drilled

in the base plate of the cell housing to provide for temperature control via a circulating, constant-temperature water bath (Model Number: 1160, VWR Scientific, Niles, IL).

The coupled spectroscopy diffusion cell consisted of a donor chamber and a receptor chamber. A 1 cm diameter hole was drilled into each of the chambers to serve as a pathway for diffusion. The prototype of the coupled spectroscopy diffusion cell was developed by Philbrick.[164] The donor chamber for the model system was fabricated from polycarbonate and the receptor chamber was made from a standard optical grade quartz cuvette. At the beginning of each experiment an O-ring was placed on the skin and both were inserted between the opening of the donor chamber and the receptor chamber. The entire system was then placed under compression to form a good seal.

A difficulty encountered here was that the standard quartz cuvettes were unable to withstand the large compressive forces. The original diffusion cell design was modified to improve the structural integrity of the optical cuvette. The modified design consisted of a hollow rectangular polycarbonate vessel with optical grade quartz windows inserted into two oppositely facing sides. The polycarbonate frame was designed to minimize the amount of stress placed on the quartz glass. A pathway for the transmission of UV-vis radiation was provided by the quartz glass windows. A schematic and picture of the dual-beam diffusion cell are shown in Figures 4-6 and 4-7, respectively.

The light exiting each compartment of the cell was collected with a dedicated spectrometer (Model Number: SU 2000, Ocean Optic Instruments, Dunedin, FL). The photodiode array of each spectrometer measured the light intensity at 740 equally spaced wavelengths between 200 and 400 nm. This wavelength range
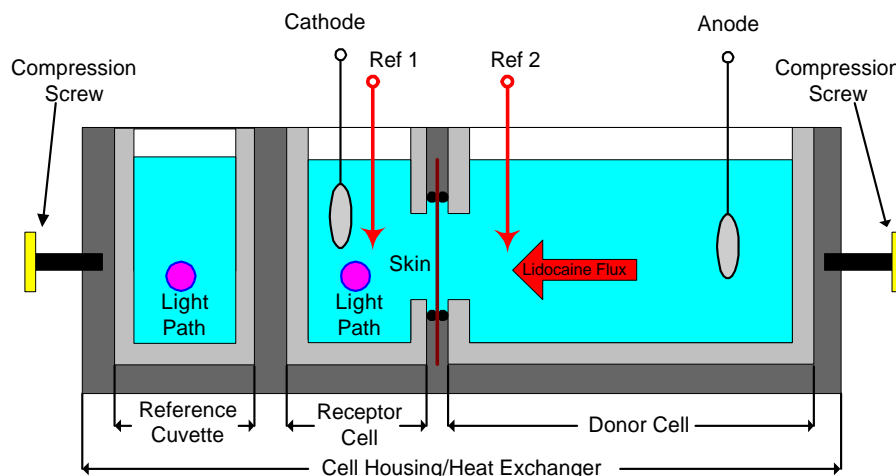
Figure 4-6: Dual spectrometer diffusion cell configuration.
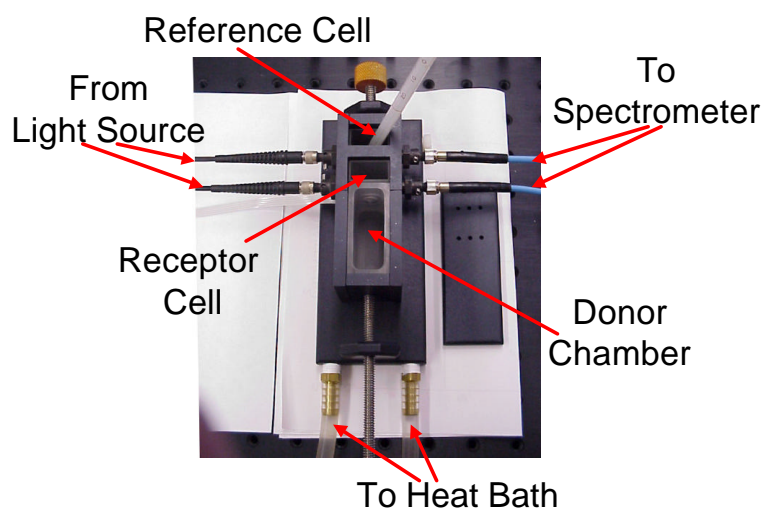
Figure 4-7: Dual spectrometer diffusion cell photograph.

was selected to coincide with the deuterium lamp manufacturer's specifications for maximum stability and output efficiency.

The absorbance was calculated after the experiments were completed with Microsoft Excel spreadsheet software. The general form of the absorbance relationship is presented by

$$A_{i,k} = \log \frac{I_{i,0} - I_{i,dark}}{I_{i,k} - I_{i,dark}} \tag{4-18}$$

where $A_{i,k}$ is the absorbance at wavelength i for spectrum k. The light intensity at wavelength i, in the absence of the chromophore is denoted by $I_{i,0}$, and $I_{i,dark}$

is the intensity at wavelength i, when light is absent from the spectrometer. Prior to each diffusion study the light source was blocked with a black metal plate and spectra were collected by the spectrophotometers. These spectra provided for direct evaluation of the dark signal and corresponded to the baseline response of the photodiode array.

4.4.2   Software Control

The LabVIEW G® software driver for the spectrometers, as purchased from Ocean Optic Instruments, lacked an option for storage of the intensity spectra in spreadsheet-compatible output files. The LabVIEW G® driver was modified to enable collection of the spectra from the reference cell and the diffusion cell. An option was added which allowed the user to select the range of wavelengths for the collection of intensity data. The option helped to reduce the size of the output files. An additional option allowed the user to specify the time interval between collection of subsequent spectra. The changes to the software driver facilitated the control of the UV-vis absorption spectroscopy experiment and storage of data with the computer.

4.4.3   Calibration Studies

A multi-step calibration procedure was completed prior to the transdermal iontophoresis experiments. The first part of the calibration was designed to characterize the transient behavior of the spectrometers. This was accomplished by placing deionized water in both the reference cell and the diffusion cell and collecting spectra intermittently for 2.4 hours. Since no chromophore was present, any changes in the absorbance response were assumed to be caused by systematic changes in the equipment. The results from the assessment of system drift are presented in Section 9.1.

The second part of the calibration was designed to identify the range of lido-caine concentrations for which the absorbance response could be described by Beer-Lambert theory. This was accomplished by collecting absorption spectra from solutions with known lidocaine concentrations. The approach was to succes-sively add small aliquots of concentrated lidocaine solution to an initially dilute mixture. All mixing was performed in the coupled spectroscopy diffusion cell in order to incorporate the effects of the cell geometry on the absorption response. The concentration of the lidocaine solutions ranged from 0.5 μM to 1.8 mM. The extinction coefficient at each wavelength in the spectra was calculated from the absorbance data according to the Beer-Lambert law. The results of the lidocaine calibration studies are presented in Section 9.2.

An additional study was conducted to identify the influence of prolonged im-mersion of skin in electrolyte solutions on the absorbance response. The goal was to determine the rate at which chromophoric species diffuse from the skin. The approach provided for the calculation of the relative contributions of skin species and lidocaine to the overall absorbance response. For the study, skin was placed in the coupled spectroscopy diffusion cell and immersed in a buffered solution of 150 mM NaCl. Absorbance spectra were collected over approximately 2.5 hours at three-minute intervals. The temperature of the diffusion cell was maintained at 32°C. A detailed description of the work is provided in Section 9.3

4.5   Investigation of Transdermal Iontophoresis with Coupled Spectroscopy

The coupled spectroscopy methodology was applied to investigate transder-mal iontophoresis upon completion of the calibration studies. The system was maintained at 32°C. Transdermal iontophoresis was simulated by periodically ap-plying a DC current bias of 14 mA/cm^2 and monitoring the absorption response with the spectrometers. At the start of the experiment skin was immersed in

buffered 150 mM NaCl and 3.5 ml of the lidocaine cocktail were added. The temperature was maintained at $32°C$ by the circulating water bath. Replicate impedance spectra were collected while the current was maintained at $0~\mu A/cm^2$. The electrochemical impedance spectroscopy experiments were conducted under variable-amplitude galvanostatic control. The experimental results are described in Section 9.4.

CHAPTER 5
DEVELOPMENT OF VAG MODULATION FOR SKIN IMPEDANCE STUDIES

A preliminary goal of this research was to develop an appropriate methodology for measuring skin properties by electrochemical impedance spectroscopy. Ideally, in the absence of an applied current bias the impedance spectroscopy experiment should not alter skin properties. In Section 5.1 it is demonstrated that the traditional methodology for conducting skin impedance experiments can alter skin transport properties. An adaptive modulation strategy was implemented to prevent the impedance experiment from changing skin properties. Development and application of the adaptive modulation strategy is described in Section 5.2. Skin impedance spectra collected by the adaptive methodology were shown to be consistent with a membrane with unaltered properties. As a result, the adaptive modulation technique was applied extensively in subsequent skin impedance experiments.

5.1   Preliminary Investigation of Skin Impedance

The conventional methodology for studying skin transport properties by electrochemical impedance spectroscopy is to apply a constant-amplitude sinusoidal current signal and measure the potential response over a wide range of perturbation frequencies.[131,151,233] A preliminary study was conducted to determine the influence of current modulation amplitude on the impedance response of skin. The objective of the preliminary work was to determine whether skin impedance spectra obtained with the traditional constant-amplitude galvanostatic modulation technique were consistent with a membrane with unaltered properties. For

example, the skin was assumed to be unaltered by the impedance experiment if the corresponding spectrum satisfied the Kramers-Kronig relations.

There is a general consensus in the literature that the stratum corneum exhibits a nonlinear response to electrical impulses between 0.1 V and 2 V, especially at frequencies below 10 Hz.[2,3,153,154] In a literature survey, Prausnitz reported that direct current densities between 0.1 μ/cm^2 and 75 μ/cm^2 can also introduce a nonlinear response in skin (for a more complete discussion see, for example, Section 2.6).[3]

The objective of this investigation was to determine the threshold value of current or potential for the onset of nonlinear behavior. This was accomplished by adjusting the amplitude of the applied-current perturbation and checking the impedance response for consistency with the Kramers-Kronig (KK) relations. As described in Section 4.1.4, the Kramers-Kronig relations are a set of integral equations which transform the real and imaginary components of complex quantities. Data that conform to the Kramers-Kronig relations are linear, stationary, causal and stable. Therefore, spectra that were found to be consistent with the Kramers-Kronig relations were associated with a membrane with constant transport properties.

It is possible that the nonlinear skin impedance response described in the literature was induced by the applied electrical perturbation. The preliminary impedance studies were designed to identify a set of experimental input parameters which could yield a skin impedance response that was linear for the majority of the frequency range. The approach was to collect a series of eight constant-amplitude galvanostatic impedance scans, all with different applied perturbation amplitudes, from the same piece of skin. The skin was immersed in 150 mM NaCl electrolyte solution which was buffered at a pH of approximately 7. The modulation amplitudes for the impedance experiments were adjusted between 10 and

100 μA. In accordance with the constant-amplitude galvanostatic modulation method, the magnitude of the current perturbation was held constant for all measuring frequencies within a given scan. The current perturbation for the first scan was 10 μA and the perturbation magnitude was adjusted incrementally at the start of each impedance experiment.

The impedance-plane plot of selected skin impedance spectra from the study is presented in Figure 5-1 (for a more complete discussion of impedance data presentation, please refer to Section 4.1.1). The high-frequency asymptotes of the impedance were approximately uniform for all spectra collected. The high-frequency asymptote corresponds to the electrolyte solution resistance is located near the origin of the impedance-plane plot. The impedance spectra displayed the typical depressed semicircular shape for modulation values less than or equal to 30 μA. The depressed semicircular shape suggested that the skin possessed a distribution of characteristic time constants.
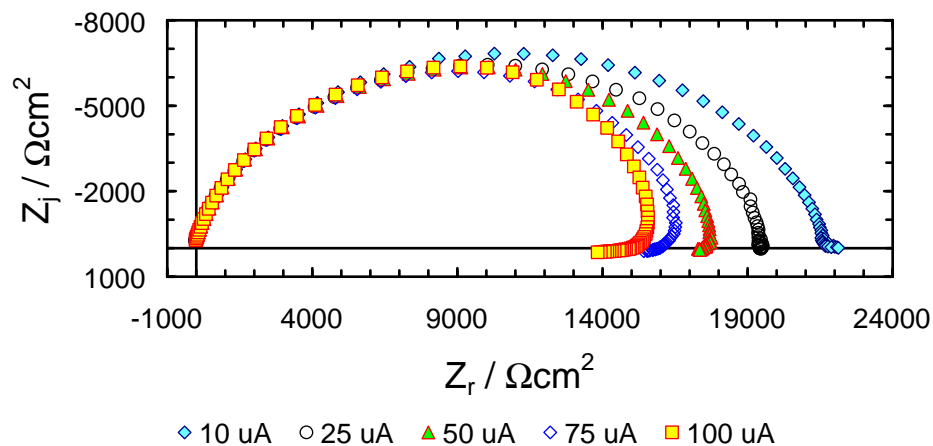
Figure 5-1: Impedance response of skin when subjected to a series of constant-amplitude modulated experiments. The amplitudes of the current perturbations are indicated by the legend. The results are presented in temporal order.

The spectra collected at modulation amplitudes above 30 μA exhibited a continuous decrease in skin impedance as the perturbation frequency was swept below 100 Hz. The reduction of skin impedance can be observed by the asymmetric

"curl" or "hook" in the data located in the lower right hand region of Figure 5-1. The curvature of the "hook" was proportional to the perturbation amplitude. The data points associated with the "hook" represent the low-frequency impedance response of skin. The low-frequency asymptote of the impedance corresponds to the polarization resistance of skin. Ideally, a system with linear transport properties should have a polarization resistance which is independent of the applied current.

The decrease in polarization resistance associated with perturbation amplitudes greater than 30 μA suggested that skin properties had been altered. Rigorous support for the proposed effect of the perturbations on skin properties was provided by assessing the data for consistency with the Kramers-Kronig relations. The details of the assessment procedure are presented in the next section.

5.1.1 Kramers-Kronig Consistency Check of Preliminary Impedance Data

The impedance spectra were assessed for consistency with the Kramers-Kronig relations by regressing the Voigt circuit Measurement Model to the data. Detailed examples of the assessment procedure are provided here. However, a more complete discussion of the approach used to apply the Measurement Model for assessing impedance data for consistency with the Kramers-Kronig relations is provided in Section 4.1.4. For the first part of the assessment procedure, complex fits of the Measurement Model to the spectra yielded a maximum of 2 line shapes. The limited number of line shapes resulted in large fitting errors.

Visual inspection of the impedance-plane plot of skin impedance revealed that the high-frequency asymptote, which corresponds to the electrolyte solution resistance, was negative. An apparent negative solution resistance is a common symptom of instrumental artifact. The difficulty was circumvented by performing an imaginary fit of the Measurement Model to the 10 μA modulated spectrum. The

solution resistance for this regression was set to 0 Ω. An appropriate solution resistance was selected by iteratively adjusting the solution resistance until the normalized real residual errors from the regression were normally distributed about a mean of 0 Ω.

The normalized residual errors were calculated at each frequency by dividing the fitting errors by the impedance magnitude of the real and imaginary components according to

$$\text{Real residual error} = \frac{Z_{r,data} - Z_{r,model}}{Z_{r,data}} \tag{5-1}$$

$$\text{Imaginary residual error} = \frac{Z_{j,data} - Z_{j,model}}{Z_{j,data}} \tag{5-2}$$

where $Z_{r,data}$ and $Z_{j,data}$ represent the measured values of the real and imaginary impedance components. The terms $Z_{r,model}$ and $Z_{j,model}$ correspond to the calculated values for the real and imaginary impedance quantities. It was determined that an electrolyte solution resistance of -55 Ω yielded the best distribution of residual errors for the 10 μA modulated experiment. Therefore, the electrolyte solution resistance was set to -55 Ω for all of the subsequent regressions. A similar approach was applied for regressing the Measurement Model to other impedance spectra with an apparent negative solution resistance.

The selection of a negative solution resistance for the regressions was not consistent with the state of the system. However, the goal here was to develop a method for obtaining improved fits of the Voigt circuit model to skin impedance spectra. For this discussion, an improved fit was associated with an increase in the number of model parameters used to represent the impedance spectrum. The added line shapes helped to reduce the magnitude of the normalized residual fitting errors. For example, the regressions where the electrolyte solution resistance was set to -55 Ω yielded a minimum of 6 shapes for all of the impedance

spectra. The fitting errors for the regressions were within the noise level of the measurements. The improved fits of the Measurement Model made it possible to determine whether the low-frequency impedance response of skin satisfied the Kramers-Kronig relations. An emphasis was placed on the low-frequency portion of the spectra because the data contains information on skin properties which are affected by iontophoresis.

The low-frequency portions of the skin impedance spectra were assessed for consistency with the Kramers-Kronig relations by regressing the Measurement Model to the imaginary component of the experimental data. The circuit element parameters obtained from the regressions were used to estimate the real component at each frequency. Normalized real residual errors which fell outside the 95.4% confidence interval were considered to be inconsistent with the Kramers-Kronig relations. A sample plot for the frequency-dependent real residual errors from an imaginary fit of the Measurement Model to the spectrum collected by the 50 μA perturbation is presented in Figure 5-2. The solid yellow circles correspond
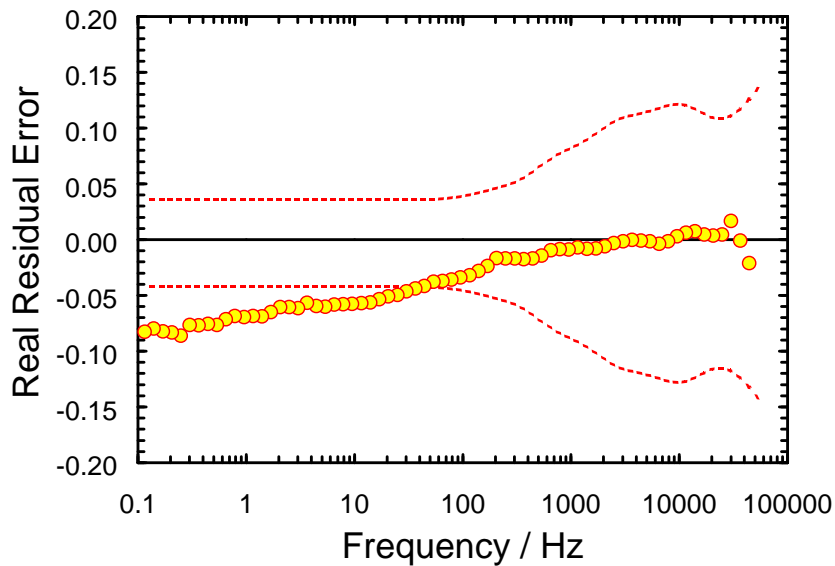
Figure 5-2: Normalized real residual errors from an imaginary fit of the Measurement Model to the 50 μA spectrum. Red lines indicate the 95.4% confidence interval.

to the normalized errors for the prediction of the real component of skin imped-
ance. The red lines represent the 95.4% confidence interval. The residual errors fell
outside the confidence interval at frequencies below 44.3 Hz and therefore, were
considered to be inconsistent with the Kramers-Kronig relations. This procedure
was repeated for each impedance spectrum collected in this investigation.

The regressions revealed that the spectra collected with current perturbation
magnitudes less than 35 μA were consistent with the Kramers-Kronig relations
over the entire frequency range. The conformity of the data implied that skin prop-
erties were not changed by the experiment. At higher current perturbation ampli-
tudes there was a critical frequency, below which data were inconsistent with the
Kramers-Kronig relations. The inconsistent data implied that skin properties had
changed. The measuring frequencies at which skin properties began to change for
each current perturbation amplitude are listed in Table 5-1.

Table 5-1: Minimum frequencies and associated membrane potential differences
for Kramers-Kronig consistent portions of skin impedance spectra.

Parameter	Current Perturbation Amplitude / μA							
	10	100	75	50	25	30	35	30
Low Freq. Cut-off / Hz	0.1	2056	249	44.3	0.1	0.116	0.37	0.1
Potential at Cut-off / V	$\pm$ 0.32	$\pm$ 0.65	$\pm$ 1.32	$\pm$ 1.25	$\pm$ 0.69	$\pm$ 0.84	$\pm$ 0.94	$\pm$ 0.86

5.1.2 Proposed Driving Force for Skin Property Changes

It has been reported in the literature that skin properties begin to change when
the potential difference across the membrane exceeds a critical value.[3] Galvanos-
tatic or square wave current control was applied in those studies. The literature
results were used to formulate a working hypothesis that the changes in mem-
brane properties observed in the preliminary impedance spectroscopy study were
caused by large potential differences across the skin.

Skin impedance experiments employing the traditional constant-amplitude galvanostatic modulation method maintain the current perturbation amplitude at a constant value over the entire frequency-range. As the experiment progresses from high-frequency to low-frequency the impedance of skin typically increases in magnitude from approximately 50 Ωcm^2 to as high as 250 kΩcm^2. Since a uniform current perturbation amplitude is used throughout the experiment, the largest potential drop across the membrane will be observed in the low-frequency portion of the impedance spectrum. Since the current perturbation is maintained at a uniform amplitude, deviations from linearity in the low-frequency impedance response of skin would be consistent with the concept of potential as being the cause of changes to the epidermis.

The voltage difference for the experiments presented in Section 5.1 was calculated according to Ohm's law by multiplying the current modulation amplitude by the complex impedance at each frequency. The potential difference across skin at the threshold frequencies for which property changes were observed is presented in Table 5-1. The results indicate that skin properties were constant for potential drops less than approximately 800 mV.

The frequency-dependent potential drop across the epidermis associated with the impedance data displayed in Figure 5-1 is presented in Figure 5-3. The potential difference across the skin in response to the 100 μA perturbation increased continuously as the experiment progressed from high-frequency to low-frequency until a maximum value of 2.23 V was observed at 24 Hz. For frequencies below this maximum, the potential difference decreased for the remainder of the impedance scan. A similar trend was observed for the 75 μA scan, however, the maximum potential difference of 1.77 V occurred at 11.5 Hz. A maximum potential difference of 1.27 V was observed for the 50 μA perturbation at 3.65 Hz. The

maximum potential difference for the scans conducted at modulation values of 10 and 25 μA were approximately 300 mV and 700 mV, respectively. The maximum potential drops associated with these perturbation amplitudes occurred at the minimum perturbation frequency of 0.1 Hz.
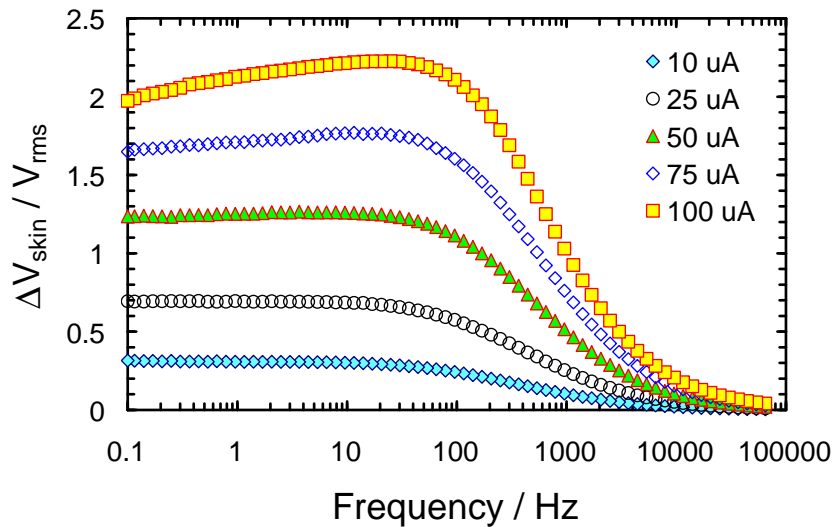
Figure 5-3: Potential difference across the skin as a function of frequency. The data corresponds to the impedance experiments presented in Figure 5-1. The current perturbation amplitudes used to induce to the voltage drops across the epidermis are indicated by the legend. The results are presented in temporal order.

The observation of a maximum potential difference across the membrane at an intermediate frequency for scans conducted with current modulation amplitudes of 35 μA and greater suggested that the properties of skin changed continuously for all subsequent perturbation frequencies. The driving force for the changes was likely provided by the large amplitude electric fields induced by the AC current perturbation. For example, the internal structure of the stratum corneum may have been temporarily rearranged.

5.1.3 Deviation in Potential Response from Linearity

The regressions of the Measurement Model to the imaginary component of the impedance provided estimates for the polarization resistance of skin. This was accomplished by extrapolating the Kramers-Kronig consistent portion of the imped-

ance response to zero-frequency (*i.e.,* the D.C. current response). The regressed values of polarization resistance were multiplied by the current perturbation amplitudes used for the respective impedance scans to calculate the expected potential drops across the skin at zero-frequency. Similarly, the actual potential difference across skin was estimated by multiplying the modulus of the impedance at the lowest measuring frequency (0.1 Hz) by the amplitude of the current perturbation. Both estimates for potential drop across the epidermis at each current perturbation amplitude are presented in Figure 5-4. The open squares represent the expected potential difference at zero-frequency and the solid squares correspond to the measured potential drop across the skin at 0.1 Hz.
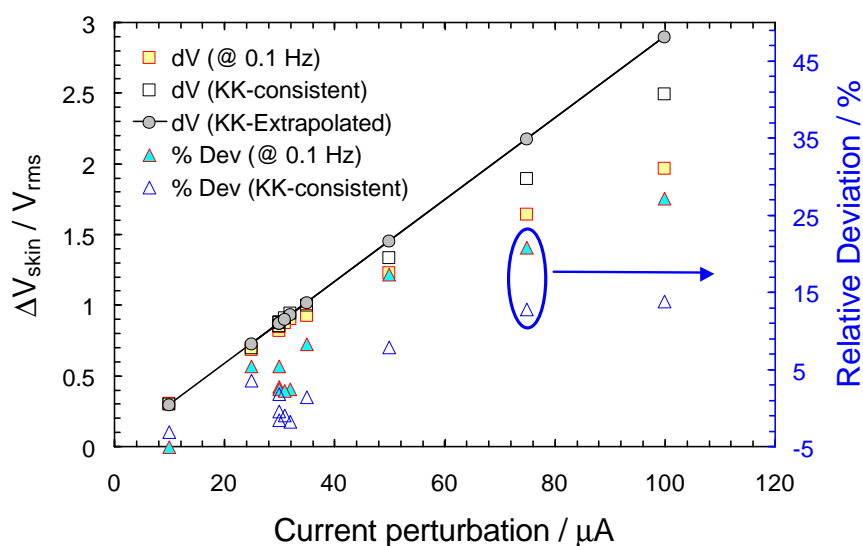
Figure 5-4: Calculated DC limit of potential difference across skin in response to a series of constant-amplitude galvanostatic impedance scans. The triangles represent the relative deviation in the measured low-frequency voltage difference across skin as compared to the voltage difference across a membrane with a polarization resistance independent of potential.

It was shown in Section 5.1.1 that skin impedance spectra collected at perturbation magnitudes less than 35 μA conformed to the Kramers-Kronig relations over the entire frequency range. Since the spectra were consistent with the Kramers-Kronig relations, it was implied that skin transport properties were not altered

by the impedance experiments. The extrapolated polarization resistance values associated with the Kramers-Kronig consistent spectra collected with current perturbations less than 35 μA were used to calculate the expected potential response of a membrane with constant electrical properties to current perturbation amplitudes greater than 35 μA.

The approach was to plot the estimated potential differences from the impedance experiments with perturbation magnitudes less than 35 μA as a function of current. A linear model was regressed to the data set. The slope and intercept calculated from the regression were 2.7x10$^3\Omega$ and 3.97 V, respectively. The r^2 correlation parameter for the regression was 0.966 indicating that the data set was reasonably described by a linear model. The linear model for the expected potential difference across skin as a function of current is presented by the solid black line in Figure 5-4.

The potential difference across skin calculated from the linear model at each perturbation amplitude was selected as a reference for comparison with the calculated potential difference from the impedance experiments. The deviation of skin impedance from linearity was calculated by subtracting the measured potential difference across skin from the potential difference obtained from the linear model according to

$$\text{Relative error } \Delta V_{skin} = \frac{\Delta V_{calculated} - \Delta V_{model}}{\Delta V_{calculated}} x 100\% \qquad (5\text{-}3)$$

where $\Delta V_{calculated}$ is voltage difference across skin calculated from the impedance at 0.1 Hz or the extrapolated polarization resistance and ΔV_{model} is the voltage difference across skin predicted by the linear model. The difference in voltage quantities at each perturbation current represented the deviation in the measured voltage response from the response expected from skin with constant properties.

The relative deviations in the potential drops across the epidermal membrane are also presented as a function of the current perturbation magnitude in Figure 5-4. The filled triangles represent the percent relative deviation in the potential response at 0.1 Hz to the expected response of skin with properties independent of potential. The open triangles correspond to the relative percent difference in the potential response estimated by the Kramers-Kronig consistent polarization impedance obtained from regression of the Measurement Model to each spectrum from constant skin properties.

The relative percent differences in the low-frequency potential responses for the spectra collected with current perturbation amplitudes below 35 μA were all less than 10%. The deviation in the measured potential difference from the ideal response was proportional to the current for perturbation amplitudes greater than 35 μA. Furthermore, the relative deviations in the potential response estimated from the impedance at 0.1 Hz were generally larger than for potential difference calculated from the Kramers-Kronig consistent polarization resistance.

This study indicated that traditional constant-amplitude galvanostatic modulation of impedance spectroscopy experiments can alter the properties of skin. A working hypothesis was proposed that there is a critical value of potential difference across the membrane at which skin properties begin to change. An adaptive modulation strategy was developed to maintain the potential difference across the membrane below the critical value. The development of the adaptive modulation protocol is discussed in the next section.

5.2   Development of VAG Modulation Technique

The preliminary constant-amplitude galvanostatic impedance studies indicated that skin properties can change during an experiment. The changes occurred at high current perturbation amplitudes where the induced potential differences

across the skin were on the order of 1 V. An adaptive modulation technique for collecting impedance spectra was implemented to prevent the experiment from altering skin properties. The adaptive method for collecting impedance spectra applied variable-amplitude galvanostatic (VAG) modulation.[235] The development of the variable-amplitude galvanostatic modulation technique is described in Section 4.1.2 and Appendix B.

Impedance experiments were conducted to verify the efficacy of the variable-amplitude galvanostatic modulation in preventing changes to skin properties. The approach was to collect replicate skin impedance spectra under variable-amplitude galvanostatic and constant-amplitude modulation. Multiple perturbation amplitudes were selected for each modulation technique. The spectra from the respective modulation strategies were assessed for consistency with the Kramers-Kronig relations. The consistent portions of the spectra associated with each modulation technique were compared to determine which approach did not alter skin properties.

The experimental approach was repeated for samples of skin immersed in buffered solutions of $CaCl_2$ and NaCl. The results from the impedance experiments of skin in $CaCl_2$ electrolyte are described in detail. The results from the impedance studies of skin in NaCl are not presented as they were comparable to the $CaCl_2$ experiments. Minor differences in the skin impedance results for the two electrolyte solutions are described in Section 5.2.2

The impedance spectra obtained by the two modulation techniques are presented in the impedance-plane in Figure 5-5. The shapes of the skin impedance spectra were directly related to the modulation technique and the magnitude of the current perturbation. For example, the spectra corresponding to the 1 μA constant-amplitude and 10 mV VAG experiments exhibited a semicircular shape.

In contrast, the spectra corresponding to the 10 μA fixed-amplitude galvanostatic experiments displayed a distinctive "hook" in the low-frequency range. The "hook" shape was similar to the skin impedance response observed in the experiments discussed in Section 5.1.
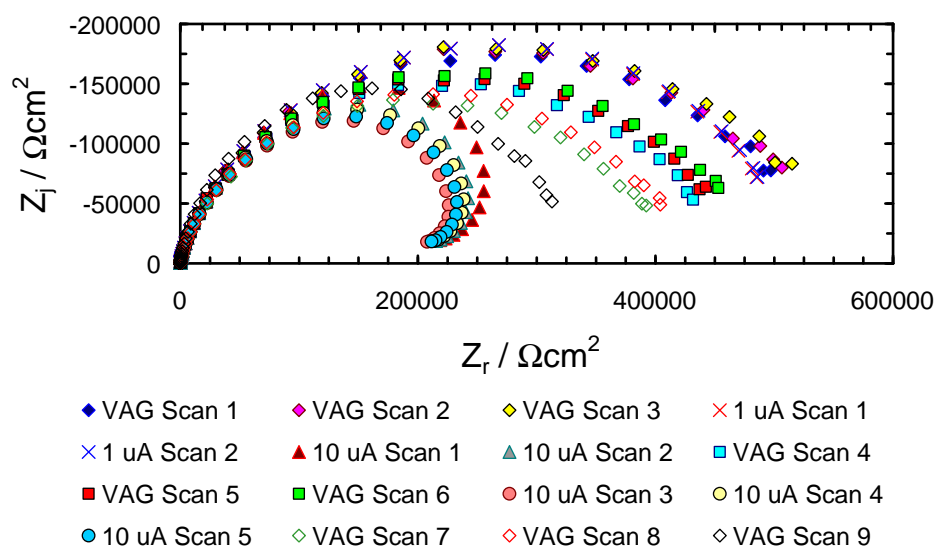
Figure 5-5: Impedance response of skin as measured by VAG and constant-amplitude galvanostatic modulation. The skin was immersed in buffered $CaCl_2$ electrolyte.

The spectra for the first series of 10 mV VAG experiments, denoted by the solid diamonds in Figure 5-5, displayed the highest impedance values. The frequency-dependent impedance responses of the three spectra obtained by VAG modulation were approximately uniform. Spectra collected with a 1 μA constant-amplitude current perturbation are indicated by the cross marks in Figure 5-5. The impedance response of skin at the 1 μA perturbation amplitude was similar to the spectra collected by 10 mV VAG modulation.

The results from the 10 μA constant-amplitude impedance experiments are shown by the solid triangles in Figure 5-5. As the constant-amplitude current perturbation was increased from 1 μA to 10 μA, the impedance decreased dramatically in the low-frequency portion of the spectra. The decrease in skin impedance

was characterized by the "hook" shape of the low-frequency portion of the 10 μA spectra. Spectra from subsequent constant-amplitude 10 μA showed a continuous decrease in impedance from experiment to experiment. The decrease in impedance from scan to scan suggested that skin properties had been changed.

The recovery of skin to the 10 μA perturbations was monitored by collecting three 10 mV VAG impedance spectra which are indicated by the curves with filled squares in Figure 5-5. As the modulation technique was switched from 10 μA constant-amplitude galvanostatic control to 10 mV VAG control, the shape of the impedance spectra changed from a "hook" back to a semi-circle. Subsequent 10 mV VAG scans demonstrated a continuous increase in skin impedance for a given frequency. The increase in skin impedance, as measured by the three 10 mV VAG scans, suggested that the membrane properties had recovered. However, the recovery toward the impedance response measured from the first 10 mV VAG scan was incomplete over the course of the experiment.

A quantitative assessment of the relative recovery of skin properties was made by comparing the calculated polarization resistance of each spectra to the polarization impedance associated with the first 10 mV VAG scan. This spectrum was used as the reference response because the largest magnitudes of skin impedance were observed for this data set. The recovery of the impedance response following the first group of 10 μA constant-amplitude galvanostatic scans, as measured by a 10 mV VAG technique, was 85%, 89% and 91%, respectively.

The spectra from the second set of 10 μA constant-amplitude galvanostatically modulated experiments is presented by the solid circles in Figure 5-5. Upon changing modulation technique back to 10 μA constant-amplitude galvanostatic control, the impedance response once again exhibited a "hook" in the low-frequency region. Successive replicates collected by 10 μA constant-amplitude galvanostatic

modulation decreased continuously in the low-frequency portions of the spectra. The low-frequency impedance of skin corresponding to the second set of 10 μA constant-amplitude galvanostatic scans was less than the response associated with the first set of 10 μA constant-amplitude galvanostatic scans.

The 10 mV VAG modulated impedance scans collected after the second set of constant-amplitude galvanostatic impedance spectra indicated skin impedance had partially recovered. The relative recovery in the low-frequency region of the impedance spectra was 77%, 80% and 83%, respectively. The analysis described here strongly suggested that skin properties were altered by the 10 μA constant-amplitude galvanostatically modulated impedance experiments.

An interesting result of this study, was that the changes in skin properties occurred at lower perturbation amplitudes than the experiments described in Section 5.1. The difference can be explained by the higher impedance response of the skin sample used for this investigation. For a given current perturbation amplitude, the potential difference across the high impedance skin was higher than for the low impedance skin studied in Section 5.1. This observation was consistent with the hypothesis that skin properties begin to change above a critical potential.

Rigorous support for the apparent changes in skin properties caused by the 10 μA constant-amplitude impedance experiments was provided by assessing the spectra for consistency with the Kramers-Kronig relations. The spectra from the 10 mV VAG modulated experiments were also evaluated for consistency with the Kramers-Kronig relations to determine whether the adaptive modulation technique measured skin properties in a noninvasive manner.

5.2.1 Kramers-Kronig Consistency Check of Impedance Spectra

The Measurement Model approach developed by Agarwal *et al.*[237−239] was applied to check impedance spectra for consistency with the Kramers-Kronig rela-

tions. The Kramers-Kronig relations must be satisfied for spectra that are linear, causal, stationary, and stable. Data that conforms to the Kramers-Kronig relations is consistent with a system with constant properties. In contrast, data that does not satisfy the Kramers-Kronig relations indicates that the system has changed.

The Measurement Model was regressed to the complex impedance of the spectra obtained by the constant-amplitude and variable-amplitude galvanostatic modulation techniques. Since replicate impedance spectra were collected for each experimental protocol the frequency-dependent error structures were determined. Subsequent regressions of the Measurement Model to the data set was weighted according to the error structure of the measurement. For example, data with large standard deviation values are weighted less than data with small standard deviations. Error structure weighting generally enhances the amount of information which can be extracted from the data. The error structure was calculated for each set of experimental conditions. The parameter values corresponding to the error structure model shown in Equation (4-15) are presented in Table 5-2.

Table 5-2: Error structure parameters of skin impedance spectra. Skin sample was immersed in $CaCl_2$ solution and parameters are listed in temporal order of experiments.

Modulation Method	Error Structure
10 mV VAG	$\alpha=1.48\text{x}10^{-3} \pm 1.28\text{x}10^{-5}$; $\beta=4.36\text{x}10^{-3} \pm 6.23\text{x}10^{-6}$
1 μA Galv.	$\alpha=1.81\text{x}10^{-3} \pm 6.89\text{x}10^{-5}$; $\gamma=1.72\text{x}10^{-4} \pm 5.51\text{x}10^{-6}$
	$\Delta = 7.07\text{x}10^{-1} \pm 3.32\text{x}10^{-4}$
10 μA Galv.	$\beta =3.98\text{x}10^{-3} \pm 4.41\text{x}10^{-5}$; $\gamma=2.91\text{x}10^{-4} \pm 1.42\text{x}10^{-5}$
10 mV VAG	$\alpha=1.55\text{x}10^{-3} \pm 7.68\text{x}10^{-5}$; $\gamma=3.98\text{x}10^{-4} \pm 2.00\text{x}10^{-5}$
10 μA Galv.	$\alpha=1.84\text{x}10^{-3} \pm 3.51\text{x}10^{-5}$; $\beta=1.84\text{x}10^{-3} \pm 1.55\text{x}10^{-5}$
10 mV VAG	$\alpha=5.42\text{x}10^{-4} \pm 2.47\text{x}10^{-5}$; $\beta=4.04\text{x}10^{-3} \pm 1.08\text{x}10^{-5}$

After the error structure was determined, the Measurement Model was regressed to the spectra to filter out Kramers-Kronig inconsistent data. The regressions were weighted according to the error structure. The first step was to perform a real fit to the data and predict the imaginary part. Data located outside

the confidence interval at high frequencies was considered to be inconsistent with the Kramers-Kronig relations. The inconsistent high-frequency data points were omitted from subsequent regressions. Low-frequency data corresponding to the real component of the impedance located outside of the confidence interval was considered not to satisfy Kramers-Kronig relations. The analysis of the spectra obtained from each modulation technique is discussed separately below.

KK consistency check for 10 mV VAG spectra. The normalized real residual errors for a fit of the Measurement Model to the real part of the impedance data are presented in Figure 5.6(a). The real residual errors are indicated by the solid circles and the noise level of the measurement is illustrated by the dashed green lines. The real residual errors were generally on the order of 1% and were mostly within the noise level of the measurement. As the residual errors were small and randomly distributed about 0, it was concluded that a good fit of the model to the data had been obtained.

The normalized residual errors from the prediction of the imaginary part of the impedance are presented in Figure 5.6(b). The solid triangles correspond to the imaginary residual errors and the dashed red lines correspond to the 95.4% conference interval. The residual errors were less than 5% of the measurement value and were contained within the 95.4% confidence interval at high-frequency. Therefore, the entire data set was included for the imaginary fit. The solution resistance calculated from the real fit was set to a constant value for the imaginary fit. The same procedure for eliminating inconsistent high-frequency data was applied to the other skin impedance spectra described in this work.

The normalized residual fitting errors corresponding to the regression of the Measurement Model to the imaginary component of skin impedance are displayed in Figure 5.7(a). The imaginary residual errors were all less than 5% of the mea-
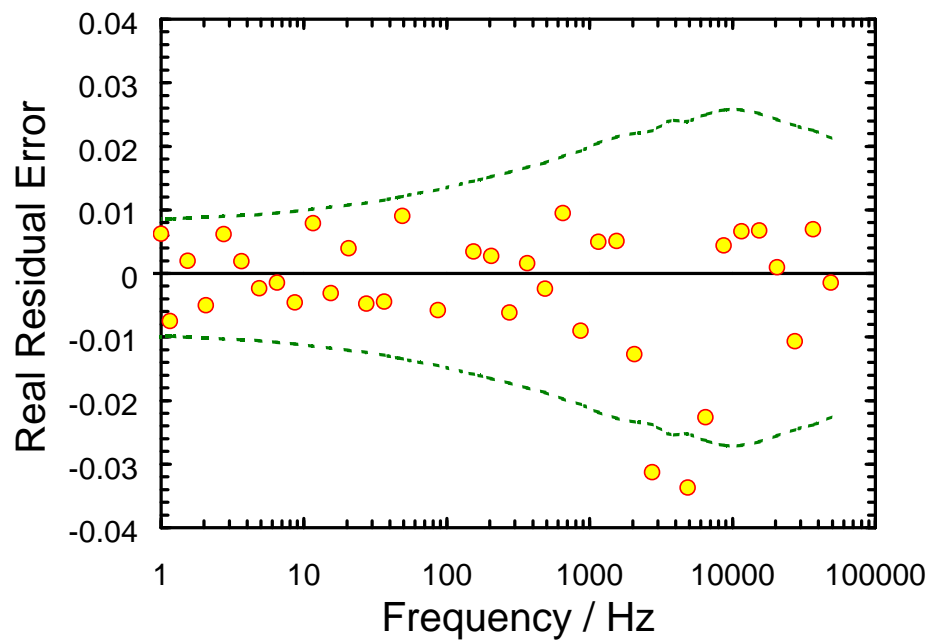
(a)
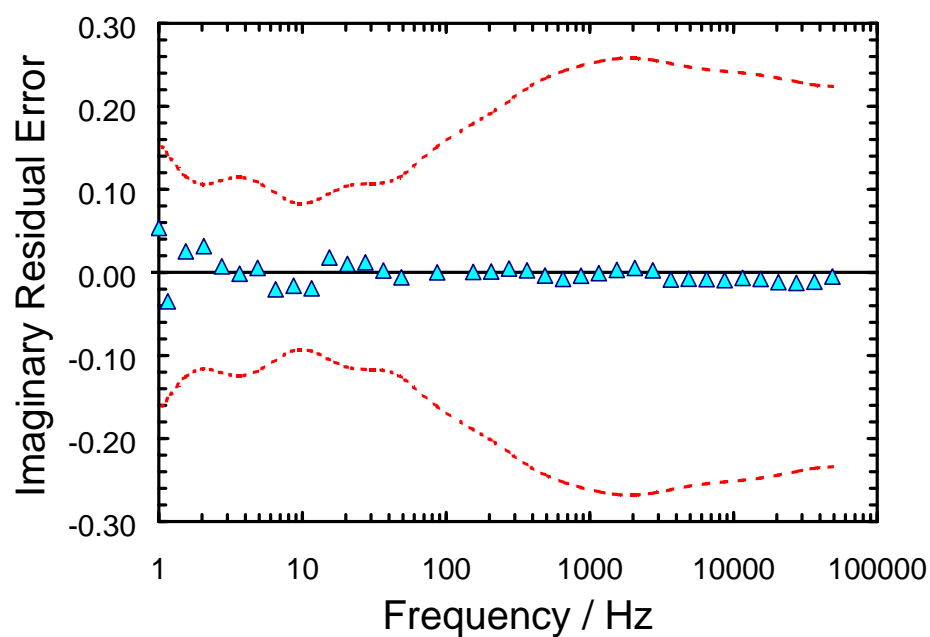
(b)

Figure 5-6: Normalized residual errors from real fit of the Measurement Model to a 10 mV VAG scan of skin in CaCl$_2$ electrolyte. (a) Fitting errors (b) Errors from prediction of imaginary part of the impedance.

surement values, randomly distributed and completely contained within the noise level of the measurement. These results indicated that the Measurement Model provided a good fit to the skin impedance data.

The prediction of the real part of the impedance from the fit to the imaginary component of impedance is illustrated in Figure 5.7(b). The normalized real residual errors were all contained within the 95.4% confidence interval. This observation led to the conclusion that the entire spectrum was consistent with the Kramers-Kronig relations. Consistency with the Kramers-Kronig relations was observed for all impedance spectra collected by the 10 mV VAG modulation technique.

Although not presented here, the impedance spectra collected by 1 μA constant-amplitude galvanostatic modulation were also consistent with the Kramers-Kronig relations over the entire frequency range. The consistency of impedance spectra collected at the 1 μA perturbation amplitude indicated that the properties of skin were not altered by the measurement technique. An important aspect of these experiments was that the potential difference across the skin was not larger than 0.55 V. The transdermal voltage drops associated with the 1 μA spectra are significantly smaller than for the 10 μA constant-amplitude galvanostatically modulated spectra discussed in the next section.

KK consistency check for 10 μA constant-amplitude galvanostatic spectra. The procedure for identifying data that is not consistent with the Kramers-Kronig relations described in Section 5.2.1 was applied here. The normalized real residual errors for a fit to the real part of the data are presented in Figure 5.8(a). The residual errors demonstrated significant trending and were on the order of 10% of the measurement. Furthermore, many of the residual errors were located outside the
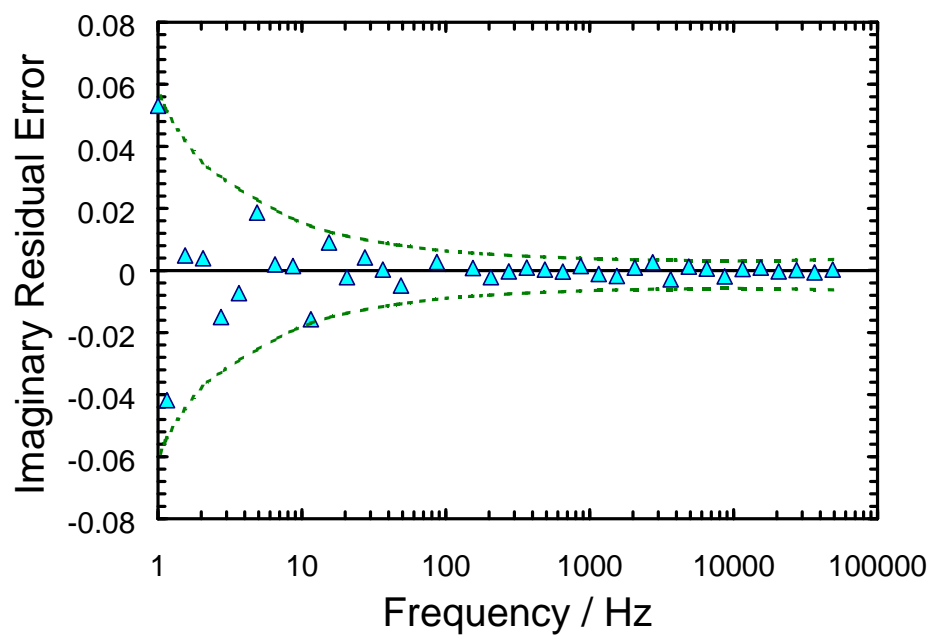
(a)
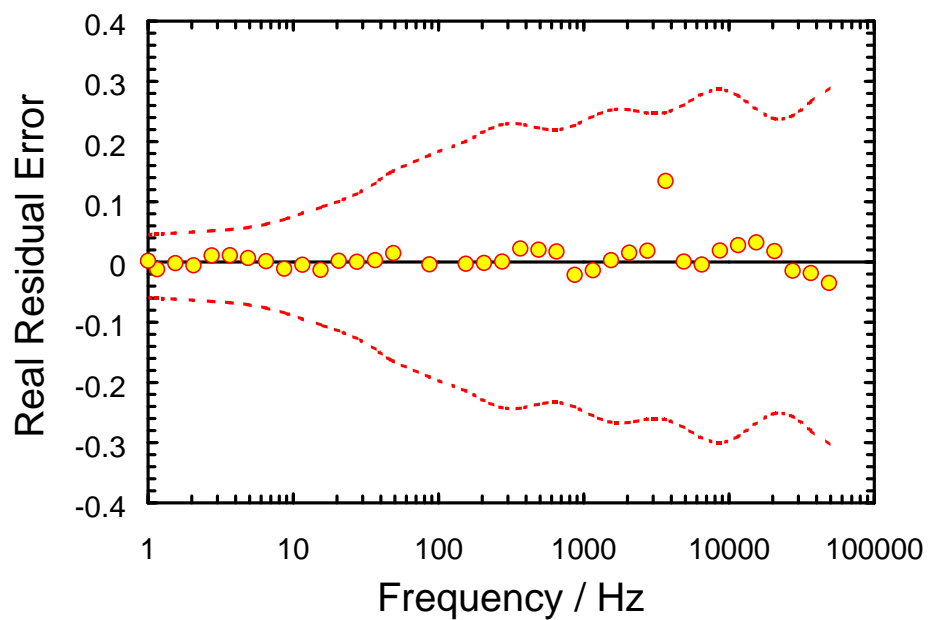
(b)

Figure 5-7: Normalized residual errors from an imaginary fit of the Measurement Model to a 10 mV VAG scan of skin in $CaCl_2$ electrolyte. (a) Fitting errors (b) Prediction of real part of the impedance.

noise level of the measurement. The distribution characteristics of the real residual errors were consistent with a poor fit.

The residual errors associated with the prediction of the imaginary part of the impedance are shown in Figure 5.8(b). The imaginary residual errors were approximately equal to 10 percent of the impedance at frequencies greater than 100 Hz. The residuals associated with frequencies below 100 Hz were as large as 200% of the measurement value. The skin impedance data collected at frequencies above 10 kHz fell within the 95.4% confidence interval. Despite the relatively poor quality of this fit, the entire spectrum was included for the fit of the measurement model to the imaginary part of the impedance.

The normalized residual errors for the fit of the Measurement Model to the imaginary part of the impedance are presented in Figure 5.9(a). All of the residual errors fell within the noise level of the measurement and were approximately equal to 1% of the measurement. The residuals from the prediction of the real part of the impedance are presented in Figure 5.9(b). The real residual errors for frequencies less than 100 Hz were located outside the confidence interval. Furthermore, the magnitude of the residual errors increased with decreasing frequency. Therefore, the impedance data collected at frequencies below 100 Hz were considered to be inconsistent with the Kramers-Kronig relations.

The inconsistent data points were obtained when the potential variation across the skin exceeded 1.06 V which corresponded to the measurement at 100 Hz. During the impedance experiment, the potential difference across the membrane continued to increase until 5 Hz where a maximum of approximately 4.97 V was observed. The range of potential for which changes in membrane properties were observed was consistent with the reported threshold of voltage for skin changes of 0.1 to 2 V.[3]
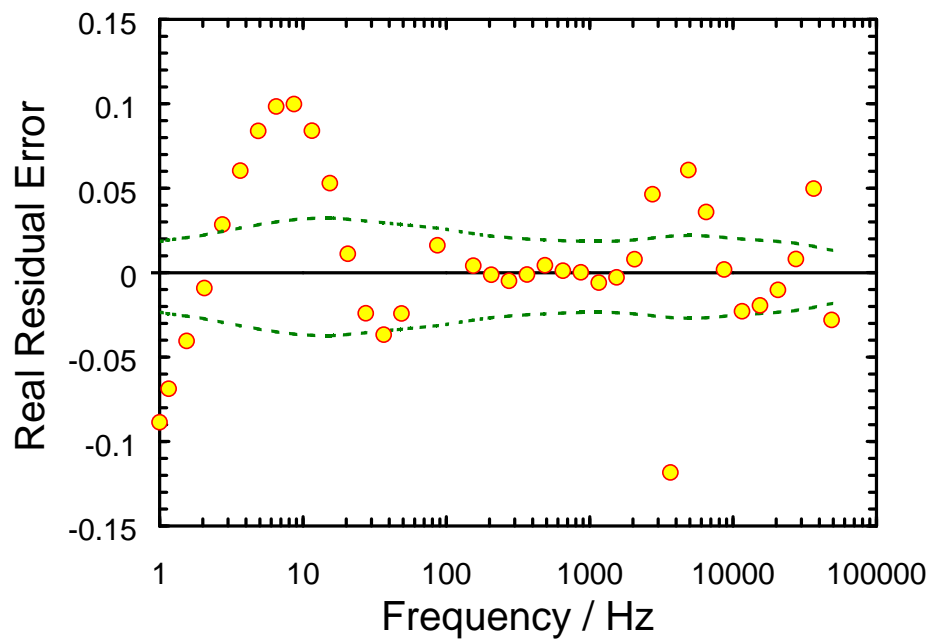
(a)
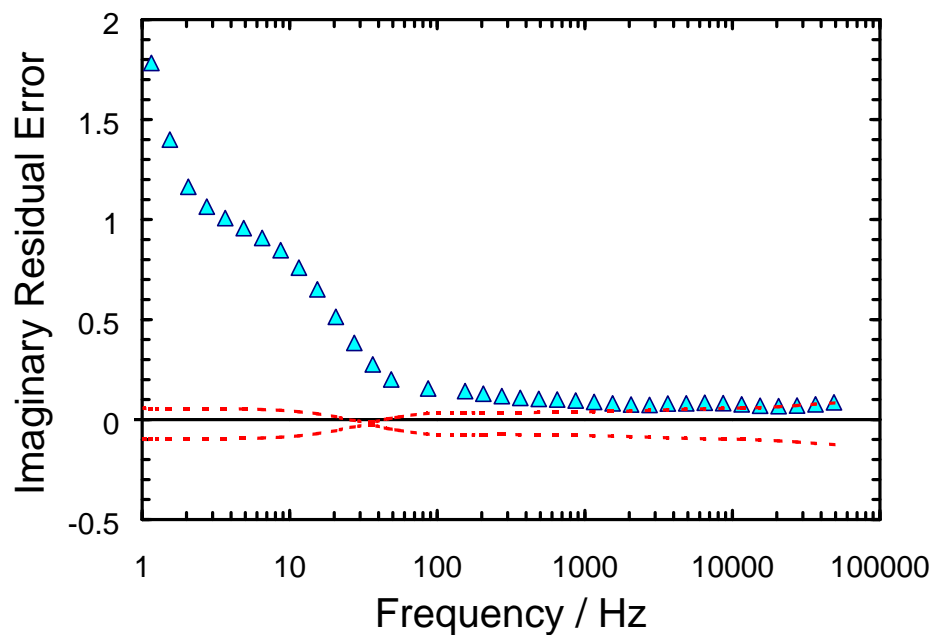
(b)

Figure 5-8: Normalized residual errors from a fit of the Measurement Model to the real part of a 10 μA constant-amplitude galvanostatic scan of skin in $CaCl_2$ electrolyte. (a) Fitting errors (b) Errors from prediction of imaginary part of the impedance.
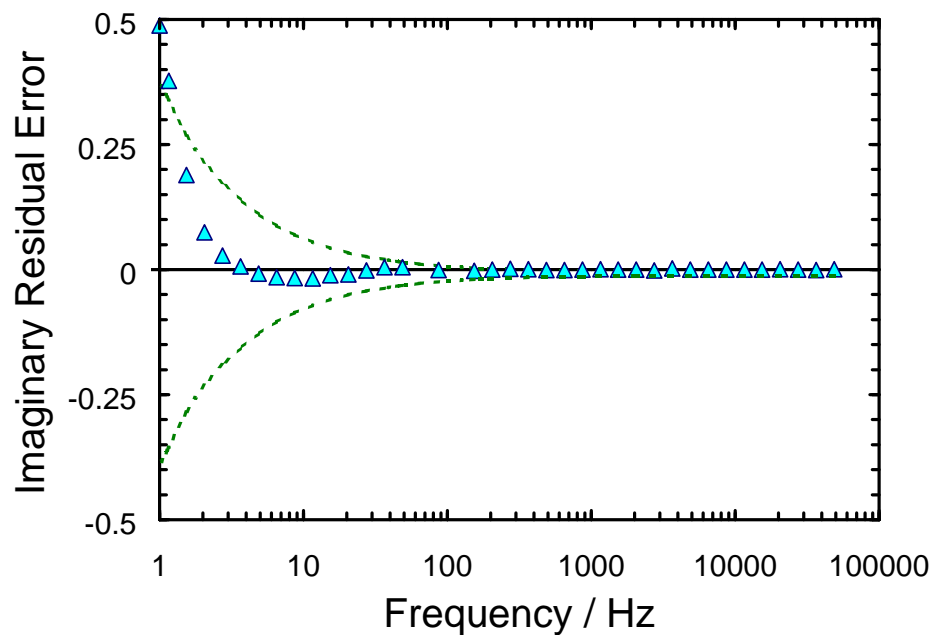
(a)
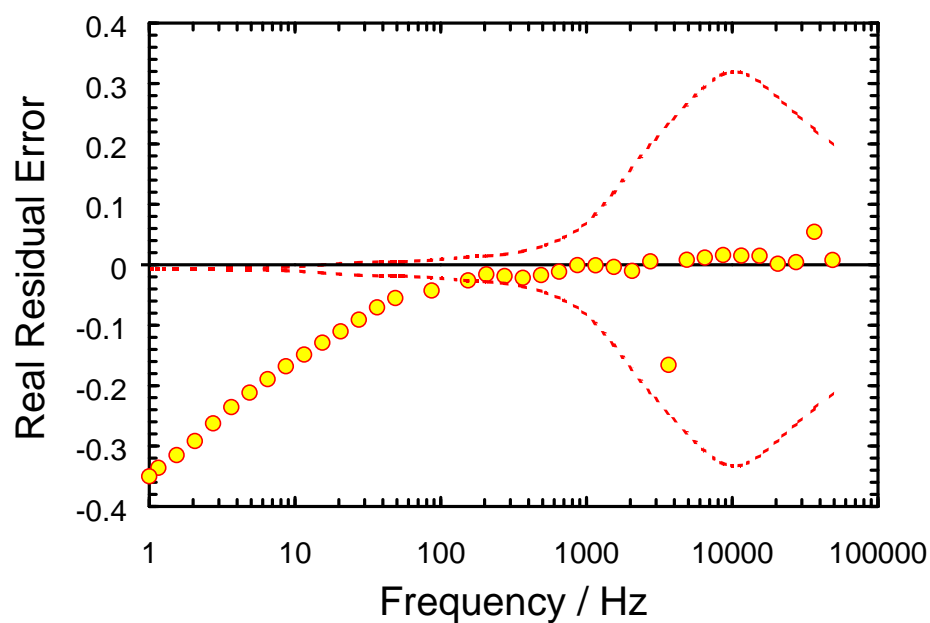
(b)

Figure 5-9: Normalized residual errors from a fit of the Measurement Model to the imaginary part of a selected 10 μA constant-amplitude galvanostatic scan of skin in CaCl$_2$ electrolyte. (a) Fitting errors (b) Prediction of real part of the impedance.

5.2.2   Comparison of Modulation Methods

The magnitude of skin impedance as measured by the 10 mV VAG and 10 μA constant-amplitude galvanostatic modulation methods presented the previous sections are plotted as a function of frequency in Figure 5-10. The solid circles and
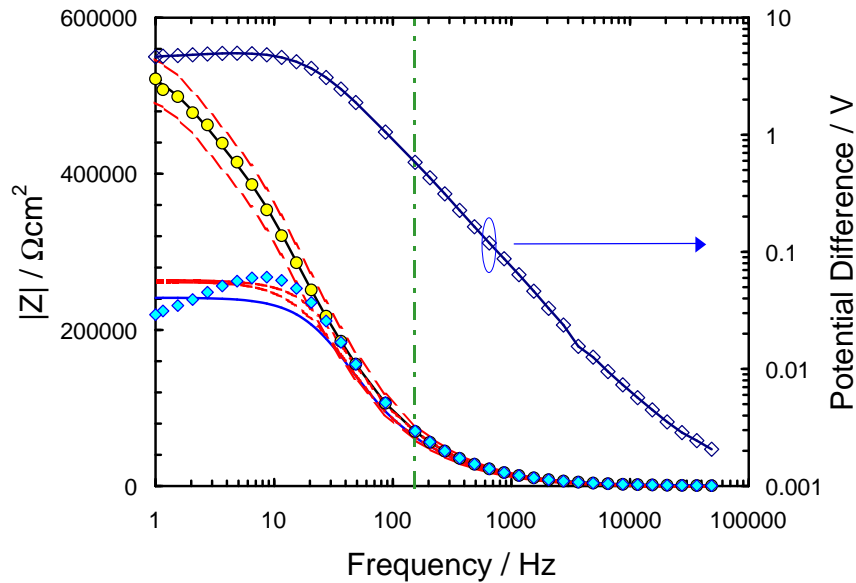
Figure 5-10: Skin impedance as a function of frequency collected by both VAG and constant-amplitude modulation. The filled circles and filled diamonds correspond to spectra collected by 10 mV VAG and 10 μA constant-amplitude modulation. The solid lines represent the fits of the Measurement Model to the data. The open diamonds correspond to the potential drop across skin induced by the 10 μA current perturbation.

solid diamonds correspond to the responses measured by the 10 mV VAG and 10 μA constant-amplitude galvanostatic modulation techniques, respectively. The regression of the Measurement Model to the 10 mV VAG spectrum, illustrated by the solid black line, demonstrated excellent agreement with the data. The entire data set was located within the confidence interval which is signified by the dashed lines.

The Measurement Model fit to the spectrum collected by 10 μA galvanostatic control, shown by the solid line with vertical cross marks, did not coincide with the data at frequencies below 150 Hz. The data corresponding to this low-frequency

range were located outside the confidence interval for the Kramers-Kronig consistent prediction for skin impedance. The inconsistent data provided an indication that skin properties were altered by the 10 μA constant-amplitude galvanostatically modulated impedance experiment.

The potential difference across skin induced by the 10 μA perturbations is denoted by the open diamonds in Figure 5-10. The vertical dashed line located at 150 Hz represents the critical frequency below which skin properties began to change. The voltage difference across the membrane at this frequency was 580 mV which was consistent with the concept that large electric fields can alter the properties of skin. The potential difference drop across skin associated with the Kramers-Kronig consistent 10 mV VAG spectrum is not shown as a maximum amplitude of 10 mV was maintained over the entire frequency range.

In summary, it was demonstrated that impedance spectra collected by 10 mV variable-amplitude galvanostatic (VAG) modulation and 1 μA constant-amplitude galvanostatic modulation were consistent with the Kramers-Kronig relations. This implied that the impedance experiment did not significantly alter, in a statistical sense, skin transport properties. In contrast, spectra collected by the traditional constant-amplitude galvanostatic modulation method at the 10 μA perturbation amplitude were not consistent with the Kramers-Kronig relations. The inconsistent data points were located in the low-frequency portion of the spectra. The failure of the data to conform with the Kramers-Kronig relations implied that skin properties had been altered. Subsequent spectra collected by variable-amplitude galvanostatic modulation were consistent with the Kramers-Kronig relations.

The data from the 10 μA constant-amplitude galvanostatically modulated experiments which did not satisfy the Kramers-Kronig relations were observed when the potential difference across the skin exceeded approximately 0.5 V. This obser-

vation was consistent with the concept that the properties of skin begin to change above a critical potential. The range of potential for which skin changes were detected in this study was in agreement with the potential and current step-change experiments discussed in Section 8.1 of this report.

Although the impedance spectra from the 10 μA constant-amplitude galvanostatic scans did not conform to the Kramers-Kronig relations for the skin samples immersed in NaCl and $CaCl_2$ electrolytes, differences were noted in the recovery of epidermal properties following the large current perturbation experiments. For example, impedance spectra collected by 10 mV variable-amplitude galvanostatic modulation following the 10 μA experiments indicated that the skin impedance recovered $\sim 66\%$ in NaCl electrolyte and $\sim 80\%$ in $CaCl_2$ electrolyte. The difference in the recovery of skin impedance to the 10 μA perturbations suggested that divalent cations can reduce the effect of large electric fields on epidermal transport properties. The improved recovery of skin in $CaCl_2$ electrolyte as opposed to NaCl electrolyte has also been reported in the literature.[152]

5.3   Comparison of Experiments with Literature Results

The majority of skin impedance spectra described in the literature were collected by either constant-amplitude potentiostatic[133,205,211] or constant-amplitude galvanostatic modulation.[150,152,151,207] Impedance data obtained with these modulation methods may be corrupted by nonlinear or nonstationary phenomena. For example, transient processes, such as skin hydration (see, for example, Section 6.2), can cause the open-circuit potential across the membrane to change. In general, potentiostatic impedance experiments are conducted by modulating a sinusoidal constant-amplitude voltage perturbation about the open-circuit potential measured at the beginning of the experiment. Therefore, changes in the open-

circuit potential that occur within the time required to complete a perturbation cycle can introduce artifacts in the impedance measurements.

Many researchers have adopted the constant-amplitude galvanostatic modulation technique to mitigate the influence of changes in the open-circuit potential on skin impedance measurements.[151,152] Theoretically, the net current across a system will be zero at the open-circuit condition. By modulating the sinusoidal current perturbation about a 0 $\mu A/cm^2$ DC current bias, the open-circuit potential is maintained over the course of the impedance experiment. Despite this attractive feature, the regulation of skin impedance experiments by the constant-amplitude galvanostatic method can be problematic. For example, the constant-amplitude current perturbation can cause the voltage difference across skin to surpass 1 V. The literature indicates that skin properties begin to change when the potential across the membrane exceeds 0.1-2 V.[3]

Kalia *et al.* developed a modulation technique to reduce the impact of the impedance experiment on skin transport properties.[152] A 2 MΩ resistor was placed in series with the skin. In this configuration, the 1 V sinusoidal potential perturbation used to probe the system produced a 0.25 μA (80 nA/cm^2) constant-amplitude current signal. The approach had the advantage that the critical potential for membrane alterations could be avoided when the skin polarization resistance was less than 1 MΩ/cm^2. The efficacy of the impedance regulation method for preventing changes to skin transport properties was demonstrated for *in vivo* experiments.[152]

The development of the novel variable-amplitude galvanostatic (VAG) modulation method for skin impedance experiments was described in this chapter. The regulation technique provided spectra that were not subjected to large potential swings across the membrane. Skin impedance spectra were collected in this

work by (VAG) regulation and by the traditional constant-amplitude galvanostatic modulation strategy. The results were compared to assess the influence of each modulation technique on skin properties.

The Voigt circuit measurement model was regressed to each type of spectra. As the model was consistent with the Kramers-Kronig relations, data corrupted by nonlinear or nonstationary behavior could be identified. Spectra collected with the constant-amplitude galvanostatic technique did not conform to the Kramers-Kronig relations. In contrast, spectra obtained by variable-amplitude galvanostatic modulation were consistent with the Kramers-Kronig relations which implied that the skin was not altered by the experiment. By preventing large potential differences across skin, the electrical and transport properties of the membrane were measured in a noninvasive manner.

Electrical circuit models have been used extensively in the literature to analyze skin impedance data.[133,211−213] As described in Section 3.6.1, the general procedure is to assign system physical properties to the individual elements of the circuit. There are several flaws in this approach. For example, electric circuit analogs are not unique, which can lead to multiple interpretations of skin impedance spectra. Furthermore, the circuit elements are assumed to react linearly independent of time and applied potential. These conditions cannot be guaranteed *a priori* for human skin impedance data.

The work presented here marked the first application of electric circuit models for determining the measurement characteristics of skin impedance data. Portions of the spectra that were free of instrumental artifact and nonstationary behavior were identified. The results indicated that the modulation of skin impedance experiments by the novel variable-amplitude galvanostatic methodology provides for more accurate assessment of the electrical and transport properties of skin.

CHAPTER 6
RESULTS AND DISCUSSION OF SKIN IMPEDANCE STUDIES

The development of the variable-amplitude galvanostatic modulation technique for electrochemical impedance spectroscopy was described in Chapter 5. It was demonstrated that skin impedance spectra collected by the adaptive modulation strategy were consistent with the Kramers-Kronig relations. This indicated that the macroscopic electrical and transport properties of the membrane were not altered by the experiment. Therefore, the variable-amplitude galvanostatic modulation strategy was applied extensively in the studies discussed here.

As stated earlier, an objective of the impedance studies was to characterize influence of current and potential on skin properties. The experiments presented here were designed to identify the impedance response of skin under open-circuit and applied-current conditions. The open-circuit impedance studies provided information on the dynamics of skin hydration and the recovery of the skin properties after the applied current was terminated. The impedance spectra collected under iontophoretic conditions revealed the influence of applied current on skin properties. The results from the applied-current study are presented in Section 6.5.

Many of the impedance spectra collected in the initial studies had negative values for the real part of the impedance at high frequencies. The high-frequency asymptote of the real part of the impedance corresponds to the solution resistance. The negative solution resistance measurements were thought to be an instrumental artifact. The work performed to determine the source of the high-frequency artifact is described in Section 6.1.

The impedance experiments aimed at identifying the influence of prolonged electrolyte exposure on skin transport properties are presented in Section 6.2. The objective was to characterize the dynamics of skin hydration. The study provided a baseline for evaluating changes in skin properties caused by the addition of water into the membrane.

It has been proposed that the recovery of skin properties after large electrical perturbations is more rapid in divalent cation solutions than in monovalent cation solutions.[152] The influence of solution composition on skin properties is described in Section 6.3.

It was shown in Chapter 5 that large potential swings can alter skin electrical and transport properties. The large potential drops across the skin were induced by the constant amplitude-galvanostatic modulation technique. A supplemental impedance study using variable-amplitude galvanostatic modulation was performed to confirm that skin can be altered by large potential signals. The results from the investigation are presented in Section 6.4.

Transdermal iontophoresis was simulated during the impedance studies by modulating the sinusoidal current perturbation about a DC current bias. The amplitude of the direct current signals were consistent with clinical iontophoresis systems.[177,201,236] A discussion of this work is provided in Section 6.5.

The final study described in this chapter was designed to identify the regional variation in the impedance response of heat-separated excised human skin. For most of the experiments performed in this work, pieces of skin were extracted from adjacent locations of a given donor sample. The experiments described in Section 6.6 provide an estimate of the variation in skin properties associated with the membranes used for this work.

6.1 Influence of Reference Electrode on High-Frequency Impedance Response

As mentioned earlier, the majority of skin impedance spectra collected in this work were obtained by Variable-Amplitude Galvanostatic (VAG) modulation control. For these studies, Ag/AgCl micro-reference electrodes were used. For many of the spectra, the real component of the impedance at high frequencies was negative. For a typical four-electrode measurement of membrane impedance, the high-frequency asymptote of the real part of the impedance should be equal to the electrolyte solution resistance.

It was hypothesized that the nonideal behavior at high-frequency was caused by the micro-reference electrodes. For example, the small surface area of the micro-reference electrodes may restrict the range of applied potential for which either the ideally nonpolarizable electrode assumption or the reversible equilibrium state is valid.[137] An alternative explanation is that the negative electrolyte solution resistance values were an artifact of the potentiostat or the Frequency Response Analyzer. Measurement or bias errors from the impedance equipment are usually caused by limitations of the internal circuitry and are commonly observed at high frequencies for low impedance systems.

During iontophoresis the electrical and transport properties of skin will be influenced by an applied DC current bias. Changes in skin properties will most likely appear in the low-frequency portion of the impedance spectra. Therefore, impedance spectra with negative high-frequency asymptotes for the real component of the complex impedance should still contain the essential information on skin transport properties. The main limitation posed by the apparent negative solution resistance was that only one or two line shapes could be obtained from the regression of the Measurement Model to the impedance data (see, for example, Section 4.1.4). The small number of line shapes often resulted in large fitting er-

rors. The poor fitting behavior made it difficult to determine whether a particular impedance spectra was consistent with the Kramers-Kronig relations. This limited the interpretive power of the Measurement Model technique for assessing the influence of a given set of experimental control variables on skin properties.

The object of this study was to determine the influence of reference electrodes on the high-frequency impedance response of skin. The approach was to collect replicate impedance spectra under similar experimental conditions using both Ag/AgCl micro-reference electrodes and calomel reference electrodes. Spectra collected with the calomel electrodes were compared to the data collected with the Ag/AgCl micro-reference electrodes. Calomel reference electrodes were selected for the comparison as they are commonly used for electrochemical measurements and are stable over a wide range of potentials.[136]

The impedance experiments were conducted under constant-amplitude galvanostatic control. Perturbation amplitudes of 100 μA and 10 μA were superimposed about a 0 μA DC current bias to produce four sets of seven replicate scans. The skin was soaked for 48 hours in 50 mM $CaCl_2$ buffered electrolyte prior to the study to allow the membrane to become fully hydrated. The same piece of skin and same electrolytic solution were used for all experiments. A custom, two-compartment diffusion cell was constructed from polycarbonate sheeting to accommodate the larger dimensions of the calomel reference electrodes. All of the impedance experiments were performed with the custom cell. The results from the 10 μA experiments are not presented, as the trends were similar to the 100 μA studies discussed below.

Selected impedance spectra collected with each type of reference electrode were then assessed with the Kramers-Kronig relations according to methodology described in Section 4.1.4. The entire frequency range of the spectra were checked for

consistency with the Kramers-Kronig relations. Inconsistency with the Kramers-Kronig relations was assumed to be caused by instrumental artifacts.

6.1.1 Results

The impedance response of skin to the 100 μA perturbations measured by the calomel and Ag/AgCl micro-reference electrodes are presented in impedance-plane form by Figures 6.1(b) and 6.1(a), respectively. The high-frequency asymptotes of the real part of the impedance are located near the origin of the figures. The spectra collected by the calomel reference electrodes, shown in Figure 6.1(b), displayed positive impedance values in the high-frequency region. In contrast, the high-frequency asymptotes of the impedance spectra collected with the Ag/AgCl micro-reference electrodes, displayed in Figure 6.1(a), were negative.

The low-frequency impedance of this piece of skin was approximately 5 kΩcm^2 regardless of the reference electrode type. The low polarization resistance values were probably caused by prolonged exposure to water. Since the focus of the study was to analyze the high-frequency response of the reference electrodes, the low polarization resistance values were not considered to be prohibitive.

6.1.2 K-K Consistency Check for Calomel Electrode Data

Complex fits of the Measurement Model were performed for all of the impedance spectra collected by the 100 μA galvanostatic modulation. Modulus weighting was applied for the regressions. Seven line shapes were obtained for all of the impedance spectra. In general, the line shape model showed good agreement with the data obtained with the calomel reference electrodes. The error structure for the measurements, as defined by Equation (4-15), was calculated. The parameters α and δ were included in the model and were equal to 4.17×10^{-4} and 7.63×10^{-2}, respectively.

(a)

(b)
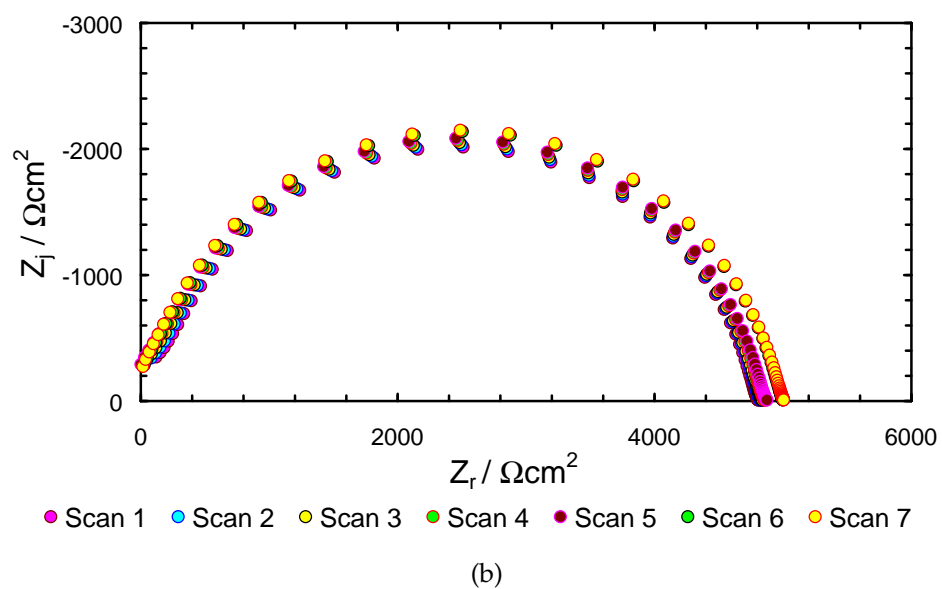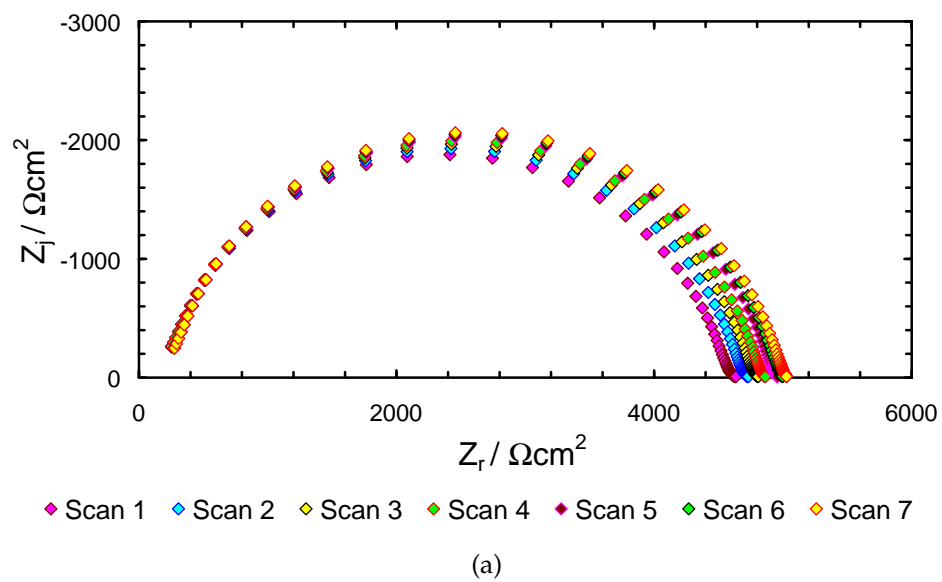
Figure 6-1: Impedance-plane plots of successive 100 μA impedance scans of fully hydrated skin. (a) Measured with Ag/AgCl micro-reference electrodes. (b) Measured with calomel reference electrodes.
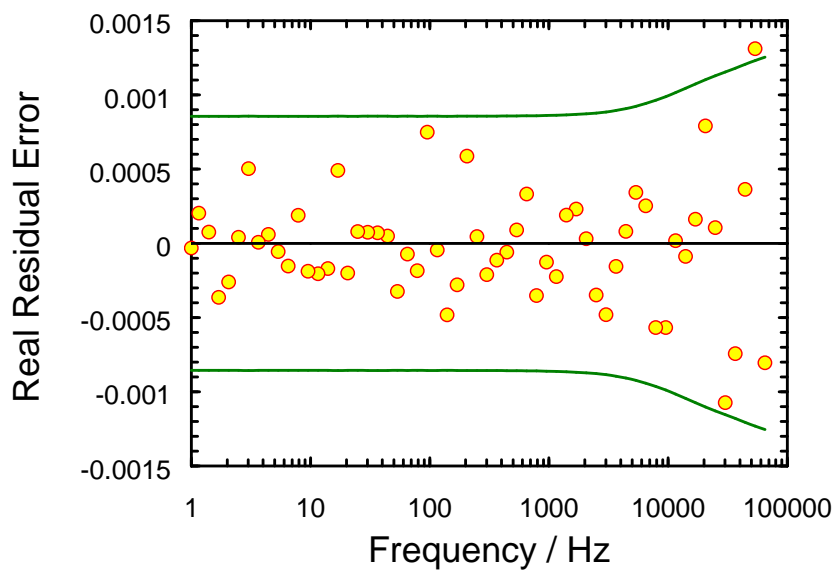
(a)
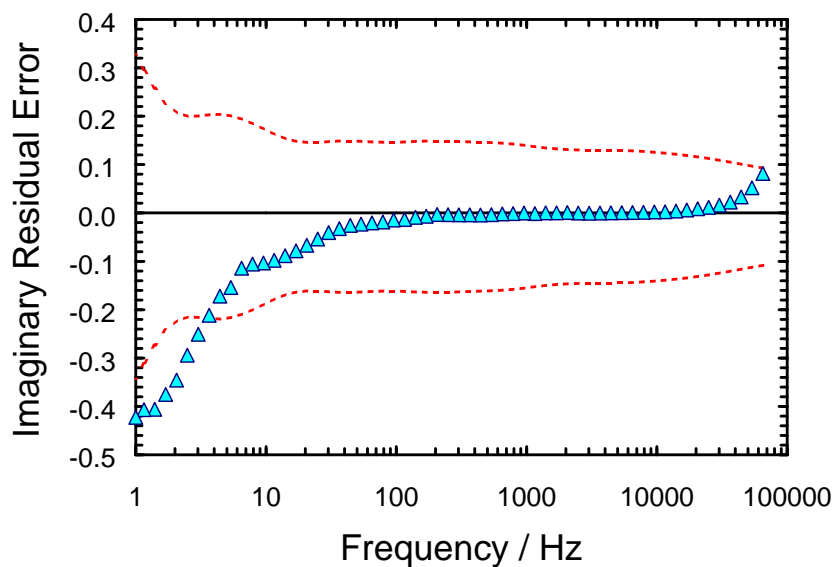
(b)

Figure 6-2: Normalized residual errors from a fit of the Measurement Model to the real part of skin impedance. Spectrum was obtained from hydrated skin in buffered CaCl$_2$ electrolyte and collected with calomel reference electrodes. (a) Regression fitting errors. (b) Errors from prediction of imaginary part of the impedance.

The fourth spectrum collected with the calomel reference electrodes was assessed for consistency with Kramers-Kronig relations. The regressions of the Measurement Model to the data were weighted by the error structure. The fit to the real part of the complex impedance yielded 8 line shapes. The normalized residual fitting errors from the regression are displayed in Figure 6.2(a). The solid circles and solid lines correspond to the fitting errors and the noise level of the measurement, respectively. The residual errors were generally less than 1% of the real part of the impedance and fell within the noise level of the measurement. In addition, the residual errors were normally distributed about the x-axis. The relatively small magnitude and normal distribution of the residual errors indicated a good fit of the model to the data.

The residual errors for the prediction of the imaginary component of the impedance are presented in Figure 6.2(b). The residual errors correspond to the solid triangles and the 95.4% confidence interval is shown by the dashed lines. The errors were on the order of 10% of the measured impedance for frequencies above 10 Hz. The normalized residual errors for frequencies above 5 Hz were within the confidence interval indicating that the high-frequency data conformed to the Kramers-Kronig relations.

The Measurement Model was regressed to the imaginary component of the impedance. The objective was to determine whether the low-frequency portion of the spectrum also satisfied the Kramers-Kronig relations. Eight line shapes were obtained from the imaginary fit. The normalized fitting errors are presented in Figure 6.3(a). The noise level for the measurement is indicated by the solid line and the residual errors are shown by the solid triangles. The fitting errors were all less than five percent of the imaginary component of the impedance. The noise level for the imaginary fit was approximately 40% of the impedance at 1 Hz. The noise
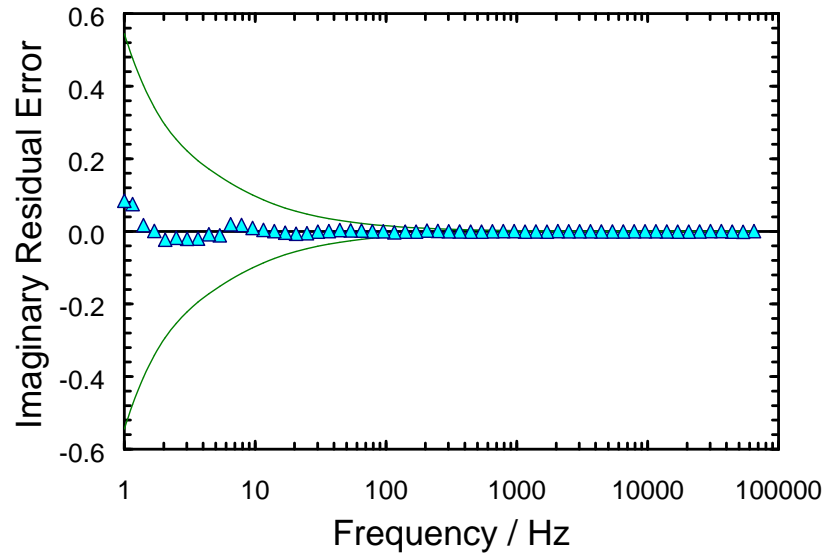
(a)
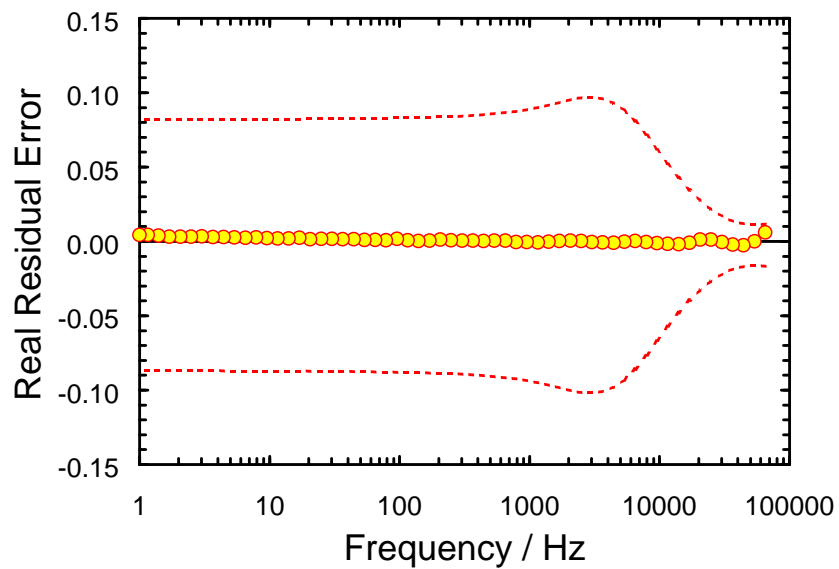
(b)

Figure 6-3: Normalized residual errors from an imaginary fit of the Measurement Model to a selected impedance spectrum of hydrated skin measured with calomel reference electrodes. (a) Normalized fitting errors from regression. (b) Errors for prediction of the real component of the impedance.

level gradually decreased with increasing frequency, reaching an asymptotic value of 5% of the impedance for frequencies greater than 100 Hz. All of the residual errors were located within the noise level of the measurement which implied that a statistically valid fit had been obtained.

The relative residual errors from the prediction of the real part of the impedance are presented in Figure 6.3(b). The normalized residuals are indicated by the solid triangles and the 95.4% confidence interval is shown by the dashed red lines. The residual errors were all less than 2% of the measurement and fell within the 95.4% confidence interval. This indicated that the impedance spectrum collected with the calomel reference electrodes was consistent with the Kramers-Kronig relations. Therefore, it was concluded that the electrical and transport properties of skin were not altered by the low-frequency perturbations.

6.1.3 K-K Consistency Check for Micro-Reference Electrode Data

Regression of the Measurement Model to impedance spectra collected with the Ag/AgCl micro-reference electrodes proved to be problematic. For example, complex fits weighted by the modulus of impedance yielded only one line shape. The frequency-dependent error structure model presented by Equation (4-15) was regressed to the residual errors from the complex fits. The appropriate error structure for the measurements included the model parameters α and δ which were equal to 2.35×10^{-3} and 4.73, respectively. The fourth impedance spectrum was then assessed for consistency with the Kramers-Kronig relations. The regressions of the Measurement Model were weighted by the error structure.

A real fit to the data yielded three line shapes. The normalized fitting errors are presented in Figure 6.4(a). The residual errors exhibited significant trending and fell outside the noise level at high frequencies. The magnitude of the fitting errors were as large as 75% of the real part of the impedance at high frequencies.

The large fitting errors at high frequencies were probably caused by the negative values of the real part of the impedance.

The residual errors for the prediction of the imaginary part of the impedance, shown in Figure 6.4(b), also demonstrated significant trending. Many of the residual errors were located outside the confidence interval. The three data points outside the confidence interval at high-frequency were considered inconsistent with the Kramers-Kronig relations. The inconsistent data points were not included for the fit of the Measurement Model to the imaginary part of the impedance.

Nine line shapes were obtained from the imaginary fit to a skin impedance spectrum collected with the Ag/AgCl micro-reference electrodes. The residual fitting errors are presented as a function of frequency in Figure 6.5(a). The errors were normally distributed and were less than 5% of the imaginary part of the impedance. The normalized errors from the prediction of the real impedance are presented in Figure 6.5(b). The residual errors were between 2% and 10% for frequencies above 5 kHz. The remainder of the errors were all on the order of 1%. Since all of the data fell within the confidence interval, this portion of spectrum was considered to be consistent with the Kramers-Kronig relations.

6.1.4   Comparison of Calomel and Micro-Reference Electrodes

The low-frequency portions of the spectra collected with the calomel and the Ag/AgCl micro-reference electrodes satisfied the Kramers-Kronig relations. However, only the data collected with the calomel electrodes conformed to the Kramers-Kronig relations at high-frequency. It is emphasized that all of the spectra were collected under identical conditions with the exception of the reference electrode type. Therefore, the inconsistent data in the high-frequency portions of the spectra collected with the micro-reference electrodes was assumed to be caused by instrumental artifact.
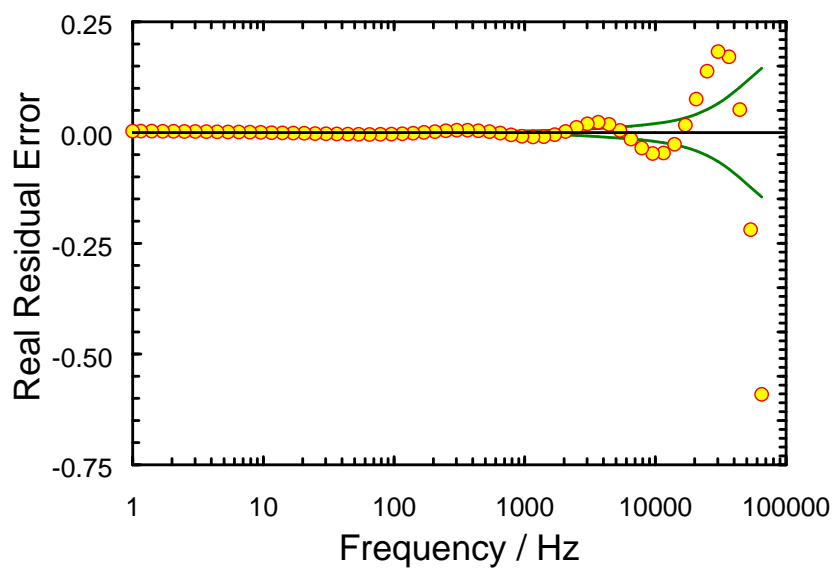
(a)
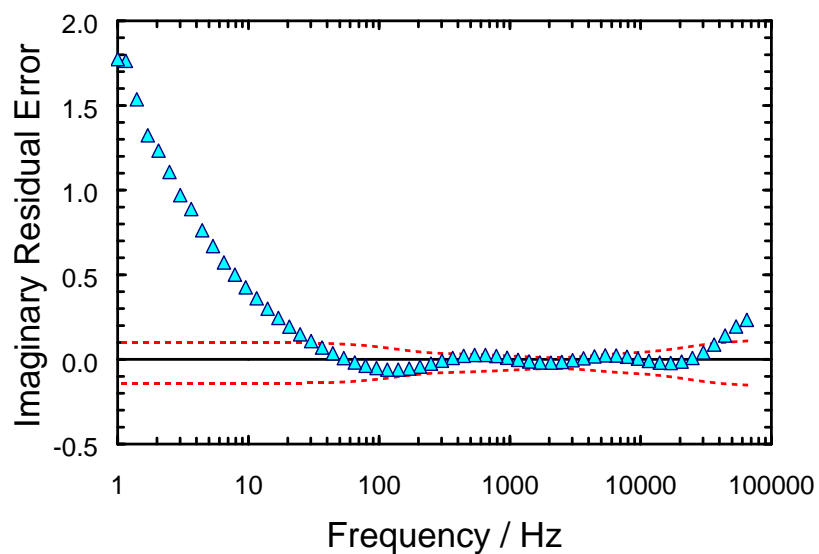
(b)

Figure 6-4: Normalized residual errors from a real fit of the Measurement Model to a selected impedance spectrum of hydrated skin measured with Ag/AgCl micro-reference electrodes. (a) Regression fitting errors. (b) Errors from prediction of the imaginary component of the impedance.
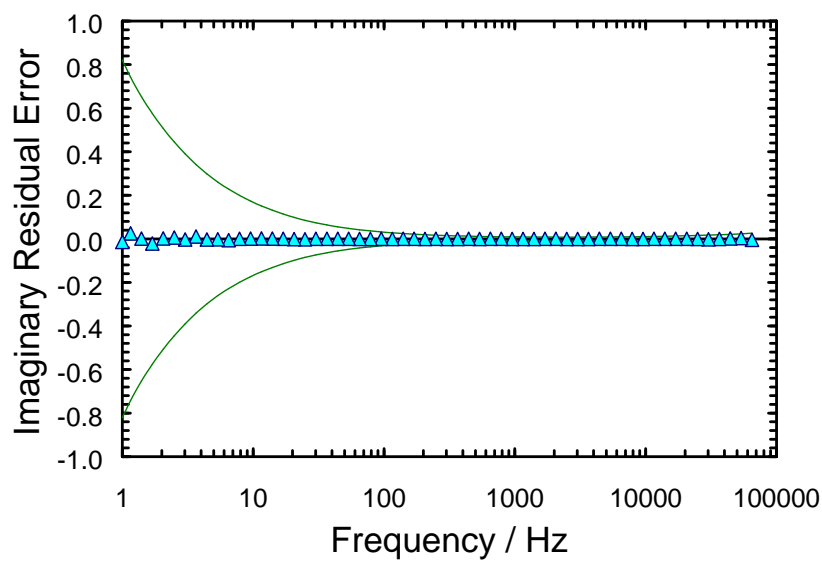
(a)
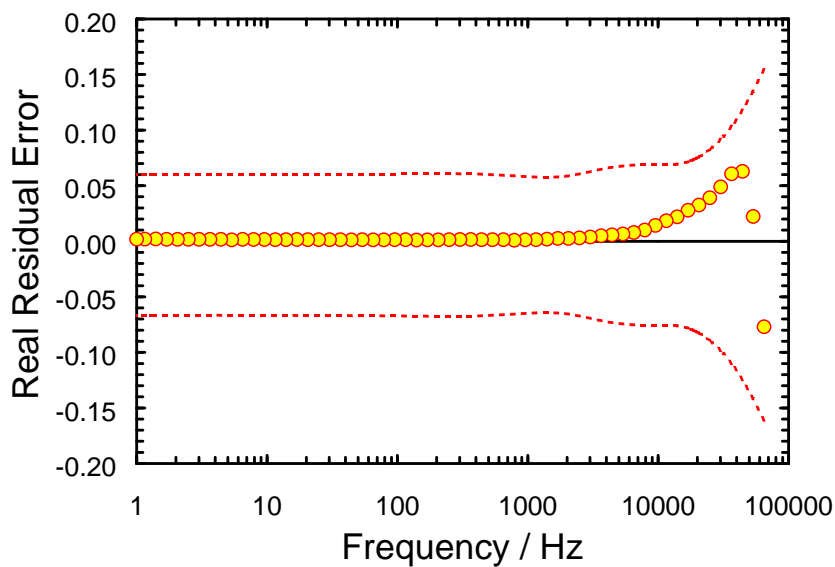
(b)

Figure 6-5: Normalized residual errors from an imaginary fit to a selected imped-
ance spectrum of hydrated skin measured with Ag/AgCl micro-reference elec-
trodes. (a) Normalized fitting errors. (b) Errors for prediction of real part of the
impedance.

The difficulty in measuring the high-frequency response of skin with Ag/AgCl micro-reference electrodes may be associated with the low impedance of the system. For example, most electrochemical systems, including skin, display the lowest values of impedance at high-frequency. Therefore, the voltage drop induced by the high-frequency current perturbation was also small. It is likely, that the relatively small magnitude of the voltage response was partly responsible for the high-frequency artifact. For example, the smaller dimensions of Ag/AgCl micro-reference electrodes may not have been adequate to sense the high-frequency response of the system.

The potential difference across the skin induced by the current perturbation was approximately equal for the experiments conducted with both types of electrodes. However, the larger dimensions of the calomel electrodes may have been sufficient to overcome the hypothesized signal-to-noise difficulties. The study described here identified, at least in part, the source of the high-frequency artifact observed in skin impedance measurements. An important outcome of this study was that the high-frequency artifact associated with the Ag/AgCl micro-reference electrodes did not effect the quality of the low-frequency skin impedance data. Therefore, the majority of relevant information on skin transport properties was included in the impedance spectra collected with Ag/AgCl micro-reference electrodes.

6.2   Influence of Hydration on Skin Impedance

The local environment of the heat-separated skin changed significantly when the samples were placed in the diffusion cell. For example, the slightly moistened epidermis was stored in between two sheets of polymer film in the refrigerator. At the start of a typical experiment the skin was removed from the refrigerator and was immersed in a warm (32°C) salt solution with approximately the same pH

and ionic strength as the electrolytic fluid within the body.[246] The goal of this study was to characterize the transient response of skin to the change of environment. In accordance with this objective, the time required for the system to achieve steady-state was identified.

Replicate electrochemical impedance spectra were collected periodically by Variable-Amplitude Galvanostatic (VAG) modulation to track the changes. The sinusoidal current perturbation was superimposed about a 0 μA DC current bias and the amplitude of the voltage response across the skin was maintained at ± 10 mV. The open-circuit potential across the membrane was measured before and after each impedance scan. Upon completion of an impedance scan the skin was allowed to relax for three minutes before the next spectrum was collected.

Separate studies were performed on two pieces of skin extracted from the same donor sample. One piece was immersed in 50 mM $CaCl_2$ electrolyte and the other in 150 mM NaCl electrolyte. The skin impedance spectra were collected periodically for 24 hours. The control parameters were uniform for all of the experiments.

The first part of this study involved the collection of 40 impedance spectra over five and a half hours. The skin was left in solution overnight and 15 additional scans were collected on the following day. All of the spectra were checked for consistency with the Kramers-Kronig relations. The selected condition for steady-state required that the low-frequency portions of 2 consecutive impedance spectra conform to the Kramers-Kronig relations. A complete description of the results for the piece of skin in the 50 mM $CaCl_2$ electrolyte solution is provided. Selected results for the study of the skin in 150 mM NaCl are also described.

6.2.1 Direct Analysis of Hydration Data

Selected impedance spectra corresponding to every fifth impedance scan from the experiments of skin in $CaCl_2$ are presented in Figure 6.6(a). The impedance

response demonstrated a gradual and continuous decrease throughout the entire observation period. The spectra corresponding to every fifth impedance scan collected after the skin was soaked overnight are presented in Figure 6.6(b). The axis limits on Figure 6.6(b) are the same as for Figure 6.6(a) to provide for direct comparison with the spectra collected at beginning of the experiment. The low-frequency asymptotes of the last spectrum collected in first 5.5 hours of the study and the first spectrum obtained after the skin was left in solution overnight were compared. The results indicated the polarization resistance of the membrane had recovered to approximately 85% of the value measured at the start of the experiment. The partial recovery suggested that the impedance experiment had a small effect on skin properties. Subsequent spectra collected on the second day exhibited a continuous decrease in skin impedance.

The open-circuit potential measurements are presented as a function of time in Figure 6-7. The open-circuit potential at the start of the experiments was 120.1 mV. The potential difference across the membrane increased to a maximum of 151.9 mV during the first half hour of this study. The open-circuit potential asymptotically decreased to 1 mV over the course of the next hour. The 1 mV potential difference was approximately equal to the potential drop measured by a multimeter in an identical electrolyte solution in the absence of skin. It is likely that the dramatic changes in open-circuit potential were caused by the formation of aqueous ionic channels in the stratum corneum. As the conductivity of the electrolyte solutions was on the order of 0.01 S/cm, a well hydrated ion-exchange membrane, such as skin, will not likely exhibit a significant open-circuit potential.

Although the open-circuit potential across the skin remained constant after 1.5 hours, the impedance response continued to change over the entire course of the investigation (see, for example, Figures 6.6(b) and 6.6(a)). Therefore, the polariza-
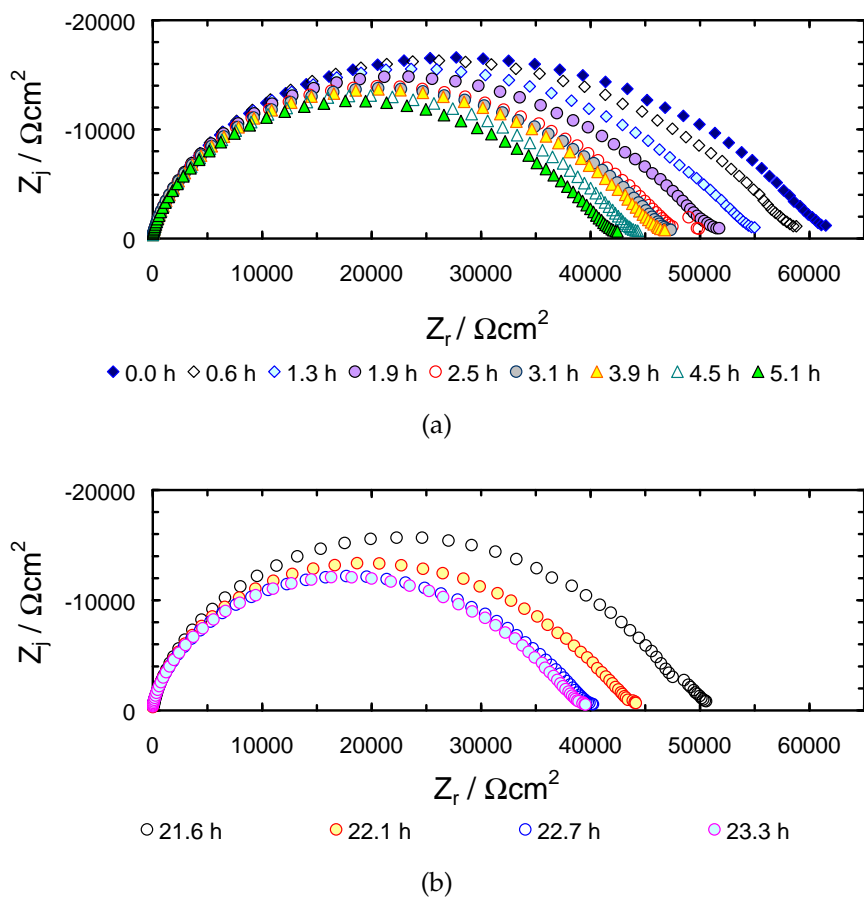
Figure 6-6: Selected sequential impedance scans of skin hydration in buffered CaCl$_2$ electrolyte. (a) Response during the initial 5.5 hours of hydration. (b) Response after skin was soaked overnight.
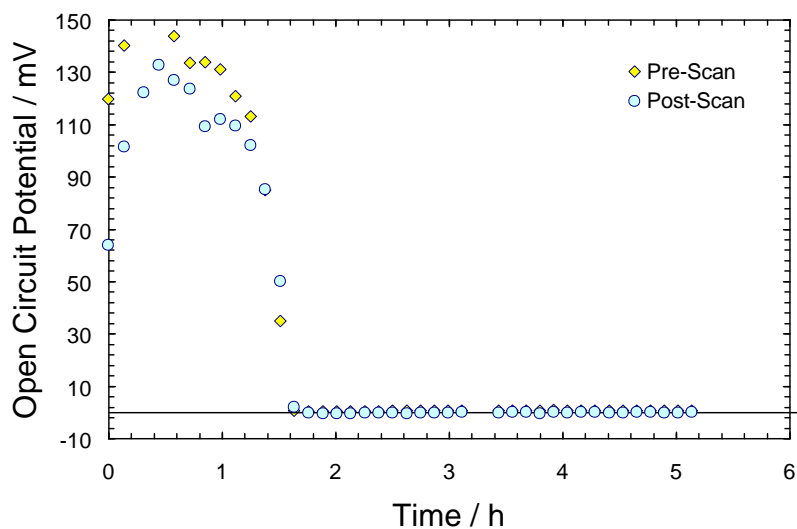
Figure 6-7: Open-circuit potential across skin during the hydration study.

tion resistance was selected as a simple parameter for characterizing changes in skin properties. Skin resistance values were normalized by the following relationship

$$R_p{}^\star = \frac{R_p - R_{p,\infty}}{R_{p,0} - R_{p,\infty}} \qquad (6\text{-}1)$$

where $R_{p,\infty}$ is the estimated asymptotic polarization resistance as time goes to infinity and $R_{p,0}$ is the polarization resistance at the start of the experiment. Two estimates for the polarization resistance were calculated. The first corresponded to the modulus of skin impedance at the lowest measuring frequency (0.1 Hz). The second estimate was the Kramers-Kronig consistent polarization resistance calculated from a fit of the Measurement Model to the experimental data.

The normalized polarization resistance of skin in divalent and monovalent electrolytes are presented in Figures 6.8(a) and 6.8(b), respectively. The solid circles and the solid triangles represent the normalized modulus of skin impedance at 0.1 Hz and the Kramers-Kronig consistent polarization resistance. The solid red line and the solid black line correspond to the fits of an exponential decay model to both sets of estimates for skin resistance.

The results indicated the skin impedance decreased continuously over the course of the experiment for both skin samples. The resistance of the skin specimens immersed in the divalent and monovalent electrolyte solutions decreased by approximately 65% and 80% respectively. For a given perturbation frequency, the Kramers-Kronig consistent polarization resistance of skin was generally lower than the modulus of skin impedance at the lowest measuring frequency. The difference between the two estimates of skin resistance implied that the response predicted for a time invariant skin sample was slightly lower than the measured quantity.
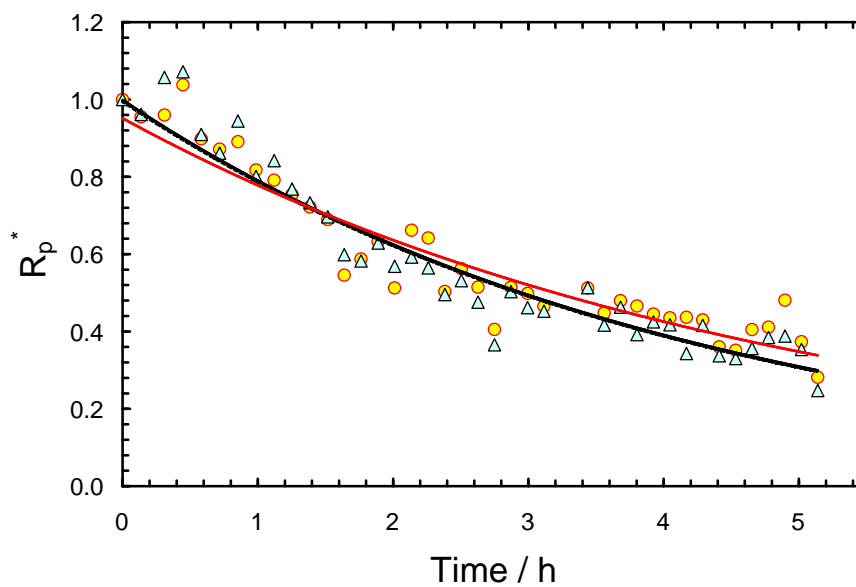
(a)
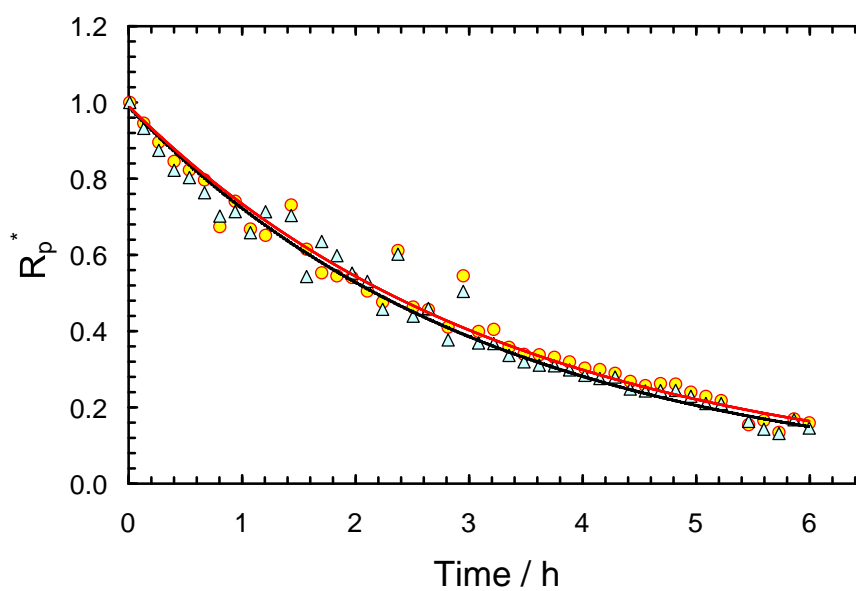
(b)

Figure 6-8: Normalized polarization resistance plots of skin. (a) Skin in buffered CaCl$_2$ electrolyte. (b) Skin in buffered NaCl electrolyte.

6.2.2   Influence of Cation Charge on Skin Hydration

The Measurement Model approach developed by Agarwal *et al.*[238,239] was applied to assess selected impedance spectra for consistency with the Kramers-Kronig relations. As stated earlier, the assessment procedure was used to identify when the properties of skin achieved steady-state. The methodology for the assessment procedure is described in Section 4.1.4. The piece of skin immersed in $CaCl_2$ solution did not achieve steady-state until after the skin was soaked overnight. In contrast, the properties of skin in NaCl electrolyte changed continuously over the course of the experiment. As proposed in Section 5.2.2, it is possible that the charge of the electrolyte cations influenced the hydration dynamics of skin.

It is unlikely that the impedance experiments were responsible for the slow approach toward steady-state, since the potential differences across the membrane induced by the current perturbations were on the order of 10 mV. Despite the continuous changes in the skin samples studied here, the majority of skin specimens studied by electrochemical impedance spectroscopy in this work displayed a stationary response within the first hour of being immersed in electrolyte (see, for example, Section 5.2.1).

6.3   Influence of Electrolyte Cation Charge on Skin Impedance

The literature suggests that the charge of electrolyte cations influences the efficiency of iontophoretic transport.[20,131,133,247] For example, the transport numbers corresponding to a series of different inorganic univalent cations were found to be approximately 0.6. In contrast, the transport numbers of various inorganic divalent cations were in the range of 0.2-0.4. The results suggested that specific interactions, such as electrostatic binding, occur between divalent cations and the negative background charge sites of the stratum corneum. Additional iontophor-

etic studies indicated that the recovery of skin impedance to electric current is enhanced in the presence of divalent cations in comparison to monovalent cations.[152] The results described in Sections 5.2.2 and 6.2.2 are consistent with these observations.

A possible mechanistic explanation for the enhancement of skin recovery rates by divalent cations is derived from electrostatic theory. For example, the force between a negative charge and a divalent cation is twice that of monovalent cation. The enhanced driving force associated with the divalent cations could provide for preferential adsorption on the negatively charged regions of the stratum corneum. The larger electrostatic interactions in the interior of stratum corneum may reduce the impact of large electric fields on skin properties.

The object of this study was to investigate the effect of electrolyte cation charge on the recovery of skin to large electric fields. An additional goal of the investigation was to confirm that skin transport properties can be monitored nonnivasively by variable-amplitude galvanostatic modulated impedance spectroscopy. The objectives were accomplished by subjecting 2 pieces of skin, one immersed monovalent cation electrolyte and the other in divalent electrolyte, to a similar series of impedance experiments.

The approach was to collect 10 mV VAG modulated impedance spectra intermittently over the course of three hours to monitor skin hydration. Large electric fields were induced across the skin by the subsequent collection of four 10 μA constant-amplitude galvanostatically modulated impedance spectra. The recovery of skin properties to the large perturbations was monitored through the collection of four 10 mV VAG modulated impedance spectra. The DC current bias was 0 $\mu A/cm^2$ for all of the experiments. The Measurement Model, described in Section 4.1.4, was regressed to the data to identify portions of the spectra of that

were inconsistent with the Kramers-Kronig relations. The inconsistent data was assumed to be caused by changes in skin properties.

The epidermal membranes were extracted from adjacent locations on the same skin sample to minimize intra-individual variability. The first sample was immersed in buffered 150 mM NaCl buffered electrolyte and the second sample in buffered 50 mM $CaCl_2$ electrolyte. The concentration of the solutions was consistent with the ionic strength of the electrolytic fluid within the human body.[246]

6.3.1 Impedance of Skin Immersed in Monovalent Electrolyte

The impedance spectra from the skin immersed in NaCl electrolyte solution are shown in the impedance-plane in Figure 6-9. The band of spectra with the
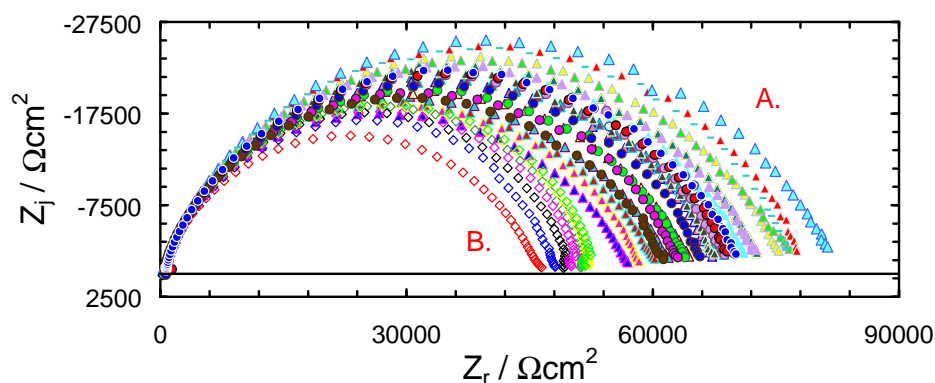
Figure 6-9: Impedance-plane plot of skin immersed in 150 mM NaCl buffered electrolyte. The filled symbols to the left of marker (A.) correspond to spectra collected by 10 mV VAG modulation. The hollow symbols to the right of marker (B.) represent the 10 μA modulated experiments.

solid symbols located to the left of marker (A.) correspond to the experiments conducted by VAG control. The group of spectra to the right of marker (B.) were collected by 10 μA modulation. Visual comparison of the data revealed that the skin impedance measured by the 10 μA perturbation was lower than the response measured by VAG control. During the first three hours of the study, skin impedance increased gradually under VAG control. Upon changing to 10 μA constant-amplitude galvanostatic control, the impedance dropped dramatically. The 10 mV

VAG modulated impedance spectra collected during the hour after the constant-amplitude experiments revealed a partial recovery of the skin impedance response.

Since more than 30 impedance spectra were collected in this investigation, it was difficult to evaluate the temporal evolution of the system directly from the impedance-plane plot. The Kramers-Kronig consistent polarization resistance of skin was once again selected as a simple parameter to represent membrane properties. The results from the assessment procedure are described in Section 6.3.3.

Skin polarization resistance is plotted as a function of time in Figure 6-10. The solid circles and solid triangles represent the data collected by 10 mV VAG modulation and 10 μA constant-amplitude galvanostatic control, respectively. The potential difference across the skin at the minimum measuring frequency is shown by the open symbols of Figure 6-10.
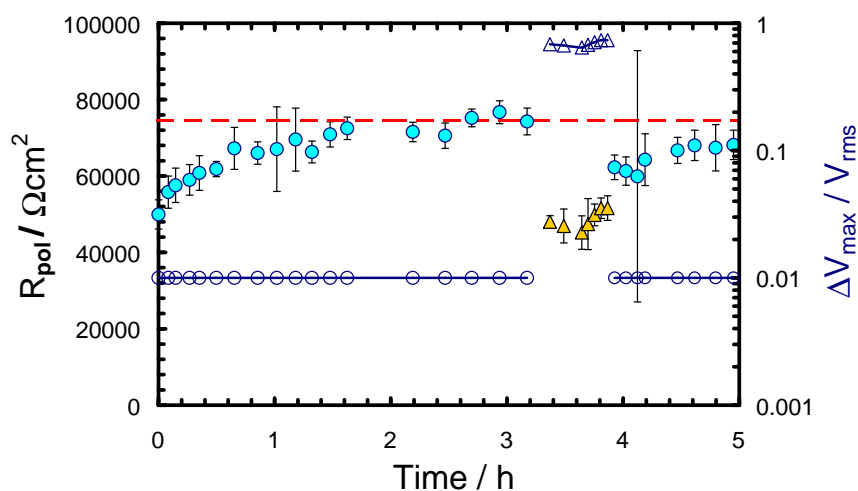
Figure 6-10: Polarization impedance and potential difference across skin immersed in buffered 150 mM NaCl electrolyte. The solid circles and solid triangles correspond to the polarization resistance of skin is measured by VAG and constant-amplitude galvanostatic modulation, respectively. Similarly, the open circles and open triangles refer to the membrane potential difference at the lowest perturbation frequency for the VAG and constant-amplitude galvanostatically modulated experiments.

The polarization resistance of the skin approached an asymptote of 75 kΩcm^2 during the first three hours of this study. In accordance with the VAG modu-

lation procedure, the potential drop across the skin was approximately 10 mV while the spectra were collected. As the modulation strategy was changed to 10 μA constant-amplitude control, the polarization resistance dropped to approximately 50 kΩcm^2. The maximum potential difference across skin for the constant-amplitude studies was approximately 1 V. The polarization impedance recovered to within 90% of its original value while the next series of VAG experiments was performed. The incomplete recovery of skin impedance suggested that the alterations induced by the large electric fields were irreversible on the 1 hour time scale of these experiments.

6.3.2   Impedance of Skin Immersed in Divalent Electrolyte

The impedance spectra of the skin sample immersed in buffered CaCl$_2$ electrolyte are presented in the impedance-plane in Figure 6-11. The band of spectra with the solid symbols located to the left of marker (A.) correspond to the experiments conducted by VAG control. The group of spectra to the right of marker (B.) were collected by 10 μA modulation. The impedance of skin collected by constant-amplitude modulation was always less 10 mV VAG control measurements. The difference in the impedance responses of the two modulation strategies was more pronounced than for the spectra of skin in NaCl electrolyte.

The skin impedance spectra were approximately uniform in magnitude after one hour. The approach toward a steady-state impedance response was more rapid in this electrolyte than for the skin immersed in NaCl electrolyte. Upon changing the modulation technique to 10 μA control the impedance of skin decreased. The skin impedance recovered rapidly when the modulation strategy was switched back to 10 mV VAG control. Since the recovery of skin was so rapid, a second set of 10 μA impedance experiments was performed. The spectra associated with the 10 μA experiments also demonstrated a dramatic reduction in
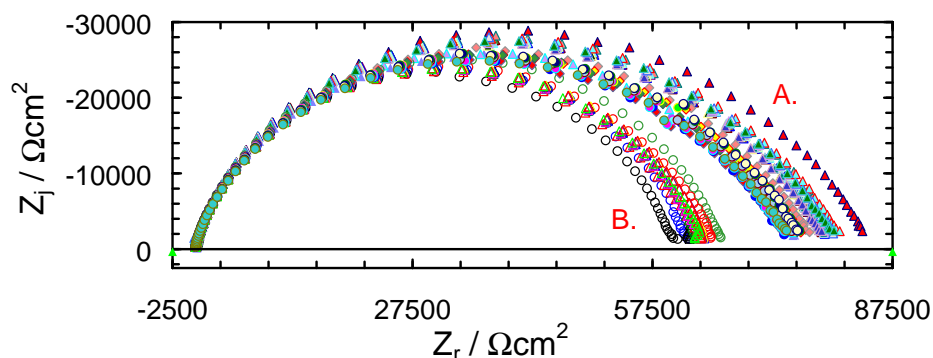
Figure 6-11: Impedance-plane plot of skin immersed in 50 mM $CaCl_2$ buffered electrolyte. The filled symbols to the left of marker (A.) correspond to spectra collected by 10 mV VAG modulation. The hollow symbols to the right of marker (B.) represent the 10 μA modulated experiments.

skin impedance. The recovery process was once again monitored by 10 mV VAG modulated impedance spectroscopy. The spectra from the VAG experiments indicated that the electrical and transport properties of skin had almost completely recovered.

The temporal evolution of the polarization resistance of skin in $CaCl_2$ electrolyte is presented in Figure 6-12. The initial value of skin polarization resistance was 75 kΩcm^2. The resistance did not change significantly during the three-hour interval where skin properties were monitored by 10 mV VAG modulated impedance spectroscopy. Upon switching the modulation strategy to 10 μA constant-amplitude control the polarization resistance dropped to approximately 65 kΩcm^2 and continued to decrease as subsequent 10 μA spectra were collected. The difference in polarization resistance measured by the two modulation strategies was smaller than for the specimen immersed in NaCl solution. The maximum potential drop across the skin during the constant-amplitude scans was also on the order of 1 V.

The polarization resistance increased to 74 kΩcm^2 when the modulation technique was switched to 10 mV VAG control. Subsequent spectra collected by the VAG modulation method demonstrated similar polarization resistance values. The
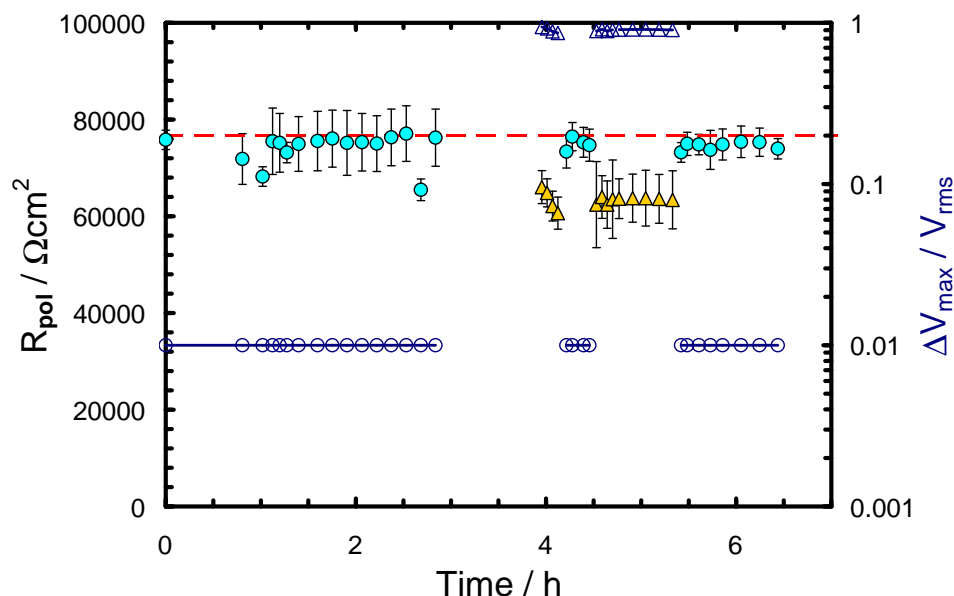
Figure 6-12: Polarization impedance and potential difference across skin immersed in buffered 50 mM $CaCl_2$ electrolyte. The solid circles and solid triangles correspond to the polarization resistance of skin as measured by VAG and constant-amplitude galvanostatic modulation, respectively. Similarly, the open circles and open triangles refer to the membrane potential difference at the lowest perturbation frequency for the VAG and constant-amplitude galvanostatically modulated experiments.

uniform magnitude of the low-frequency response associated with these impedance spectra were consistent with a complete recovery of skin properties.

6.3.3 Kramers-Kronig Consistency Assessment

In Sections 6.3.1 and 6.3.2 it was demonstrated that the impedance responses of skin measured by 10 mV VAG and 10 μA constant-amplitude galvanostatic modulation were different. The potential difference across skin in the low-frequency portions of the impedance spectra collected by 10 μA constant-amplitude galvanostatic modulation were on the order of 1 V, whereas, the VAG modulation studies maintained the potential drop at a magnitude of 10 mV. The influence of the large potential perturbations induced by the 10 μA constant-amplitude galvanostatic control technique on skin properties was assessed by checking the impedance spectra for consistency with the Kramers-Kronig relations. In addition, the spec-

tra obtained under 10 mV VAG control were evaluated for compliance with the Kramers-Kronig relations.

The results from the assessment procedure are summarized here. The low-frequency portions of the VAG spectra of skin in monovalent and divalent solutions satisfied the Kramers-Kronig relations within one hour after being immersed in electrolyte. In contrast, the spectra of skin in 150 mM NaCl collected by $10~\mu$A constant-amplitude galvanostatic modulation were inconsistent with the Kramers-Kronig relations at frequencies below 25 Hz. Similarly, the spectra of skin in $CaCl_2$ electrolyte were inconsistent at frequencies below 100 Hz. The results from the 10 μA constant-amplitude studies implied that skin properties were altered. The alterations were associated with potential swings on the order of 1 V.

The greatest influence of cation charge on the impedance response of skin was observed for the spectra collected after the 10 μA constant-amplitude galvanostatic modulated scans. For example, the impedance spectra of skin in $CaCl_2$ electrolyte were consistent with the Kramers-Kronig relations whereas the spectra associated with the skin in NaCl electrolyte were not. The Kramers-Kronig consistent spectra collected from the specimen in $CaCl_2$ electrolyte were compatible with the hypothesis that skin properties recover more rapidly and completely in the presence of divalent cations (see, for example, Section 5.2.2).

6.4   Influence of Large-Amplitude AC Potential Swings on Skin

It was demonstrated in Sections 5.1.1, 5.2.1, and 6.3.3 that skin impedance data collected by constant-amplitude galvanostatic modulation was inconsistent with the Kramers-Kronig relations. The inconsistent data points were generally located in the low-frequency portions of the spectra where skin exhibits its largest impedance. For skin samples with a polarization resistance on the order of 100 kΩcm^2, the constant-amplitude modulation technique can induce potential swings which

exceed 1 V. Electrochemical systems typically demonstrate nonlinear behavior at elevated potentials;[137] therefore, it was hypothesized that potential, and not current, was responsible for the change in skin impedance.

The influence of potential on skin properties was investigated here by collecting replicate impedance spectra by variable-amplitude galvanostatic modulation. The approach was to periodically increase the target potential drop across the epidermis from 10 mV to 1V. The relatively large range of potential was selected to identify the threshold amplitude at which the properties of skin begin to change. The impedance spectra were assessed for consistency with the Kramers-Kronig relations to identify corrupted data.

It was assumed for these experiments that the 10 mV target perturbation amplitude was sufficiently low as not to change the properties of skin. The assumption was later validated by confirming that the spectra collected at this target potential amplitude satisfied the Kramers-Kronig relations. The 10 mV VAG skin protocol was used to monitor the recovery of skin following each set of elevated target amplitude experiments. Four replicates were collected for each set of experimental conditions. The magnitudes of the target potential difference across the skin for the replicate scans were 50, 100, 250, 500 and 1000 mV.

The impedance spectra collected at the prescribed target voltages are presented in Figure 6-13. The spectra with open diamonds to the left of marker (A) represent the initial group of 10 mV VAG impedance scans. The data indicated that the impedance of skin was largest at the beginning of the experiment. The spectra with solid yellow diamonds to the left of marker (B) represent the impedance response to the 50 mV target perturbation. The spectra with open circles to the left and right of symbol (C) correspond to the 100 mV target perturbation measurements. The spectra with solid yellow triangles to the left of marker (D) represent
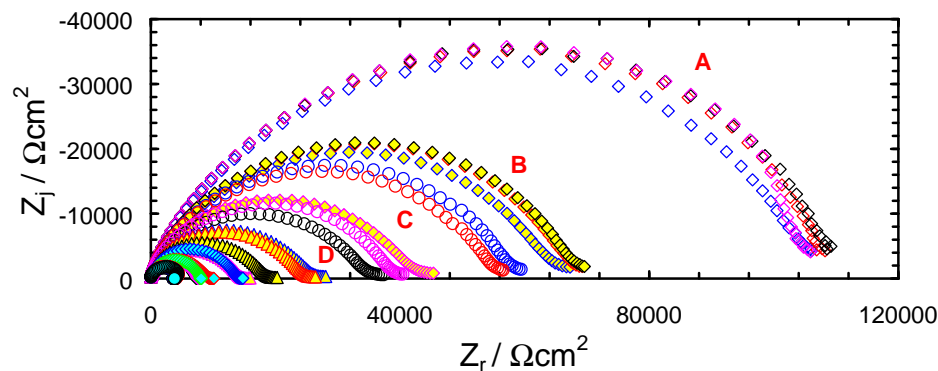
Figure 6-13: Impedance-plane plot of skin where the target potential drop across the skin was increased periodically. The spectra to the left of markers (A)-(D) represent the measurements collected by the VAG modulation technique with target voltages of 10, 50, 100, and 250 mV, respectively.

the data collected at the 250 mV amplitude. The solid blue diamonds and the solid

blue triangles correspond to the spectra collected at the 500 mV and 1V target am-

plitudes.

In general, the magnitude of the impedance decreased as the amplitude of tar-

get perturbations was increased. Furthermore, for target amplitudes greater than

or equal to 250 mV the impedance of successive skin spectra decreased with time.

The results suggested that skin transport properties were altered by the large po-

tential signals.

The recovery of skin impedance to the elevated potential swings is presented

in Figure 6-14. The open diamonds to the left of marker (A) correspond to the ini-

tial group of 10 mV VAG impedance spectra. This group of replicates served as a

baseline for comparison with subsequent spectra. The spectra denoted by the solid

circles to the left of marker (B) were collected after the 50 mV VAG measurements.

The open triangles to the right of marker (C) were collected after the 100 mV VAG

impedance scans were completed. The solid triangles, open circles and filled di-

amonds represent the impedance response of skin following the 250 mV, 500 mV

and 1 V impedance experiments. A general trend was observed where skin imped-

ance increased as the target potential of the VAG impedance scans was switched to 10 mV after the application of the higher amplitude signals. The impedance continued to increase as successive 10 mV VAG spectra were collected which implied that the changes induced by the large potential swings were partly reversible.
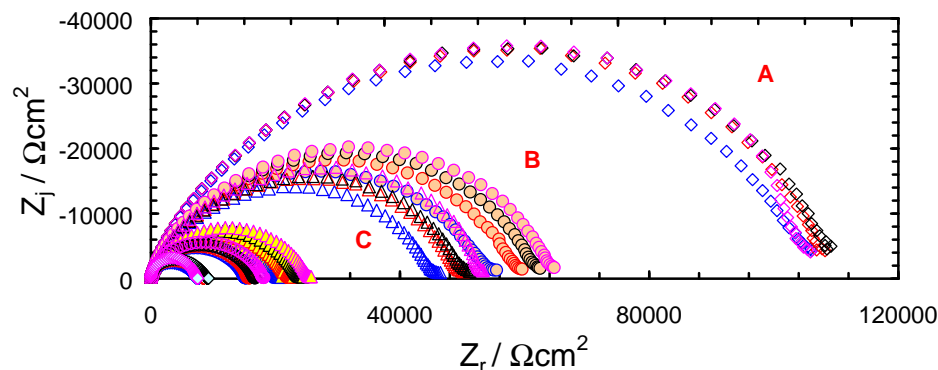
Figure 6-14: Skin polarization resistance upon completion of the elevated target potential impedance scans. The spectra to the left of markers (A) and (B) correspond to the 10 mV VAG scans collected at the start of the experiment and after the 50 mV VAG experiments, respectively. The band of spectra to the right of (C) correspond to the 10 mV VAG experiments conducted after the 100 mV VAG scans.

Selected spectra from each set of experimental conditions were assessed with the Kramers-Kronig relations. Impedance data collected at measuring frequencies below 5 Hz at the 10 mV target perturbation level were generally inconsistent with the Kramers-Kronig relations. The inconsistent behavior was likely caused by nonstationary effects; *e.g.* hydration of the membrane or the recovery of skin properties to the high amplitude potential swings.

A larger portion of the low-frequency data collected at the higher target perturbation amplitudes was inconsistent with the Kramers-Kronig relations. For example, the spectra collected with a target perturbation of 1 V were inconsistent at frequencies below 200 Hz. The results are in agreement with the proposal that skin properties begin to change at a critical potential. The magnitude of the voltage across skin where the properties began to change in this work was 250 mV.

The data presented in Figures 6-13 and 6-14 clearly indicated that there was a strong effect of potential on skin properties. However, it was difficult to assess from the impedance-plane plots the magnitude and character of the changes in skin properties induced by the 500 mV and 1 V potential swings. As the influence of potential perturbations on skin is greatest at low-frequencies, the polarization resistance was selected as a simple parameter for evaluating alterations to the membrane. The polarization resistance and potential difference across the skin are displayed as a function of time in Figure 6-15. The filled diamonds correspond to skin polarization resistance and the filled circles represent the potential drop across the membrane.
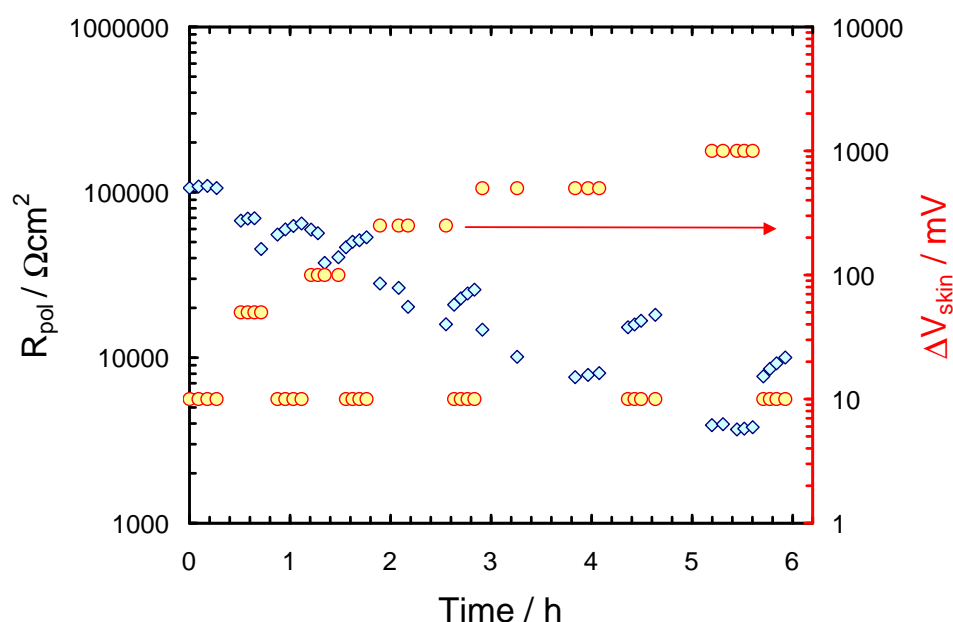
Figure 6-15: Polarization resistance (solid blue diamonds) and voltage drop across the skin (solid yellow circles) for the elevated target potential impedance scans.

The polarization resistance of skin decreased as the potential difference across the membrane increased. The greatest changes in skin polarization resistance were observed when the target potential was set to 500 mV and 1 V. The polarization resistance associated with these spectra was an order of magnitude lower than the resistance measured after 10 mV VAG scans at the start of the experiment. Skin

polarization resistance, measured by the 10 mV VAG modulation technique, increased pseudoexponentially with time following the experiments collected with target voltages greater than 50 mV. The 10 mV VAG results indicated that the changes in membrane properties induced by the large potential swings were partially reversible. Presentation of the impedance data in this fashion allowed for easier interpretation of the influence of potential on skin properties.

6.5   Influence of DC Current Bias on Skin Impedance

During transdermal iontophoresis DC current is applied to provide an additional driving force to enhance the delivery rates of therapeutic compounds across the skin. The objective of this study was to determine the effect of DC current on skin transport properties. The response of the membrane under applied-current conditions and the recovery of skin properties were studied by impedance spectroscopy. Six amplitudes of applied DC current in the range of 0 μA/cm^2 to 855 μA/cm^2 were studied. The current range used for the study was consistent with the currents applied by clinical iontophoretic transdermal devices. A minimum of four impedance scans were collected under constant-amplitude galvanostatic control for each applied-current magnitude. The sinusoidal current perturbation was equal to 7.5% of the DC bias amplitude to optimize the signal-to-noise ratio of the potential response.

At the start of the experiment, four VAG modulated impedance scans with a target potential difference of 10 mV were collected. The spectra provided a baseline of skin properties and the initial hydration state of the membrane. The skin was allowed to relax at the open-circuit condition for a minimum of six minutes before collecting subsequent spectra. After skin hydration was studied, four impedance spectra were collected at the 71 μA/cm^2 applied bias condition. The recovery of skin to DC current was monitored through the collection of four 10 mV

VAG spectra. The procedure of alternating the modulation method for successive impedance scans was repeated as the DC current bias amplitude was increased incrementally.

6.5.1 Comparison of Skin Impedance Spectra

The impedance-plane plot corresponding to impedance response of skin immersed in buffered 50 mM $CaCl_2$ solution under applied-current conditions is presented in Figure 6.16(a). The solid blue symbols correspond to the spectra collected at the beginning of the experiment at an applied bias of 0 $\mu A/cm^2$. The solid yellow symbols and solid red symbols correspond to the measurements obtained at applied bias amplitudes of 71 $\mu A/cm^2$ and 140 $\mu A/cm^2$. The solid purple symbols are spectra collected under the 285 $\mu A/cm^2$ applied bias. The open red diamonds and solid green diamonds are the measurements collected with bias amplitudes of 570 $\mu A/cm^2$ and 855 $\mu A/cm^2$.

All of the skin spectra exhibited a depressed semicircular shape in the impedance-plane. As the current was increased, the polarization resistance and the characteristic time constant for the system decreased. A secondary process in the low-frequency region of the spectra was observed for the experiments conducted with applied-current densities greater than 71 $\mu A/cm^2$.

The variable-amplitude galvanostatic modulated spectra collected as the skin recovered from the applied currents are presented in Figure 6.16(b). The symbols for the spectra are coded in the same manner as the applied-current bias scans presented in Figure 6.16(a). With the exception of the hydration spectra, skin impedance increased as successive replicates were collected at the 10 mV target perturbation amplitude. This trend indicated that skin properties were recovering from the applied-currents. The recovery of skin impedance was incomplete over the 4 hours of this study.
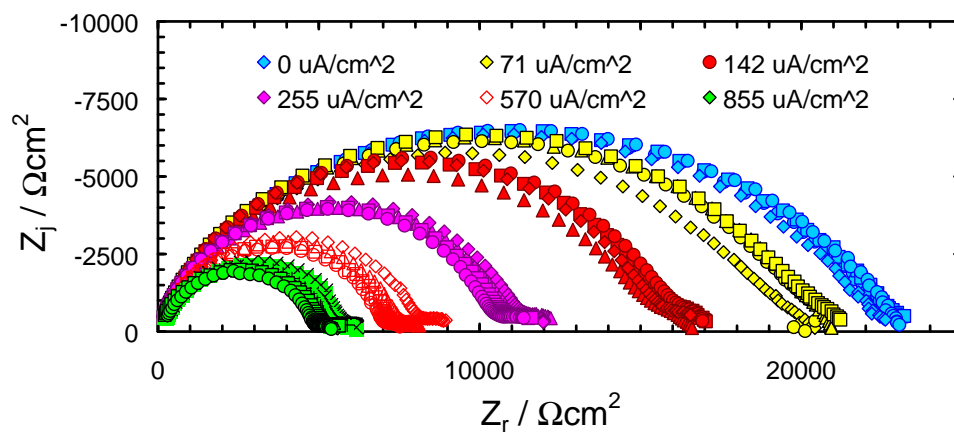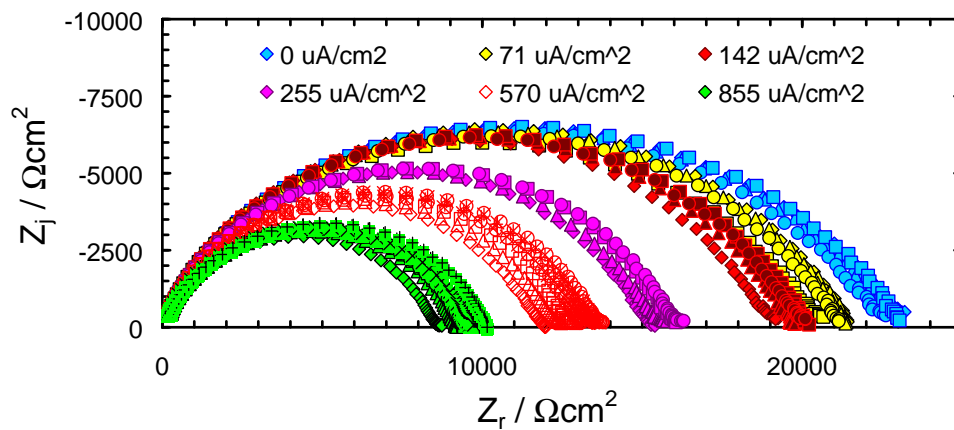
Figure 6-16: Impedance spectra collected to determine the influence of DC current on skin properties. The current bias amplitudes are indicated by the legends. (a) Skin impedance under applied-current conditions. (b) Recovery of skin impedance to applied current bias.

6.5.2 Identification of Corrupted Data

Selected impedance spectra for each set of experimental conditions were assessed for consistency with the Kramers-Kronig relations according to the methodology described in Section 4.1.4. For example, the Measurement Model was fit to the four spectra collected under the 255 μ/cm2 DC bias condition. The error structure associated with this set of data was determined. The error structure was used to weight subsequent regressions to identify portions of the impedance spectra that were inconsistent with the Kramers-Kronig relations. As mentioned earlier, this process was repeated for the spectra collected under each set of experimental conditions.

In general, the spectra were consistent with the Kramers-Kronig relations over the entire frequency range. This behavior was observed regardless of the applied current. The general form of the skin impedance response was correlated to the experimental methodology *i.e.,* whether the system was probed under an applied-current bias or at the open-circuit condition. For example, a secondary process, in the form of a small capacitive loop, was observed in the low-frequency portions of the applied-current spectra. The attribute became more prominent as the current amplitude was intensified. In contrast, the secondary peak was absent in the majority of spectra collected at the 0 μ/cm^2 bias amplitude.

The data associated with the secondary peak were consistent with the Kramers-Kronig relations; however, a complete mechanistic explanation for the feature is not known. Since the response was observed exclusively in the spectra collected under a DC current bias, it is likely that the large stationary electric fields induced by the applied current interacted with the skin differently than the significantly smaller fields during the 10 mV VAG experiments.

6.5.3 Polarization Resistance and Open-circuit Potential Data

The Kramers-Kronig consistent polarization resistance was used to track the recovery of skin properties after DC current was applied. The polarization resistance, the measured impedance at 1 Hz and the corresponding voltage drop across skin are presented by the circles, triangles and diamonds, respectively, in Figure 6-17. The impedance at 1 Hz is, in general, approximately equal to the polarization resistance of heat-separated cadaver skin.[3,233]
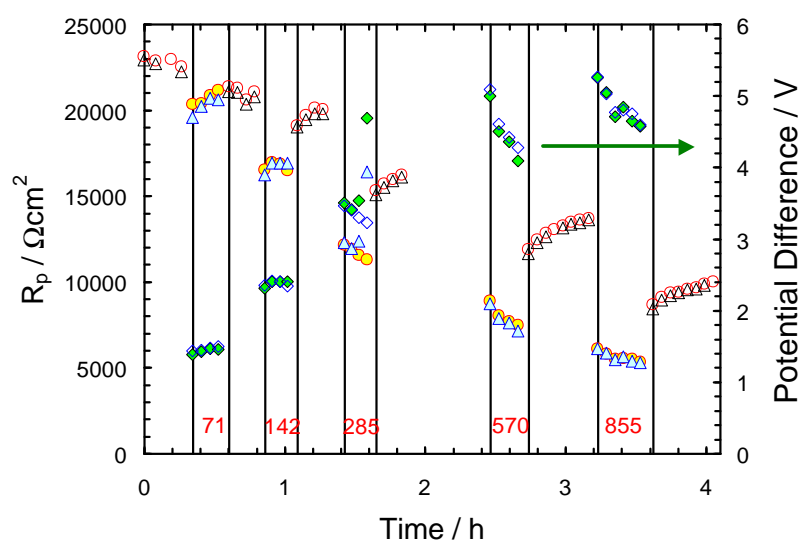
Figure 6-17: Skin polarization resistance in response to 6 amplitudes of applied current. Open symbols correspond to measurements collected under VAG modulation. Solid symbols represent the measurements taken during applied-current bias conditions. The circles and triangles are the impedance at 1 Hz and polarization resistance of skin, respectively. The open and solid diamonds represent the potential drop across the skin.

The predicted polarization resistance and impedance at 1 Hz from the first series of 10 mV VAG impedance scans was approximately 23 kΩcm^2. The polarization resistance associated with this set of impedance experiments corresponded to the maximum for the study. In general, skin polarization resistance decreased as the applied bias was increased. The reduction in polarization resistance was proportional to the applied-current density. At applied-current densities greater than 285 μA/cm^2, the polarization resistance decreased continuously as consecu-

tive impedance scans were collected. The reduction in skin resistance indicated that the membrane had been altered.

The polarization resistance of skin associated with the 10 mV VAG impedance experiments demonstrated slightly more complex behavior. For example, after the spectra were collected at the 71 μA/cm^2 bias current, skin resistance was approximately 21 kΩcm^2. This quantity was approximately equal to the polarization resistance associated with the 71 μA/cm^2 bias spectra. As the polarization resistance was identical for the two experimental conditions, the result strongly suggested that the 71 μA/cm^2 current bias had not significantly altered skin properties. Spectra collected by variable-amplitude galvanostatic modulation after skin was subjected to the larger DC current bias signals demonstrated an increase in polarization resistance with time. The trend indicated that the alterations induced by the elevated currents were partially reversible.

The open-circuit potential across the skin was measured before and after each impedance experiment. The open-circuit measurements are presented as a function of time in Figure 6-18. In general, the open-circuit potential prior to the 10 mV VAG modulated impedance scans was greater than the value measured after the spectra were collected. The opposite trend was observed for all of the impedance spectra collected under applied bias conditions. The reduction in the open-circuit potential associated with the 10 mV VAG was likely caused by the introduction of electrolyte solution into the membrane.

The increase in potential difference across the skin for the applied bias studies was greatest for the first group of spectra collected after completion of the 10 mV VAG modulated experiments. For example, the open-circuit potential increased by 131 mV during the first impedance scan with the 71 μA/cm^2. The difference in open-circuit potentials measured before and after the collection of subsequent
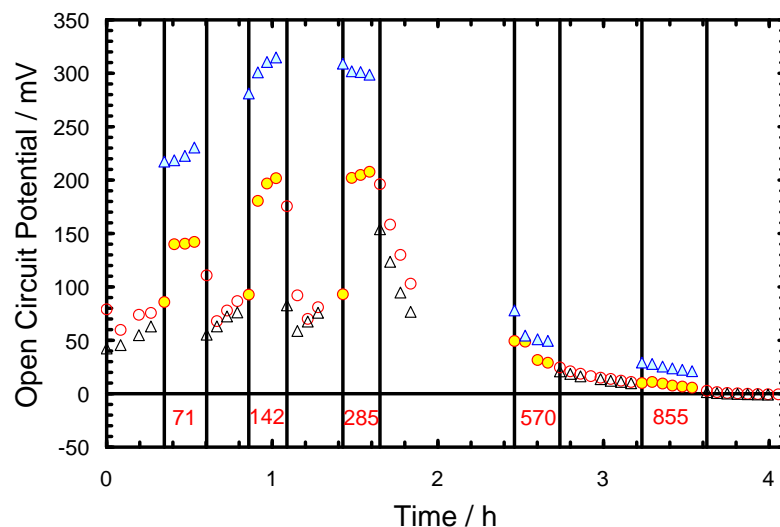
Figure 6-18: Open-circuit potential difference across the stratum corneum before and after impedance scans. Open circles and open triangles correspond to measurements collected before and after the 10 mV VAG impedance scans, respectively. Solid circles and solid triangles correspond to measurements collected before and after constant-amplitude impedance scans with an applied-current bias, respectively.

impedance spectra at this current bias was approximately 85 mV. The increase in open-circuit potential after application of the DC current suggested that the membrane had been charged.

The open-circuit potential recovered to 110 mV at the start of the first VAG modulated impedance experiment upon completion of the 71 μA/cm^2 applied bias study. The open-circuit potential associated with the next three 10 mV VAG spectra were approximately equal to the 80 mV difference measured at the start of this study. As the applied bias was increased to 142 μA/cm^2 the open-circuit potential increased 280 mV. During the six minute rest prior to the next impedance scan the potential difference decreased to 180 mV. After the second impedance spectrum at the 142 μA/cm^2 bias amplitude was collected, the open-circuit potential increased to 300 mV. A similar before-and-after trend was observed for remaining spectra collected under the 142 μA/cm^2 current bias.

The open-circuit potential measurements corresponding to the impedance spectra collected with 10 mV VAG modulation were approximately equal to 80 mV. After the first impedance spectrum at the 285 μA/cm^2 bias amplitude was obtained, the open-circuit potential increased to 310 mV. As the skin was allowed to relax after this scan, the open-circuit potential decreased to 190 mV. Upon completion of the next spectrum at the 285 μA/cm^2 current condition, the open-circuit potential increased to 300 mV. The same behavior was observed for the remaining spectra collected with the 285 μA/cm^2 current bias.

The open-circuit potential measurements associated with the 10 mV VAG impedance spectra collected after the 285 μA/cm^2 bias experiments decreased steadily with time. The measurements collected with the fourth 10 mV VAG spectrum were approximately equal to 80 mV. This magnitude was approximately equal to the open-circuit potential measured at the beginning of this study. It should be noted that the potential difference induced by the 285 μA/cm^2 current bias was greater than 3 V. The open-circuit potential difference measured with the 570 μA/cm^2 and 855 μA/cm^2 bias spectra were all less than 80 mV. Furthermore, the magnitude of the measurements decreased with time. Under these applied-current conditions, the potential difference across the skin was greater than 4-5 V at the lowest perturbation frequencies of the impedance scan.

The relatively small open-circuit potentials associated with the impedance spectra collected at bias amplitudes greater than or equal to 285 μA/cm^2 suggested that the internal structure of the skin had been altered by the large electric field. Modifications to the internal structure of the skin could provide for easier access of the electrolyte solution into the interior of the membrane. The integration of electrolyte would cause the conductivity of skin to increase and the open-circuit potential to decrease. The low open-circuit potentials and the relatively small po-

larization resistance of skin associated with these high current bias experiments were consistent with the proposed structural modifications.

In summary, it was shown that there was a significant effect of current on the transport properties of skin. The impedance studies indicated that the polarization resistance of skin decreased in response to an increase in current. A comparison of the open-circuit potential across skin before and after impedance spectra were collected strongly suggested that the epidermis became charged when the DC current bias was between 71 $\mu A/cm^2$ and 285 $\mu A/cm^2$.

The experiments described here provided an estimate of the polarization behavior of skin under applied-current conditions. For these studies, the current bias was applied for approximately 3 to 4 minutes, which corresponded to the time required to collect an complete impedance spectrum. As the permeability of skin to most therapeutic compounds is typically small, clinical protocols for transdermal iontophoresis will likely require that current be applied for much longer periods of time. The response of cadaver skin to the prolonged application of DC current is discussed in Chapter 8.

6.6   Variation of Properties with Location

The literature indicates that skin properties vary with body location.[14,15,16,17,18] The experiments described here provided an initial estimate of the variation in the transport properties of the skin samples used for this body of work. Four pieces of skin were extracted from adjacent locations of the same donor sample. The skin was inspected with a magnifying glass to confirm that macroscopic holes were not present. The sample was essentially free of hair follicles and the surface texture was relatively uniform.

The impedance response of each piece of skin was measured. The impedance spectra were collected by VAG modulation control where the target poten-

tial across the membrane was set to 25 mV. Four impedance spectra were collected for each piece of skin studied. The skin samples were immersed in buffered 50 mM $CaCl_2$. The impedance-plane plot for a single spectrum for each piece of skin is presented in Figure 6.19(a). A schematic of the relative spatial locations where the pieces of skin were extracted is shown in Figure 6.19(b).

The polarization resistance values for the specimens listed according to extraction site were approximately $180, 10, 20$ and $120 \text{ k}\Omega\text{cm}^2$. The distribution of impedance values clearly demonstrated that skin properties did not track continuously with the spatial origin of the samples. Large variability in skin impedance was also observed for pieces of the heat-separated cadaver skin obtained from different donors. Since a large database of impedance measurements was collected in this work, a statistical analysis of variance was performed to estimate the contributions from each source to the total variation in skin properties. A detailed discussion of the statistical analysis is provided in Chapter 7.

6.7   Comparison of Impedance Data with Literature Results

The work presented in Section 6.2 described the detailed analysis of the influence of membrane hydration on skin transport properties. Open-circuit potential measurements and skin impedance spectra were collected to infer when the system had achieved steady-state. The open-circuit potential across the skin decreased from ~ 120 mV to a uniform reading of ~ 1 mV within the first 1.5 hours of the experiment. The impedance spectra indicated that skin polarization resistance decreased continuously over the 5 hour time-frame of the experiment. The spectra did not conform to the Kramers-Kronig relations at low frequencies which indicated that the system was still evolving. Impedance spectra collected on the next day satisfied the Kramers-Kronig relations; therefore, the skin was assumed to be completely hydrated.
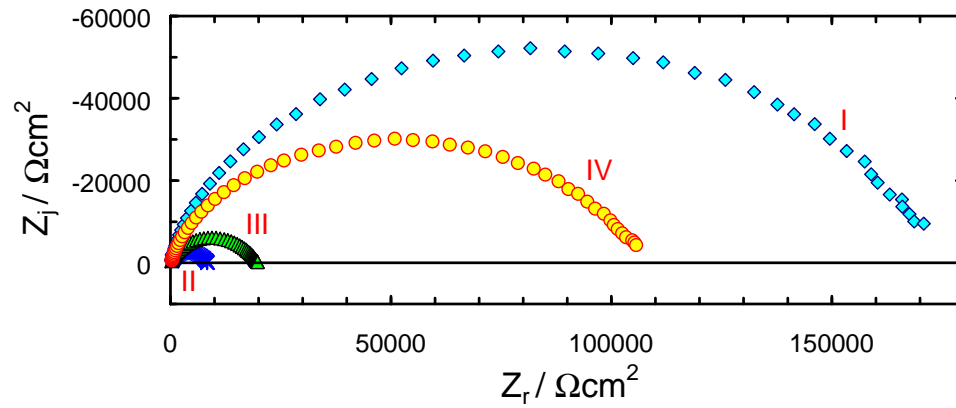
(a)
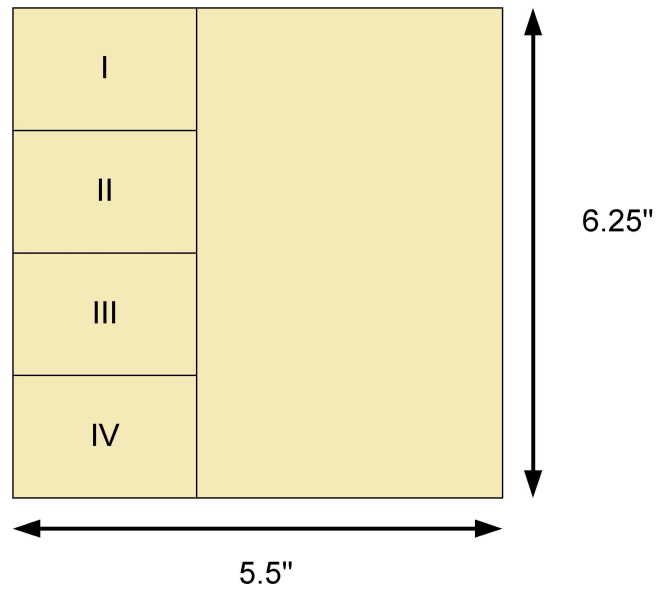
(b)

Figure 6-19: Impedance spectra and the relative location for skin sample extraction of four pieces of skin. (a) Impedance response of 4 pieces of heat-separated skin taken from adjacent locations of the same donor sample. (b) Schematic of the relative location for skin sample extraction.

An important implication of the study was that the electrochemical impedance spectroscopy technique is more sensitive to changes in skin hydration than open-circuit potential measurements. Although approximately 24 hours were required for the skin used in these experiments to achieve steady-state, the majority of other skin samples presented in the remainder of this work demonstrated a uniform response within one hour of being immersed in electrolyte.

A limited number of reports which describe the influence of hydration on skin impedance are available in the literature.[152,206] The continuous decrease in impedance as a function of immersion time observed in this work is consistent with the reported results.[152,206] Successive skin impedance collected in those investigations were compared visually to identify when the skin hydration process was complete. A unique feature of the work presented here was that skin spectra were tested for consistency with Kramers-Kronig relations to determine the steady-state condition. The advantage of this approach is that data must be stationary in order to satisfy the Kramers-Kronig relations. The assessment procedure described in this work provides for more accurate identification of the steady-state condition.

The influence of large sinusoidal voltage swings on skin impedance was described in Section 6.4. Variable-amplitude galvanostatic (VAG) modulation was applied to maintain the amplitude of the potential perturbations at prescribed levels. Skin polarization resistance was found to be inversely proportional to the potential perturbation amplitude. Impedance spectra collected by 10 mV VAG modulation following the large perturbation amplitude experiments demonstrated an increase in skin polarization resistance with time. The impedance recovery rate was not correlated to the voltage perturbation amplitude.

The trends suggest that the relatively large electric fields caused the internal structure of the epidermis to become more porous. The more open arrange-

ment could provide for additional ionic current pathways which would reduce the membrane resistance. The transient increase in resistance observed after the large potential swings were terminated is consistent with the relaxation of the structural alterations. The incomplete recovery of the polarization impedance following the large voltage experiments imply that the time-constant for the relaxation of the proposed structural alterations is large in comparison to the time scale of the experiment. An alternative explanation is that the changes were partially irreversible.

The behavior described in Section 6.4 is generally consistent with a similar DC potentiometric study of excised human skin.[248] One important difference noted in that work was that the recovery rate of skin impedance was proportional to the applied voltage. The discrepancy can be explained by the type of voltage signal used for the investigation. For example, a prescribed amplitude of DC voltage was applied for a minimum of 10 minutes. The electric field within the skin induced by the applied voltage would be permanently oriented. Consistent with the hypothesis that the internal structure of skin was modified by the electric field, the extent of membrane polarization in response to the DC voltage would be expected to be larger than for an alternating signal of the same amplitude. The smaller relative changes in skin impedance described in Section 6.4 are consistent with this scenario.

The use of electrochemical impedance spectroscopy in transdermal iontophoresis research has been generally limited to the measurement of skin transport properties during hydration and after the application of DC current.[150,152,166,205,248] A unique aspect of the work described in Section 6.5 was that skin impedance spectra were also collected under applied-current conditions. The advantage of

this approach is that the influence of the D.C. current bias on the electrical properties of skin could be assessed directly.

The spectra collected using this methodology demonstrated that skin impedance decreases in response to an applied DC current. The reduction in skin impedance was proportional to the amplitude of applied current. The observed behavior is consistent with reported *in vivo*[150,152,206] and *in vitro* results.[166,205,248] The literature indicates that spectra collected after current application demonstrate a larger and more rapid reduction of skin impedance in vivo than *in vitro*.[206] The dynamics of skin impedance changes described in Section 6.5 are consistent with the reported behavior.

The procedure for extracting the epidermis from the dermis has been described as a potential source for the slower kinetics and smaller quantitative amounts of reduced impedance observed in the *in vitro* studies than for the in vivo investigations.[206] For example, the elevated temperature at which the epidermis is extracted may alter or even close some of the current conducting pathways of the epidermis.

The current bias experiments demonstrated that skin impedance increased after applied current was terminated. The recovery process was significantly slower than the more rapid reduction observed under applied bias conditions. As described earlier, it is likely that the DC current by his caused the membrane to become polarized. The results are consistent with a slow relaxation process. The experiments described in Section 6.5 are also in agreement with the literature.[206,248]

In summary, the results presented in this chapter were generally consistent with the literature. Additional characteristics of skin impedance were detected under a variety of experimental control conditions. An important aspect of this work was that a small capacitive loop was observed in the low-frequency portions of spectra collected under applied bias conditions. The distinctive attribute

was absent in spectra collected at the open-circuit condition. The secondary peak is not mentioned in the literature. The feature could not be detected in those experiments because impedance spectra were not collected while an applied current bias was active. It would be interesting to repeat the current bias experiments *in vivo* to determine if the low-frequency feature is also present. The absence of a low-frequency capacitive loop would imply the epidermal extraction procedure alters skin.

CHAPTER 7
STATISTICAL ANALYSIS OF VARIATION IN SKIN IMPEDANCE

A large database of impedance spectra was assembled during the course of this work. The measurements were collected from pieces of heat-separated cadaver skin from a variety of different donors. For a given donor sample, the impedance responses from multiple pieces of skin were measured. As demonstrated in Section 6.6, skin properties from the same donor displayed a wide distribution of impedance values. A similar variability was also noted when the impedance response of skin from different donors was compared. The objective of this analysis was to apply standard statistical methods to compare the sample-to-sample variation in skin impedance with the variation of pieces taken from the same donor sample. A discussion of the analysis of variance in skin impedance data is provided in Section 7.1. In addition, the effect of electrolyte cation charge on skin impedance was assessed in a separate analysis. The work for the influence of cation charge is described in Section 7.5.

The impedance spectra analyzed here were collected by variable-amplitude galvanostatic (VAG) modulation. The target potential drop across the skin was set to 25 mV or less and the DC current bias was fixed at 0 μA/cm^2. It was demonstrated earlier in this work (please refer to Sections 5.2 and 6.3) that VAG modulation of skin impedance measurements can be noninvasive, especially when the target voltage response is kept below 250 mV. The spectra were assessed for consistency with the Kramers-Kronig relations to estimate the polarization resistance of skin with constant properties. Therefore, it was assumed that the observed dis-

tribution of impedance values could be attributed to inherent differences in the various pieces of skin.

For the discussion presented here, the terminology donor sample refers to the complete portion of skin obtained from a given donor and piece refers to a small segment of skin taken from the sample. The classification scheme is illustrated in Figure 7-1. The epidermal membranes were extracted from the dorsal and abdominal regions of human cadavers. As the skin specimens were taken from the same regions of the body it was assumed that the distribution of skin properties was associated with differences between individuals and/or differences within the sample. The objective of the statistical analysis was to determine the contribution to the overall variance in skin properties from each effect. Alternatively stated, the aim here was to determine whether the inter-individual distribution of properties was different from the intra-individual variation.
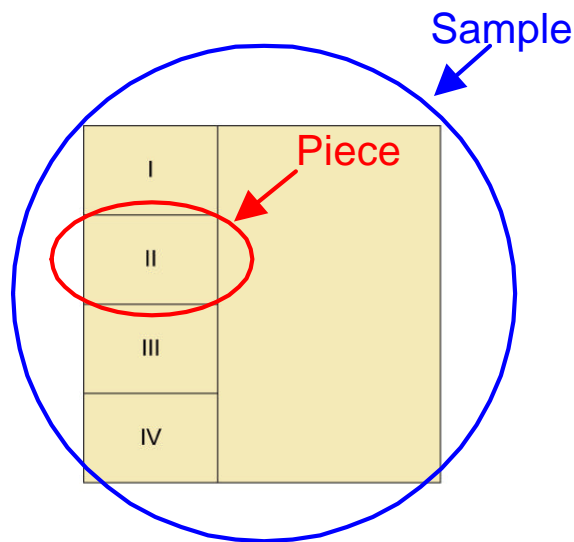
Figure 7-1: Proposed sources of variation in skin properties.

The observation sets for the analysis corresponded to impedance measurements collected immediately after the skin was immersed in electrolyte. A series of 3-5 impedance spectra was collected for each piece of skin during the hydra-

tion period. The skin samples were provided by 18 different donors from which 127 pieces were extracted to perform the experiments. A total of 32 pieces were immersed in divalent cation electrolyte solutions and 95 in monovalent cation solutions. The entire observation set consisted of 508 impedance spectra. A sample of skin was considered in the analysis only if studies were conducted on pieces of skin that were immersed in both monovalent and divalent electrolytes. As the ionic strength of the monovalent and divalent electrolyte solutions was uniform, the effect of cation charge on skin impedance was assessed by performing Student's *t*-tests and *F*-tests. Further discussion of the respective test procedures is provided in Section 7.5.

7.1 Statistical Model for Skin Impedance Data

The Generalized Linear Model (GLM) was used to represent the experimental data because a deterministic process model of skin impedance is not yet available. The GLM model is a statistical model that describes populations which are normally distributed about a mean value. The selection of the GLM model was based on the assumption that donor samples were chosen at random from the general population. Furthermore, it was also assumed that pieces of skin cut from a given donor sample were randomly selected. Under these assumptions, deviations from the mean value are caused by either donor-to-donor variations, site-to-site variations within a sample, or randomly distributed measurement errors.

The location from which a piece of skin was selected was a subset of the donor sample; therefore, the nested form of the Generalized Linear Model[249] was applied. The nested form of the Generalized Linear Model is represented by

$$y_{ijk} = \mu + \alpha_i + \beta_{ij} + \epsilon_{ijk} \tag{7-1}$$

where μ is the mean value for the population, $\alpha_i(i = 1, 2 \ldots a)$ are the contributions to the observations due the donor sample and $\beta_{ij}(k = 1, 2 \ldots b)$ are the contribu-

tions from the locations on a given donor sample. The term, $\epsilon_{ijk}(k = 1, 2 \ldots n)$, represents the measurement error. It is assumed that the parameters, α_i, β_{ij} and ϵ_{ijk} are normally distributed with mean values of 0 and respective variances of $\sigma^2(\alpha)$, $\sigma^2(\beta(\alpha))$ and $\sigma^2(\epsilon)$.

The total variance in the impedance data for the Generalized Linear Model can be decoupled according to

$$\sigma^2(\text{Total}) = \sigma^2(\text{Donor}) + \sigma^2(\text{Location(Donor)}) + \sigma^2(\text{Residual}) \qquad (7\text{-}2)$$

where $\sigma^2(\text{Total})$ is the total variance of the population. The term, $\sigma^2(\text{Donor})$ corresponds to the contribution to the variance in skin properties from the different donor samples. Similarly, $\sigma^2(\text{Location(Donor)})$ is the variance in skin properties within same donor sample. The final term, $\sigma^2(\text{Residual})$, is the variance of the residual errors. The variance model was applied to the polarization resistance and critical frequency data sets for each electrolyte type. The relative magnitude of the donor-to-donor and site-to-site variations were then compared to the variance in the residual error. The approach made it possible to determine whether the variance in skin properties among the donor samples and the variance for pieces of skin from the same sample were significantly larger than the variance in the residual error.

The relative contributions to the total variance from the various terms of the Generalized Linear Model were assessed through SAS[©] v8.0 software. Separate analyses were performed where the polarization resistance and the critical frequency were selected chosen as the dependent variables. Type III statistical analysis was implemented since the data set was unbalanced, *i.e.,* more skin samples were tested in monovalent electrolyte than in divalent electrolyte.[250] The output from the SAS procedure was presented in standard ANOVA tabular format. The table columns correspond to the independent variable name, degrees of freedom,

mean square of the regression errors, *F*-test parameter and one-sided probability for acceptance of the null hypothesis.

The null hypothesis and alternative hypothesis for the effect of donor sample and location from which the skin was obtained on the polarization resistance are presented in Table 7-1. Acceptance of the null hypothesis for donor type implies that the variance of property values among the donor samples was insignificant. Similarly, acceptance of the null hypothesis for the effect of location on polarization resistance implies that the site from which the skin was obtained provided no significant difference in property values.

Table 7-1: Proposed hypotheses for model effects on polarization resistance

Variable	Hypothesis type	Equation
Donor	Null	$H_0 : \sigma^2(\text{Donor}_{R_p}) = 0$
Donor	Alternative	$H_a : \sigma^2(\text{Donor}_{R_p}) \neq 0$
Location(Donor)	Null	$H_0 : \sigma^2(\text{Location(Donor)}_{R_p}) = 0$
Location(Donor)	Alternative	$H_a : \sigma^2(\text{Location(Donor)}_{R_p}) \neq 0$

7.2 Analysis of Skin Impedance Data for Normal Distribution Characteristics

The analysis of variance procedure is extremely sensitive to the condition of normality.[251] Consistency checks were performed prior to the analysis to verify that data sets were normally distributed. An example of the variation in skin impedance is provided by the histogram of critical frequency for pieces of skin immersed in monovalent electrolyte presented in Figure 7.2(a). The data points were clustered near the origin and clearly was not normally distributed. The histogram for the experimentally determined critical frequency of skin in divalent electrolyte exhibited similar behavior. The distributions of skin polarization resistance in both types of electrolyte also demonstrated gross departures from normality.

A statistical method which is commonly applied to shift distributions toward normality is to scale the experimental data by the square root or logarithm of

the measured quantities.[252] Both transformations were applied to the polarization resistance and critical frequency data but the logarithmic transformation provided distributions that most closely approximated the normal distribution. An example of the shift toward normality produced by the logarithmic transformation is illustrated by the histogram of skin critical frequency measured in monovalent electrolytes presented in Figure 7.2(b). An equal number of sampling intervals was selected for both histograms to ensure that the scaling was uniform. The normal distributions corresponding to the observed mean and standard deviation for both data sets are shown by the red lines. The measured skin critical frequency data set was clustered near the origin of Figure 7.2(a). The normal distribution curve was centered to the right of the median value which indicated that the population was not normally distributed. In contrast, the histogram of the transformed critical frequencies illustrated that the data were distributed over a wider range. Furthermore, the normal distribution curve was centered within 4% of the median value.

Although these observations strongly suggested that the logarithmic transformation produced normally distributed data, the approximation to normality was also assessed by the kurtosis and skewness coefficients of the population. The kurtosis measures the "flatness" or "peakedness" of a population relative to the normal distribution. A negative kurtosis coefficient implies the distribution is flatter than normal, whereas a positive value implies a more peaked distribution. The kurtosis coefficient is calculated according to

$$\text{Kurtosis} \equiv \frac{n(n+1)}{(n-1)(n-2)(n-3)} \sum_{i=1}^{n} \left(\frac{x_i - \bar{x}}{\sigma} \right)^4 - \frac{3(n-1)^2}{(n-1)(n-2)} \tag{7-3}$$

where n, $\bar{x}$ and σ are the total number of observations, the mean and the standard deviation of the data set, respectively. The analysis of variance procedure is extremely sensitive to the kurtosis coefficient. For example, the probability of rejection under the null hypothesis of a flat distribution greatly exceeds a selected
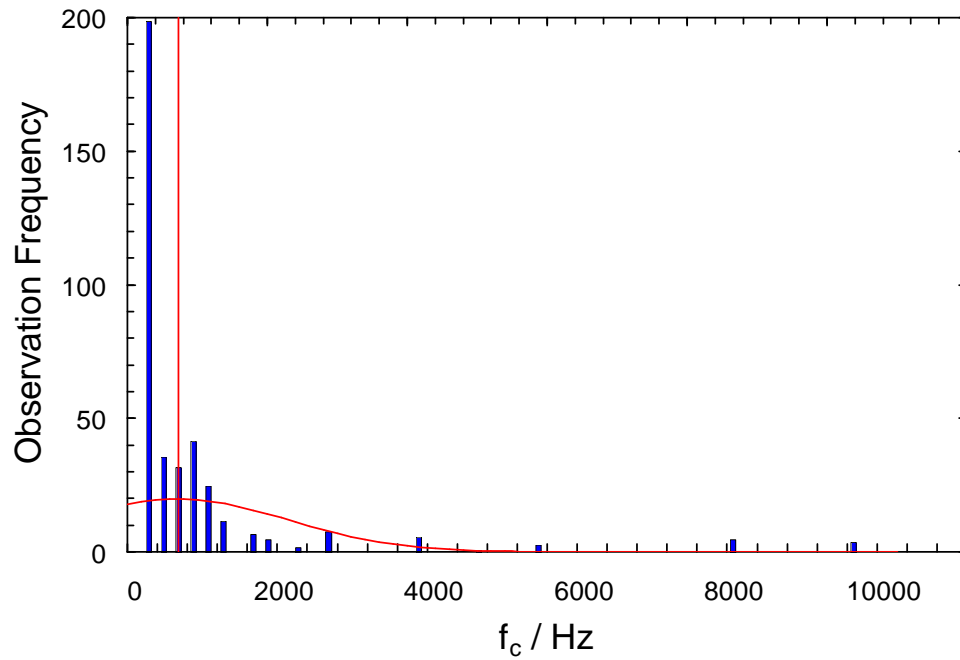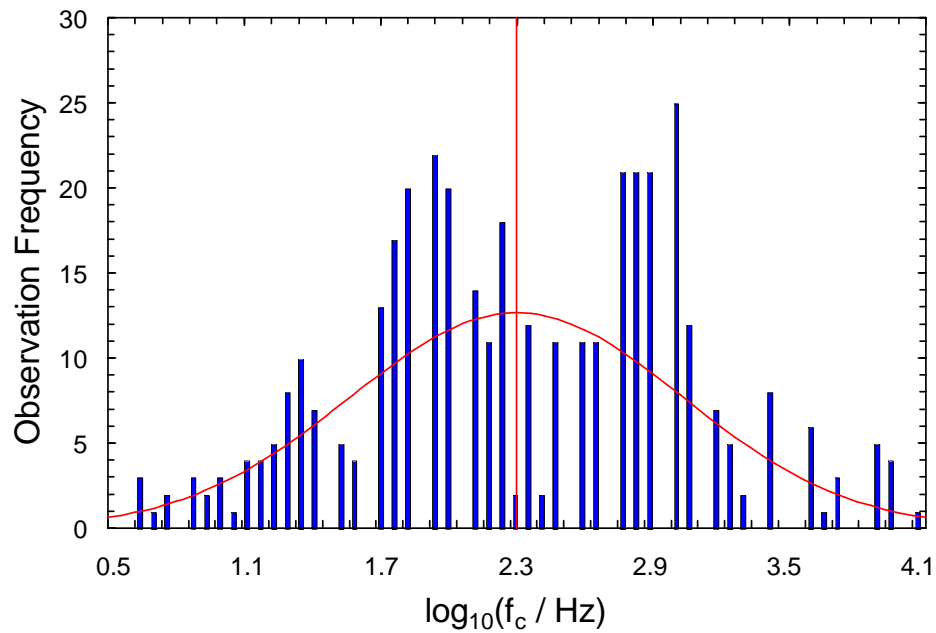
Figure 7-2: Histograms of the critical frequency of heat-separated epidermis. (a) Distribution of measured critical frequency values. (b) Data transformed by the base 10 logarithm.

significance level, α, and for a peaked distribution the probability is considerably less than α.[251]

The skewness represents the asymmetry of the data relative to the normal distribution. The effect of skewness on the significance levels of variance tests is much less extreme than the effect of the kurtosis coefficient.[251] Positive skewness indicates an asymmetric distribution where the tail is stretched toward more positive values, *i.e.,* to the right side of the mean. Alternatively, a negative skewness coefficient corresponds to a distribution that extends toward more negative values, *i.e.,* to the left side of the mean. The skewness is defined by

$$\text{Skewness} \equiv \frac{n}{(n-1)(n-2)} \sum_{i=1}^{n} \left(\frac{x_i - \bar{x}}{\sigma} \right)^3 \tag{7-4}$$

where n, $\bar{x}$ and σ are defined in the same manner as for the kurtosis coefficient. The skewness and kurtosis coefficients for the measured and logrithmically transformed critical frequency data from impedance experiments of skin immersed in monovalent and divalent electrolyte are presented in Tables 7-2 and 7-3, respectively. Similar distribution statistic tables for the measured and logarithmic transformed polarization resistance data sets are presented in Appendix C. Also, included in Appendix C are the square root transformed distribution statistics.

The skewness and kurtosis coefficients describing the distribution of experimentally determined critical frequencies of skin immersed in monovalent electrolyte were 20.79 and 4.35, respectively. The relatively large magnitude of the distribution parameters indicated that the population was peaked and severely skewed toward more positive values in comparison to the normal distribution. The histogram corresponding to the transformed values illustrated that the data sets was approximately normally distributed. The skewness and kurtosis coefficients were -6.13x10^{-3} and -4.82x10^{-1}, respectively. The distribution parameters indicated that the transformed data set was essentially centered about the mean

Table 7-2: Distribution statistics for critical frequency as a function of electrolyte type

Variable	Divalent	Monovalent
Mean	435.33	715.66
Standard Error	93.54	77.57
Median	78.75	169.66
Mode	53.65	954.10
Standard Deviation	1020.44	1547.50
Sample Variance	1.04×10^6	2.39×10^6
Kurtosis	14.04	20.79
Skewness	3.67	4.35
Minimum	11.56	3.66
Maximum	5.37×10^3	1.16×10^4
Sum	5.18×10^4	2.85×10^5
Degrees of Freedom	119	398
Confidence Level(95.0%)	185.24	152.50

and slightly depressed relative to the normal distribution. The transformed polarization resistance data sets displayed similar trends for measurements collected with monovalent and divalent electrolytes. In summary, the logarithmic transformation of the experimental data produced distributions that were approximately normal and thus satisfied the required conditions for proper interpretation of the ANOVA investigations.

7.3 Variance Components of Polarization Resistance

The variance components of the $\log_{10}$ transformed skin polarization impedance data for samples immersed in monovalent and divalent electrolyte solutions are presented in Table 7-4. The results for the monovalent and divalent skin populations were very similar. For example, the sample-to-sample contributions to the overall variance for the monovalent and divalent data sets were 20% and 17%, respectively. The within-sample variance provided the largest contribution to the total variance of skin polarization resistance. The relative contributions for the monovalent and divalent data were 76% and 82%, respectively. The variance in the residual errors for both electrolyte types provided less than 4% of the total.

Table 7-3: Distribution statistics for $\log_{10}$ of critical frequency as a function of electrolyte type

Variable	Divalent	Monovalent
Mean	2.03	2.30
Standard Error	6.01×10^{-2}	3.72×10^{-2}
Median	1.90	2.23
Mode	1.73	2.98
Standard Deviation	6.55×10^{-1}	7.33×10^{-1}
Sample Variance	4.30×10^{-1}	5.38×10^{-1}
Kurtosis	1.55×10^{-1}	-4.82×10^{-1}
Skewness	8.53×10^{-1}	-6.13×10^{-3}
Minimum	1.06	0.56
Maximum	3.73	4.06
Sum	241.90	891.90
Degrees of Freedom	119	388
Confidence Level(95.0%)	0.119	0.073

The results indicated that the intra-individual variability in the transformed polarization resistance data was greater than the inter-individual variability.

Table 7-4: Calculated contributions to the overall variance in the $\log_{10}$ of skin polarization resistance

Electrolyte	σ^2(Total)	σ^2(Donor)	σ^2(Location(Donor))	σ^2(Residual)
Monovalent	0.239	6.04×10^{-2}	0.229	1.01×10^{-2}
Divalent	0.225	4.70×10^{-2}	0.223	1.98×10^{-3}

The analysis of variance parameters for determining whether the variance components were statistically significant are presented in Tables 7-5 and 7-6. The significance level, α, for the comparisons was 0.05. The F-test parameter and probability values for acceptance of the null hypothesis for the effect of the donor from which a piece of skin was extracted on the polarization resistance of the specimens immersed in monovalent electrolyte were 2.45 and 0.46%, respectively. The F-test parameter and probability values for effect of location from which a piece of skin was obtained were 89.93 and less than 0.01%. The null hypothesis could not be accepted for both effects, as F-test probabilities for acceptance of the null hypothesis were extremely small. The results implied that contributions to the overall

variance in the polarization impedance data caused by differences in the donor samples and variations in a given sample associated with specimen location were significant for skin immersed in monovalent electrolyte.

Table 7-5: Calculated contributions to the total variance in the $\log_{10}$ of skin polarization resistance. Results from pieces immersed in monovalent electrolyte

Variable	DOF	Type III SS	Mean Sq.	F-stat	Pr$>$ F
Donor type	16	32.96	2.06	2.45	0.0046
MS Error (Donor)	79.14	66.53	0.841	-	-
Location(Donor)	79	71.75	0.908	89.93	$<$ 0.0001
MS Error Location(Donor)	292	2.95	0.0101	-	-

Table 7-6: Calculated contributions to the total variance of the $\log_{10}$ of skin polarization resistance for pieces immersed in divalent electrolyte

Variable	DOF	Type III SS	Mean Sq.	F-stat	Pr$>$ F
Donor type	11	19.93	1.74	2.32	0.0488
MS Error (Donor)	19.99	14.96	0.748	-	-
Location(Donor)	20	13.66	0.683	345.96	$<$ 0.0001
MS Error Location(Donor)	87	0.172	1.98×10^{-3}	-	-

Similar results were obtained from the variance model for the observation set of skin immersed in divalent electrolyte. The F-statistic and probability for acceptance of the null hypothesis for the effect of donor sample on the variation in polarization resistance were 2.32 and 4.88%, respectively. The regression parameters for the effect of extraction site within a donor sample on the variation in polarization impedance were 345.96 and 0.01%, respectively. The null hypothesis was rejected for both effects. This implied that variation in polarization resistance of skin specimens in divalent solutions was large. Furthermore, the variation in polarization resistance within a given donor was at least as large as the interindividual variation.

7.4 Variance Components of Critical Frequency

The variance components of the $\log_{10}$ transformed skin critical frequency data for samples immersed in monovalent and divalent electrolyte solutions are pre-

sented in Table 7-7. The sample-to-sample contributions to the overall variance in the transformed critical frequency data for the monovalent and divalent data sets were 24% and 10%, respectively. The within-sample variance provided the largest contribution to the total variance of skin critical frequency. For example, the intra-individual variance of the monovalent and divalent data comprised 74% and 89% of the total variance. The variance in the residual errors for both electrolyte types provided less than 3% of the total. The results indicated that the intra-individual variability in the transformed critical frequency data was greater than the inter-individual variability.

Table 7-7: Calculated contributions to the overall variance in the $\log_{10}$ of skin critical frequency

Electrolyte	σ^2(Total)	σ^2(Donor)	σ^2(Location(Donor))	σ^2(Residual)
Monovalent	0.400	0.124	0.388	1.22×10^{-2}
Divalent	0.385	$4.21\times10{-2}$	0.379	6.42×10^{-3}

The statistical significance of the contributions to the overall variance in skin critical frequency, as described by the variance model of Equation (7-2), was evaluated. The parameters for the analysis of variance in skin critical frequency for samples immersed in monovalent and divalent electrolyte solutions are presented in Tables 7-8 and 7-9, respectively. A 5% significance level was selected for the comparisons. The null hypothesis for the analysis proposed that there was an insignificant effect of donor sample on the total variance of critical frequency data set of skin immersed in monovalent electrolyte.

Table 7-8: Calculated contributions to the total variance of the $\log_{10}$ of skin critical frequency for pieces immersed in monovalent electrolyte

Variable	DOF	Type III SS	Mean Sq.	F-stat	Pr$> F$
Donor type	16	66.23	4.14	2.91	0.0009
MS Error (Donor)	79.10	112.33	1.42	-	-
Location(Donor)	79	121.24	1.535	125.97	< 0.0001
MS Error Location(Donor)	292	3.56	1.22×10^{-2}	-	-

Table 7-9: Calculated contributions to the total variance of the $\log_{10}$ of skin critical frequency for pieces immersed in divalent electrolyte

Variable	DOF	Type III SS	Mean Sq.	*F*-stat	Pr> *F*
Donor type	11	25.61	2.33	1.72	0.14
MS Error (Donor)	19.98	27.00	1.351	-	-
Location(Donor)	20	24.68	1.234	192.21	< 0.0001
MS Error Location(Donor)	87	0.558	6.42×10^{-3}	-	-

The *F*-test parameter and probability values for acceptance of the null hypothesis were 2.91 and 0.09%, respectively. Similarly, the *F*-test parameter and probability values for effect of location from which a piece of skin was obtained were 192.21 and less than 0.01%. The null hypothesis for the effect of donor sample on the critical frequency for skin immersed in monovalent electrolyte was rejected, as there was only a 0.09% chance of selecting two pieces of skin from different donors with similar critical frequencies. Alternatively stated, the variation in critical frequency attributed to differences in skin from the donor population was significant.

The *F*-parameter and probability value for the effect of donor sample of skin immersed in divalent electrolyte were 1.72 and 14.0%, respectively. Therefore, the null hypothesis could not be rejected unconditionally. The *F*-statistic and probability value for the site-to-site variation of critical frequency were 192.21 and less than 0.01%, respectively; hence, the null hypothesis was rejected. This implied the variation in critical frequency of skin immersed in divalent electrolyte associated with site-to-site differences was greater than variation caused by sample-to-sample differences.

In summary, the analysis of variance study indicated that there was a significant variation in the $\log_{10}$ polarization impedance and critical frequency of skin for pieces obtained from the same donor sample and for pieces taken from different donors. The variation in properties was similar irrespective of the cation charge in the electrolyte. In other words, the intra-individual variation of skin properties

was as great or greater than the inter-individual variation. The results indicated that pieces of skin taken from the same donor cannot be considered as identical specimens. Furthermore, the variability in the properties of excised skin extracted from different donors was also large enough to restrict direct comparison of any two randomly selected samples. The characteristics of the variation in skin properties described above are compared with the literature in Section 7.7.

7.5 Effect of Electrolyte on Skin Properties

The results described in Sections 5.2.2, 6.2.2 and 6.3 indicated that the charge of the cation in the ionic solutions used for an experiment can influence the impedance response of the skin. The mean values and variances of the polarization resistance and critical frequency data corresponding to skin specimens immersed in monovalent and divalent solutions were compared to assess the statistical significance of the effect of electrolyte composition on skin impedance. The data sets were classified according to electrolyte type. Student's t-tests and F-tests were applied to each class of measurements. As these tests require the observation set to be normally distributed, the base 10 logarithmic transformed data sets were selected for analysis.

The null hypotheses for the Student's t-test and the F-test were that the respective means and variances of the monovalent and divalent data sets were equal. Acceptance of the null hypothesis would imply that there was no effect of cation charge on the impedance response of skin. The null and alternative hypotheses for the Student's t-test and F-test are presented in Tables 7-10 and 7-11.

Table 7-10: Proposed hypotheses for comparison of means

Variable	Hypothesis type	Equation
R_p or f_c	Null	$H_0 : \mu_1 = \mu_2$
R_p or f_c	Alternative	$H_a : \mu_1 \neq \mu_2$

Table 7-11: Proposed hypotheses for comparison of variance

Variable	Hypothesis type	Equation
R_p or f_c	Null	$H_0 : \sigma_1{}^2 = \sigma_2{}^2$
R_p or f_c	$H_a : \sigma_1{}^2 > \sigma_2{}^2$	

The subscript 1 corresponds to skin transport properties in monovalent electrolyte and, similarly, subscript 2 corresponds to similar skin parameter values in divalent electrolyte. There was no *a priori* justification for assuming an equality of variances, therefore the *F*-test was applied first. The information obtained from the *F*-test guided the selection of an appropriate *t*-test since it can be applied under the assumption of equal or unequal variances. The input parameters for the *F*-tests were the degree of freedom for each class of measurements and the *F*-statistic which is defined by the ratio of variance in data set 1 to variance in data set 2.

The *F*-test parameters for comparison of the transformed polarization resistance and critical frequency variances are presented in Tables 7-12 and 7-13, respectively. As the calculated *F*-statistic was less than the critical *F*-value for the 95% significance level in both cases the null hypothesis could not be rejected. There was a 31.8% chance that the calculated *F*-statistic for the polarization resistance was less than the critical *F*-value and there was a 7.32% chance that the critical frequency *F*-statistic was less than the critical *F*-value. Although the *F*-tests suggested that there was a small possibility that the variances in skin properties for each type of electrolyte were equal, the Student's *t*-test was applied assuming unequal variances.

The input parameters for the Student's *t*-test were the adjusted degree of freedom and the *t*-statistic which is the difference between the two means divided by the weighted standard deviation of the entire sample population. The parameters for the *t*-tests of polarization resistance means and critical frequency means for

Table 7-12: *F*-test statistics for comparison of variances in the $\log_{10}$ of polarization resistance for each electrolyte type

Statistic	Monovalent	Divalent
Mean	4.46	4.73
Sample Variance	3.02×10^{-1}	2.80×10^{-1}
Observations	388	119
Degrees of Freedom	387	118
F-statistic	1.08	
$\Pr(F < F_{\text{critical}})$	3.18×10^{-1}	
F_{critical}	1.29	

Table 7-13: *F*-test parameters for comparison of variances in the $\log_{10}$ of critical frequency for each electrolyte type

Statistic	Monovalent	Divalent
Mean	2.30	2.03
Sample Variance	5.38×10^{-1}	4.30×10^{-1}
Observations	388	119
Degrees of Freedom	387	118
F-statistic	1.25	
$\Pr(F < F_{\text{critical}})$	7.32×10^{-2}	
F_{critical}	1.29	

the two electrolytes are listed in Tables 7-14 and 7-15, respectively. As the absolute value of the calculated *t*-statistic exceeded the critical *t*-value for both comparisons means the null hypothesis was rejected for each population. The rejection of the null hypothesis implied that the mean values of skin properties in each electrolyte were different. Alternatively stated, the impedance response of skin in divalent electrolyte was different from that of monovalent electrolyte. The result is in agreement with the hypothesis that divalent cations interact with the stratum corneum in a manner differently than monovalent cations.

7.6   Correlation Between Critical Frequency and Polarization Resistance

The contributions to the overall variance in the critical frequency and polarization resistance of excised stratum corneum showed a similar dependence on donor sample and location within a sample. This result suggested that the properties were correlated. The strength of the correlation between critical frequency

Table 7-14: Student's *t*-test output statistics for comparison of means in the $\log_{10}$ of polarization resistance for each electrolyte type

Statistic	Monovalent	Divalent
Mean	4.46	4.73
Sample Variance	3.02×10^{-1}	2.80×10^{-1}
Observations	388	119
Hypothesized Mean Difference	0	
Degrees of Freedom	202	
t-value (two-tailed)	4.84	
$\Pr(t < t_{\text{critical}})$	2.60×10^{-6}	
t_{critical} (two-tailed)	1.97	

Table 7-15: Student's *t*-test output statistics for comparison of means in the $\log_{10}$ of critical frequency for each electrolyte type

Statistic	Monovalent	Divalent
Mean	2.30	2.03
Sample Variance	5.38×10^{-1}	4.30×10^{-1}
Observations	388	119
Hypothesized Mean Difference	0	
Degrees of Freedom	216	
t-value (two-tailed)	-3.76	
$\Pr(t < t_{\text{critical}})$	2.17×10^{-4}	
t_{critical} (two-tailed)	1.97	

and polarization resistance of skin was assessed by linear regression. The $\log_{10}$ transformed critical frequency and polarization resistance were selected as the dependent and independent variables, respectively. Separate regressions were performed on the monovalent and divalent observation sets.

The relationship between the critical frequency and polarization resistance is presented in graphical form by Figure 7-3. The open circles represent the data set for skin in monovalent electrolyte and the open diamonds represent the data set of skin in divalent electrolyte. The solid line represents the relationship between the critical frequency and polarization resistance obtained by a regression of a linear model to the entire data set. The estimated linear expression relating the two quantities is presented by

$$\log_{10}(f_c) = -1.218 \times \log_{10}(R_p) + 7.743 \qquad (7\text{-}5)$$
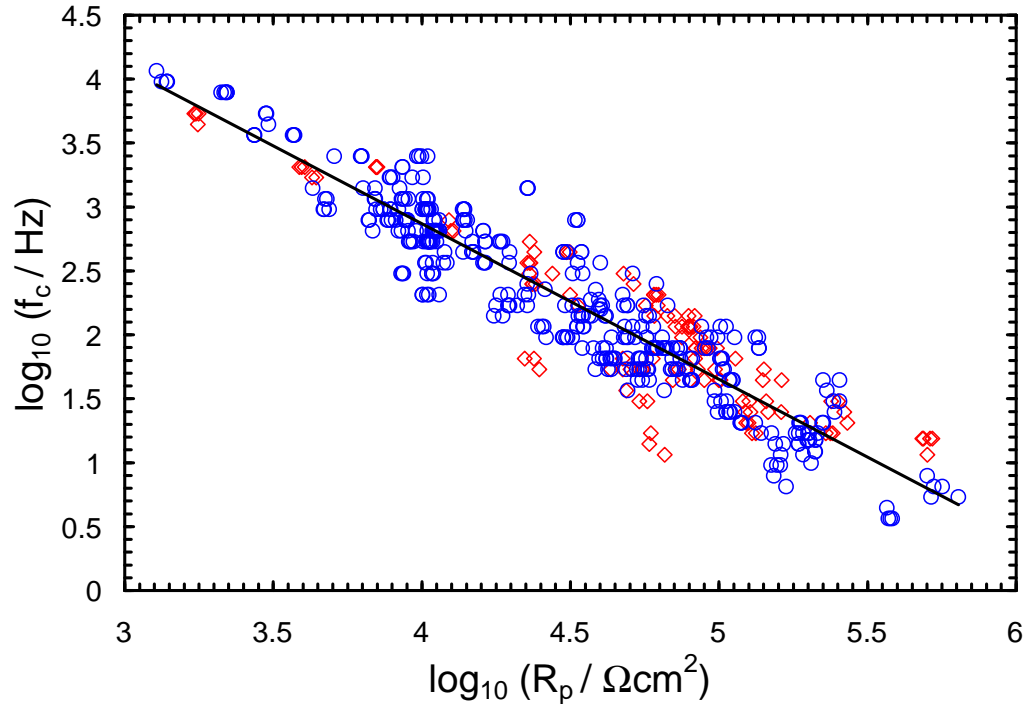
Figure 7-3: Relationship of characteristic skin impedance parameters, $\log_{10}(f_c)$ and $\log_{10}(R_p)$.

where $\log_{10}(f_c)$ and $\log_{10}(R_p)$ correspond to the logarithmic transformations of the critical frequency and the polarization resistance of skin. The Pearson's correlation coefficient for the regression was -0.936 which indicated that a decrease in critical frequency is associated with a decrease in the polarization resistance.

The correlation between $\log_{10}(f_c)$ and $\log_{10}(R_p)$ may suggest that a single time constant can be used to describe the entire system. Although this type of simple relationship is attractive, care must be taken before assigning a single parameter to describe the skin system. For example, the depressed semicircular impedance response of skin implies that there is a distribution of relaxation processes in the system. This has prompted the application of constant phase elements for modeling skin impedance. A major restriction of this type of distributed model is that the time constants for the system must be symmetrically distributed about the critical frequency.

7.7 Comparison of Variation in Skin Impedance with Literature Results

The literature indicates that stratum corneum properties, such as thickness and lipid composition, display considerable variation with location on the body (inter-individual variation).[13,14,16,17,253] and between individuals for a given anatomical region (inter-individual variation).[16] There is a general consensus that differences in the composition and structure of stratum corneum lipids are responsible for variations in the permeability and impedance in skin.[13,24,35,46,67] Despite this consensus, the relationship between the state of stratum corneum lipids and the macroscopic transport properties of the membrane has not been completely characterized.[16]

Statistical analysis was applied to *in vivo* skin data to determine that the inter-individual variability of stratum corneum lipid components was significantly larger than the intra-individual variability.[16] The regional variation in skin impedance was also found to be significant; however, the variation between individuals was not assessed. In the work described in this chapter, the nested form of the Generalized Linear Model[249] was applied to evaluate similar sources of variation in impedance data from the hydration of heat-separated cadaver skin. The results indicated that the intra-individual variability in skin impedance was greater than the person-to-person variability.

The large variability in skin impedance could have significant impact on the design and placement of transdermal iontophoresis devices if similar results are found for *in vivo* human skin. For example, low skin impedance has been associated with relatively high membrane permeability.[112,131,163] Identification of these low impedance sites could guide the placement of transdermal delivery devices on the body. This type of placement strategy has other advantages. It was demonstrated earlier in this text (see, for example, Section 5.2) that large potential dif-

ferences can alter skin properties. Topical irritation during clinical transdermal iontophoresis studies has been associated with high impedance skin.[254] Therefore, placement of the iontophoretic transdermal patch over low impedance skin may prevent patient discomfort.

Statistical analysis techniques, such as Student's t-tests and F-tests, were implemented in this work to identify the influence of electrolyte cation charge on the impedance of heat-separated cadaver skin. The evaluations revealed that the impedance response of skin in monovalent cation solutions was different from the response in divalent cation electrolyte. The result that cation type influences skin impedance is in agreement[152] and in conflict[207] with reported findings. The inconsistent literature results were obtained by the same research group using a similar methodology. For example, electric circuit models were regressed to the impedance spectra to obtain representative quantities for skin resistance and capacitance. The effect of cation type on the recovery of skin to iontophoresis was assessed using circuit parameters.

Despite the similar of the experimental approach, important differences were present in the two investigations. For example, a different circuit network was regressed to each set of skin impedance data. The standard deviations of the regressed circuit elements were approximately 10-20% of the parameter values. In addition, the number of skin samples probed in the studies were 2 and 5, respectively. There is a strong possibility that the relatively large uncertainty in the circuit parameters coupled with the small sample sizes led to erroneous conclusions for the effect of cation type on skin impedance. The work presented in this chapter was much less susceptible to these type of errors because the number of skin samples investigated was at an order of magnitude larger. The larger sample size would improve the confidence of the statistical of regressions.

CHAPTER 8
POTENTIAL AND CURRENT STEP-CHANGE STUDIES

The influence of alternating current and potential on the properties of skin was demonstrated in Chapters 5 and 6. The results indicated that skin properties begin to change at a critical potential. The majority of the impedance studies were conducted with a zero DC current bias, *i.e.,* at the open-circuit condition. Under such conditions the skin was allowed to partially depolarize during each complete perturbation cycle of the impedance scan. Since a nonzero current bias is applied during transdermal iontophoresis to enhance drug delivery rates, it is likely that the skin will become polarized. The influence of a nonzero current bias on skin properties was investigated by impedance spectroscopy (see, for example Section 6.5), however, the current was only applied for approximately five minutes.

Transdermal iontophoretic delivery rates are typically small;[133,255] therefore, protocols for commercial iontophoretic devices will likely require current to be applied for much longer periods of time. The purpose of this work was to determine the response of skin to elevated DC current and potential signals. The major difference of this study from the previous work described in this text is that the DC bias signals were applied for longer time intervals. The general approach was to perturb the skin from the open-circuit condition with a step-change in DC current or potential. The system response was monitored at the elevated condition for a minimum of 20 minutes. The skin was then allowed to relax at the open-circuit condition. The results for the potential and current step-change studies are presented in Sections 8.1 and 8.2, respectively.

8.1 Potential Step-Change Results

The experimental data presented here were obtained according to the methodology described in Section 4.2. Impedance spectra were not collected for these studies. Electrical properties, such as the polarization impedance, were estimated by regressing a linear model to the current-potential data collected at potentials between 10 and 100 mV. It was assumed that skin properties were not altered at these relatively low perturbation amplitudes. Microsoft Excel$^{©}$ was used for the regressions where current was selected as the independent variable and potential as the dependent variable. A fit of the linear model to the data yielded estimates for the DC electrical properties of skin. For example, the slope of the linear model represents the polarization resistance and the intercept is the open-circuit potential. Confidence in the linear model was provided by the r^2 correlation parameter for each regression.

8.1.1 Model Predictions of Skin Polarization Resistance

The linear model was regressed to the low-amplitude potential bias data for all four sets of experiments. A sample plot of the current-potential data with the regression line is provided by Figure 8-1. The polarization resistance, open-circuit potential and r^2 coefficients for the four sets of experiments are presented in Table 8-1.

The linear model provided excellent fits to the data sets, as the r^2 coefficients were all greater than 0.997. The estimated values of the polarization impedance ranged from 14.6 kΩcm^2 to 25.1 kΩcm^2. The open-circuit potentials obtained from the fits were between 12.7 mV and 25.3 mV. The polarization impedance and open-circuit potential values from the regressions were comparable to the measurements obtained in impedance spectroscopy studies.
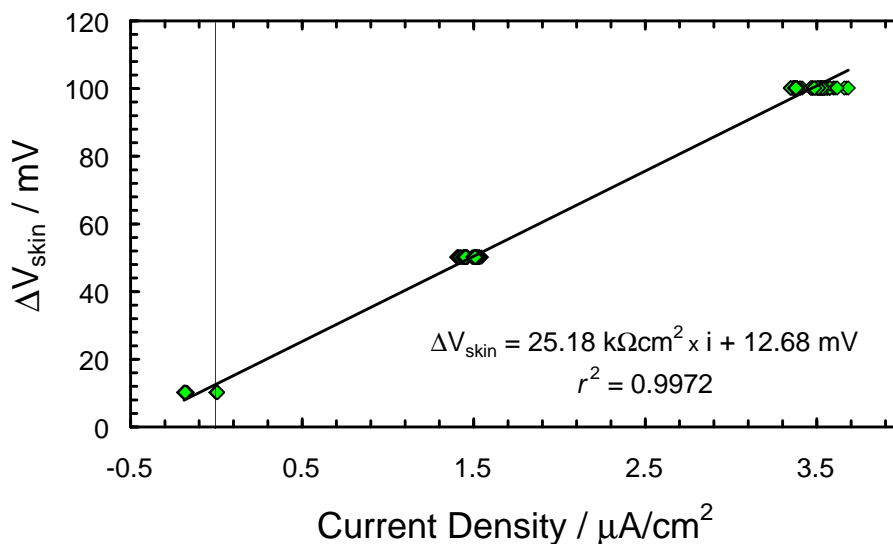
Figure 8-1: Sample regression of linear model to potential step-change data to predict skin properties.

Table 8-1: Regression parameters for estimation of skin properties

Sample	R_{pol}, Ω cm^2,	V_{OC}, mV	r^2
NaCl I	25182	12.7	0.9972
NaCl II	14623	22.7	0.9999
CaCl$_2$ I	21328	19.7	0.9992
CaCl$_2$ II	21239	25.3	0.9997

8.1.2 Calculated Deviation From Constant Properties

The polarization resistance of a system with constant electrochemical properties should be independent of the applied current or potential. Ideally, iontophoretic devices should not alter the properties of skin. An acceptable alternative requires that electrically induced changes be reversible within a limited time frame. The goal of this analysis was to determine the deviation of the measured current response in comparison to a system with constant properties. For example, skin with a potential independent polarization resistance should exhibit a proportional increase in measured current for a given increase of potential. The polarization resistance is the constant of proportionality that relates the current density to the electrostatic potential.

The deviation from constant properties was assessed by comparing the measured current to the response expected from skin with a potential independent polarization resistance. The approach here was to predict the current response to potential step-changes greater than 100 mV from the polarization resistance calculated by the regression procedure described in Section 8.1. The predicted current for skin with constant properties was calculated according to

$$I_{predict,linear} = \frac{(V_{applied} - V_{OC})}{R_{pol}} \tag{8-1}$$

where $V_{applied}$ is the applied potential in volts, V_{OC} is the open-circuit potential in volts and R_{pol} is the polarization resistance in units of ohm-square centimeters. The difference between the predicted current and the measured current was calculated for all of the step-change studies. This difference provided a measure of the departure from a linear response in skin properties induced by the potential step-change. The average difference in current over the potential bias interval was also calculated. The standard deviation of the difference provided a measure of the nonlinear and nonstationary condition of the current response.

The deviation in the measured current response from skin with a constant polarization resistance is presented as a function of time and potential in Figure 8-2. The deviation in current is plotted on the left ordinate and the applied potential is plotted on the right ordinate. For potential step-changes lower than 250 mV, the observed deviation in the measured current response was generally less than 100 nA/cm². As the applied potential was increased to 250 mV, the deviations in the current response increased to approximately 1 μA/cm². For the 500 mV experiments the current deviation was, in general, smallest immediately after the step-change was applied and increased continuously for approximately 10 minutes. For the remainder of the 500 mV bias interval the deviation in current ranged from 2-6 μA/cm². At the 500 mV bias level the deviations in current response from

skin with constant properties were generally greater for membranes immersed in NaCl solution than the samples in CaCl$_2$ solution.
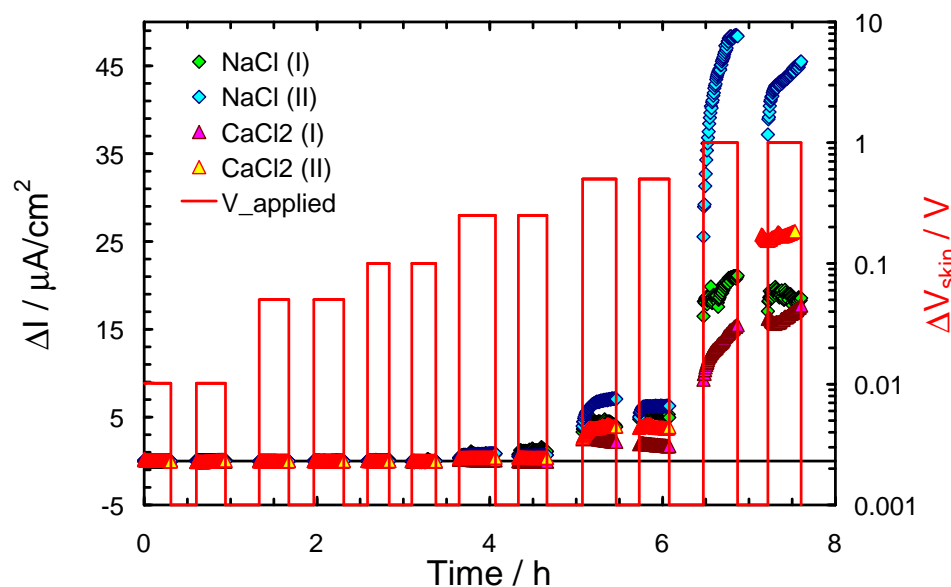
Figure 8-2: Deviation in the measured current from the current associated with potential independent polarization resistance skin.

The largest deviations in measured current were observed for the 1 V step-changes. For example, the deviations in the current response ranged between 5 μA/cm^2 and 55 μA/cm^2. During the 1 V bias intervals the deviations in current increased continuously with the exception of the second bias interval of the first skin sample immersed in NaCl solution. Similar to the 500 mV bias results, the magnitude of the current deviations were, in general, larger for skin samples immersed in NaCl solution than those in CaCl$_2$ solution.

The results indicated that there is a critical potential between 100 mV and 250 mV where the properties of skin begin to change. The range of potential at which skin properties become altered was consistent with the impedance spectroscopy studies. As the magnitude of the potential step-change was increased above this range the measured current response was higher than expected for skin with a constant polarization resistance. For applied bias amplitudes above the critical

potential, the magnitude of the deviation in current increased nonlinearly with increasing values of potential bias. In general, the relative deviation in measured current response from a constant property system was greater for skin immersed in NaCl electrolyte than in $CaCl_2$ electrolyte. The larger deviations observed for the monovalent electrolyte solutions was also consistent with the electrochemical impedance spectroscopy studies presented in Sections 5.2.2, 6.2.2 and 6.3.

8.2 Current Step-Change Results

The electrochemical impedance studies and the potential step-change experiments described in Sections 5.2 and 8.1, respectively, indicated that skin properties become altered above a critical potential. The objective of this study was to determine whether skin properties change above a critical current. The approach here was to subject skin to a series of step-changes in current and monitor the potential response. The amplitudes of the current step signals were 1.4 μA/cm^2, 14 μA/cm^2 and 140 μA/cm^2. In general, the current step-change was held at the elevated condition for 40 minutes. The experimental protocol of the studies presented here was analogous to the methodology described in Section 8.1. However, in this case, a current step-change was applied across the skin and the potential response was measured.

Two pieces of skin were extracted from the same donor sample and subjected to the same series of current step-changes. The amplitude and sequence of the applied-current signals were identical. The skin specimens were immersed in buffered 150 mM NaCl electrolyte. A series of four 10 mV VAG impedance spectra were collected at the open-circuit condition *i.e.*, $i_{DC,applied}$ = 0, before and after the applied DC current steps. The spectra provided information on the recovery of skin properties to the elevated current signals. The results from the studies with

first skin sample are described in detail in Sections 8.2.1 and 8.2.2. A comparison of the responses for both pieces of skin is provided in Section 8.2.3.

8.2.1 Measured Potential Difference Across the Skin

The potential difference across the first piece of skin for each applied-current amplitude is presented as a function of time in Figure 8-3. The data corresponding to Intervals 1-8 represent the potential measurements collected while the current step-changes were applied. The solid green diamonds and open black diamonds correspond to the open-circuit potentials measured before and after the impedance spectra were collected.
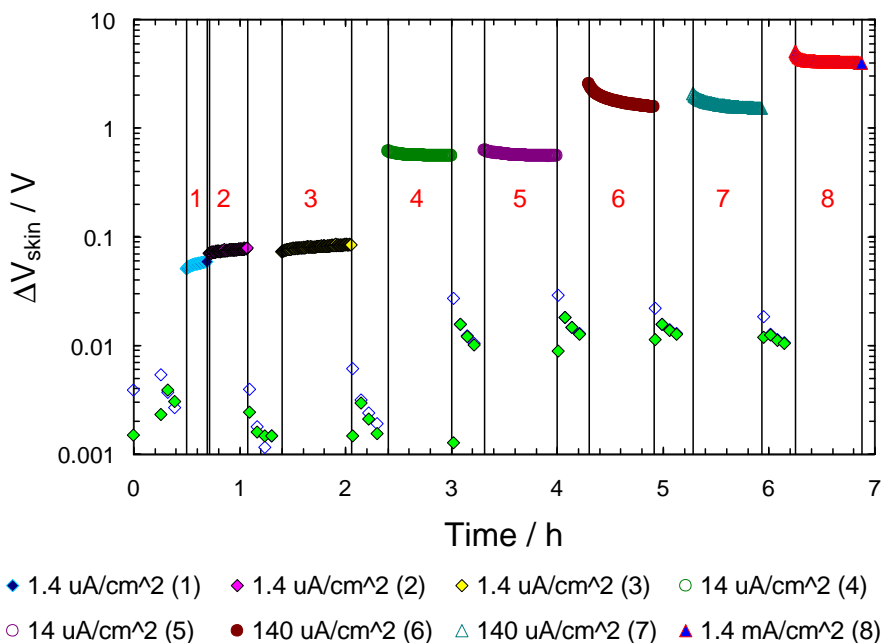
Figure 8-3: Potential difference across epidermis. The amplitudes of the current step changes causing the voltage drops are indicated in the legend. The solid green diamonds and open black diamonds correspond to the open-circuit potential measurements collected before and after the impedance scans.

Prior to the application of the first 1.4 μA/cm^2 current step-change the open-circuit potential difference across the skin was on the order of 5 mV. Immediately after the 1.4 μA/cm^2 current was terminated the potential difference across the membrane was 51 mV. While a 1.4 μA/cm^2 current signal was applied during

Intervals 2 and 3 the potential difference across the skin gradually increased to 86 mV. The increase in the potential difference was consistent with an increase in the polarization resistance of skin. The open-circuit potential measurements collected after the applied current was terminated were approximately 5 mV. The open-circuit potential decreased with time during all of the recovery periods following the current step-changes. The relaxation of open-circuit potential suggested that the skin had become slightly charged while the step-change was applied.

Intervals 4 and 5 correspond to the voltage responses to the 14 μA/cm^2 perturbations. The membrane potential difference was 627 mV immediately after the current step-change was applied. The potential difference across the membrane decreased continuously while the current was applied. The potential drop at the end of step-change Interval 4 was 569 mV. A gradual decrease in the potential difference across the skin was also observed during Interval 5. For example, the voltage difference across the epidermis was 638 mV immediately after the 14 μA/cm^2 signal was applied and 567 mV just before the current was terminated. The gradual decrease in the potential difference across skin indicated that the membrane polarization resistance had decreased. The results were consistent with the hypothesis that skin properties begin to change as the potential difference across the membrane exceeds 250 mV.

The open-circuit potentials measured immediately after the 14 μA/cm^2 current was terminated were on the order of 20 mV. During a given recovery period, the open-circuit potential decreased over time. The decay in the open-circuit potential response suggested that the state and/or distribution of charge within the skin changed during the application of the 14 μA/cm^2 current signal. For example, it is possible that the passage of current modified the internal structure of

the epidermis to provide greater access for the cations and neutralize the negative background charge of skin. This type of process could have the effect of reducing the open-circuit potential.

Intervals 6 and 7 correspond to the potential drops across the skin induced by the 140 μA/cm^2 step-changes. Similar to the 14 μA/cm^2 results, the membrane potential difference also declined continuously while the current was applied. For example, the potential difference decreased from 2.62 V to 1.60 V during Interval 6. Similarly, the voltage drop across the skin decreased from 2.11 V to 1.55 V during Interval 7. The open-circuit potentials were also approximately 20 mV after the 140 μA/cm^2 step-change signals. The open-circuit potential decreased for each subsequent measurement collected after elevated current signal had been terminated.

The amplitude of the final current step-change, represented by Interval 8, was 1.4 mA/cm^2. The potential difference decreased from 5.18 V to 4.07 V while the current was held at the elevated condition. The potential difference induced by the largest step-change was significantly larger the hypothesized voltage threshold for onset of changes in skin properties. In general, the reduction in potential difference with time for all current step-changes above 1.4 μA/cm^2 strongly suggested that the polarization resistance of skin had decreased. The procedure used to calculate the polarization resistance is described in the next section.

8.2.2 Calculated Polarization Resistance

Skin polarization resistance was calculated according to Ohm's law by dividing the measured potential difference by the applied current. The polarization resistance should be independent of current and time for a system with constant properties. The calculated polarization resistance of skin is illustrated in Figure 8-4. The data indicated by Intervals 1-8 correspond to the skin resistance

at the different current step-change amplitudes. The solid diamonds represent the Kramers-Kronig consistent polarization resistances calculated from the impedance spectra.
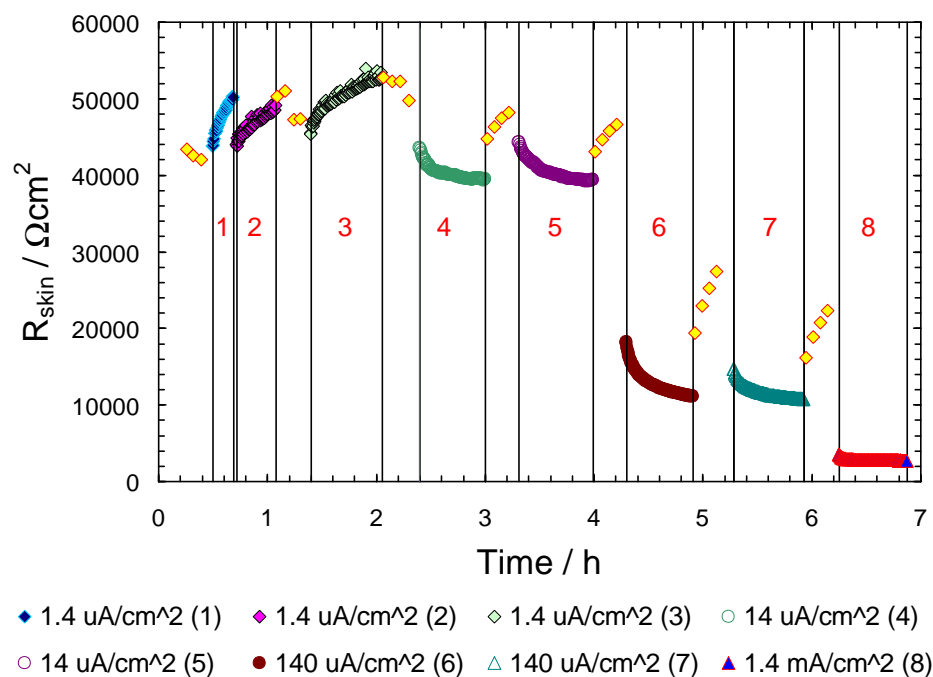
Figure 8-4: Calculated polarization resistance of skin. The current step-change amplitudes are indicated by the legend.

The polarization resistance corresponding to the first impedance scan collected before the start of the 1.4 μA/cm^2 step-change was 43.5 kΩcm^2. Subsequent measurements collected at the open-circuit condition were approximately 43 kΩcm^2. The calculated polarization resistance during the first 1.4 μA/cm^2 step-change increased from 43.9 kΩcm^2 to 50.3 kΩcm^2. During Interval 2, where the applied current was also 1.4 μA/cm^2, the skin resistance increased from 44.1 kΩcm^2 to 49.3 kΩcm^2. The estimated polarization resistances from the four impedance spectra collected after Interval 2 were all approximately 49 kΩcm^2.

The skin resistance also increased over the course of the final 1.4 μA/cm^2 step-change (Interval 3). Immediately after the 1.4 μA/cm^2 signal was applied the skin resistance was 45.6 kΩcm^2. At the end of Interval 3 the resistance increased to

52.8 kΩcm^2. The impedance spectra collected after Interval 3 indicated that the polarization resistance was approximately 51 kΩcm^2. The entire spectrum for each of the four replicates collected was consistent with the Kramers-Kronig relations.

As the magnitude of the step-change was increased to 14 μA/cm^2 for Intervals 4 and 5, the time-dependent trend of the polarization resistance reversed. For example, the skin resistance decreased continuously from 43.7 kΩcm^2 to 39.6 kΩcm^2 during Interval 4. Similarly, the calculated polarization resistance was 44.5 kΩcm^2 as the 14 μA/cm^2 step-change was applied at the start of Interval 5 and 39.5 kΩcm^2 just before the applied current was stopped.

A dramatic reduction in the skin resistance was observed when the 140 μA/cm^2 current was applied during Intervals 6 and 7. At the start of Interval 6, the polarization resistance was 18.4 kΩcm^2. This corresponded to a 61% reduction in the polarization resistance in comparison to the resistance calculated from the final impedance spectra collected after Interval 5. Over the course of Interval 5 the skin resistance decreased continuously to a final value of 11.2 kΩcm^2 just before the current was stopped.

The skin recovered partially while the impedance spectra were collected in between Intervals 6 and 7. For example, the Kramers-Kronig consistent polarization resistance increased from 21.4 kΩcm^2 to 28.6 kΩcm^2 while the skin was allowed to relax at the open-circuit condition. At the start of Interval 7 the skin resistance dropped to 14.8 kΩcm^2. This corresponded to a 48% decrease the skin resistance in comparison to the open-circuit condition. The final skin resistance measurement from the 140 μA/cm^2 current signal was 10.9 kΩcm^2.

The skin resistance estimates from the impedance spectra collected at the open-circuit condition after Interval 7 indicated a partial recovery of membrane properties. For example, the resistance just after the 140 μA/cm^2 current bias was ter-

minated was 17.8 kΩcm^2. The resistance estimated from the last impedance scan measured at the open-circuit condition was 23.2 kΩcm^2.

As the 1.4 mA/cm^2 step-change was applied during Interval 8, the polarization resistance dropped to 3.6 kΩcm^2. While the skin was held at the elevated current the resistance continued to decrease to 2.8 kΩcm^2. The results indicated that the polarization resistance was an order of magnitude lower than the resistance measured in the absence of current.

The calculated polarization resistance data demonstrated that skin behaves nonlinearly in response to current step-changes. The character of the response is related to the magnitude of the applied current. For example, the skin resistance increased while the 1.4 μA/cm^2 step-changes were applied. The potential difference across the skin at this current was always less than 90 mV. This potential difference was less than the proposed threshold for the onset of changes to skin properties.

The skin resistance decreased with time for step-changes larger than 1.4 μA/cm^2. The magnitude and relative degree of the change in resistance was proportional to the applied current. The potential drop across the skin induced by the applied current at amplitudes greater than 1.4 μA/cm^2 was at least 0.55 V. This magnitude of potential difference was above the proposed threshold for the alteration of skin properties. Simply stated, the departure from the linear response was proportional to the amplitude of the current step-change. Where large changes to skin properties were observed, the potential difference across the skin was greater than 250 mV.

8.2.3   Comparison of Responses for Skin Samples 1 and 2.

The response of Skin Samples 1 and 2 to the 14 μA/cm^2 and 140 μA/cm^2 current step-changes were compared. The objective was to determine whether the

amplitude of the applied current was a determinant for the onset of skin property changes. It should be noted that the skin specimens were subjected to 1.4 μA/cm^2 step-changes prior to the collection of the data presented here. The responses of both pieces of skin to the 1.4 μA/cm^2 signals remained constant while current was applied. The impedance spectra collected after the 1.4 μA/cm^2 current step were consistent with the Kramers-Kronig relations which implied that skin properties had not been altered.

The measured potential differences across both skin samples during the application of the first 14 μA/cm^2 step-changes are shown in Figure 8.5(a). The solid red line and dashed blue line correspond to the potential differences across Skin Samples 1 and 2, respectively. The potential responses of Sample 1 decayed in a pseudoexponential manner, whereas the potential remained essentially constant for Skin Sample 2. The magnitude of the potential difference across Skin Sample 2 was less than 100 mV over the course of the entire step-change. In contrast, potential difference across Skin Sample 1 measured during the application of current was greater than 500 mV.

The effect of the current step-changes on each piece of skin was assessed by examining the time dependence of the polarization resistance. The calculated polarization resistance for each piece of skin during the 14 μA/cm^2 step-changes are presented in Figure 8.5(b). The solid triangles and solid diamonds correspond to the resistances calculated from the impedance spectra. As stated earlier, the spectra collected prior to the application of current were consistent with the Kramers-Kronig relations.

The polarization resistance of Skin Sample 1 estimated from the impedance spectrum collected prior to the application of current was 49.9 kΩcm^2. Immediately after the step-change was applied the resistance dropped to 43.7 kΩcm^2 and

decreased exponentially while current amplitude was held at 14 μA/cm^2. The reduction in skin resistance indicated that the epidermis had been altered. These results are consistent with the hypothesis that skin properties begin to change as the membrane potential difference exceeds approximately 250 mV.

The resistance of Sample 2 remained constant at approximately 2.9 kΩcm^2 throughout the entire step-change Interval. The skin resistance calculated from the impedance spectra collected prior to the current step-change was also equal to 2.9 kΩcm^2. The constant resistance observed for Skin Sample 2 implied that the 14 μA/cm^2 current had not altered the macroscopic transport properties of the membrane.

The membrane potential difference of Skin Samples 1 and 2 in response to the 140 μA/cm^2 step-changes is presented by Figure 8.6(a). Similar to the 14 μA/cm^2 results, the potential response of Skin Sample 1 decreased exponentially with time. Although not visible at this scale, the potential across Skin Sample 2 also decayed with time. The magnitude of the membrane potential difference was approximately 300 mV. The variation of resistance with time suggested that the properties of Skin Sample 2 had been altered.

The influence of the applied current on the polarization resistance is shown in 8.6(b). The resistance of Skin Sample 1 dropped from 46.7 kΩcm^2 to 18.4 kΩcm^2 as the 140 μA/cm^2 step-change was applied. The resistance continued to decrease while the skin was subjected to the current. Although not visible at this scale, the resistance of Skin Sample 2 also decayed with time. The resistance changes in both samples occurred while the potential difference across the membrane was greater than 250 mV.

The low-frequency portions of impedance spectra collected after the 140 μA/cm^2 step-changes were not consistent with the Kramers-Kronig relations. The incon-

sistent impedance data indicated that skin properties had been changed. The combination of the impedance and step-change results were consistent with the proposed 250 mV threshold for potential induced property changes. In summary, the properties of heat-separated skin could be altered by the application of current. However, changes were not observed until the potential across the skin exceeded 250 mV.
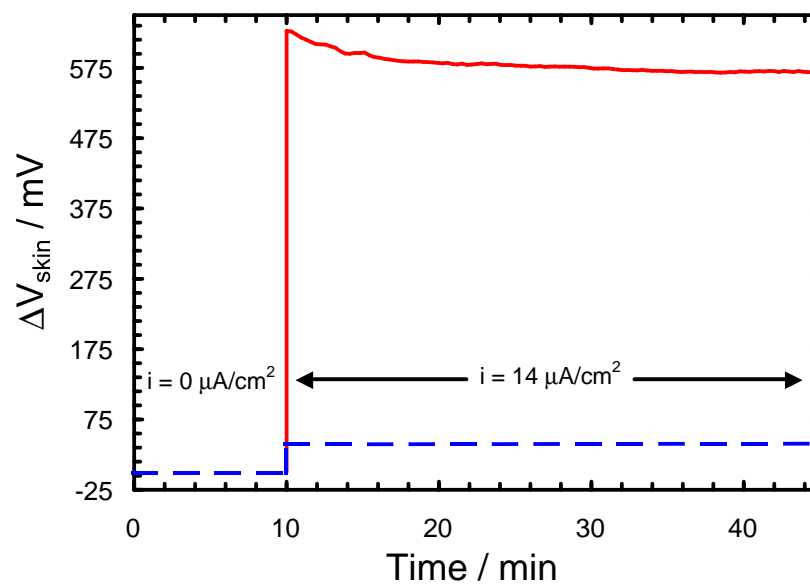
(a)
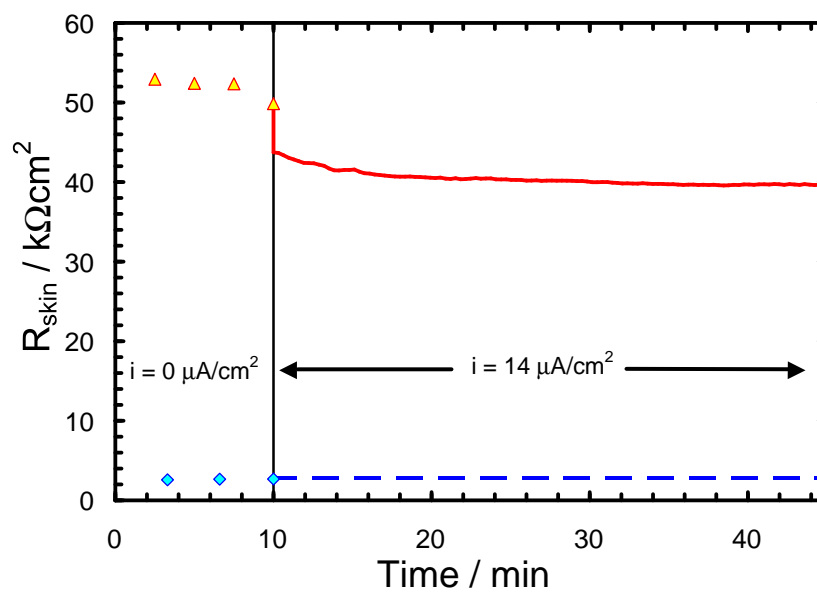
(b)

Figure 8-5: Response of skin samples to 14 μ/cm^2 step-change. The solid red line and dashed blue line represent the responses for the first and second piece of skin. (a) Potential difference across epidermis. (b) Calculated polarization resistance of skin.
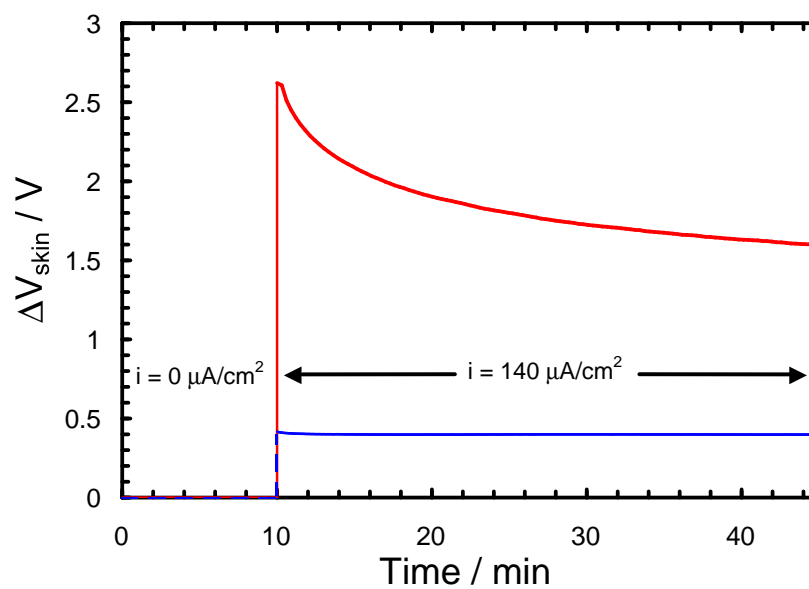
(a)
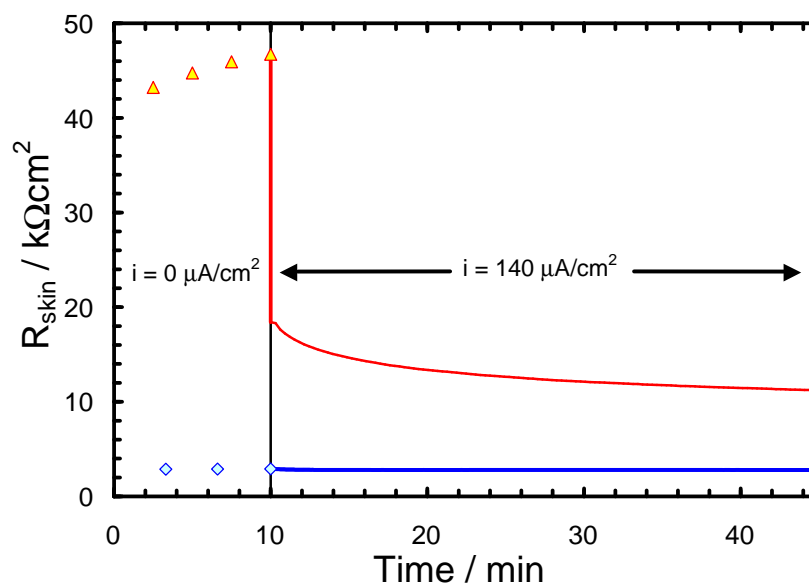
(b)

Figure 8-6: Response of skin samples to a 140 μ/cm^2 step-change. The solid red line and dashed blue line represent the responses for the first and second piece of skin. (a) Potential difference across epidermis. (b) Calculated polarization resistance of skin.

CHAPTER 9
TRANSDERMAL LIDOCAINE FLUX MEASUREMENTS

Prior to the investigation of transdermal lidocaine delivery rates under applied-current conditions, the stability of the dual-beam UV-vis absorption spectroscopy system was characterized. The first part of the study identified the drift in slave and master channels of the dual-beam spectroscopy system (for a more detailed description of the experimental apparatus, please refer to Section 4.4.1). The time dependent behavior of the spectrometers was determined and a strategy was developed to account for the natural drift of the UV-vis apparatus in the light absorbance calculations. Once the temporal characteristics of the measurement system were identified, a calibration curve was developed to relate lidocaine concentration with the absorbance response. Absorbance spectra from a series of lidocaine solutions with concentrations in the range of 0 μM to 1.8 mM were collected. Linear regressions were performed on the absorbance data at selected wavelengths to obtain a family of lidocaine extinction coefficients. The range of concentrations for which the absorbance response obeyed Beer-Lambert theory was determined (for additional discussion, please refer to Section 4.4).

9.1   Spectroscopy System Stability

A series of 51 spectra were collected at three minute intervals over 2.4 hours to identify the stability of the UV-vis light source and the 2 spectrometer channels. For the study, the 2 output fibers of the 100 μm bifurcated cable were connected to the inlet reference and receptor ports of the optically coupled spectroscopy cell. A 200 μm fiber optic cable was connected from the light-path outlets of the optically

coupled spectroscopy cell to the entrance ports of the spectrometer. The master and slave channels measured the light intensity through the reference and receptor compartments, respectively. A schematic of the experimental configuration is provided by Figure 4-5. The integration time required for collection of the spectra was 300 ms.

At the beginning of the experiment three spectra were collected with the light source blocked to determine the baseline response of the spectrometers. The average intensity of the dark spectra was subtracted from the measured intensity of the remaining spectra to calculated the light throughput at each wavelength. For example, the dark-corrected intensity was calculated according to

$$I^*_i = I_i - \bar{I}_{i,dark} \qquad (9\text{-}1)$$

where I_i and $\bar{I}_{i,dark}$ are the measured intensity and the average intensity with the light source blocked at each wavelength.

Mean values of the adjusted intensity were calculated as a function of wavelength from the 51 spectra collected with each spectrometer. The average adjusted intensities for the slave channel and master channel are presented by the filled triangles and filled circles in Figure 9-1. The average intensity for both channels was negligible at wavelengths below 180 nm. The signal response increased from approximately 250 intensity units to 3800 intensity units for wavelengths ranging from 215 nm to 255 nm. The intensity of both spectrometer channels gradually decreased to 1000 intensity units for wavelengths between 255 nm and 475 nm. The intensity of the spectra from both spectrometers displayed similar shape and magnitude over the range of wavelengths studied. The consistency between the two signals suggested that one of spectrometer channels could serve as a reference for system drift.

The measure of system drift was calculated by the percent relative standard deviation. The expression applied here to quantify signal drift was defined by

$$\text{Relative Standard Deviation} = \frac{\sigma(I_i^*)}{\mu(I_i^*)} \times 100\% \qquad (9\text{-}2)$$

where $\sigma(I_i^*)$ and $\mu(I_i^*)$ are the standard deviation and mean value of the adjusted intensity at each wavelength, respectively. The relative standard deviations of the dark-corrected intensities for both spectrometers, shown by empty symbols in Figure 9-1, were also correlated.
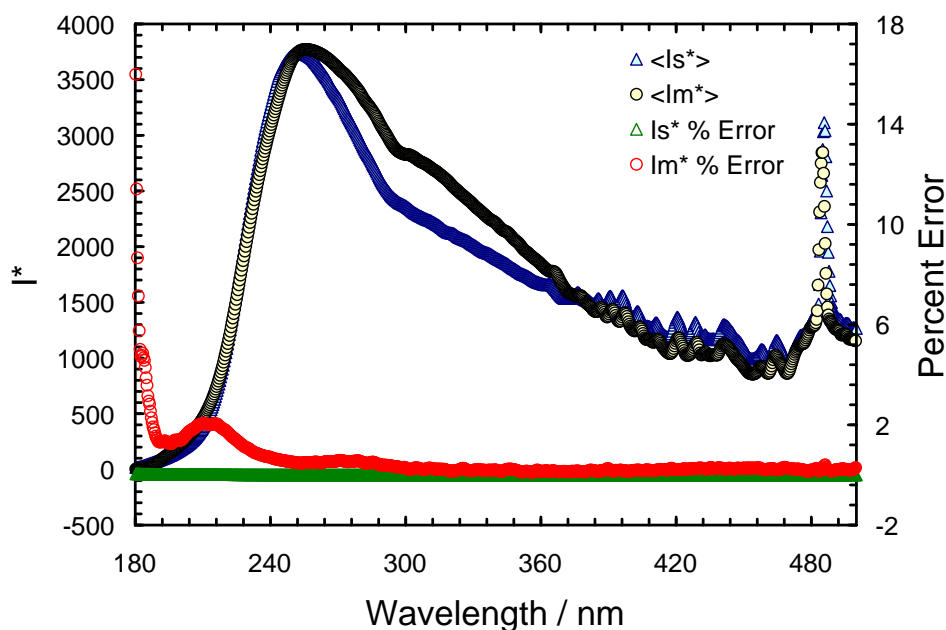
Figure 9-1: Mean values for the dark-corrected transmission intensity spectra collected over 2.4 hours.

The largest relative standard deviations were observed between 180 and 195 nm. The maximum relative standard deviation of the spectra collected on the master channel was equal to 16% of the signal amplitude. The maximum was observed at 180 nm which corresponded to the shortest wavelength of the spectrum. The normalized standard deviation of the master spectrometer decreased rapidly between 180 nm and 200 nm to less than 3% of the dark-corrected intensity. The relative standard deviation of slave spectrometer was less than 3% over the entire

range of wavelengths. The lower relative standard deviations associated with the slave spectrometer indicated that this channel was more stable than the master channel.

Although the stability of the slave spectrometer was greater than the master spectrometer, the error analysis indicated that both light signals through the spectroscopy system were, to a good approximation, stationary over the 2.4 hour collection interval. Since the magnitude and standard deviation of both spectrometers were correlated, the ratio of slave spectrometer and master spectrometer intensities was used to assess reduction in signal intensity during the transdermal iontophoresis experiments. The approach was to monitor the receptor chamber of the diffusion cell with the slave spectrometer. The master spectrometer measured the signal response of UV-vis light through a cuvette of deionized water.

During a typical transdermal iontophoresis study lidocaine is transported from the donor chamber into the receptor compartment of the optically coupled spectroscopy cell. As lidocaine accumulates in the receptor compartment, the intensity of the slave channel will decrease in response to the addition of the chromophore. In contrast, deionized water does not absorb light in the UV-vis portion of the electromagnetic spectrum. Therefore, changes in signal intensity measured by the master spectrometer were caused by random fluctuations or by a shift in the baseline response of this channel. The ratio of the two signals acted as a filter for the nonstationary component of the measurement.

The ratios of the dark-corrected intensity signals from each spectrometer were calculated for all of the spectra collected in the study. The relative standard deviation and mean values from the adjusted intensity are presented as a function of wavelength in Figure 9-2. The standard deviation of the intensity ratio exhibited a maximum value of at 180 nm which corresponded to 10% of the signal magnitude.

The relative standard deviation decreased sharply and continuously between 180 nm and 200 nm to 3% of the intensity ratio. For wavelengths longer than 210 nm, the relative standard deviations of the intensity ratio were less than 1% of the signal. In general, the standard deviations of the intensity ratio were between the deviations of the slave and master spectrometers shown in Figure 9-1. The result was not surprising since the stability of the intensity ratio should be weighted by the error contributions from each channel.
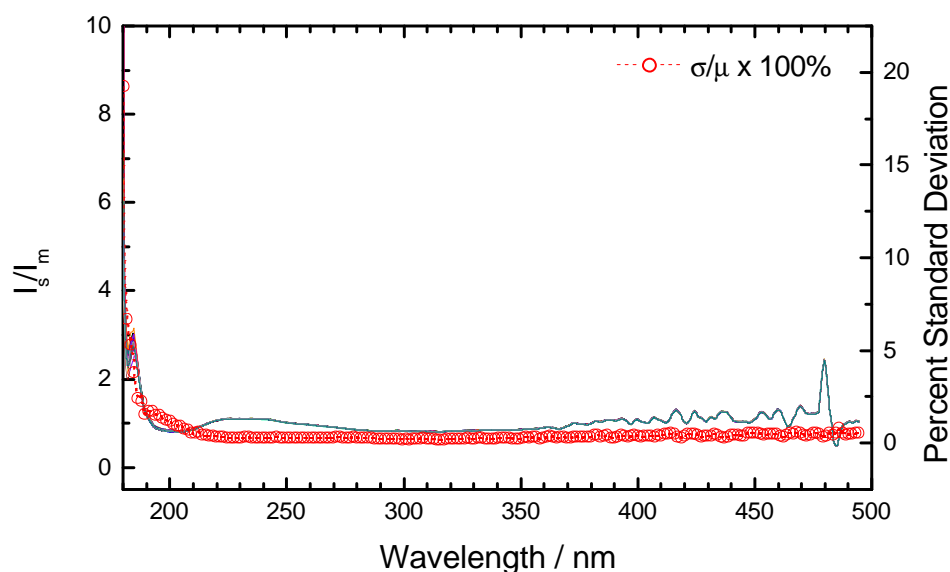
Figure 9-2: Ratio of slave and master spectrometer transmission intensities.

The error analysis described above demonstrated that the ratio of the light intensity signals collected from each spectrometer could account for the natural evolution of the measurement system. Therefore, the intensity ratio was used to calculate the lidocaine extinction coefficients and to determine the delivery rates of lidocaine by transdermal iontophoresis.

9.2   Lidocaine Calibration Study.

The results from the calibration experiments for relating lidocaine concentration to the signal intensities of the absorbance spectrometers are presented here.

Lidocaine extinction coefficients were calculated according to Beer-Lambert the-
ory.[243] According to the theory, the extinction coefficient is a linear proportional-
ity constant which relates chromophoric concentration to light absorbance magni-
tude (for a more complete discussion of the subject, please refer to Section 4.4). In
practice, the absorbance response is linear over a limited range of chromophoric
concentrations. The linear response range for this system was determined experi-
mentally by collecting spectra from a series of solutions with known lidocaine con-
centrations. The concentration of the lidocaine solutions was varied incrementally
between 0.5 μM and 1.8 mM. The optically coupled diffusion cell was monitored
by the slave channel and the reference cuvette, filled with deionized water, was
monitored by the master channel. Three spectra were collected for each lidocaine
concentration.

The analysis presented in Section 9.1 indicated that the drift in the 2 spectrom-
eters was correlated. The absorbance for the dual-beam system at a given wave-
length is defined by

$$A^* = \log_{10}\left(\frac{I_{s,0} - I_{s,dark}}{I_{m,0} - I_{m,dark}}\right) - \log_{10}\left(\frac{I_s - I_{s,dark}}{I_m - I_{m,dark}}\right) \tag{9-3}$$

where the first logarithmic term corresponds to the intensity ratio of the two spec-
trometers at zero concentration. The second logarithmic term is the ratio of dark-
corrected signal intensities at a given lidocaine concentration. The difference be-
tween the logarithmic ratios yields an absorbance which accounts for the time
dependent signal drift.

9.2.1 Comparison of Absorbance Spectra.

The family of calculated absorbance spectra from the calibration study are pre-
sented in Figure 9-3. The absorbance increased significantly as the lidocaine con-
centration was increased for spectral wavelengths between 210 and 280 nm. The

change in absorbance at low lidocaine concentrations was greatest in the 215-230
nm portion of the spectra. For lidocaine concentrations greater than 200 μM a
broad, secondary absorbance peak developed in the 240-275 nm region of the absorbance spectra.
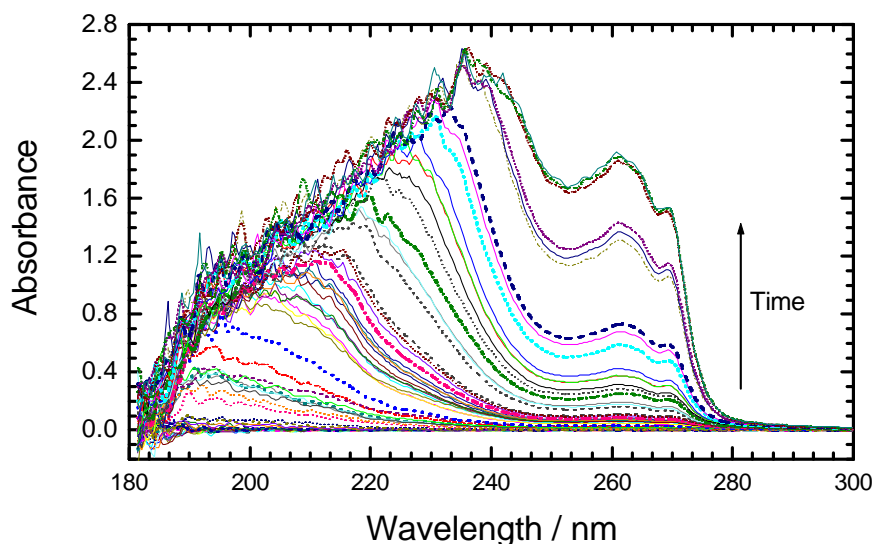
Figure 9-3: Normalized absorbance spectra for calibration of lidocaine concentration.

As the concentration of lidocaine was increased, the absorbance measurements
became scattered near the maximum absorbance of a given wavelength. The randomly distributed data points were located at wavelengths between 180 and 240
nm. The scattered absorbance values were first observed at the shortest wavelengths when the lidocaine concentration was below 25 μM. Randomly distributed
absorbance values appeared at longer wavelengths as the chromophoric concentration was increased.

The scattered absorbance data was caused by the reduction of the light throughput intensity of the receptor chamber to the dark signal amplitude. As the effective
signal intensity was equal to zero, the addition of more chromophore to the system could not change the absorbance response. Variations in the absorbance after

the light throughput signal had been extinguished, were proportional to the noise level of the measurement.

9.2.2 Determination of Lidocaine Extinction Coefficients.

As stated above, extinction coefficients can, in principle, be calculated directly by dividing the measured absorbance response of a chromophore by its concentration. The absorbance for this system was a function of electromagnetic radiation wavelength. Therefore, a spectrum of wavelength-dependent extinction coefficients was calculated according to the methodology described above. The accuracy of the extinction coefficients was assessed by dividing selected absorbance spectra with known lidocaine concentrations by the spectrum of calculated extinction coefficients. The approach yielded a family of lidocaine concentrations which were a function of wavelength. The standard deviation of the lidocaine concentrations was greater than the mean value for some of the spectra; therefore, an alternative methodology was developed to determine the extinction coefficients.

The approach used and this work to identify the linear response range plot the absorbance at a given wavelength as a function of lidocaine concentration and subsequently regressing a line to the data to calculate the extinction coefficient. The calculated absorbance at selected wavelengths is presented as a function of lidocaine concentration in Figure 9-4.

The absorbance data for a given wavelength demonstrated a bimodal linear profile. Alternatively stated, there were two regions of linearity with differing slopes. For example, a linear relationship was observed for the absorbance measurements corresponding to lidocaine concentrations less than 200 μM. At higher concentrations the data points were also linear, however, the slope was greater than the slope for low-concentrations. The data analysis toolbox of Microsoft Excel$^{\copyright}$ was used to regress a linear model to the absorbance data. The slope of
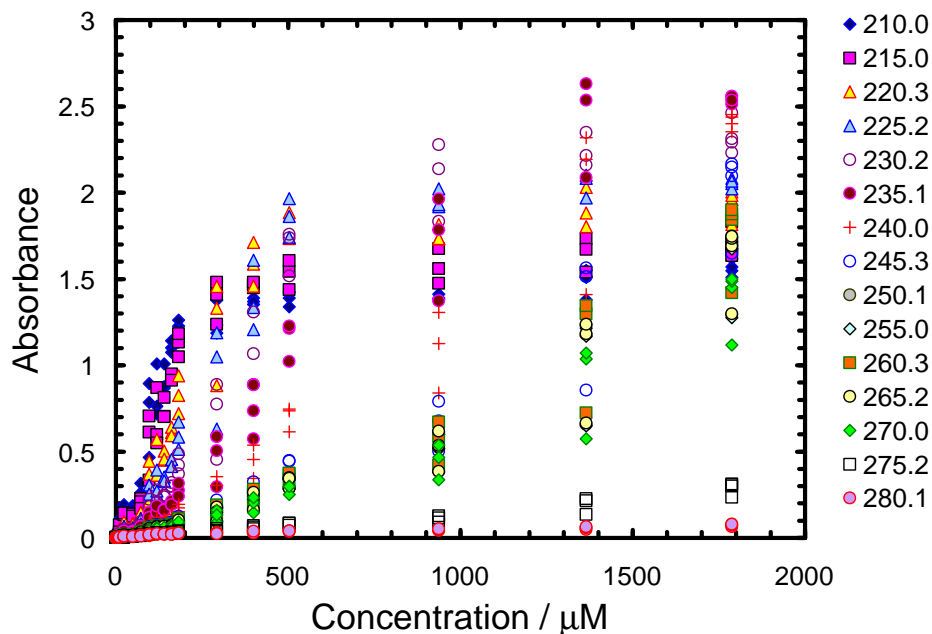
Figure 9-4: Absorbance as a function of lidocaine concentration at selected wavelengths.

the line drawn through the absorbance response for a given wavelength corresponded to the extinction coefficient. Since the absorbance should be zero in the absence of a chromophore, the x-intercept of the line should be zero for a properly calibrated system.

Regression of a linear model to the entire collection of absorbance-concentration data was intractable because of the bimodal structure described above. The alternative regression strategy implemented here, involved dividing the absorbance-concentration data set into two portions. For example, separate regressions were performed on the absorbance measurements corresponding to lidocaine concentrations up to 200 μM and for the data set associated with concentrations greater than 200 μM. The concentration ranges associated with the truncated data sets roughly corresponded to the two regions of linearity observed in the complete collection of absorbance-concentration data.

The regression parameters corresponding to absorbance data corresponding to lidocaine solutions with concentrations greater than 200 μM are shown in Table 9-1.

Table 9-1: Regression parameters for calculation of extinction coefficients from absorbance data of lidocaine solutions with concentrations greater than 200 μM

Wavelength / nm	Slope (ϵ) / M^{-1}	Intercept	r^2
210.0	160.17	1.2684	**0.7099**
215	189.57	1.3816	**0.6288**
220.3	340	1.3973	**0.5079**
225.2	557.93	1.21	**0.5615**
230.2	942.18	0.8444	**0.7407**
235.1	1376.3	0.2793	0.9089
240	1431.2	-0.1127	0.9407
245.3	1201.8	-0.2439	0.9169
250.1	960.57	-0.2026	0.9086
255	951.67	-0.2019	0.9072
260.3	1047.2	-0.2187	0.9113
265.2	960.8	-0.1991	0.9094
270	822.94	-0.1645	0.9096
275.2	156.46	-0.0067	0.9119
280.1	28.544	0.0215	0.9101

The columns of the table correspond to radiation wavelength, slope, which is equivalent to the extinction coefficient, x-intercept and linear correlation coefficient, respectively. The r^2 values from the model fits to the absorbance data corresponding to wavelengths shorter than 235 nm, as indicated in bold, were less than 0.9. The relatively small magnitude of the correlation coefficients indicated that the linear model provided poor fits to the shorter wavelength data. This implied that corresponding extinction coefficients data should not be included in the estimation of lidocaine concentrations greater than 175 μM. In contrast, the r^2 parameters for wavelengths greater than 235 nm all exceeded 0.9. The large r^2 values for wavelengths between 235 nm and 280 nm implied that the extinction coefficients associated with these longer wavelengths were suitable for calculating a lidocaine concentrations greater than 175 μM.

A second family of extinction coefficients was determined by regressing the linear model to the absorbance data obtained from the lidocaine solutions with concentrations from 0 μM to 200 μM. The model was regressed to the absorbance

Table 9-2: Extinction coefficients and regression parameters calculated from absorbance data of lidocaine solutions with concentrations less than 175 μM

Wavelength / nm	Slope (ϵ) / M^{-1}	Intercept	r^2
210.0	6833.9	-0.0341	0.9513
215	5912	-0.046	0.9431
220.3	4036.2	-0.0358	0.9232
225.2	2859.8	-0.0263	0.9243
230.2	2054.9	-0.0172	0.9278
235.1	1339.2	-0.0094	0.9305
240	854.68	-0.0046	0.9449
245.3	558.9	-0.0018	0.9549
250.1	466.95	-0.001	0.9599
255	465.63	-0.0011	0.9567
260.3	506.43	-0.0017	0.957
265.2	479.95	-0.0027	0.9538
270	433.01	-0.0014	0.9566
275.2	210.28	0.0002	0.9663
280.1	143.76	0.0016	0.9277

data at the same wavelengths analyzed for the high-concentration solutions. The model parameters retained from the low-concentration data set are presented in Table 9-2.

The minimum correlation coefficient associated with the low-concentration spectra was 0.948 which corresponded to the 225 nm absorbance data. The large correlation coefficients associated with this data indicated that of the model fits were good. The largest magnitude of the intercepts was 1.19x10^{-2} which corresponded to the 220 nm absorbance data. In general, the x-intercepts were at least four orders of magnitude smaller than the extinction coefficient. The excellent fitting characteristics of the regression parameters implied that the entire collection of calculated extinction coefficients was suitable for for calculating lidocaine concentrations from absorbance spectra. The results were consistent with a properly calibrated absorption spectroscopy system.

Since two regions of linearity, corresponding to low-concentration and high-concentration lidocaine solutions, were observed in the absorbance data, a two-

step procedure was developed for calculating lidocaine concentrations from the coupled spectroscopy transdermal delivery studies. While the predicted lidocaine concentrations were less than 200 μM the family of extinction coefficients listed in Table 9-2 were used. Once the concentration exceeded 200 μM the extinction coefficients in Table 9-1 were selected for calculating lidocaine concentrations. The strategy provided for the determination of receptor compartment lidocaine concentrations in the range of 0.5 μM to 1.8 mM.

An alternative presentation of the extinction coefficients obtained from the two-step regression procedure is shown in Figure 9-5. The extinction coefficients associated with the low-concentration and high-concentration data sets are indicated by the filled triangles and open circles, respectively. The plot was intended to provide a graphical illustration of the distribution of lidocaine extinction coefficients. The general structure of the two groups was similar for wavelengths longer than 235 nm.

In the shorter wavelength regions of Figure 9-5 the extinction coefficients from the to data sets diverged. For example, the low-concentration data trended downwards with increasing wavelengths, whereas, the high-concentration values increased. The detailed analysis of the regression parameters described above made it possible to determine that the short wavelength extinction coefficients associated with the high-concentration measurements were not appropriate for calculating lidocaine concentrations.

The calibration procedure described here increased the range of lidocaine concentrations for which the absorbance response obeyed Beer-Lambert theory by a factor of 7 in comparison to earlier work.[164] The expanded concentration range for the linear absorbance response suggested that the addition of the secondary reference cell had properly accounted for system drift.
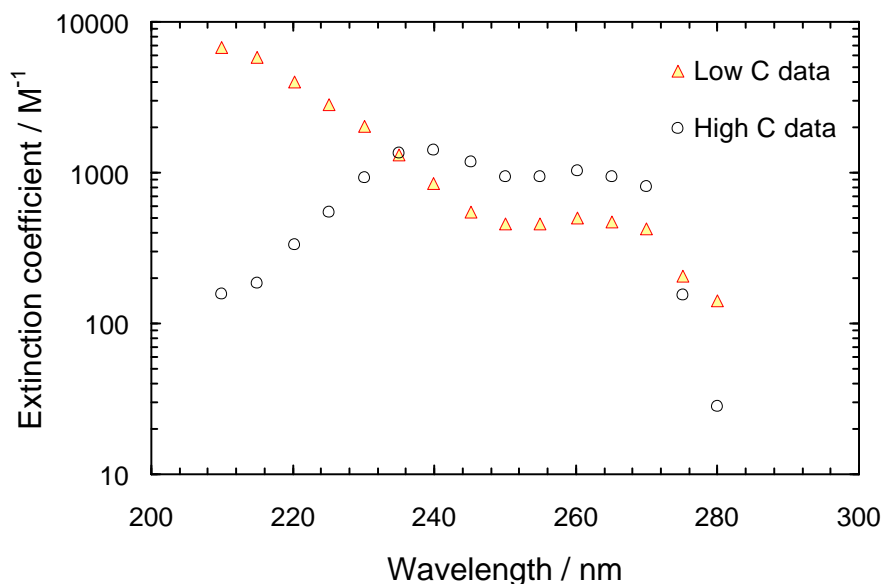
Figure 9-5: Dependence of calculated extinction coefficient on light wavelength. The solid triangles and open circles correspond to the calculated extinction coefficients

9.3   Absorbance Changes from Skin Species

The methodology described in Section 4.4.3 was applied for the experiments presented here. In previous optically coupled transdermal flux experiments a broad secondary absorbance peak was observed at wavelengths between 240 nm and 300 nm.[164] The secondary peak was not observed in the lidocaine calibration studies for that work. Therefore, it was concluded that chromophoric species were emanating from the skin. The object of this work was to determine the time dependent absorbance response of excised human epidermis in the absence of electrical current. The idea was to extract the contribution of skin chromophores to the overall absorbance response of the transdermal iontophoresis experiments. The methodology used here made it possible to determine whether the broad secondary peak observed at longer wavelengths in the earlier work was a reproducible phenomena.

The skin absorbance spectra from the hydration study are presented in Figure 9-6. The largest absorbance response occurred at wavelengths below 220 nm. The

data points were discontinuous and randomly distributed for this range of wave-lengths. The behavior was similar to the results described in Section 9.2 when the light throughput signal at a given wavelength was extinguished. The absorbance was essentially zero at wavelengths greater than 320 nm.
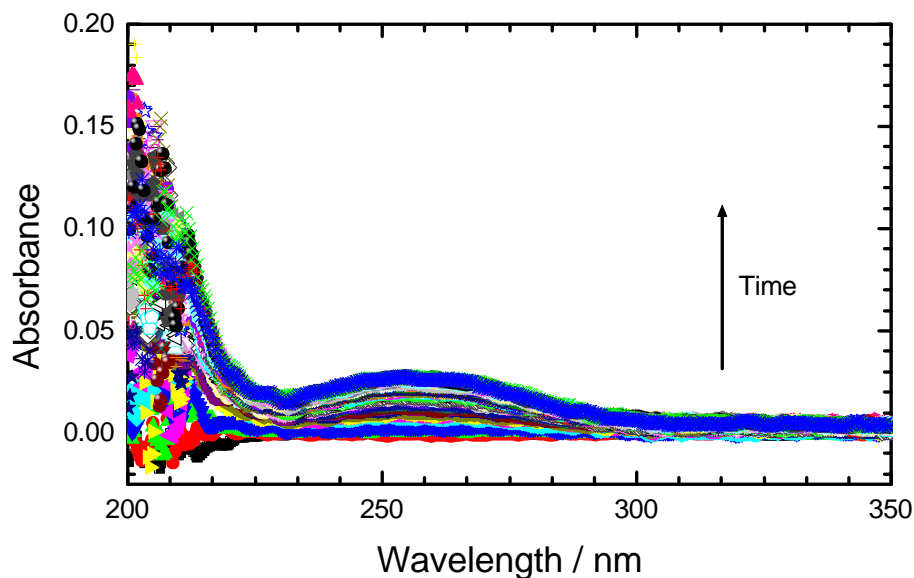
Figure 9-6: Absorbance spectra of skin immersed in buffered NaCl solution.

As the skin was soaked in the electrolyte a broad absorbance peak appeared between 225 nm and 320 nm. The maximum absorbance was 0.03 corresponding to a wavelength of 262 nm. The maximum absorbance represented a 6% change in the signal response over the course of 2.5 hours. In comparison, the absorbance from the lidocaine calibration experiments exceeded 0.03 when the chromophoric concentration was greater than 75 μM. If the lidocaine flux is large enough during transdermal iontophoresis the contribution of the skin chromophores to the overall absorbance response should be negligible. Although, it is possible that current could enhance the diffusion rate of chromophoric compounds from the skin.

An experiment was conducted where skin was subjected to a -500 μA/cm^2 for 30 minutes. For the study, NaCl electrolyte was inserted in both chambers of the

diffusion cell. The skin sample was soaked in the electrolyte for 30 minutes before current was applied. Although not presented here, the maximum absorbance at wavelengths between 225 nm and 320 nm was approximately 0.02. The rate of absorbance change in this portion of the spectra was uniform regardless of whether current was applied.

A 50% increase in absorbance was observed in the spectra collected after current was terminated. The results suggest that the chromophoric skin species were diffusing back into the donor chamber by either migration or electroosmosis in response to the electric field. As the potential difference across the skin was greater than 5 V it is quite likely that the skin had been altered by the applied DC current. Upon termination of the current, the electric field began to relax and skin chromophores were free to diffuse into the receptor chamber. Despite the increase in absorbance associated with the application of current, the relative magnitude was negligible in comparison to the absorbance response observed in the calibration studies when the lidocaine concentration exceeded 100 μM.

9.4 Transdermal Delivery of Lidocaine by Iontophoresis

A preliminary experiment was performed to verify the efficacy of the coupled spectroscopy approach for measuring transdermal delivery rates of lidocaine under iontophoretic conditions. The methodology described in Section 9.4 was applied for this work. The temporal sequence of the applied currents for the investigation is listed in Table 9-3.

The 60 absorbance spectra obtained from the transdermal iontophoresis study are illustrated in Figure 9-7. The absorbance response between 200 and 280 nm is presented because significant differences in signal intensity were not detected at other wavelengths. In general, the absorbance increased with time where the rate of change depended on wavelength and magnitude of applied current. The trends

Table 9-3: Optically coupled spectroscopy experiment settings

Time / min	Current / mA/cm^2	Comments
0-9	0	Skin Hydration
10-35	0	Lidocaine Added
35-67	0.71	Current On
67-86	0	Current Off
86-111	1.4	Current On
111-134	2.8	"
134-181	5.6	"

observed in the data were consistent with transport of the lidocaine chromophore across skin.
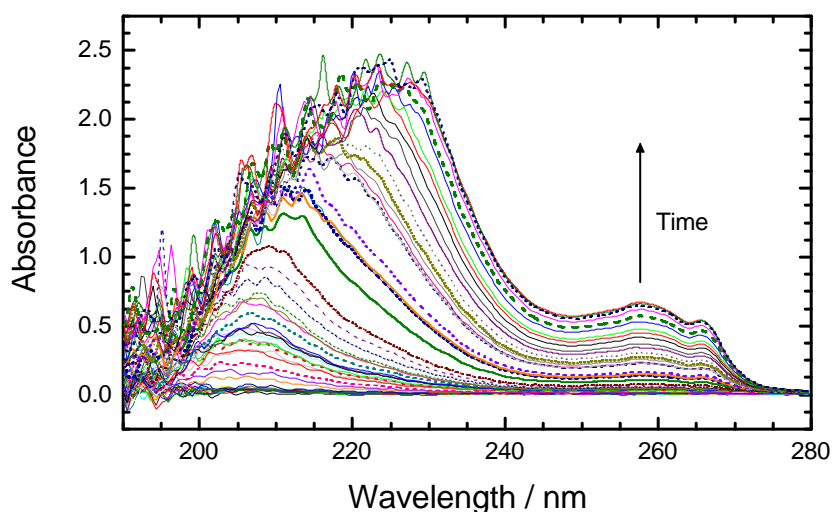
Figure 9-7: Evolution of the absorbance response during the transdermal iontophoresis experiment.

A specific feature of the spectral data set was that the absorbance response remained constant over the first 50 minutes of the experiment. After the initial stationary period, the signal intensity began to increase with time at wavelengths between 200 and 220 nm. The change in absorbance response corresponded to a 15 minute delay between the application of the 0.71 μA/cm^2 current bias and the detection of lidocaine. The results suggest that the skin had not become fully saturated with the lidocaine chromophore during the passive ($i_{applied}$=0 μA/cm^2) segment of the experiment.

The evolution of the absorbance spectra associated with remainder of the experiment is not described because specific trends are difficult to identify at the scale presented in Figure 9-7. Instead, macroscopic transport quantities, such as lidocaine concentration and transdermal flux, were calculated using Microsoft Excel© spreadsheet software. For example, the absorbance at selected wavelengths of each spectra were divided by the extinction coefficients calculated in Section 9.2.2 to determine lidocaine concentration. The procedure was repeated for each spectra to produce a family of 60 chromophore concentrations which were a function of time. The calculated lidocaine concentration profile is presented by the open circles in Figure 9-8. The red line corresponds to a combination of linear and parabolic fits to the data. A general trend of increasing concentration with time was observed. The relative degree of change was proportional to the amplitude of applied current. The trends indicated that lidocaine was being transported across the skin by the current.

The concentrations calculated according to Beer-Lambert theory were subsequently used to estimate lidocaine flux. For example, the average lidocaine flux over the time interval required to collect two spectra was calculated by

$$N_i(t) = \frac{\Delta c_i}{\Delta t} \frac{V}{A} \tag{9-4}$$

where V is the receptor cell volume, A is the cross-sectional area of skin available for transport, and Δc_i is the change in chromophore concentration over the time interval, Δt. Lidocaine fluxes were calculated for all successive pairs of absorbance spectra.

Some of the estimated fluxes were found to be negative, especially during the first 85 minutes of the study. This time period corresponded to the skin hydration, the first iontophoretic (i_{app} = 0.71 μA/cm^2) and the subsequent passive diffusion portions of the investigation. The relatively small changes in the absorbance spec-
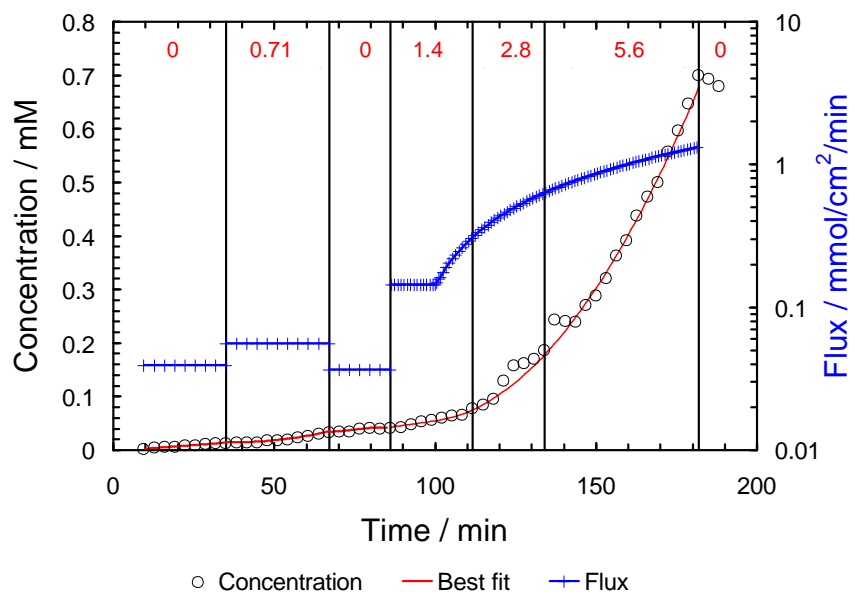
Figure 9-8: Temporal evolution of the calculated lidocaine concentration and flux in the receptor cell.

tra were in agreement with the small driving forces for transdermal transport. As transport was unfavorable at these experimental conditions, it is reasonable to assume that changes in the absorbance signal were primarily caused by random fluctuations in the spectrometer. The stochastic errors associated with these spectra would then propagate through to the concentration and flux calculations. The negative fluxes observed at the start of the experiment are consistent with this assumption.

Although negative fluxes were calculated from the low-current iontophoretic spectra, lidocaine concentration generally increased over the entire interval; therefore, the average flux over the entire observational period was calculated rather than over the shorter time intervals corresponding to the collection of successive spectra. During the latter portions of the experiment when the iontophoretic current amplitude was greater than or equal to 1.4 μA/cm^2 the absorbance increased

more rapidly from spectrum-to-spectrum which was consistent with increased transdermal lidocaine transport. Furthermore, the large relative changes in absorbance associated with these experiments helped to improve the signal-to-noise ratio of the measurement.

The flux profiles, as calculated by Equation (9-4) are presented by the solid lines with vertical cross marks in Figure 9-8. The magnitude of lidocaine flux is denoted by the right-hand ordinate of the plot. The flux was approximately 30-40 μmol/cm^2/min during the passive portion of the experiment when the iontophoretic current was 0 mA/cm^2. As the current was increased to 0.71 mA/cm^2, the flux increased instantaneously to approximately 55 μmol/cm^2/min. The flux then decreased to 30 μmol/cm^2/min during the recovery period after the first interval of iontophoretic transport. The slight increase in delivery rate during the 0.71 mA/cm^2 current application cycle suggested that the iontophoresis protocol had enhanced the transport of lidocaine.

The transdermal lidocaine flux increased significantly during the 1.4 mA/cm^2 iontophoresis treatment interval. For example, a uniform delivery rate of approximately 150 μmol/cm^2/min was observed for the first twelve minutes of 1.4 mA/cm^2 applied current. The flux over the remainder of this treatment cycle increased continuously to a final amplitude of 340 μmol/cm^2/min. The fluxes associated with this portion of the experiment were, at a minimum, three times larger than the lidocaine delivery rates measured during the 0.71 mA/cm^2 iontophoretic segment of the study. Alternatively stated, the magnitude of lidocaine flux had tripled by doubling the current.

The transdermal delivery rate of lidocaine also increased continuously from 340 μmol/cm^2/min to 1.3 mmol/cm^2/min over the course of the 2.8 and 5.6 mA/cm^2 current treatments. The flux measurements indicated that the application of cur-

rent increased the transdermal flux of lidocaine; however, the delivery rates were not controlled at a constant level.

Skin polarization resistance was selected as a simple parameter to evaluate the influence of the applied currents on membrane transport properties. The profiles corresponding to skin polarization resistance and transdermal lidocaine flux are presented in Figure 9-9. The solid yellow circles and the solid lines correspond to the polarization impedance measured by impedance spectroscopy and by the Solartron 1286 potentiostat, respectively. The blue lines with vertical hash marks signify the transdermal delivery rates of lidocaine.
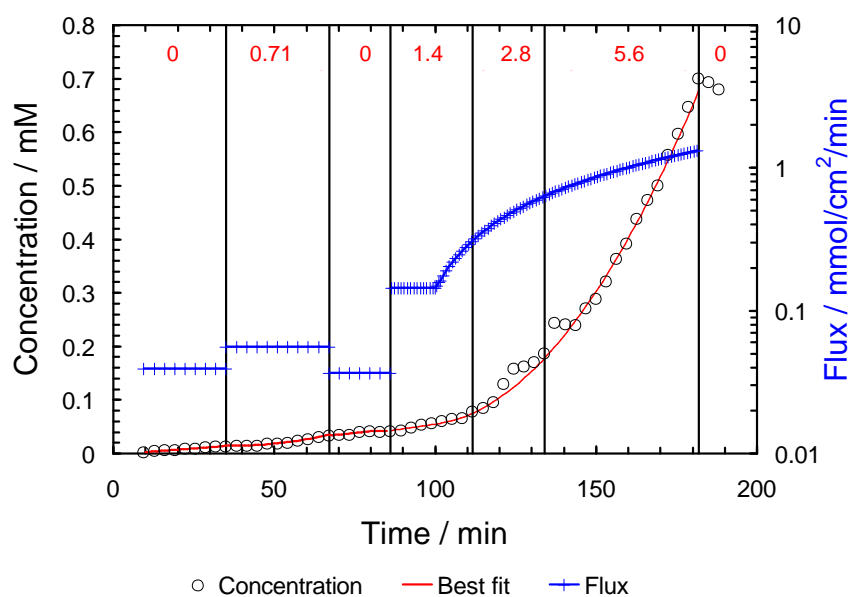
Figure 9-9: Temporal evolution of skin polarization resistance and transdermal lidocaine flux.

The polarization resistance of skin was approximately 400 kΩ/cm^2 at the start of the experiment. As the 0.71 mA/cm^2 iontophoretic current was applied, the resistance decreased by over an order of magnitude to approximately 20 kΩ/cm^2. Over the course of this transdermal iontophoresis treatment cycle, skin resistance

dropped to 15 kΩ/cm^2. The transdermal voltage difference associated with the 0.71 mA/cm^2 current also decreased from 14 V to approximately 12 V. It is likely that the large potential differences induced by the current altered the properties of the skin. The transdermal voltage differences measured in this work were well above the threshold for potentially induced changes in skin properties observed in Sections 5.2 and 8.1 of this work and reported in the literature.[3]

The impedance spectra collected after the 0.71 mA/cm^2 current bias was terminated, indicated that skin polarization resistance increased from 60 kΩ/cm^2 to 100 kΩ/cm^2. The resistance associated with the third impedance spectrum was approximately one-fourth of the magnitude measured at the beginning of the experiment. The slow and incomplete recovery suggested that the changes in skin properties were not completely reversible over the time scale of over this portion of the experiment.

The application of the 1.4 mA/cm^2, 2.8 mA/cm^2, and 5.6 mA/cm^2 iontophoretic currents caused the polarization resistance of skin to decrease to approximately 10, 5, and 2 kΩ/cm^2, respectively. The trend represented a simple linear relationship between current amplitude and skin polarization resistance. The relative reductions in skin resistance were approximately a factor of 5 smaller than decrease associated with the 0.71 mA/cm^2 and 1.4 mA/cm^2 currents. The combined results suggest that there is an asymptotic limit for the reduction of skin polarization resistance under the influence of applied current.

The lidocaine fluxes observed in this work were approximately an order of magnitude smaller than the delivery rates reported in the literature under similar experimental conditions.[143] The discrepancy in the results can be partially explained by the higher lidocaine concentration (10 mM) and lower pH (4.5) of the donor compartment solution used for that study. For example, the lower

pH would increase the concentration of ionic lidocaine which would improve the transport efficiency of the iontophoretic current.

The transdermal delivery rates of lidocaine reported by Philbrick were several orders of magnitude lower than the fluxes measured in this work.[164] The range of applied-current biases for this investigation was in agreement with clinical therapeutic protocols; however, the iontophoretic currents were approximately two orders of magnitude larger than for the study described above. In addition, the potential difference across the skin for the experiments was at least 14 V which was well above the threshold for changes to the membrane transport properties.[3] Therefore, the enhanced iontophoretic delivery of lidocaine observed here was probably caused by a coupling of these two effects.

In summary, the work presented here indicates that the coupling of UV-vis absorption spectroscopy with electrochemical impedance spectroscopy can be a potentially useful methodology for studying transdermal iontophoresis. Electrochemical impedance spectroscopy provided for the measurement of skin electrical and transport properties and UV-vis absorbance spectroscopy provided for the measurement of transdermal lidocaine flux. In the previous chapters it was shown that electrochemical impedance spectroscopy is a robust technique for monitoring skin properties. The first three sections of this chapter demonstrated that the dual-beam UV-vis spectroscopy system developed for this work was properly calibrated.

The transdermal iontophoresis experiments presented above are preliminary results which clearly demonstrate that the application of electrical current increases transdermal lidocaine flux. The difficulty in obtaining constant transdermal delivery rates during iontophoresis may have been associated with the limitations in the potentiostat for driving controlled currents at large potentials. For example,

the voltage difference across the skin induced by the iontophoretic current was between 12 and 14 volts. This corresponds to the upper stability limit of the 1286 potentiostat. Although the potentiostat reported current was being delivered at the prescribed level, it is likely that the signal-to-noise ratio of the current signal was not optimal. Recommendations are provided in Chapter 13 to improve the accuracy of the optically coupled spectroscopic measurements.

CHAPTER 10
MATHEMATICAL MODEL OF TRANSDERMAL IONTOPHORESIS

A mathematical model was developed to simulate steady-state transdermal iontophoresis. Under the assumption that the stratum corneum is the dominant barrier to transdermal drug delivery, only the macroscopic transport properties of this section of the epidermis were considered. For example, the low permeability, high electrical resistance and negative background charge of the stratum corneum were explicitly incorporated into the model. The system geometry was designed to mimic iontophoretic transport within the experimental diffusion cell. A nice feature of the model presented here is that it can be adapted to simulate clinical iontophoretic systems by adjusting the input parameters.

The objective of this work was to calculate the influence of controlled variables on the concentration, flux and potential profiles within the skin. This work was intended to provide insight into the influence of skin properties, such as background charge, on the transport process. Results from the model simulations were also compared with the fluxes obtained from UV-vis absorption spectroscopy experiments.[164] The transdermal iontophoresis simulation results are presented in Chapter 11.

10.1   System Description

The simulated transdermal iontophoresis system consisted of three distinct regions: a donor solution, the skin and a receptor solution. The dimensions of the simulated system were consistent with the experimental apparatus. For example, the receptor and donor compartments were 2 cm long and the skin was mod-

eled as being 20 μm thick. A schematic of the simulated system is provided by Figure 10-1.
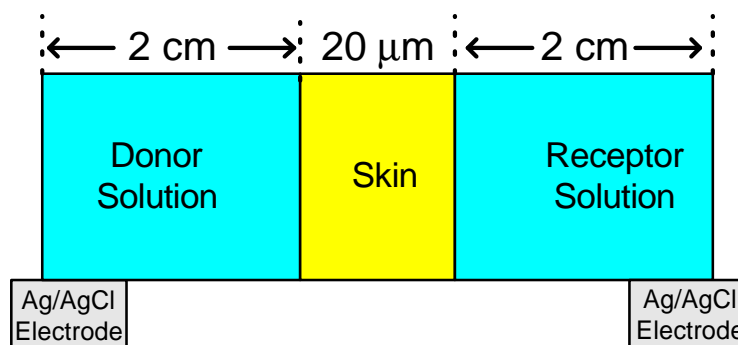
Figure 10-1: Dimensions of the simulated system for transdermal iontophoresis. Figure not to scale.

The governing equations for each region were formulated to reflect the physical characteristics of the system. For example, the skin was assumed to consist of a uniformly charged barrier. The diffusion path length through the skin was assumed to be longer than the thickness of the membrane due to the highly complex structure of the membrane.[256,257] A tortuosity factor was introduced into the governing equations to account for the extended path length.[258] The diffusion coefficients of all ionic species were reduced by the tortuosity.

The ionic selective character of the skin was therefore associated solely with the tendency for exclusion of ionic species of like charge. Under conditions of iontophoretic operation, therapeutic agents are driven from the donor solution to the receptor solution. The boundaries of the system represent the Ag/AgCl working electrodes that drive current through the system. The total current throughout the system was assumed to be uniform.

The governing equations for the model were derived from macroscopic transport theory for dilute solutions.[136] These equations are discussed in more detail in the Governing Equations section of this chapter. The flux of ionic species accounted for transport by migration and diffusion. The model is general in the

sense that it can account for any number of ionic species. Partial dissociation of ionic species was described by equilibrated homogeneous reactions. In this way, dissociation of water and buffers was treated explicitly.

The species present in the simulated system were Ca^{2+}, Na^+, Cl^-, H^+, OH^-, lidocaine cation, dissociated HEPES buffer anion, undissociated HEPES buffer and the fixed negative charge sites within the skin. The inorganic species correspond to the major ionic components present in the human body.[246] In addition, the charge of the skin was treated to be an immobile ionic species. Local electroneutrality was assumed to apply. The list of dependent variables included the concentration of each species and the electrical potential. Thus, for n independent species, a set of n+1 nonlinear ordinary differential equations and algebraic equations were solved using a Newton-Raphson iterative scheme.

10.2 Boundary Conditions

The boundary conditions in the donor and receptor phases required that the concentrations of the species approached the bulk values. Continuity of concentration and flux was assumed to apply at the boundaries between regions. Potential was specified at the donor boundary. The boundary conditions correspond to the location of the electrodes. The electrodes used to drive current through the skin were assumed to be Ag/AgCl, which is reversible to the chloride ions. Since chloride ions were the only species reacting at the electrodes, chloride was the only species with a nonzero flux at the electrode. The heterogeneous reaction at the anode was

$$Ag + Cl^- \rightarrow AgCl + e^- \tag{10-1}$$

 where silver was oxidized. The boundary condition at the cathode corresponded to the reduction of the silver ion. The cathodic reaction is described by

$$AgCl + e^- \rightarrow Ag + Cl^- \tag{10-2}$$

The relationship describing the flux of chloride ions at the electrode surface is presented by

$$N_{Cl^-} = \frac{i_{total}}{F z_{Cl^-}} \tag{10-3}$$

where i_{total} is the applied-current density. The boundary condition states that all of the current was carried by the flux of chloride ions at the electrode.

10.3 Bulk Solution Compositions

The composition of the donor solution can have a significant influence on the transport rates of the therapeutic agent.[148,81,170,259] In this region there are relatively high concentrations of the active agents. This allows for flexibility in evaluating the transport rates of a variety of different active species. Therapeutic compounds will often have molecular weights that are orders of magnitude larger than the ions used included in this model. To compensate for the disparity in molecular weights a model drug species was selected with a diffusion coefficient an order of magnitude lower than the remaining species.

The bulk concentrations of ionic species present in the donor solution and the receptor solution were selected to be consistent with the ionic content of the body and drug formulations, respectively.[246] The ideal solution diffusion coefficients corresponding to each of these species are presented in Table 10-1. The diffusion coefficients of the lidocaine ion, the HEPES buffer ion and the undissociated HEPES species were calculated using the Wilke-Chang correlation.[260] Evaluation of the diffusion coefficient by this method requires the molal volume of the solute at the normal boiling point as an input parameter. The molal volume was estimated using Schroeder's Additive Method.[260] This method provides estimates for molal volumes, which are accurate to within three percent.

Table 10-1: Diffusion coefficients and bulk solution concentrations for the species present in the transdermal iontophoretic simulation

Species	D_i / $\times 10^5$ cm^{2}s^{-1}	Donor Solution $c_{i,bulk}$ / M	Receptor Solution $c_{i,bulk}$ / M
Na$^+$	1.3341	0.250	0.14
Ca^{2+}	0.792	0.100	0.050
Lidocaine$^+$	0.59†	5.00×10^{-3}	1.00×10^{-6}
Cl$^-$	2.032	0.453	0.256
H$^+$	9.31	1.00×10^{-7}	3.89×10^{-8}
OH$^-$	5.26	1.00×10^{-7}	2.57×10^{-7}
HEPES$^+$	0.734	2.20×10^{-3}	4.20×10^{-3}
HEPES	0.720	7.80×10^{-3}	5.80×10^{-3}

10.4   Governing Equations

The governing equations for the steady-state model of transdermal iontophoresis were developed according to dilute solution theory.[136,137] The ionic strength of the solutions simulated in the system was less than 0.5 M; therefore, specific interactions between individual ions were considered to be negligible. The entire system was simulated as being electrically neutral and at equilibrium. The approach provided for concentration, flux and electrostatic potential profiles throughout the entire transdermal iontophoretic system domain.

10.4.1   Molar Flux

The molar flux of the species was assumed to obey Nernst-Planck behavior. The flux density of species i, is represented by

$$N_i = -u_i z_i F c_i \nabla \Phi - D_i \nabla c_i + v c_i \qquad (10\text{-}4)$$

the terms associated with the flux equation correspond to the quantities defined in Equation (3-1). For example, the total flux was assumed to be composed of contributions from migration, diffusion and convection, respectively. The mobility of the species in solution was related to diffusivity by the Nernst-Einstein relation

$$D_i = u_i RT \tag{10-5}$$

where u_i is the mobility of species, i, R, is the universal gas constant and T is the absolute temperature.

The fluxes determined by experiment correspond to surface averaged quantities, therefore, the design equations for the model were cast in one-dimensional form. The one-dimensional formulation led to a model appropriate for probing variations in potential, flux, pH and concentration in the direction of iontophoretic transport. Migration, diffusion and convection terms were included in the flux. An assumption was made in this work that the contribution from convection to the total flux was negligible in comparison to the contributions from migration and diffusion. The complete expression for flux density in the direction of transport is described by

$$N_i(x) = -u_i z_i F c_i \frac{d\Phi}{dx} - D_i \frac{dc_i}{dx} \tag{10-6}$$

where, as stated earlier, convection in the direction of transport was assumed to be negligible.

10.4.2 Material Balance Expressions

The general expression for the conservation of mass for the components in the system is described by

$$\frac{\partial c_i}{\partial t} = -\nabla \cdot N_i + R_i \tag{10-7}$$

where $-\nabla \cdot N_i$ is the volume averaged accumulation rate. Since the system was at steady-state the first term in the conservation equation was zero. The term corresponding to R_i represents the production rate from homogeneous reactions involving species i. Homogeneous reactions considered in this system are the dissociation of water and moderation of pH by the HEPES buffer.

A detailed description of the treatment of the homogeneous reactions is provided below. Provision was made in the donor solution for replenishment of species and in the receptor for clearance of the transported species. The appropriate expression for the divergence flux of the iontophoretic system considered here is presented by

$$-\nabla \cdot N_i = -\frac{dN_{ix}}{dx} - \frac{dN_{iy}}{dy} \tag{10-8}$$

Contributions to the total divergence are divided into two components. The first term corresponds to transport in the direction of iontophoresis. The second term, in the y-direction, corresponds to convective flux in the direction perpendicular to current flow. The y-component of the flux allowed for the addition of material to the donor solution and the removal of material from the receptor solution.

Conservation of mass was obeyed because the total amount of material entering the donor solution was equal to the amount of material leaving the receptor solution. The flow of species through the system is illustrated in Figure 10-2. The vertical arrows correspond to the species flux in the direction normal to iontophoretic transport. The horizontal arrows represent the iontophoretic flow of material through the solution chambers and the skin.
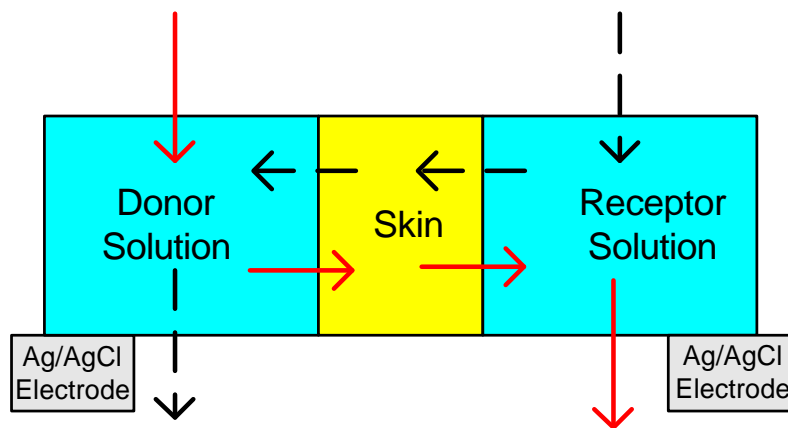
Figure 10-2: Flow pattern of dissolved species through the system domain. Figure not to scale.

The y-component of the divergence was calculated by adding a term to the flux expression which was proportional to the difference in the local and bulk solution concentrations. The divergence of flux in the y-direction is given by

$$-\frac{dN_{iy}}{dy} = -v_y \frac{dc_i}{dy} \tag{10-9}$$

where v_y is the bulk solution velocity in the direction normal to iontophoretic transport. Numerical evaluation of the flux derivative in the y-direction proceeded according to

$$-\frac{dN_{iy}}{dy} = -v_y \frac{c_i - c_{i,bulk}}{\Delta y} \tag{10-10}$$

where $c_{i,bulk}$ is the bulk concentration of the species of interest, Δ_y represents the linear distance required for c_i to equal $c_{i,bulk}$ and v_y is the y-component velocity. For the simulations presented here the ratio of velocity and characteristic distance, Δy, was considered to be constant. This term provided a driving force for transport in the direction normal to the iontophoretic flux.

10.4.3 Homogeneous Reactions

The electrolytic solutions associated with the iontophoretic system contained buffers to moderate changes in pH. In addition, the dissociation of water was included in the model. The reactions were considered to be in equilibrium. The homogeneous reactions were not explicitly evaluated with the flux divergence terms in the conservation equations. Instead, algebraic manipulations were performed to eliminate the reaction terms. The manipulations allowed for the flux divergence terms and the reaction terms to be evaluated separately. A detailed account of this procedure is provided below.

The general stoichiometric expression for the dissociation of a 1:1 buffer salt is described according to

$$\text{HBuff} \rightleftharpoons \text{H}^+ + \text{Buff}^- \tag{10-11}$$

where HBuff represents the undissociated buffer, H^+ is the dissolved hydrogen ion and $Buff^-$ represents the base of the dissociated buffer.

The equilibrium relationship for the buffer reaction is

$$\frac{c_{H^+} c_{Buff^-}}{c_{HBuff}} = K_{Buffer} \tag{10-12}$$

The other homogeneous reaction corresponds to the dissociation of water which proceeds according to

$$H_2O \rightleftharpoons H^+ + OH^- \tag{10-13}$$

Similar to the buffer reaction, the equilibrium relationship for the water dissociation reaction is

$$c_{H^+} c_{OH^-} = K_w \tag{10-14}$$

Since the reactions for the dissociation of water and dissociation of buffer were assumed to be equilibrated, Equations (10-14) and (10-12) must be satisfied simultaneously.

For a system at steady-state the material balance equations for the species involved in the homogeneous reactions are presented by

$$-\nabla \cdot N_{H^+} + R_{H^+} = 0 \tag{10-15}$$

$$-\nabla \cdot N_{OH^-} + R_{OH^-} = 0 \tag{10-16}$$

$$-\nabla \cdot N_{Buff^-} + R_{Buff^-} = 0 \tag{10-17}$$

$$-\nabla \cdot N_{HBuff} + R_{HBuff} = 0 \tag{10-18}$$

Since the buffer dissociation reaction was assumed to be at equilibrium, the consumption rate of the undissociated buffer was equal to the production rate of

dissociated buffer ion. This relationship is described by

$$R_{\text{HBuff}} = -R_{\text{Buff}^-} \qquad (10\text{-}19)$$

where R_{HBuff} and R_{HBuff^-} are the production rates of the undissociated buffer molecules and buffer ions, respectively.

The homogeneous production rate in the material balance expression for the undissociated buffer, Equation (10-18), can be replaced by Equation (10-19). The equivalent form of the undissociated buffer mass conservation equation can be added to material balance expression for the buffer ion, Equation (10-17), to yield

$$-\nabla \cdot N_{\text{HBuff}} - \nabla \cdot N_{\text{Buff}^-} = 0 \qquad (10\text{-}20)$$

The manipulations described above combined the mass conservation equations for the undissociated buffer and buffer ions into a single expression.

Algebraic elimination of the remaining reaction rate terms from the material balance expressions was performed by equating the hydronium ion production rate to the production rates of hydroxide ions plus buffer anions. For example, the production rate of hydronium ions is described according to

$$R_{\text{H}^+} = R_{\text{OH}^-} + R_{\text{Buff}^-} \qquad (10\text{-}21)$$

which implies that the dissociation of water molecules and buffer salts contribute to the formation of hydronium ions.

The net production rate of hydronium ions, described by Equation (10-21), was used to eliminate the homogeneous reaction terms in material balance equations for the hydronium, hydroxide and buffer ions. The approach was to subtract Equations (10-16) and (10-17) from Equation (10-15). The expression obtained from the manipulation consisted of the flux divergences for the H^+, OH^- and

Buff$^-$ ions. The combination of the material balance equations is described by

$$-\nabla \cdot N_{\text{H}^+} + \nabla \cdot N_{\text{OH}^-} + \nabla \cdot N_{\text{Buff}^-} = 0 \qquad (10\text{-}22)$$

which states that the accumulation rate of the hydrogen ions was equal to the production rates of hydronium ions plus buffer ions.

The algebraic elimination strategy presented here reduced the number of independent relationships from four to two. The final two relationships required for solution of the system of equations were the equilibrium reaction expressions presented in Equations (10-12) and (10-14).

10.4.4 Electroneutrality

The entire domain of this system was considered to be electrically neutral. The expression for electroneutrality is

$$\sum_i z_i c_i \qquad (10\text{-}23)$$

which states that the sum of the ionic concentrations multiplied by the respective ionic charge numbers is equal to zero. Electroneutrality is a valid approximation for moderately dilute systems. The electroneutrality condition is generally satisfied in the bulk phases of electrochemical systems because of the large electrical forces required to separate charge.

10.4.5 Numerical Method

The system of differential equations was cast in finite-difference form and was solved numerically using the BAND routine developed by Newman.[261] The BAND algorithm was implemented because it reduces the computational effort required to solve systems with tridiagonal coefficient matrices. In order to account for differences in scale between the skin, which has a thickness on the order of 10-20 microns, and the donor and receptor chambers, the mesh size was expanded in

the donor and receptor chambers. All equations were written to be of the order of

the square of the mesh size, and convergence was quadratic.

CHAPTER 11
MODEL SIMULATION RESULTS

The simulation results from the mathematical model of transdermal iontophoresis described in Chapter 10 are presented here. A series of simulations was performed with skin of different resistance values under a 100 μA/cm^2 applied DC bias. The predicted potential profiles within the stratum corneum from the simulations are presented in Figure 11-1. The skin with polarization resistances of 2.9 kΩcm^2 and 4.1 kΩcm^2 displayed nonlinear potential profiles. A general feature of the results was that the decreased diffusivity of the mobile species associated with the assumed tortuosity caused the skin to serve as the dominant resistance in the system.
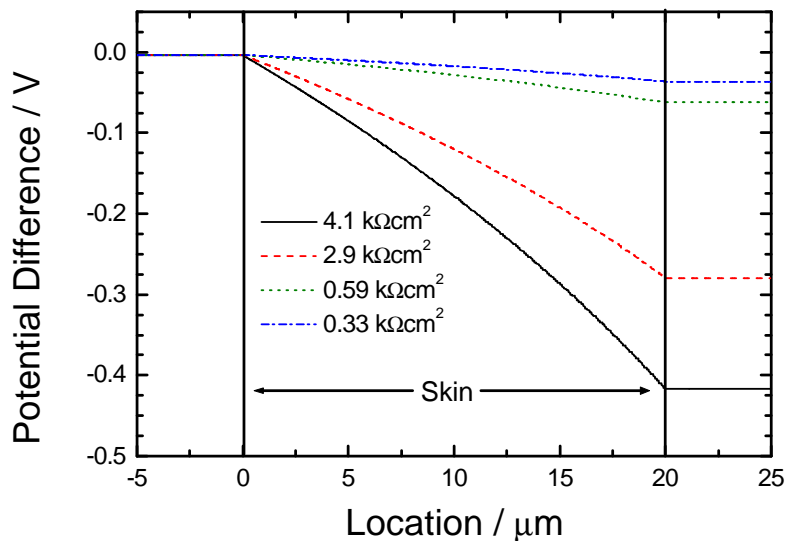
Figure 11-1: Potential profile within the stratum corneum.

A key result was that the electric field within the skin was significantly larger than in the surrounding ionic solutions. For example, the field strength within the

skin with the 4.1 kΩcm^2 polarization resistance was approximately 20.7 kV/cm. The electric field within the skin with the lowest polarization resistance was approximately 1.7 kV/cm. The large electric field within the skin provided the dominant driving force for the transport of ionic species.

11.1   Calculated Flux Profiles

The flux profiles for the skin with the 4.1 kΩcm^2 polarization resistance are presented in Figure 11-2. The fluxes of the calcium and sodium ions are indicated by the black and blue curves. The magnitudes of the calcium and sodium fluxes are indicated by the left-hand ordinate. The red triangular symbols correspond to the flux of chloride ions. The magnitude of chloride ion flux is indicated by the right hand ordinate.
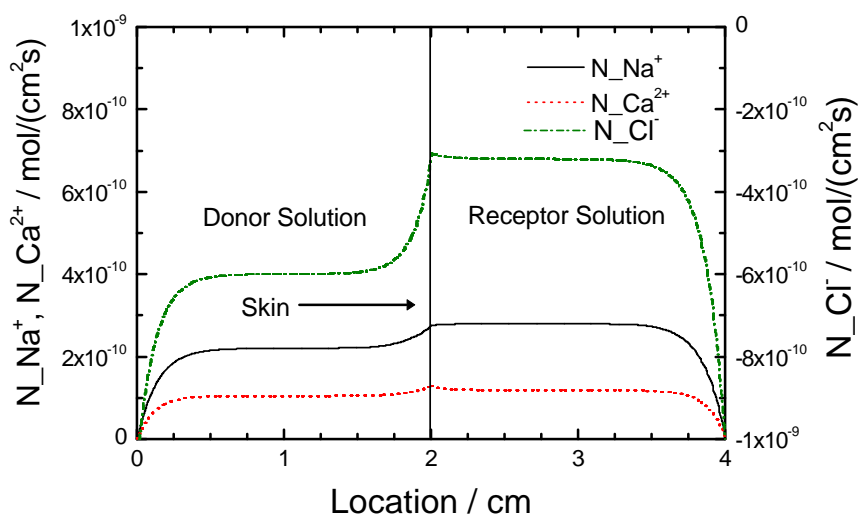
Figure 11-2: Calculated flux profiles of the major ionic species throughout system domain.

The fluxes of all species except for the chloride ion were equal to zero at the boundaries of the system. Throughout the interior of the system domain, all species fluxes were nonzero with the highest values observed near the skin surface. This result, which mimics the behavior of the experimental system, was made possible by the inclusion of terms to account for replenishment of species
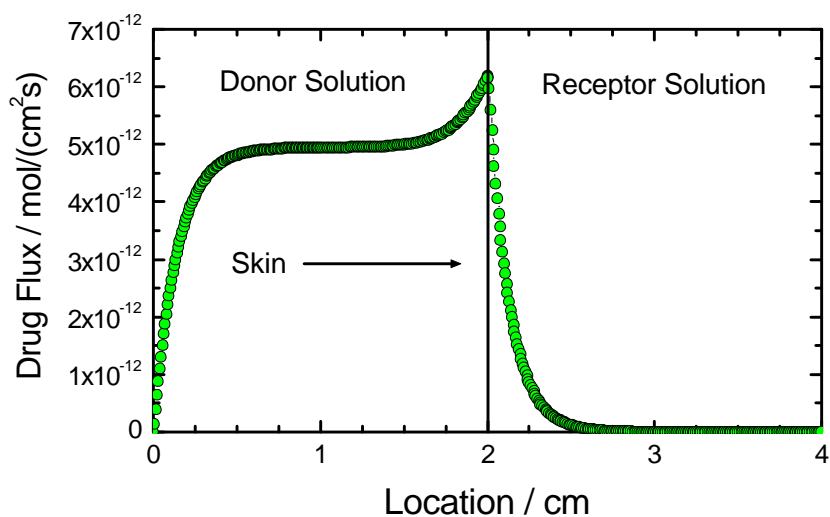
Figure 11-3: Calculated flux profile of lidocaine throughout system domain.

in the donor solution and for clearance of species in the receptor. Overall conservation of mass and charge forced the iontophoretic fluxes to be nonzero.

The simulated drug flux profile is indicated by the solid green circles in Figure 11-3. The drug flux, calculated from this simulation, was highest at the surface of the skin facing the donor solution. The drug flux profile in the adjacent receptor solution shows a dramatic decrease as the distance from the interior surface of the skin increases. This observation was consistent with the expected behavior of a species entrance into the receptor compartment and subsequent removal by convection. A similar behavior described by these results is that the drug enters the body and is carried away by the circulatory system of the patient.

The flux profile for the simulated system was several orders of magnitude lower than for the transdermal iontophoretic delivery rates of lidocaine described in Section 9.4. In addition, the model predicted drug fluxes that were approximately an order of magnitude lower than the fluxes reported in the work of Philbrick.[164] The discrepancy between the predicted and measured transdermal drug fluxes may have been caused by an inaccurate prediction of the lidocaine

diffusion coefficient. Furthermore, the predictions obtained here are for skin exhibiting polarization resistance values that are approximately an order of magnitude lower than typically measured values.[1,111] Numerical difficulties present at the interface between the skin surface and adjacent electrolyte solutions prevented simulation of more realistic values of skin impedance.

11.2 Influence of Buffer on pH Within Stratum Corneum

A separate study was conducted with unbuffered and buffered systems. For the simulations an array of skin resistance values was selected. The objective was to determine the influence of the buffer in mediating solution pH. The results from the buffered and unbuffered systems are presented in Figure 11.4(a) and Figure 11.4(b), respectively.

An interesting feature of this work is that the concentration profiles within the skin were significantly different than in the surrounding solutions. For example, the coupling between the electroneutrality condition (which accounted for the fixed background charge), the homogeneous reactions, and the species fluxes caused the pH to have a local maximum within the skin that was higher than in the surrounding solutions. Local maxima of pH were observed for both the unbuffered and buffered systems. As expected, the maximum pH value for the unbuffered system was higher than for the buffered system. The magnitude of the maximum pH was highest for skin with the highest impedance values.

It has been proposed that extremes in pH can be a source of skin irritation.[148,158] The results here demonstrate that extremes in pH may be predicted by accounting for the coupling of physical phenomena. This work suggests that simulations of skin with higher polarization impedance will yield larger observed values of local pH maxima within the skin.
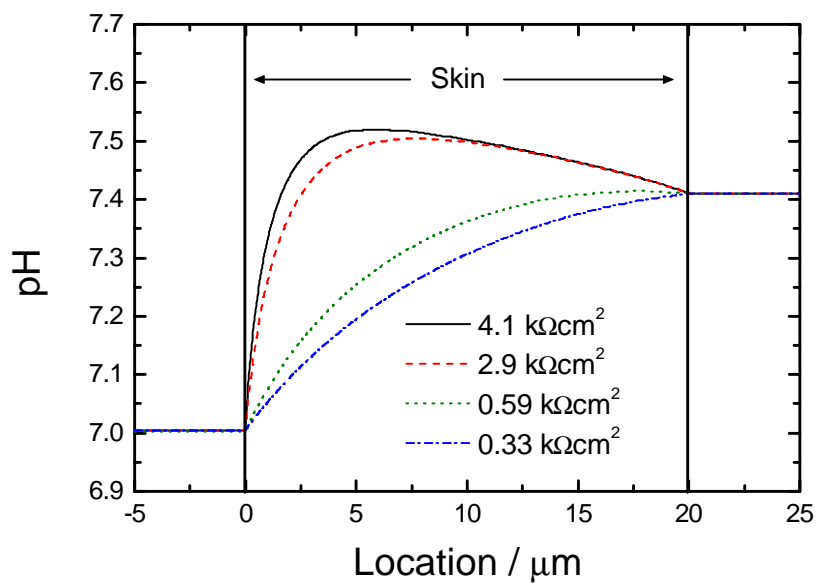
(a)
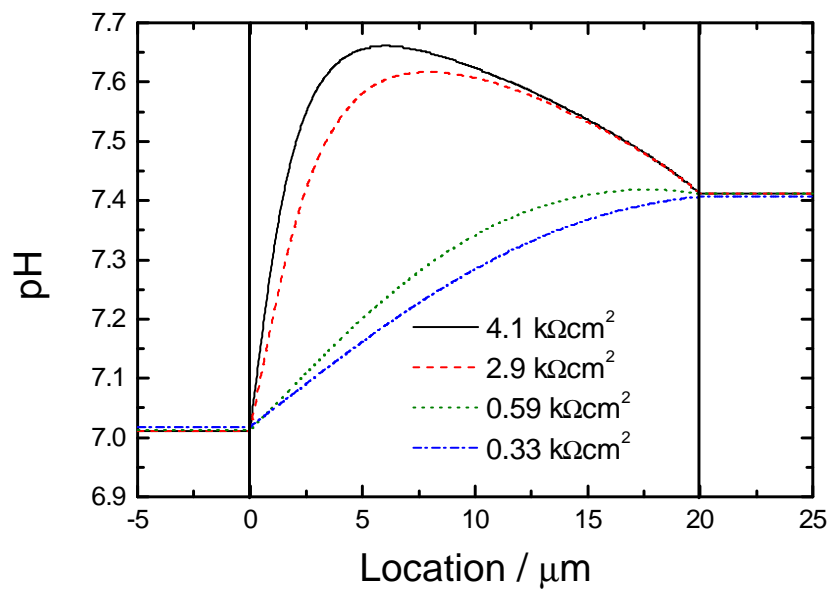
(b)

Figure 11-4: Calculated pH profiles within stratum corneum. (a) Buffered electrolyte system. (b) Unbuffered electrolyte system.

CHAPTER 12
CONCLUSIONS

An object of this work was to determine the influence of applied electrical signals on skin transport properties. The work was designed to support the development of devices for transdermal delivery of therapeutic compounds by iontophoresis. In accordance with this goal, electrochemical impedance spectroscopy was implemented to monitor the electrical and transport properties of heat-separated cadaver skin under a variety of conditions. For example, experiments were conducted where a nonzero DC current bias was applied across heat-separated human cadaver skin to simulate *in vivo* transdermal iontophoresis. Recovery of skin properties to applied current was monitored by impedance spectroscopy at open-circuit conditions corresponding to the application of a 0 $\mu A/cm^2$ DC bias.

Two modulation strategies were implemented for the electrochemical impedance spectroscopy studies of human skin: (1) constant-amplitude galvanostatic modulation and (2) variable-amplitude galvanostatic modulation. Constant-amplitude galvanostatic modulation is the traditional control method used for skin impedance experiments. For a typical experiment, a constant-amplitude sinusoidal current perturbation is applied and the potential response is measured over a wide range of frequencies. Skin exhibits a characteristically high impedance in the low-frequency portions of the impedance spectra. Therefore, at low frequencies the constant-amplitude sinusoidal current perturbation can induce potential swings across the membrane which often exceed 1 V. Statistical error analysis of skin impedance spectra obtained by this methodology proved to be inconsistent

237

with the Kramers-Kronig relations. The inconsistent data points were located in the low-frequency portions of the spectra. The results implied that skin properties had been altered.

Variable-amplitude galvanostatic modulation was implemented as the second control strategy for the skin impedance experiments. The approach was to predictively adjust the amplitude of the current perturbation to prevent large potential swings across the membrane. Impedance spectra collected by the adaptive modulation strategy were shown to be consistent with the Kramers-Kronig relations which indicated that skin properties were not modified by the experiment. The work strongly suggests that potential perturbations on the order 1 V can alter skin properties. As the variable-amplitude galvanostatic control strategy avoids large potential fluctuations, the methodology should be applied for monitoring skin transport properties by electrochemical impedance spectroscopy.

The work described up to this point established that variable-amplitude galvanostatic modulation of impedance spectroscopy provides for noninvasive measurement of skin transport properties at the open-circuit condition. The methodology was applied for subsequent electrochemical impedance spectroscopy and step-change experiments designed to identify the influence of an applied DC electrical bias on skin. For the step-change studies both applied-current and potential signals were applied across the epidermis for at least 20 minutes. The amplitude of the DC bias was increased periodically to determine the potential or current at which skin properties begin to change. The results indicated that alterations occurred when the potential difference across the membrane exceeded 100-250 mV. The deviation in the response signal from a membrane with constant electrical properties was proportional to the magnitude of the potential difference across skin.

The influence of solution composition on the recovery of skin properties to large electrical signals was assessed. Impedance spectroscopy experiments were conducted on skin specimens immersed in electrolyte solutions with monovalent and divalent cations. An identical methodology was used to study the skin in each type of electrolyte. The recovery of skin properties to large electrical perturbations was found to be more complete and more rapid for the sample immersed in the solution with divalent cations. This observation could have important implications for the development of iontophoretic drug formulations. For example, if the same behavior is identified *in vivo* divalent cation salts could be added as supporting electrolyte to the therapeutic mixtures of iontophoretic systems.

Another important aspect of this work identified the sources of variation in the electrical and transport properties of heat-separated cadaver skin. A large body of impedance data was collected in this work. For example, 127 pieces of heat-separated human epidermis from 18 cadavers were studied by electrochemical impedance spectroscopy. The samples displayed a wide distribution of impedance responses. Statistical analysis was performed to determine the contributions to the overall variation in properties. The impedance data included in the analysis was obtained from the skin hydration studies which were conducted under identical experimental conditions. Therefore, the sources contributing to the variation were assumed to be caused by differences between the cadavers and by variations within a given skin sample.

A generalized linear model was used to extract the contributions to the overall variation of skin properties. The variation of skin impedance within a given sample was found to be larger than the variation associated with differences between the cadavers. The analysis suggests that caution should be exercised when comparing the impedance results from two pieces of skin.

A mathematical model was developed to simulate transdermal iontophoresis. The object of this work was to calculate the influence of controlled variables on the concentration and flux profiles within the skin. The flux of ionic species was assumed to be driven by both migration and diffusion. A unique feature of this work was that the potential profile within the skin was calculated explicitly. Equilibrated homogeneous reactions were included to account for partial dissociation of water and buffers. The species present in the simulated system were assumed to be Ca^{2+}, Na^+, Cl^-, H^+, $OH-$, drug cation, drug counter anion, and dissociated and undissociated buffer species. In addition, the charge of the skin was treated to be an immobile ionic species.

An interesting feature of this work is that the concentration profiles within the skin were significantly different than in the surrounding solutions. For example, the coupling between the electroneutrality condition (which accounted for the fixed background charge), the homogeneous reactions, and the species fluxes caused the pH to have a local maximum within the skin that was higher than either of the surrounding solutions. The largest local pH maxima were observed in the simulations of skin with the largest polarization resistances.

Transdermal delivery rates of the model drug lidocaine were measured by UV-vis spectroscopy. A custom dual-channel spectrometer apparatus was developed to provide for the simultaneous measurement of transdermal lidocaine flux and skin transport properties under iontophoretic conditions. The absorption spectroscopy system was shown to be properly calibrated. The calibration procedure provide for the calculation of lidocaine delivery rates across the skin. It was demonstrated in this work that the transdermal flux of lidocaine was increased by over an order of magnitude when current was applied. The largest transdermal delivery rates were observed at the largest amplitudes of applied current. The

results indicate that iontophoresis can improve the delivery efficiency of charged therapeutic compounds across skin.

In summary, the experimental work described in this text identified the influence of controlled variables such as current, potential and solution composition on the electrical and transport properties of heat-separated human skin. The delivery rates of lidocaine across the skin were measured by UV-vis absorption spectroscopy. The results indicated that the applied electrical current enhanced the transdermal flux of lidocaine. The mathematical model of transdermal iontophoresis provided information on the effect of coupled phenomena, such as equilibrated dissociation reactions and electroneutrality, on the concentration and flux profiles within a homogeneous membrane with properties similar to human stratum corneum.

CHAPTER 13
SUGGESTED RESEARCH

A large database of impedance spectra was collected in this work to determine the effect of applied electrical signals on skin transport properties. The spectra were regressed to the Voigt circuit model to identify data that was inconsistent with the Kramers-Kronig relations. Identification of the inconsistent data provided a means for determining changes in skin properties. In this manner, the influence of a given set of experimental parameters on membrane properties could be determined.

Although this approach is robust, additional information could be extracted by regressing a process model to the impedance spectra collected in this work. The process model would likely include terms associated with the mass transfer resistance of ions entering and exiting the stratum corneum. In addition, the adsorption of electrolyte cations to the negative background charge of skin could provide a mechanism for the observed capacitance of the membrane. The model parameters associated with this type of formulation would directly correspond to the physical properties of the skin. Regression of the model to the impedance spectra collected in this work would provide for direct calculation of the influence of electrical signals on the physical properties of the skin.

Heat-separated human cadaver skin was used as the model membrane for this study. The primary transport barrier for the delivery of therapeutic compounds is the stratum corneum. The entire stratum corneum was contained in the epidermal membranes used for this study. The work presented in this report addressed

and identified many of the important factors affecting drug transport across intact human skin during iontophoresis. However, there are differences between heat-separated human cadaver skin and intact human skin.[97,152,148,206,207] For example, the polarization impedance of human cadaver skin was found to be approximately an order of magnitude lower than for human skin *in vivo*.[152] These differences suggest that the experimental methods presented in this work should be applied for *in vivo* transdermal iontophoresis investigations to identify the influence of controlled variables on the efficiency of drug transport.

It was demonstrated in Chapter 9 that the coupling of UV-vis absorption spectroscopy with electrochemical impedance spectroscopy represents a promising methodology for monitoring transdermal iontophoresis. The UV-vis absorption spectroscopy system was shown to be properly calibrated. Preliminary transdermal iontophoresis experiments indicated that electrical current enhanced lidocaine flux.

Despite the successful application of UV-vis absorption spectroscopy for the measurement of the lidocaine delivery rates across skin, there remain unresolved issues. For example, some of the absorption measurements that indicated lidocaine concentration decreased for short intervals during the transdermal flux experiments. As passive diffusion was small and positive across the skin, the unusual result was probably caused by measurement error. Hence, it is recommended that additional transdermal iontophoresis experiments be performed to determine the source of the anomalous behavior. In addition, UV-vis absorption spectroscopy is an inferential technique, therefore, supplemental experimental methods, such as mass spectroscopy or high-performance liquid chromatography, should be implemented to directly measure lidocaine concentrations in the receptor chamber of the diffusion cell. This approach could be used to validate

the accuracy and precision of the UV-vis absorption spectroscopy measurements under iontophoretic conditions.

The influence of controlled variables such as solution composition and applied current on the delivery of a model drug across the stratum corneum was assessed by the steady-state model of the transdermal iontophoresis. The stratum corneum was simulated as a homogeneous membrane with uniform properties. The actual structure and composition of human stratum corneum is much more complex than for the transdermal system simulated here. Despite this limitation, the important factors affecting transdermal delivery of ionic drug compounds by iontophoresis, such as the negative background charge and low permeability of stratum corneum, were considered.

Interactions with the negative background charge of the stratum corneum were coupled through the electroneutrality condition. Specific interactions, such as the binding of solution cations with the negative background charge of skin, were not considered. A mechanism for binding could be included in the model by introducing a Gibbs adsorption isotherm at the interface between the negative charge sites of the skin and the electrolyte solution. The driving force for the adsorption reactions should be proportional to the electrostatic potential difference at the interface. The model could also be refined to account for additional equilibrated homogeneous reactions such as the dissociation of stratum corneum fatty acids. These types of refinements would provide for an improved model of transdermal iontophoresis.

APPENDIX A
PREPARATION OF EPIDERMIS

Heat separated human cadaver skin was used for all of the experimental studies. The thickness of the skin samples was on the order of 100 μm which corresponded to the uppermost layers of the epidermis. The stratum corneum composed the top 20 μm of the membranes. The skin samples were extracted from the cadavers at ALZA Corporation and were shipped by over-night express mail in insulated containers. The procedure for separating the epidermis from the dermis is described here.[262]

1. If frozen skin was used, it was allowed to partially thaw. The partially thawed skin was cut into 10 cm x 15 cm pieces. Half of the underlying tissue and fat were trimmed with a scalpel or scissors such that the dermis and epidermis remained intact.

2. The full-thickness skin was rinsed in a pan of room-temperature deionized water for several minutes.

3. The full-thickness skin was then rinsed in a pan of 32 C° deionized water and allowed to soak for several minutes.

4. The full-thickness skin was transferred to a large beaker or pan of deionized water with an initial temperature of 62.0 C°. The skin was submerged with a glass stirring rod for one minute. The time and temperature were measured by a stopwatch and digital thermometer, respectively.

5. The warm skin was transferred onto plastic sheeting or a piece of lab-bench liner for separation of the epidermis. At the start of the separation procedure the edge of the dermis was held with tweezers and the epidermis with lightly impacted with the edge of a round-tipped spatula. After approximately 4 cm^2 of the epidermis was separated, the dermis was held down with a gloved hand and the epidermis pushed away with the spatula or gloved finger.

6. The epidermis was placed a pan of deionized water, floating the epidermis with the dermal side facing the water to rinse the epidermis. This step was repeated several times to remove excess fat from the skin. The epidermis was shipped for use or was stored for later use.

7. The epidermis was prepared for storage by floating it in a pan of water and placing a piece of release liner (polymer sheeting) under the epidermis. The release liner was used to pick up the epidermis and wrinkles in the membrane removed. The epidermis was placed between a second piece of release liner and gently agitated to remove excess water. The epidermis was packaged in plastic bag, sealed, and stored at 4 C$^\circ$ for a period not longer than 3 weeks.

APPENDIX B
VAG MODULATION FOR IMPEDANCE SPECTROSCOPY

In order to maintain linearity in an electrochemical system, the potential must be kept below a critical value which is characteristic to the system under study. A typical impedance scan starts at high frequency and the frequency is decreased incrementally until the minimum measuring frequency is attained. Electrochemical systems frequently exhibit a three order of magnitude increase in impedance as the frequency is swept from high to low. For a constant-amplitude galvanostatically modulated experiment, the potential difference will reach its greatest value where the impedance exhibits its greatest value. Wojcik *et al.*[235] developed an algorithm to adjust the current perturbation at each measuring frequency to prevent large potential differences during the course of an electrochemical impedance spectroscopy experiment.

B.1 Design Equations

The first set of operations performed in the predictive algorithm estimate the impedance value at the next measuring frequency in the scan. For all but the first 3 measuring frequencies, the predicted impedance is obtained from a second order accuracy linear extrapolation of the previously measured impedance values. Throughout the course of an experiment, the predicted impedance value is used with a set value for the desired potential difference in the system to calculate the current perturbation at the next measuring frequency according to

$$\Delta\widetilde{I}(\omega) = \frac{\Delta\widetilde{V}_{target}}{|Z(\omega)|_{estimated}} \tag{B-1}$$

where $\Delta \widetilde{V}_{target}$ is the desired potential response and $|Z(\omega)|_{estimated}$ is the guess value for the first impedance measurement. A good estimate for the first value of the impedance is the electrolytic solution resistance. The impedance value measured at the first frequency is then used to predict the appearance at the second frequency according to

$$Z(\omega_k) = Z(\omega_{k-1}) + O\left(\log\left(\frac{\omega_k}{\omega_{k-1}}\right)\right)^2 \tag{B-2}$$

For the third measuring frequency, the impedance is predicted by the two point formula

$$Z(\omega_k) = 2Z(\omega_{k-1}) - Z(\omega_{k-2}) + O\left(\log\left(\frac{\omega_k}{\omega_{k-1}}\right)\right)^2 \tag{B-3}$$

For the remainder of the impedance scan, the impedance is predicted by

$$Z(\omega_k) = 3Z(\omega_{k-1}) - 3Z(\omega_{k-2}) + Z(\omega_{k-3}) + O\left(\log\left(\frac{\omega_k}{\omega_{k-1}}\right)\right)^2 \tag{B-4}$$

An essential feature of the variable amplitude modulation technique is that dynamic adjustment of the current measuring resistor is required to achieve acceptable signal-to-noise ratios. Appropriate measuring resistor selection was achieved in this work using a custom software control interface written in LabVIEW G® for Windows. The application of variable-amplitude galvanostatic modulation was shown to be less invasive than traditional constant amplitude galvanostatic control.[263] The variable amplitude galvanostatic modulation technique has been applied to corrosion studies of copper and steel.[264]

B.2   Error Analysis of VAG Modulation Scheme

A study was performed in this work to assess the accuracy of the predictive algorithm for the skin system. A typical skin impedance spectrum was used to compare the algorithm predictions for impedance to the measured values at at

each frequency. The percent relative error was calculated according to

$$E_{relative} = \frac{|Z(\omega)|_{estimated} - |Z(\omega)|_{data}}{|Z(\omega)|_{data}} \times 100\% \qquad \text{(B-5)}$$

where $|Z(\omega)|_{estimated}$ and $|Z(\omega)|_{data}$ are the impedance quantities from the algorithm and measurement, respectively. The percent relative error as a function of frequency is presented in Figure B-1. Predictions based on the impedance data are shown by the filled triangles. The errors appear to be randomly distributed with a mean of $3.03 \times 10^{-2}\%$ and standard deviation of 1.18%. The errors contain contributions from the predictive algorithm and the experimental apparatus according to

$$E_{total} = E_{algorithm} - E_{instrument} \qquad \text{(B-6)}$$

where $E_{algorithm}$ represents the error associated with Taylor series prediction of the impedance and $E_{instrument}$ is the error contribution from the experimental apparatus.

Although the relative error for the prediction of the impedance was as large as 2.2% the influence of the error on the experiment is expected to be minimal. As long as the instrument provides an acceptable signal-to-noise ratio and linearity is maintained in the system, accurate impedance measurements should be obtained.

The numerical accuracy of the predictive algorithm was estimated from simulations of an ideal circuit network consisting of a resistor in series with a RC element (see, for example Figure, 3-3) and a second circuit network consisting of a resistor in series with a parallel combination of a resistor and a constant phase element (see, for example, Figure 3-6). The constant phase element network was included in the simulations because it provides an impedance response which is similar to that of skin. For both networks the polarization impedance and charac-
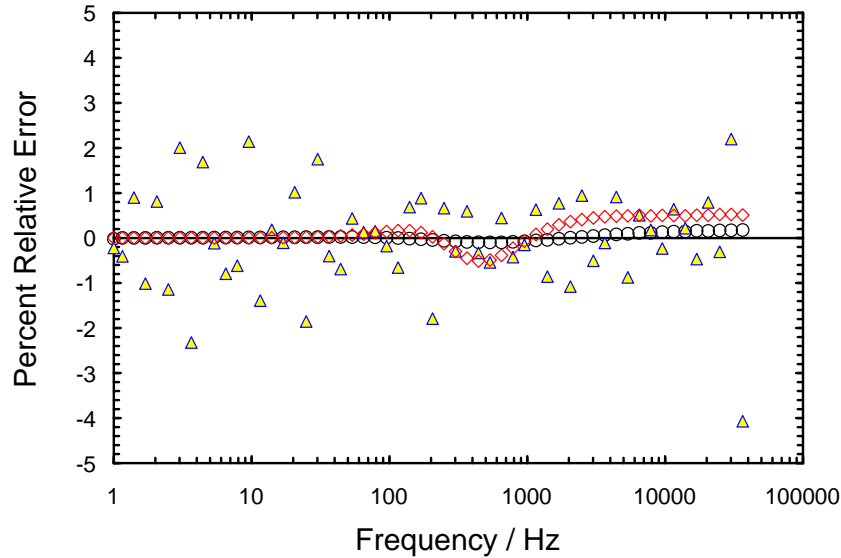
Figure B-1: Percent relative error for prediction of impedance from VAG algorithm. Open diamonds represent error for ideal circuit consisting of a resistor in series with a single RC element. The filled circles are the errors from the constant phase element circuit. The solid triangles represent the error for predicted impedance values obtained from a typical impedance spectra of skin.

teristic frequency were the same. The difference in the impedance values obtained from circuit model parameters and the algorithm predictions provided for estimates of $E_{algorithm}$.

The relative errors from the simulation with the RC network are presented by the open diamonds in Figure B-1. The absolute value of the errors was less than 0.6 %. The errors showed significant trending as a function of frequency with a mean of 1.20×10^{-1}% and standard deviation of 2.76×10^{-1}%. Similarly, the absolute value of the relative percent errors from the simulation with the constant phase element network are presented as open circles in Figure B-1. The absolute value of the relative errors for this system was less than 0.2% of the impedance magnitude. The mean and standard deviation of the percent errors was 1.97×10^{-2}% and 7.24×10^{-2}%, respectively. Trending of the errors as a function of frequency was observed. For both systems the errors were greatest close to the characteristic fre-

quency, although the spread of the data was significantly smaller for the constant phase element network.

The larger prediction errors associated with the RC element network were likely coupled to the relatively larger slope of the impedance as a function of frequency. The equations for the predictive algorithm are derived from a first-order Taylor's series expansion of the impedance. The expansion provides estimates for the impedance at the next measuring frequency by multiplying the slope of the impedance by the frequency interval. Since the slope of the RC element network is greater than the constant phase element network, especially at frequencies near the characteristic frequency, errors in the prediction of the impedance will be greater. In general, the predictive algorithm will be more accurate for systems such as skin where the impedance changes less dramatically as a function of frequency as compared to a RC element network with the same polarization impedance and characteristic frequency.

APPENDIX C
STATISTICAL OUTPUT

The results presented in this appendix were generated in the preliminary analysis of variance in the skin impedance data sets. Statistical parameters describing the distribution characteristics of the impedance data are presented in the first section. Skin polarization resistance and critical frequency were selected as characteristic parameters for the impedance spectra. The data were grouped according to electrolyte type to evaluate the influence of cation charge on the variation in skin impedance. The results from regressions of the Generalized Linear Model to various transformations of the skin impedance data are presented in Section C.2 and histograms of the skin data are presented in Section C.3.

C.1 Distribution Statistics from EIS Measurements of Skin Hydration

At the start of all experiments described in this text multiple electrochemical impedance spectra were collected to monitor skin hydration. The heat-separated epidermal membranes were immersed in inorganic chloride salt solutions of monovalent or divalent cations. As a large database of measurements was collected the polarization resistance and critical frequency were selected as representative parameters for skin transport properties. The polarization resistance and critical frequency associated with the impedance spectra of skin hydration were separated according to electrolyte type.

Student's $t-$tests and F-tests were performed on the data sets to determine whether the population means and population variances were equal for the experiments conducted in monovalent and divalent cations. Furthermore, the grouping

scheme provided for proper assessment of the contributions to the overall variation in skin properties. For example, the skin specimens were obtained multiple cadavers, therefore, the variation in skin properties could be caused by differences between the cadavers or by regional variations within a given donor sample. A detailed description of the statistical analysis procedure is provided in Chapter 7.

The analysis of variance methodology requires that the population be normally distributed. Logarithmic and square root transformations of the polarization resistance and critical frequency data were applied to determine the most appropriate representation for the measurements. Key statistical parameters, such as mean, kurtosis coefficient, and skewness, from the population of impedance measurements and transformed data sets are provided in Tables C-1 - C-3. The parameters were used to guide the statistical analysis.

Table C-1: Distribution statistics for skin polarization resistance and critical frequency as a function electrolyte type

| | Polarization Resistance | | Critical Frequency | |
Statistic	Monovalent	Divalent	Monovalent	Divalent
Mean	6.22×10^4	9.31×10^4	715.66	435.33
Standard Error	4.41×10^3	9.58×10^3	77.57	93.54
Median	3.09×10^4	7.00×10^4	169.66	78.75
Mode	1.14×10^4	3.07×10^4	954.10	53.65
Standard Deviation	8.81×10^4	1.04×10^5	1.55×10^3	1.02×10^2
Sample Variance	7.76×10^9	1.09×10^{10}	2.39×10^6	1.04×10^6
Kurtosis	12.43	7.85	20.79	14.04
Skewness	3.08	2.67	4.35	3.67
Minimum	1.28×10^3	1.72×10^3	3.66	11.56
Maximum	6.39×10^5	5.22×10^5	1.16×10^4	5.37×10^3
Sum	2.48×10^7	1.11×10^7	2.85×10^5	5.18×10^4
Count	398	119	398	119
Confidence Level(95.0%)	8.67×10^3	1.90×10^4	152.50	185.24

C.2 Analysis of Variance for EIS Measurements of Skin Hydration

The results from the analysis of variance for the Generalized Linear Model representation of the polarization impedance and critical frequency of skin samples

Table C-2: Distribution statistics for $\log_{10}$ of skin polarization resistance and critical frequency as a function electrolyte

	Polarization Resistance		Critical Frequency	
Statistic	Monovalent	Divalent	Monovalent	Divalent
Mean	4.456	4.727	2.30	2.03
Standard Error	0.028	0.049	3.72×10^{-2}	6.01×10^{-2}
Median	4.498	4.845	2.23	1.90
Mode	4.058	4.487	2.98	1.73
Standard Deviation	0.550	0.529	7.33×10^{-1}	6.55×10^{-1}
Sample Variance	0.302	0.280	5.38×10^{-1}	4.30×10^{-1}
Kurtosis	-0.568	1.090	-4.82×10^{-1}	1.55×10^{-1}
Skewness	4.77×10^{-2}	-0.930	-6.13×10^{-3}	8.53×10^{-1}
Minimum	3.107	3.235	0.563	1.06
Maximum	5.806	5.717	4.06	3.73
Sum	1729.046	562.53	891.90	241.90
Count	388	119	388	119
Confidence Level(95.0%)	5.49×10^{-2}	9.61×10^{-2}	7.32×10^{-2}	0.119

immersed in monovalent and divalent electrolyte solutions are presented in Sections C.2.1 and C.2.2.

C.2.1   Regression to Polarization Resistance

The results from the analysis of variance for the Generalized Linear Model representation of the polarization impedance of skin samples immersed in monovalent and divalent electrolyte solutions is presented in Tables C-4 and C-5.

The *F*-test parameter and probability values for acceptance of the null hypothesis for the effect of the donor from which a piece of skin was extracted on the polarization resistance of the specimens immersed in monovalent electrolyte were 1.57 and 9.84%, respectively. The *F*-test parameter and probability values for effect of location from which a piece of skin was obtained were 152.88 and less than 0.01%. The null hypothesis was rejected for both effects as *F*-test probabilities for acceptance of the null hypothesis were so small. The results implied that there was a significant effect on polarization impedance for skin immersed in monovalent electrolyte due to the donor sample and the location from which the specimen

Table C-3: Distribution statistics for square root of skin polarization resistance and critical frequency as a function electrolyte

	Polarization Resistance		Critical Frequency	
Statistic	Monovalent	Divalent	Monovalent	Divalent
Mean	206.06	270.01	19.93	14.52
Standard Error	6.89	13.07	0.92	1.38
Median	177.53	264.51	13.03	8.87
Mode	106.94	175.14	30.89	7.32
Standard Deviation	135.76	142.62	18.20	15.04
Sample Variance	1.84×10^4	2.03×10^4	331.28	226.27
Kurtosis	2.38	2.01	6.02	5.77
Skewness	1.43	1.10	2.21	2.42
Minimum	35.79	41.43	1.91	3.40
Maximum	799.65	722.22	107.51	73.25
Sum	8.00×10^4	3.21×10^4	7733.55	1728.41
Count	388	119	388	119
Confidence Level(95.0%)	13.55	25.89	1.82	2.73

Table C-4: Calculated contributions to variance from regression of GLM model to skin polarization resistance data for pieces immersed in monovalent electrolyte

Variable	DOF	Mean Sq.	F value	Probability
Donor type	16	3.72×10^{10}	1.57	0.0984
Location(Donor)	79	2.57×10^{10}	152.88	< 0.0001

was extracted. Similar results were obtained from the regression of the statistical model to the data set for skin immersed in divalent electrolyte, however, the effect of donor sample on the polarization impedance was even greater as both probabilities for acceptance of the null hypothesis were less than 0.01%.

C.2.2 Regression to Critical Frequency

The results from the analysis of variance for error terms for the Generalized Linear Model to the critical frequencies of skin samples immersed in monovalent and divalent electrolyte solutions is presented in Tables C-6 and C-7. The F-test

Table C-5: Calculated contributions to variance from regression of GLM model to skin polarization resistance data for pieces immersed in divalent electrolyte

Variable	DOF	Mean Sq.	F value	Probability
Donor type	11	1.03×10^{11}	12.07	< 0.0001
Location(Donor)	20	7.77×10^9	87.32	< 0.0001

Table C-6: Calculated contributions to the total variance from regression of GLM model to the critical frequency of skin immersed in monovalent electrolyte

Variable	DOF	Mean Sq.	F value	Probability
Donor type	16	9.84×10^6	1.14	0.332
Location(Donor)	79	9.31×10^6	294.96	< 0.0001

Table C-7: Calculated contributions to the total variance from regression of GLM model to the critical frequency of skin immersed in divalent electrolyte

Variable	DOF	Mean Sq.	F value	Probability
Donor type	11	3.75×10^6	0.85	0.6005
Location(Donor)	20	4.05×10^6	396.28	< 0.0001

parameter and probability values for acceptance of the null hypothesis (*i.e.,* that there was no significant variance in critical frequency for skin immersed in monovalent electrolyte due to the donor sample from which the piece was obtained) were 1.14 and 33.2%. Similarly, the *F*-test parameter and probability values for effect of location from which a piece of skin was obtained were 396.28 and 60.05%.

The null hypothesis for the effect of donor sample on the critical frequency for skin immersed in monovalent electrolyte could not be rejected, as there was a 33.2% chance of selecting two pieces of skin with similar critical frequencies from different donors. Alternatively stated, there was a small variation in critical frequency due to differences in skin from the donor population. Since the *F*-test probability value for the effect of extraction site of skin immersed in divalent electrolyte was 60.05%, the null hypothesis was not rejected. The relatively high *F*-test value indicated the site-to-site variation of critical frequency was insignificant. This implied the effect of extraction location on critical frequency for skin immersed in divalent electrolyte was not as pronounced as for the skin samples immersed in monovalent electrolyte.

The analysis of variance study indicated that the polarization impedances and critical frequencies for pieces of skin obtained from the same donor sample were not correlated. In other words, the intra-individual variation of skin properties

was greater than the inter-individual variation. The results suggest that imped-ance response of skin samples extracted from the same donor cannot be consid-ered as identical specimens.

C.3   Histograms of Selected Skin Properties During Hydration

The histograms corresponding to measured values and transformed values of selected skin properties are presented here. The figures are grouped according to electrolyte. Histograms of the polarization resistance and critical frequency are presented separately.
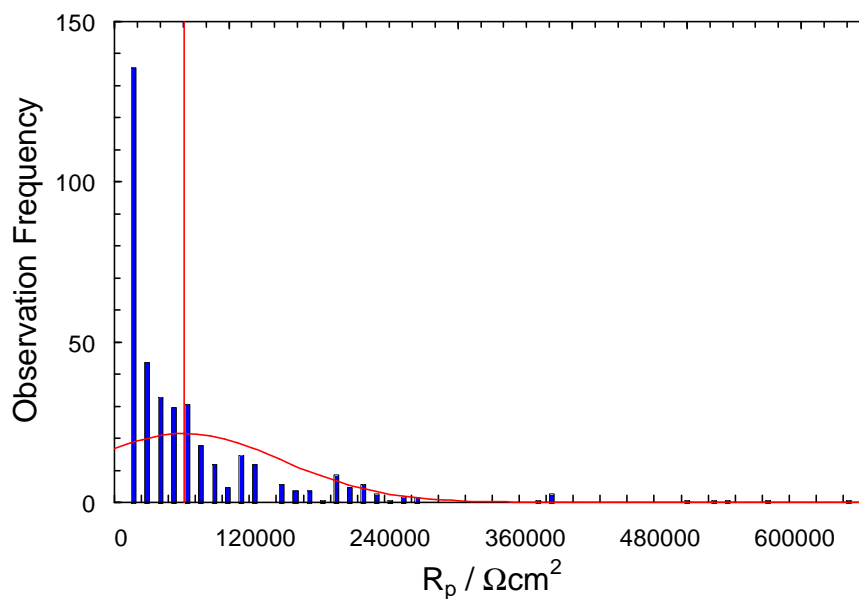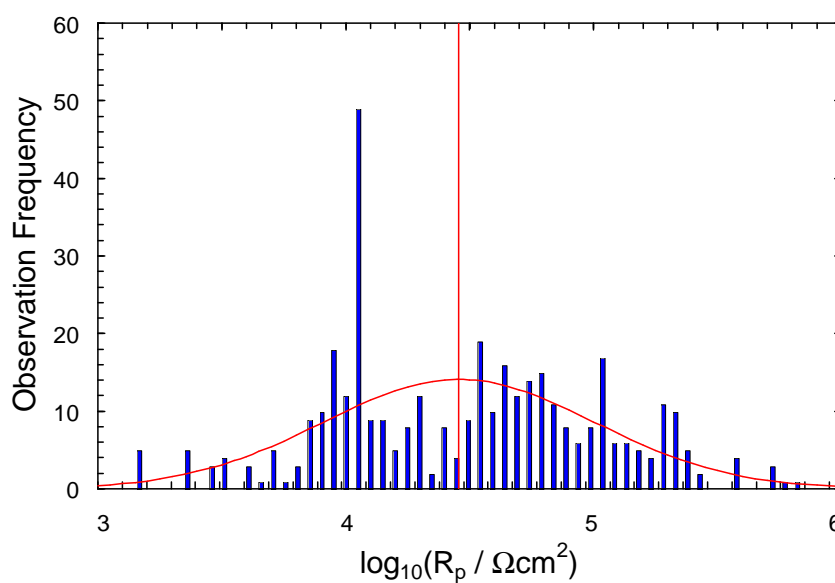
Figure C-1: Histograms of the polarization resistance of skin immersed in mono-valent electrolyte. (a) Measured values. (b) Data transformed by the base 10 logarithm.
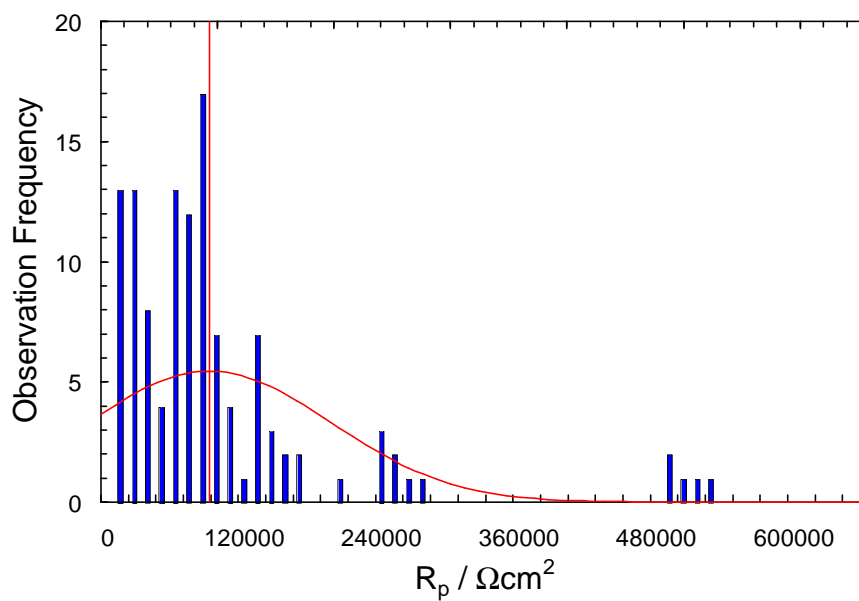
(a)
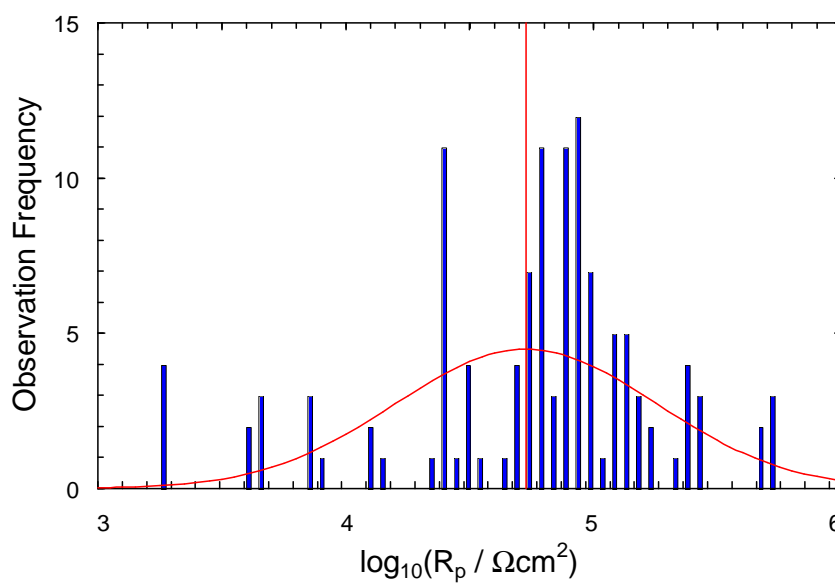
(b)

Figure C-2: Histograms of polarization resistance of skin immersed in divalent electrolyte. (a) Distribution of measured values. (b) Data transformed by the base 10 logarithm.
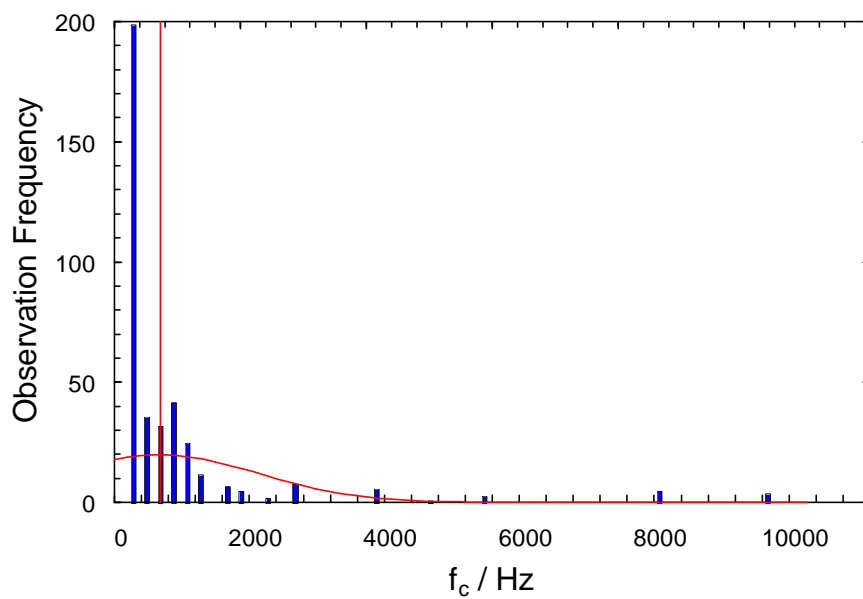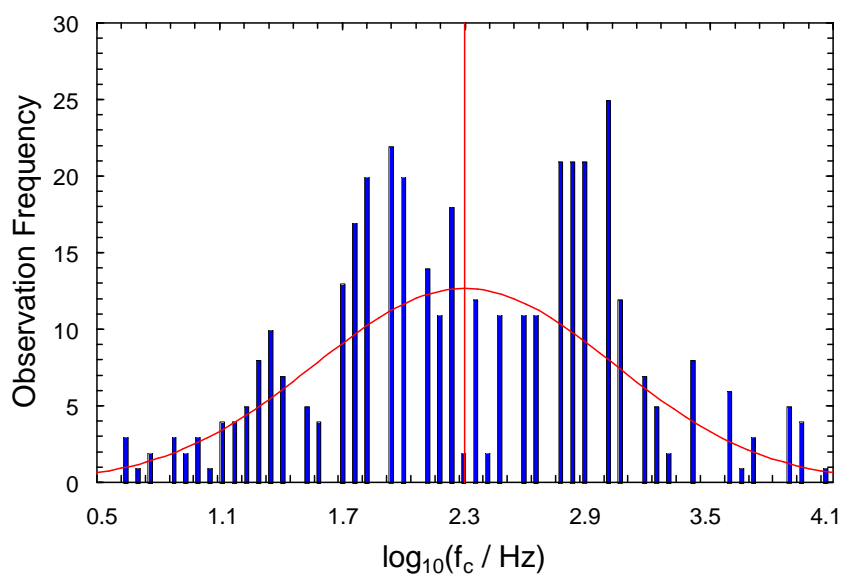
Figure C-3: Histograms of skin critical frequency for pieces immersed in monovalent electrolyte. (a) Measured values. (b) Data transformed by the base 10 logarithm.
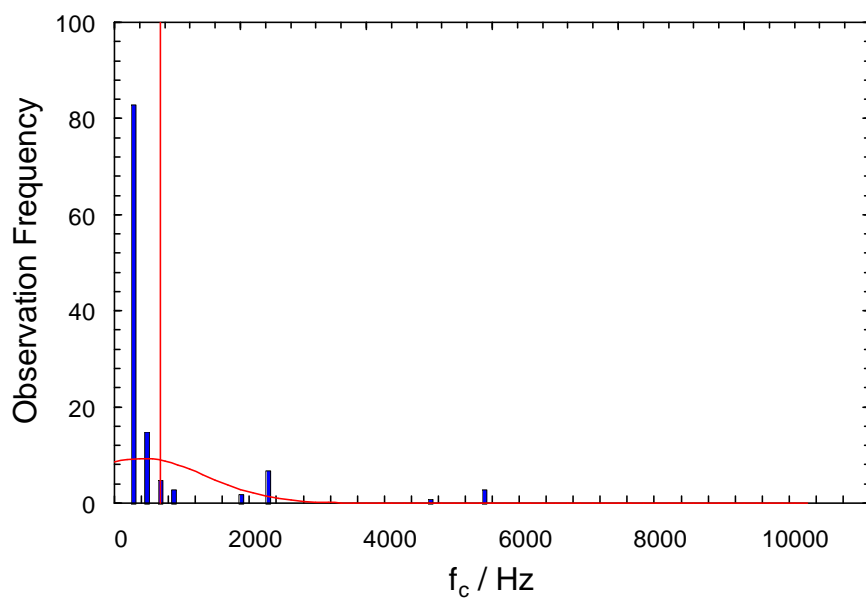
(a)
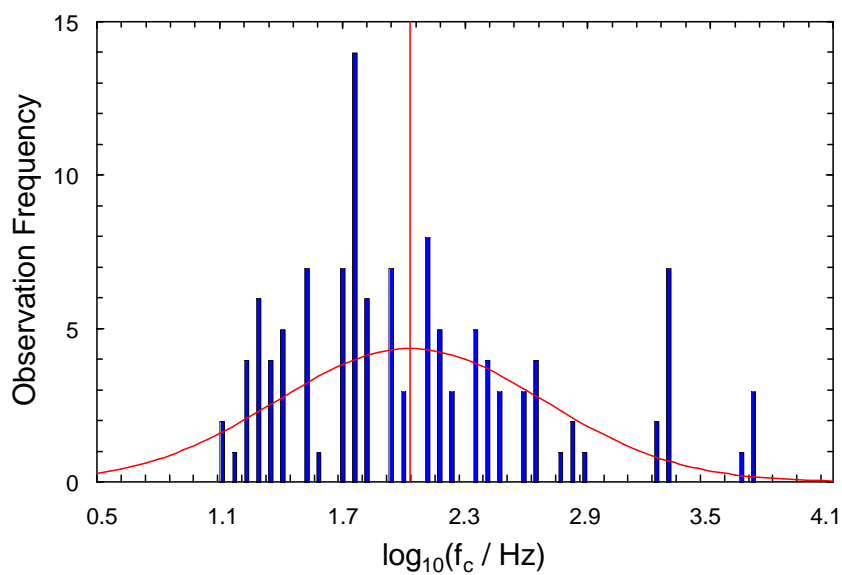
(b)

Figure C-4: Histograms of the critical frequency of skin immersed in divalent electrolyte. (a) Distribution of measured values. (b) Data transformed by the base 10 logarithm.

REFERENCES

1. G. B. Kasting and L. A. Bowman, "DC Electrical Properties of Frozen, Excised Human Skin," *Pharmaceurlcal Research*, **7** (1990) 134–143.

2. D. Panescu, K. P. Cohen, J. G. Webster, and R. A. Stratbucker, "The Mosaic Electrical Characteristics of the Skin," *IEEE Transactions on Biomedical Engineering*, **40** (1993) 434–439.

3. M. R. Prausnitz, "The Effects of Electric Current Applied to Skin: A Review for Transdermal Drug Delivery," *Advanced Drug Delivery Reviews*, **18** (1996) 395–425.

4. H. Schaefer and T. E. Redelmeier, *Skin Barrier: Principles of Percutaneous Absorption* (New York: Karger, 1996).

5. M. Orkin, H. I. Maibach, and M. V. Dahl, editors, *Dermatology*, 1st edition (Norwalk, Connecticut: Appleton and Lange, 1991).

6. A. F. Kydonieus and B. Berner, *Transdermal Delivery of Drugs, Volume I* (Boca Raton, FL: CRC Press, 1987).

7. L. A. Goldsmith, editor, *Biochemistry and Molecular Biology of the Skin* (New York: Oxford University Press, 1991).

8. S. L. Moschella and H. J. Hurley, editors, *Dermatology*, 3rd edition (Philadelphia: W.B. Saunders and Company, 1992).

9. I. M. Leigh, E. B. Lane, and F. M. Watt, editors, *The Keratinocyte Handbook* (Cambridge, Great Britain: Cambridge University Press, 1994).

10. A. K. Banga, *Electrically Assisted Transdermal and Topical Drug Delivery* (Bristol, PA: Taylor and Francis, Inc., 1998).

11. K. A. Holbrook, *Ultrastructure of the Epidermis: Chapter 1 of the Keratinocyte Handbook, edited by Leigh, I. M. and Lane, E. B. and Watt, F. M.* (Cambridge, Great Britain: Cambridge University Press, 1994) 3–39.

12. T. M. Suhonen, J. A. Bouwstra, and A. Urtti, "Chemical Enhancement of Percutaneous Absorption in Relation to Stratum Corneum Structural Alterations," *Journal of Controlled Release*, **59** (1999) 149–161.

13. R. J. Scheuplein and I. H. Blank, "Permeability of the Skin," *Physiological Reviews*, **51** (1971) 702–747.

14. M. A. Lampe, A. L. Burlingame, J. Whitney, M. L. Williams, B. E. Brown, E. Roitman, and P. M. Elias, "Human Stratum Corneum Lipids: Characterization and Regional Variations," *Journal of Lipid Research*, **24** (1983) 120–129.

15. H. Wakita, K. Nishimura, and M. Takigawa, "Composition of Free Long-Chain(Sphingoid) Bases in Stratum Corneum of Normal and Pathologic Human Skin Conditions," *The Journal of Investigative Dermatology*, **99** (1992) 617–622.

16. L. Norlén, I. Nicander, B. Rozell, S. Ollmar, and B. Forslind, "Inter- and Intra-Individual Differences in Human Stratum Corneum Lipid Content Related to Physical Parameters of Skin Barrier Function in vivo," *Journal of Investigative Dermatology*, **112** (1999) 72–77.

17. N. Y. Schürer, G. Plewig, and P. M. Elias, "Stratum Corneum Lipid Function," *Dermatologica*, **183** (1991) 77–94.

18. N. Farinelli and E. Berardesca, *The Skin Integument: Variation Relative to Sex, Age, Race, and Body Region: Chapter 2.2 of Handbook of Non-Invasive Methods and the Skin, edited by Serup, J. and Jemec, J. B. E.* (Boca Raton, Florida: CRC Press, 1995) 23–27.

19. F. Parker, *Structure and Function of the Skin: Chapter 1 in Dermatology edited by Orkin, M. and Maibach, H. I. and Dahl, M. V.*, 1st edition (Norwalk, Connecticut: Appleton and Lange, 1991).

20. J. B. Phipps, R. V. Padmanabhan, and G. A. Lattin, "Transport of Ionic Species Through Skin," *Solid State Ionics*, **28** (1988) 1778–1783.

21. G. F. Odland, *Structure of the Skin: Chapter 1 of Biochemistry and Physiology of the Skin, edited by Goldsmith, L. A.* (New York: Oxford University Press, 1991) 3–62.

22. D. T. Downing, "Lipid and Protein Structures in the Permeability Barrier of Mammalian Epidermis," *Journal of Lipid Research*, **33** (1992) 301–313.

23. J. E. Riviere and M. C. Heit, "Electrically-Assisted Transdermal Drug Delivery," *Pharmaceutical Research*, **14** (1997) 687–697.

24. B. Forslind, "A Domain Mosaic Model of the Skin Barrier," *Acta Dermato-Venereologica*, **74** (1994) 1–6.

25. R. F. Rushmer, K. J. K. Buettner, J. M. Short, and G. F. Odland, "The Skin," *Science*, **154** (1966) 343–348.

26. R. J. Scheuplein and R. L. Bronaugh, *Percutaneous Absorption: Chapter 58 in Biochemistry and Physiology of the Skin, edited by Goldsmith, L. A.* (New York: Oxford University Press, 1983) 1255–1295.

27. K. Tojo, "Mathematical Model of Iontophoretic Transdermal Drug Delivery," *Journal of Chemical Engineering of Japan*, **22** (1989) 512–518.

28. W. H. M. Craane-van Hinsberg, J. C. Verhoef, L. J. Bax, H. E. Junginger, and H. E. Boddé, "Role of Appendages in Skin Resistance and Iontophoretic Peptide Flux: Human Versus Snake Skin," *Pharmaceutical Research*, **12** (1995) 1506–1512.

29. S. Grimnes, "Pathways of Ionic Flow Through Human Skin in vivo," *Acta Dermato-Venereologica*, **64** (1984) 93–98.

30. C. Cullander and R. H. Guy, "Sites of Iontophoretic Current Flow Into the Skin: Identification and Characterization with the Vibrating Probe Electrode," *Journal of Investigative Dermatology*, **97** (1991) 55–64.

31. S. T. Kinsey, T. S. Moerland, L. McFadden, and B. R. Locke, "Spatial Resolution of Transdermal Water Mobility Using NMR Microscopy," *Magnetic Resonance Imaging*, **15** (1997) 939–947.

32. J. Hadgraft, "Structure Activity Relationships and Percutaneous Absorption," *Journal of Controlled Release*, **15** (1991) 221–226.

33. P. E. Bowden, *Keratins and Other Epidermal Proteins: Chapter 2 of Molecular Aspects of Dermatology, edited by Priestley, G. C.* (New York: John Wiley and Sons, 1993) 19–54.

34. J. E. Shaw, M. Prevo, R. Gale, and S. I. Yum, *Percutaneous Absorption: Chapter 55 of Physiology, Biochemistry and Molecular Biology of the Skin edited by Goldsmith, L. A.* (New York: Oxford University Press, 1991) 1255–1295.

35. P. W. Wertz and B. van den Bergh, "The Physical, Chemical and Functional Properties of Lipids in the Skin and Other Biological Barriers," *Chemistry and Physics of Lipids*, **91** (1998) 85–96.

36. L. Landmann, "Epidermal Permeability Barrier: Transformation of Lamellar Granule-Disks into Intercellular Sheets by a Membrane-Fusion Process, a Freeze-Fracture Study," *Journal of Investigative Dermatology*, **87** (1986) 202–209.

37. K. C. Madison, D. C. Swartzendruber, P. W. Wertz, and D. T. Downing, "Presence of Intact Intercellular Lipid Lamellae in the Upper Layers of the Stratum Corneum," *Journal of Investigative Dermatology*, **88** (1987) 714–718.

38. D. C. Swartzendruber, P. W. Wertz, D. J. Kitko, K. C. Madison, and D. T. Downing, "Molecular Models of the Intercellular Lipid Lamellae in Mammalian Stratum Corneum," *The Journal of Investigative Dermatology*, **92** (1989) 251–257.

39. H. J. Yardley and R. Summerly, "Lipid Composition and Metabolism in Normal and Diseased Epidermis," *Pharmacology and Therapeutics*, **13** (1981) 357–383.

40. R. J. Scheuplein, "Mechanism of Percutaneous Adsorption. I. Routes of Penetration and the Influence of Solubility," *The Journal of Investigative Dermatology*, **45** (1965) 334–346.

41. A. G. Matoltsy, A. M. Downes, and T. M. Sweeney, "Studies of the Epidermal Water Barrier Part II. Investigation of the Chemical Nature of the Water Barrier," *Journal of Investigative Dermatology*, **50** (1968) 19–26.

42. R. O. Potts, G. M. Guia, M. L. Francoeur, V. H. M. Mak, and R. H. Guy, "Mechanism and Enhancement of Solute Transport Across the Stratum Corneum," *Journal of Controlled Release*, **15** (1991) 249–260.

43. D. J. Bibel, R. Aly, S. Shah, and H. R. Shinefield, "Sphingosines: Antimicrobial Barriers of the Skin," *Acta Dermato-Venereologica*, **73** (1993) 407–411.

44. S. Ollmar, A. Eek, F. Sundström, and L. Emtestam, "Electrical Impedance for Estimation of Irritation in Oral Mucosa and Skin," *Medical Progress through Technology*, **21** (1995) 29–37.

45. A. S. Michaels, S. K. Chandrasekaran, and J. E. Shaw, "Drug Permeation Through Human Skin: Theory and in in vitro Experimental Measurement," *AIChE Journal*, **21** (1975) 985–996.

46. P. M. Elias, "Epidermal Lipids, Barrier Function, and Desquamation," *Journal of Investigative Dermatology*, **80** (1983) 44s–49s.

47. I. H. Blank, "Further Observations on Factors Which Influence the Water Content of the Stratum Corneum," *Journal of Investigative Dermatology*, **21** (1953) 259–271.

48. S. Monash, "Location of the Superficial Epithelial Barrier to Skin Penetration," *Journal of Investigative Dermatology*, **29** (1957) 367–376.

49. S. Monash and H. Blank, "Location and Re-formation of the Epithelial Barrier to Water Vapor," *Journal of Investigative Dermatology*, **78** (1958) 710–714.

50. T. Yamamoto and Y. Yamamoto, "Electrical Properties of the Epidermal Stratum Corneum," *Medical and Biological Engineering*, **14** (1976) 151–158.

51. K. Tojo, Y. W. Chien, C. C. Chiang, and P. R. Keshary, "Effect of Stratum Corneum Stripping on Skin Penetration of Drug," *Journal of Chemical Engineering of Japan*, **21** (1988) 544–546.

52. Y. N. Kalia, F. Pirot, R. O. Potts, and R. H. Guy, "Ion Mobility Across Human Stratum in vivo," *Journal of Parmaceutical Sciences*, **87** (1998) 1508–1511.

53. R. T. Tregear, "Interpretation of Skin Impedence Measurement," *Nature*, **205** (1965) 600–601.

54. R. O. Potts and M. L. Francoeur, "Lipid Biophysics of Water Loss Through the Skin," *Proceedings of the National Academy of Sciences of the United States of America*, **87** (1990) 3871–3873.

55. S. A. Long, P. W. Wertz, J. S. Strauss, and D. T. Downing, "Human Stratum Corneum Polar Lipids and Desquamation," *Archives of Dermatological Research*, **277** (1985) 284–287.

56. P. M. Elias, "Epidermal Barrier Function: Intercellular Lamellar Lipid Structures, Origin, Composition and Metabolism," *Journal of Controlled Release*, **15** (1991) 199–208.

57. S. Naito, M. Hoshi, and S. Yagihara, "Microwave Dielectric Analysis of Human Stratum Corneum in vivo," *Biochimica et Biophsica Acta*, **1381** (1998) 293–304.

58. E. R. Scott and H. S. White, "Direct Imaging of Ionic Pathways in Stratum Corneum Using Scanning Electrochemical Microscopy," *Solid State Ionics*, **53-6** (1992) 176–183.

59. D. A. van Hal, E. Jeremiasse, H. E. Junginger, F. Spies, and J. A. Bouwstra, "Structure of Fully Hydrated Human Stratum Corneum: A Freeze-Fracture Electron Microscopy Study," *The Journal of Investigative Dermatology*, **106** (1996) 89–95.

60. Y. A. Chizmadzhev, A. V. Indenbom, P. I. Kuzmin, S. V. Galichenko, J. C. Weaver, and R. O. Potts, "Electrical Properties of Skin at Moderate Voltages: Contribution of Appendageal Macropores," *Biophysical Journal*, **74** (1998) 843–856.

61. P. W. Wertz, K. C. Madison, and D. T. Downing, "Covalently Bound Lipids of Human Corneum Stratum," *The Journal of Investagative Dermatology*, **92** (1989) 109–111.

62. H. E. Boddé, I. van den Brink, H. K. Koerten, and F. H. N. de Hann, "Visualization of in vitro Percutaneous Penetration of Mercuric Chloride; Transport Through Intercellular Space Versus Cellular Uptake Through Desmosomes," *Journal of Controlled Release*, **15** (1991) 227–236.

63. S. Motta, M. Monti, S. Sesana, R. Caputo, S. Carelli, and R. Ghidoni, "Ceramide Composition of the Psoriatic Scale," *Biochimica et Biophysica Acta*, **1182** (1993) 147–151.

64. N. Kitson, J. Thewalt, M. Lafleur, and M. Bloom, "A Model Membrane Approach to the Epidermal Permeability Barrier," *Biochemistry*, **33** (1994) 6707–6715.

65. G. Grubauer, K. R. Feingold, R. M. Harris, and P. M. Elias, "Lipid Content and Lipid Type as Determinants of the Epidermal Permeability Barrier," *Journal of Lipid Research*, **30** (1989) 89–96.

66. S. Zellmer and J. Lasch, "Individual Variation of Human Plantar Stratum Corneum Lipids, Determined By Automated Multiple Development of High-Performance Thin-Layer Chromatography Plates," *Journal of Chromatography B*, **691** (1997) 321–329.

67. P. W. Wertz, "The Nature of the Epidermal Barrier: Biochemical Aspects," *Advanced Drug Delivery Reviews*, **18** (1996) 283–294.

68. J. P. Vietzke, M. Strassner, and U. Hintze, "Separation and Identification of Ceramides in the Human Stratum Corneum by High-Performance Liquid Chromatography coupled with Electrosprary Ionization Mass Sepectrometry and Electrospray Multiple-stage Mass Spectromety Profiling," *Chromatographia*, **50** (1999) 15–20.

69. J. A. Bouwstra, F. E. R. Dubbelaar, G. S. Gooris, A. M. Weerheim, and M. Ponec, "The Role of Ceramide Composition in the Lipid Organisation of the Skin Barrier," *Biochimica et Biophysica Acta*, **1419** (1999) 127–136.

70. M. Lafleur, "Phase Behavior of Model Stratum Corneum Lipid Mixtures: an Infrared Spectroscopy Investigation," *Canadian Journal of Chemistry*, **76** (1998) 1501–1511.

71. W. Abraham and D. T. Downing, "Deuterium NMR Investigation of Polymorphism in Stratum Corneum Lipids," *Biochimica et Biophysica Acta*, **1068** (1991) 189–194.

72. J. B. Finean and R. H. Michell, *Isolation, Composition and General Structure of Membranes: Chapter 1 of Membrane Structure, edited by Finean, J. B. and Michell, R. H.* (Amsterdam, Netherlands: Elsevier: North-Holland Biomedical Press, 1981) 1–36.

73. R. B. Gennis, *Biomembranes: Molecular Structure and Function* (New York, NY: Springer-Verlag, 1989).

74. J. F. Tocanne and J. Teissié, "Ionization of Phospholipids and Phospholipid-Supported Interfacial Lateral Diffusion of Protons in Membrane Model Systems," *Biochimica et Biophysica Acta*, **1031** (1990) 111–142.

75. R. Lange-Lieckfieldt and G. Lee, "Use of a Model Lipid Matrix to Demonstrate the Dependence of the Stratum Corneum's Barrier Properties on Its Internal Geometry," *Journal of Controlled Release*, **20** (1992) 183–194.

76. L. Stryer, *Biochemistry*, 3rd edition (New York: W. H. Freeman and Company, 1988).

77. M. Edidin, *Molecular Motion and Membrane Organization and Function: Chapter 2 of Membrane Structure, edited by Finean, J. B. and Michell, R. H.* (Amsterdam, Netherlands: Elsevier: North-Holland Biomedical Press, 1981) 37–82.

78. P. R. Cullis and M. J. Hope, *Chapter 1: Physical Properties and Functional Roles of Lipids in Membranes in Biochemistry of Lipids, Lipoproteins and Membranes, edited by Vance, D. E. and Vance, J. E.* (Amsterdam, Netherlands: Elsevier, 1991) 1–41.

79. P. W. Wertz, M. C. Miethke, S. A. Long, J. S. Strauss, and D. T. Downing, "The Composition of the Ceramides from Human Stratum Corneum and from Comedones," *The Journal of Investigative Dermatology*, **84** (1985) 410–412.

80. T. Gildenast and J. Lasch, "Isolation of Ceramide Fractions from Human Stratum Corneum Lipid Extracts by High-Performance Liquid Chromatography," *Biochimica et Biophysica Acta*, **1346** (1997) 69–74.

81. R. H. Guy and J. Hadgraft, "Physicochemical Aspects of Percutaneous Penetration and Its Enhancement," *Pharmaceutical Research*, **5** (1988) 753–758.

82. C. A. Squier, P. Cox, and P. W. Wertz, "Lipid Content and Water Permeability of Skin and Oral Mucosa," *Journal of Investigative Dermatology*, **96** (1991) 123–126.

83. M. E. DeVries, H. E. Boddé, J. C. Verhoef, M. Ponec, W. H. M. Craane-van Hinsberg, and H. E. Junginger, "Localization of the Permeability Barrier Inside Porcine Buccal Mucosa: A Combined in vitro Study of Drug Permeability, Electrical Resistance and TIssue Morphology," *International Journal of Pharmaceutics*, **76** (1991) 25–35.

84. J. A. Bouwstra, G. S. Gooris, F. E. R. Dubbelaar, A. M. Weerheim, A. M. Ijerman, and M. Ponec, "The Role of Ceramide 1 in the Molecular Organisation of Stratum Corneum Lipids," *Journal of Lipid Research*, **39** (1998) 186–196.

85. D. Chapman, *Lipid Dynamics of Cell Membranes : Chapter 2 of Cell Membranes : Biochemistry, Cell Biology, and Pathology, edited by Weissmann, Gerald and Claiborne, Robert* (New York: HP Publishing Company, Inc., 1975) 13–23.

86. K. Matsuzaki, T. Imaoka, M. Asano, and K. Miyajima, "Development of a Model Membrane System Using Stratum Corneum Lipids for Estimation of Drug Skin Permeability," *Chemical and Pharmaceutical Bulletin*, **41** (1993) 575–579.

87. G. S. K. Pilgram, A. M. Engelsma-van Pelt, G. T. Oostergetel, H. K. Koerten, and J. A. Bouwstra, "Study on the Lipid Organization of Stratum Corneum Lipid Models by (Cryo-) Electron Diffraction," *Journal of Lipid Research*, **39** (1998) 1669–1676.

88. R. Neubert, W. Rettig, S. Wartewig, M. Wegener, and A. Wienhold, "Structure of Stratum Corneum Lipids Characterized By FT-Raman Spectroscopy and DSC. II. Mixtures of Ceramides and Saturated Fatty Acids," *Chemistry and Physics of Lipids*, **89** (1997) 3–14.

89. S. Zellmer, I. Zimmermann, C. Selle, B. Sternberg, W. Pohle, and J. Lasch, "Physicochemical Characterisation of Human Stratum Corneum Lipid Liposomes," *Chemistry and Physics of Lipids*, **94** (1998) 97–108.

90. D. Bangham, Alec, *Models of Cell Membranes : Chapter 3 of Cell Membranes : Biochemistry, Cell Biology, and Pathology, edited by Weissmann, Gerald and Claiborne, Robert* (New York: HP Publishing Company, Inc., 1975) 24–34.

91. S. Y. E. Hou, A. K. Mitra, S. H. White, G. K. Menon, R. Ghadially, and P. M. Elias, "Membrane Structures in Normal and Essential Fatty Acid - Deficient

Stratum Corneum: Characterization by Ruthenium Tetroxide Staining and X-Ray Diffraction," *The Journal of Investigative Dermatology*, **96** (1991) 215–223.

92. M. Fartasch, I. D. Bassukas, and T. L. Diepgen, "Structural Relationship Between Epidermal Lipid Lamellae, Lamellar Bodies and Desmosomes in Human Epidermis: An Ultrastructural Study," *British Journal of Dermatology*, **128** (1993) 1–9.

93. B. A. I. van den Bergh, D. C. Swartzendruber, A. Bos-Van Der Geest, J. J. Hoogstraate, A. H. G. J. Schrijvers, H. E. Boddé, H. E. Junginger, and J. A. Bouwstra, "Development of an Optimal Protocol for the Ultrastructural Examination of Skin by Transmission Electron Microscopy," *Journal of Microscopy*, **187** (1997) 125–133.

94. S. H. White, D. Mirejovsky, and G. I. King, "Structure of Lamellar Lipid Domains and Corneocyte Envelopes of Murine Stratum Corneum," *Biochemistry*, **27** (1988) 3725–3732.

95. J. A. Bouwstra, G. S. Gooris, J. A. van der Spek, and W. Bras, "Structural Investigations of Human Stratum Corneum by Small-Angle X-Ray Scattering," *Journal of Investigative Dermatology*, **97** (1991) 1005–1012.

96. J. A. Bouwstra, G. S. Gooris, M. A. Salomons-de Vries, J. A. van der Spek, and W. Bras, "Structure of Human Stratum Corneum as a Function of Temperature and Hydration: A Wide-Angle-X-Ray Diffraction Study," *International Journal of Pharmaceutics*, **84** (1992) 205–216.

97. P. J. Caspers, G. W. Lucassen, R. Wolthuis, H. A. Bruining, and G. J. Puppels, "In vitro and in vivo Raman Spectroscopy of Human Skin," *Biospectroscopy*, **4** (1998) S31–S39.

98. D. L. A. de Faria and M. A. de Souza, "Raman Spectra of Human Skin and Nail Excited in the Visible Region," *Journal of Raman Spectroscopy*, **30** (1999) 169–171.

99. G. M. Golden, D. B. Guzek, R. R. Harris, J. E. McKie, and R. O. Potts, "Lipid Thermotropic Transitions in Human Stratum Corneum," *Journal of Investigative Dermatology*, **86** (1986) 255–259.

100. B. Ongpipattanakul, M. L. Francoeur, and R. O. Potts, "Polymorphism in Stratum Corneum Lipids," *Biochimica et Biophysica Acta*, **1190** (1994) 115–122.

101. F. Pirot, Y. N. Kalia, A. l. Stinchcomb, G. Keating, A. Bunge, and R. H. Guy, "Characterization of the Permeability Barrier of Human Skin in vivo," *Proceedings of the National Academy of Sciences of the United States of America*, **94** (1997) 1562–1567.

102. H. Tanojo, H. E. Junginger, and H. E. Boddé, "In vivo Human Skin Permeability Enhancement by Oleic Acid; Transepidermal Water Loss and Fourier-Transform Infrared Spectroscopy Studies," *Journal of Controlled Release*, **47** (1997) 31–39.

103. M. J. Clancy, J. Corish, and O. I. Corrigan, "A Comparison of the Effects of Electrical Current and Penetration Enhancers on the Properties of Human Skin Using Spectroscopic (FTIR) and Calorimetric (DSC) Methods," *International Journal of Pharmaceutics*, **105** (1994) 47–56.

104. E. Dreassi, G. Ceramelli, L. Fabbri, F. Vocioni, P. Bartalini, and P. Corti, "Application of Near-infrared Reflectance Spectrometry in the Study of Atopy," *The Analyst*, **122** (1997) 767–770.

105. B. W. Barry, "Lipid-Protein-Partitioning Theory of Skin Penetration Enhancement," *Journal of Controlled Release,*, **15** (1991) 237–248.

106. T. Inoue, K. Tsujii, K. Okamoto, and K. Toda, "Differential Scanning Calorimetric Studies on the Melting Behavior of Water in Stratum Corneum," *Journal of Investigative Dermatology*, **86** (1986) 689–693.

107. B. W. Barry, "Mode of Action of Penetration Enhancers In Human Skin," *Journal of Controlled Release*, **6** (1987) 85–97.

108. J. A. Bouwstra, G. S. Gooris, J. A. van der Spek, S. Lavrijsen, and W. Bras, "The Lipid and Protein Structure of Mouse Stratum Corneum: A Wide and Small Angle Diffraction Study," *Biochimica et Biophysica Acta: Lipids and Lipid Metabolism*, **1212** (1994) 183–192.

109. J. A. Bouwstra, G. S. Gooris, W. Bras, and D. T. Downing, "Lipid Organization in Pig Stratum Corneum," *Journal of Lipid Research*, **36** (1995) 685–695.

110. S. M. Gruner, P. R. Cullis, M. J. Hope, and C. P. S. Tilcock, "Lipid Polymorphism : The Molecular Basis of Nonbilayer Phases," *Annual Reviews of Biophysics and Biophysical Chemistry*, **14** (1985) 211–238.

111. Y. W. Chien, O. Siddiqui, W. M. Shi, and J. C. Liu, "Transdermal Iontophoretic Delivery of Therapeutic Peptides/Proteins 1. Insulin," *Annals of the New York Academy of Sciences*, **507** (1987) 32–51.

112. A. K. Banga and Y. W. Chien, "Iontophoretic Delivery of Drugs: Fundamentals, Developments and Biomedical Applicatons," *Journal of Controlled Release*, **7** (1988) 1–24.

113. R. R. Warner, M. C. Myers, and D. A. Taylor, "Electron Probe Analysis of Human Skin: Determination of the Water Concentration Profile," *The Journal of Investigative Dermatology*, **90** (1988) 78–85.

114. V. Aguilella, M. Belaya, and V. Levadny, "Passive Transport of Small Ions Through Human Stratum Corneum," *Journal of Controlled Release*, **44** (1997) 11–18.

115. V. H. W. Mak, R. O. Potts, and R. H. Guy, "Does Hydration Affect Intercellular Lipid Organization in the Stratum Comeum?" *Pharmaceutical Research,*, **8** (1991) 1064–1065.

116. L. A. R. M. Pechtold, W. Abraham, and R. O. Potts, "The Influence of an Electric Field on Ion and Water Accessibility to Stratum Cornenm Lipid Lamellae," *Pharmaceutical Research*, **13** (1996) 1168–1173.

117. S. J. Singer and G. L. Nicolson, "The Fluid Mosaic Model of the Structure of Cell Membranes," *Science*, **175** (1972) 720–731.

118. J. B. Caban, T. S. Moerland, S. J. Gibbs, L. McFadden, and B. R. Locke, "Transdermal Water Mobility in the Presence of Electrical Fields Using MR Microscopy," *Magnetic Resonance Imaging*, **17** (1999) 1183–1191.

119. M. E. Johnson, D. Blankschtein, and R. Langer, "Evaluation of Solute Permeation Through the Stratum Corneum: Lateral Bilayer Diffusion as the Primary Transport Mechanism," *Journal of Pharmaceutical Sciences*, **86** (1997) 1162–1172.

120. N. H. Yoshida and M. S. Roberts, "Solute Molecular Size and Transdermal Iontophoresis Across Excised Human Skin," *Journal of Controlled Release*, **25** (1993) 177–195.

121. W. I. Higuchi, S. K. Li, A. H. Ghanem, H. G. Zhu, and Y. Song, "Mechanistic Aspects of Iontophoresis in Human Epidermal Membrane," *Journal of Controlled Release*, **62** (1999) 13–23.

122. K. S. Li, A. H. Ghanem, K. D. Peck, and W. I. Higuchi, "Characterization of the Transport Pathways Induced During Low to Moderate Voltage Iontophoresis in Human Epidermal Membrane," *Journal of Pharmaceutical Sciences*, **87** (1998) 40–48.

123. K. D. Peck, A. H. Ghanem, and W. I. Higuchi, "Hindered Diffusion of Polar Molecules Through and Effective Pore Radii Estimates of Intact and Ethanol Treated Human Epidermal Membrane," *Pharmaceutical Research*, **11** (1994) 1306–1314.

124. M. S. Roberts, P. M. Lai, and Y. G. Anissimov, "Epidermal Iontophoresis: I. Development of the Ionic Mobility-Pore Model," *Pharmaceutical Research*, **15** (1998) 1569–1578.

125. R. Elderberg, *Electrical Properties of the Skin, Chapter 15 of Biophysical Properties of the Skin, Edited by Elden, H. R.* (New York: Wiley-Interscience, 1971) 513–541.

126. Y. W. Chien, O. Siddiqui, W. Shi, P. Lelawongs, and J. C. Liu, "Direct Current Iontophoretic Transdermal Delivery of Peptide and Protein Drugs," *Journal of Pharmaceutical Sciences*, **78** (1989) 376–383.

127. H. M. Sheu, S. C. Chao, T. W. Wong, J. Y. Y. Lee, and J. C. Tsai, "Human Skin Surface Lipid Film: An Ultrastructural Study and Interaction with Corneocytes and Intercellular Lipid Lamellae of the Stratum Corneum," *British Journal of Dermatology*, **140** (1999) 385–391.

128. A. Zlotogorski, "Distribution of Skin Surface pH on the Forehead and Cheek of Adults," *Archives of Dermatological Research*, **279** (1987) 398–401.

129. A. Raza, *Cutaneous Microbiology: Chapter 4 in Dermatology edited by Orkin, M. and Maibach, H. I. and Dahl, M. V.*, 1st edition (Norwalk, Connecticut: Appleton and Lange, 1991) 22–25.

130. K. Sato, K. H. Kang, and F. Sato, *Eccrine Sweat Glands: Chapter 26 of Biochemistry and Physiology of the Skin, edited by Goldsmith, L. A.* (New York: Oxford University Press, 1991) 741–762.

131. R. R. Burnette and B. Ongpipattanakul, "Characterization of the Permselective Properties of Excised Human Skin During Iontophoresis," *Journal of Pharmaceutical Sciences*, **76** (1987) 765–773.

132. G. B. Kasting and J. C. Keister, "Application of Electrodiffusion Theory for a Homogeneous Membrane to Iontophoretic Transport Through Skin," *Journal of Controlled Release*, **8** (1989) 195–210.

133. J. D. DeNuzzio and B. Berner, "Electrochemical and Iontophoretic Studies of Human Skin," *Journal of Controlled Release*, **11** (1990) 105–112.

134. Y. W. Chien, P. Lelawongs, O. Siddiqui, Y. Sun, and W. M. Shi, "Facilitated Transdermal Delivery of Therapeutic Peptides and Proteins by Iontophoretic Delivery Devices," *Journal of Controlled Release*, **13** (1990) 263–278.

135. J. Hirvonen and R. H. Guy, "Transdermal Iontophoresis: Modulation of Electroosmosis by Polypeptides," *Journal of Controlled Release*, **50** (1998) 283–289.

136. J. S. Newman, *Electrochemical Systems, Second Edition* (Inglewood Cliffs, NJ: Prentice Hall, 1991).

137. A. J. Bard and L. R. Faulkner, *Electrochemical Methods: Fundamentals and Applications* (New York: John Wiley and Sons, 1980).

138. S. Grimnes, "Skin Impedance and Electro-Osmosis in the Human Epidermis," *Medical and Biological Engineering and Computing*, **21** (1983) 739–749.

139. S. Del Terzo, C. R. Behl, and R. A. Nash, "Iontophoretic Transport of a Homologous Series of Ionized and Nonionized Model Compounds: Influence of Hydrophobicity and Mechanistic Interpretation," *Pharmaceutical Research*, **6** (1989) 85–90.

140. S. Sims, W. I. Higuchi, and V. Srivasan, "Skin Alteration and Convective Solvent Flow Effects During Iontophoresis II. Monovalent Anion and Cation Transport Across Human Skin," *Pharmaceutical Research*, **9** (1992) 1402–1409.

141. M. B. Delgado-Charro and R. H. Guy, "Characterization of Convective Solvent Flow During Iontophoresis," *Pharmaceutical Research*, **11** (1994) 929–935.

142. R. van der Geest, F. Hueber, F. C. Szoka, and R. H. Guy, "Iontophoresis of Bases, Nucleosides, and Nucleotides," *Pharmaceutical Research*, **13** (1996) 553–558.

143. P. M. Lai and M. S. Roberts, "Epidermal Iontophoresis: II. Application of the Ionic Mobility-Pore Model to the Transport of Local Anesthetics," *Pharmaceutical Research*, **15** (1998) 1579–1588.

144. J. Hirvonen, L. Murtomäki, and K. Kontturi, "Effect of Diffusion Potential, Osmosis and Ion-exchange on Transdermal Drug Delivery: Theory and Experiments," *Journal of Controlled Release*, **56** (1998) 33–39.

145. J. Hirvonen, L. Murtomäki, and K. Kontturi, "Experimental Verification of the Mechanistic Model for Transdermal Transport Including Iontophoresis," *Journal of Controlled Release*, **56** (1998) 169–174.

146. A. Luzardo-Alvarez, M. Rodriguez-Fernandez, J. Blanco-Mendez, R. H. Guy, and M. B. Delgado-Charro, "Iontophoretic Permselectivity of Mammalian Skin: Characterization of Hairless Mouse and Porcine Membrane Models," *Pharmaceutical Research*, **15** (1998) 984–987.

147. C. T. Costello and A. H. Jeske, "Iontophoresis: Applications in Transdermal Medication Delivery," *Physical Therapy (Pharmacology Series)*, **75** (1995) 554–563.

148. J. B. Phipps and J. R. Gyory, "Transdermal Ion Migration," *Advanced Drug Delivery Reviews*, **9** (1992) 137–176.

149. T. Yamamoto and Y. Yamamoto, "Dielectric Constant and Resistivity of Epidermal Stratum Corneum," *Medical and Biological Engineering*, **14** (1976) 494–500.

150. Y. N. Kalia, L. B. Nonato, and R. H. Guy, "The Effect of Iontophoresis on Skin Barrier Integrity: Non-invasive Evaluation by Impedance Spectroscopy and Transepidermal Water Loss," *Pharmaceutical Research*, **13** (1996) 957–960.

151. A. D. Woolfson, G. P. Moss, D. F. McCafferty, A. Lackermeier, and E. T. McAdams, "Changes in Skin A.C. Impedance Parameters in vivo During the Percutaneous Absorption of Local Anesthetics," *Pharmaceutical Research*, **16** (1999) 459–462.

152. Y. N. Kalia and R. H. Guy, "The Electrical Characteristics of Human Skin in vivo," *Pharmaceutical Research*, **12** (1995) 1605–1613.

153. T. Yamamoto and Y. Yamamoto, "Non-Linear Electrical Properties of Skin in the Low Frequency Range," *Medical and Biological Engineering and Computing*, **19** (1981) 302–310.

154. G. B. Kasting, "Theoretical Models for Iontophoretic Delivery," *Advanced Drug Delivery Reviews*, **9** (1992) 177–199.

155. S. Y. Oh, L. Lyung, D. Bommannan, R. H. Guy, and R. O. Potts, "Effect of Current, Ionic Strength and Temperature on the Electrical Properties of Skin," *Journal of Controlled Release*, **27** (1993) 115–125.

156. M. H. Friedman, *Principles and Models of Biological Transport* (New York: Springer-Verlag, 1986).

157. A. Y. Kabakov, "The Nature of Pacemaker Activity," *Biophysics*, **36** (1991) 628–636.

158. S. Kulkarni, A. K. Banga, and G. Betageri, "Transdermal Iontophoretic Delivery Colchicine Encapsulated in Liposomes," *Drug Delivery*, **3** (1996) 245–250.

159. M. Kirjavainen, J. Mönkkönen, M. Saukkosaari, R. Valjakka-Koskela, J. Kiesvaara, and A. Urtti, "Phospholipids Affect Stratum Corneum Lipid Bilayer Fluidity and Drug Partitioning into the Bilayers," *Journal of Controlled Release*, **58** (1999) 207–214.

160. J. C. Weaver, "Electroporation: A General Phenomenon for Manipulation Cells and Tissues," *Journal of Cellular Biochemistry*, **51** (1992) 426–435.

161. C. Featherstone, "Electroporation - An Effective Technique for Drug-Delivery and Gene-Therapy," *American Biotechnology Laboratory*, **11** (1993) 16.

162. R. Heller, M. Jaroszeski, A. Atkin, D. Moradpour, R. Gilbert, J. Wands, and C. Nicolau, "In vivo Gene Electroinjection and Expression in Rat Liver," *FEBS Letters*, **389** (1996) 225–228.

163. R. R. Burnette and T. M. Bagniefski, "Influence of Constant Current Iontophoresis on the Impedance and Passive Na^+ Permeability of Excised Nude Mouse Skin," *Journal of Pharmaceutical Sciences*, **77** (1988) 492–497.

164. S. S. Philbrick, *Characterization of Transdermal Delivery in vitro Using Optical and Electrochemical Impedance Spectroscopy*, Master's thesis, University of Florida (1998).

165. N. Monteiro-Riviere, A. Inman, and J. Riviere, "Identification of the Pathway of Iontophoretic Drug Delivery: Light and Ultrastructural Studies Using Mercuric Chloride in Pigs," *Pharmaceutical Research,*, **11** (1994) 251–256.

166. R. R. Burnette and B. Ongpipattanakul, "Characterization of the Pore Transport Properties and Tissue Alteration of Excised Human Skin During Iontophoresis," *Journal of Pharmaceutical Sciences*, **77** (1988) 132–137.

167. E. R. Scott, H. S. White, and J. B. Phipps, "Iontophoretic Transport Through Porous Membranes Using Scanning Electrochemical Microscopy: Application to in in vitro Studies of Ion Fluxes through Skin," *Analytical Chemistry*, **65** (1993) 1537–1545.

168. N. G. Turner and R. H. Guy, "Visualization and Quantitation of Iontophoretic Pathways Using Confocal Microscopy," *Journal of Investigative Dermatology Symposium*, **3** (1998) 136–142.

169. K. Tojo, C. C. Chiang, and Y. W. Chien, "Drug Permeation Across the Skin: Effect of Penetrant Hydrophilicity," *Journal of Pharmaceutical Sciences*, **76** (1987) 123–126.

170. P. M. Lai and M. S. Roberts, "An Analysis of Solute Structure-Human Epidermal Transport Relationships in Epidermal Iontophoresis Using the Ionic Mobility-Pore Model," *Journal of Controlled Release*, **58** (1999) 323–333.

171. A. K. Banga, M. Katakam, and R. Mitra, "Transdermal Iontophoretic Delivery and Degradation of Vasopressin Across Human Cadaver Skin," *International Journal of Pharmaceutics*, **116** (1995) 211–216.

172. N. H. Bellantone, S. Rim, M. L. Francoeur, and B. Rasadi, "Enhanced Percutaneous Absorption Via Iontophoresis I. Evaluation of an in vitro System and Transport of Model Compounds," *International Journal of Pharmaceutics*, **30** (1986) 63.

173. R. M. Brand and R. H. Guy, "Iontophoresis of Nicotine in vitro: Pulsatile Drug Delivery Across the Skin?" *Journal of Controlled Release*, **33** (1995) 285–292.

174. R. Brand, A. Wahl, and P. Iversen, "Effects of Size and Sequence on the Iontopheretic Delivery of Oligonucleotides," *Journal of Pharmaceutical Science*, **87** (1998) 49–52.

175. R. R. Burnette and D. Marrero, "Comparison Between the Iontophoretic and Passive Transport of Thyrotropin Releasing Hormone Across Nude Mouse Skin," *Journal of Pharmaceutical Science*, **75** (1986) 738.

176. L. L. Wearley, J.-C. Liu, and C. Y. W., "Iontophoresis-Facilitated Transdermal Delivery of Verapamil. I. In vitro Evaluation and Mechanistic Studies," *Journal of Controlled Release*, **8** (1989) 237–250.

177. E. Varghese and R. K. Khar, "Enhanced Skin Permeation of Diclofenac by Iontophoresis: in vitro and in vivo Studies," *Journal of Controlled Release*, **38** (1996) 21–27.

178. E. Manabe, S. Numajiri, K. Sugibayashi, and Y. Morimoto, "Analysis of Skin Permeation-Enhancing Mechanism of Iontophoresis Using Hydrodynamic Pore Theory," *Journal of Controlled Release*, **66** (2000) 149–158.

179. M. Heit, N. Monteiro-Riviere, F. Jayes, and J. Riviere, "Transdermal Iontophoretic Delivery of Luteinizing Hormone Releasing Hormone (LHRH): Effect of Repeated Administration," *Pharmaceutical Research*, **11** (1994) 1000–1003.

180. D. E. Goldman, "Potential, Impedance, and Rectification in Membranes," *Journal of General Physiology*, (1943) 37–60.

181. V. Srinivasan and W. I. Higuchi, "A Model for Iontophoresis Incorporating the Effect of Convective Solvent Flow," *International Journal of Pharmaceutics*, **60** (1990) 133–138.

182. K. Kontturi and L. Murtomäki, "Mechanistic Model for Transdermal Transport Including Iontophoresis," *Journal of Controlled Release*, **41** (1996) 177–185.

183. J. C. Keister and G. B. Kasting, "Ionic Mass Transport Through a Homogeneous Membrane in the Presence of a Uniform Electric Field," *Journal of Membrane Science*, **29** (1986) 155–167.

184. K. Tojo, C. C. Chiang, U. Doshi, and Y. W. Chien, "Stratum Corneum Reservoir Capacity Affecting Dynamics of Transdermal Drug Delivery," *Drug Development and Industrial Pharmacy*, **14** (1998) 561–572.

185. J. L. Anderson and J. A. Quinn, "Restricted Transport in Small Pores: A Model for Steric Exclusion and Hindered Particle Motion," *Biophysical Journal*, **14** (1974) 130–150.

186. W. D. Munch, L. P. Zester, and J. A. Anderson, "Rejection of Polyelectrolytes from Microporous Membranes," *Journal of Membrane Science*, **5** (1979) 77–102.

187. W. M. Deen, "Hindered Transport of Large Molecules in Liquid-Filled Pores," *AIChE Journal*, **33** (1987) 1409–1425.

188. M. Davidson and W. M. Deen, "Hydrodynamic Theory for the Hindered Transport of Flexible Macromolecules In Porous Membranes." *Journal of Membrane Science*, **35** (1988) 167–192.

189. B. C. Robertson and A. L. Zydney, "Hindered Protein Diffusion in Asymmetric Ultrafiltration Membranes with Highly Constricted Pores," *Journal of Membrane Science*, **49** (1990) 287–303.

190. G. A. Gerencser and B. R. Stevens, "Thermodynamics of Symport and Antiport Catalyzed by Cloned or Native Transporters," *Journal of Experimental Biology*, (1994) 1–17.

191. R. R. Burnette, *Iontophoresis. Chapter 11 of Transdermal Drug Delivery: Developmental Issues and Research Initiatives edited by J. Hadgraft and R. H. Guy* (New York: Marcel Dekker, 1989) 247–289.

192. T. Masada, W. I. Higuchi, V. Srinivasan, U. Rohr, J. Fox, C. R. Behl, and S. Pons, "Examination of Iontophoretic Transport of Ionic Drugs Across Skin: Baseline Studies with the Four-Electrode System," *International Journal of Pharmaceutics*, **49** (1989) 57–62.

193. V. Aguilella, K. Kontturi, L. Murtomäki, and P. Ramírez, "Estimation of the Pore Size and Charge Density in Human Cadaver Skin," *Journal of Controlled Release*, **32** (1994) 249–254.

194. O. Kedem and A. Katchalsky, "Thermodynamic Analysis of the Permeability of Biological Membranes to Non-Electrolyes," *Biochimica et Biophysica Acta*, **27** (1958) 229–246.

195. O. Kedem and A. Katchalsky, "Physical Interpretation of Phenomenological Coefficients of Membrane Permeability," *Journal of General Physiology*, **45** (1961) 143–179.

196. O. Kedem and A. Katchalsky, "Permeability of Composite Membranes 1. Electric Current, Volume Flow and Flow of Solute Through Membranes," *Transactions of the Faraday Society*, **59** (1963) 1918–1930.

197. M. J. Pikal, "Transport Mechanisms in Iontophoresis. I. A Theoretical model for the Effect of Electroosmotic Flow on Flux Enhancement in Transdermal Iontophoresis," *Pharmaceutical Research*, **7** (1990) 118–126.

198. N. A. Peppas and N. Sundaram, "An Analysis of Drug and Solute Transport Through Membranes Based on Potential Barriers," *Journal of Controlled Release*, **34** (1995) 37–42.

199. B. Hille, *Ionic Channels of Excitable Membranes*, 2nd edition (Sunderland, Massachusetts: Sinauer Associates, Inc., 1992).

200. Y. N. Kalia, F. Pirot, and R. H. Guy, "Homogeneous Transport in a Heterogeneous Membrane: Water Diffusion Across Human Stratum Corneum in vivo," *Biophysical Journal*, **71** (1996) 2692–2700.

201. R. van der Geest, D. A. R. Elshove, M. Danhof, A. P. M. Lavrijsen, and H. E. Boddé, "Non-Invasive Assessment of Skin Barrier Integrity and Skin Irritation Following Iontophoretic Current Application In Humans," *Journal of Controlled Release*, **41** (1996) 205–213.

202. R. Brand, P. Singh, E. Aspe-Carranza, H. I. Maibach, and R. H. Guy, "Acute Effects of Iontophoresis on Human Skin in vivo: Cutaneous Blood," *European Journal of Pharmaceutics and Biopharmaceutics*, **43** (1997) 133–138.

203. Y. N. Kalia and R. H. Guy, "Interaction Between Penetration Enhancers and Iontophoresis: Effect on Human Skin Impedance in vivo," *Journal of Controlled Release*, **44** (1997) 33–42.

204. D. Foley, J. Corish, and O. I. Corrigan, "Iontophoretic Delivery of Drugs Through Membranes Including Human Stratum-Corneum," *Solid State Ionics*, **55-6** (1992) 184–196.

205. S. M. Dinh, L. Luo, Ching-Wang, and B. Berner, "Upper and Lower Limits on Human Skin Electrical Resistance in Ionophoresis," *AIChE Journal*, **39** (1993) 2011–2018.

206. S. Y. Oh and R. H. Guy, "Effects of Iontophoresis on the Electrical Properties of Human Skin in vivo," *International Journal of Pharmaceutics*, **124** (1995) 137–142.

207. C. Curdy, Y. N. Kalia, F. Falson-Rieg, and R. H. Guy, "Recovery of Human Skin Impedance in vivo After Iontophoresis: Effect of Metal Ions," *AAPS Pharmsci 2000*, **2** (2000) 1–7.

208. T. Yamamoto and Y. Yamamoto, "Analysis for the Change of Skin Impedance," *Medical and Biological Engineering and Computing*, **15** (1977) 219–227.

209. Y. Yamamoto, T. Yamamoto, S. Ohta, T. Uehara, S. Tahara, and Y. Ishizuka, "The Measurement Principle for Evaluating the Performance of Drugs and Cosmetics by Skin Impedance," *Medical and Biological Engineering and Computing*, **16** (1978) 623–632.

210. A. V. Rawlings, A. Davies, M. Carlomusto, S. Pillai, K. Zhang, R. Kosturko, P. Verdejo, and C. Feinberg, "Effect of Lactic Acid Isomers on Keratinocyte Ceramide Synthesis, Stratum Corneum Lipid Levels and Stratum Corneum Barrier Function," *Archives for Dermatological research*, **288** (1996) 383–390.

211. K. Kontturi, L. Murtomäki, J. Hirvonen, P. Paronen, and A. Urtti, "Electrochemical Characterization of Human Skin by Impedance Spectroscopy: The Effect of Penetration Enhancers," *Pharmaceutical Research*, **10** (1993) 381–385.

212. K. Kontturi and L. Murtomäki, "Impedance Spectroscopy in Human Skin. A Refined Model," *Pharmaceutical Research*, **11** (1994) 1355–1357.

213. D. Foley, J. Corish, and O. I. Corrigan, "The Use of Complex Impedance to Examine the Effect of Passive and Iontophoretic Transdermal Drug Transport Through Excised Human Epidermal Tissue," in *Proceedings of the International Symposium for the Controlled Release of Bioactive Materials*, volume 17 (1990) 427–428.

214. Z. Lukacs, "The Numerical Evaluation of the Distortion of EIS Data due to the Distribution of Parameters," *Journal of Electroanalytical Chemistry*, **432** (1997) 79–83.

215. P. Z. Peebles, Jr. and T. A. Giuma, *Principles of Electrical Engineering* (McGraw-Hill, 1994).

216. G. R. T. Schueller and S. R. Taylor, "The Nondestructive Evaluation of Adhesively Bonded Aluminum Using Electrochemical Impedance Spectroscopy," *Journal of the Electrochemical Society*, **139** (1992) 3120–3129.

217. R. P. Buck and M. C., "Origins of Finite Transmission Lines for Exact Representations of Transport By The Nernst-Planck Equations for Each Charge Carrier," *Electrochimica Acta*, **44** (1999) 1999–2018.

218. D. E. Johnson, J. R. Johnson, and J. L. Hilburn, *Electric Circuit Analysis*, 2nd edition (Prentice Hall, 1992).

219. J. R. Macdonald, editor, *Impedance Spectroscopy : Emphasizing Solid Materials and Analysis* (New York: John Wiley and Sons, 1987).

220. C. Gabrielli, *Identification of Electrochemical Processes by Frequency Response Analysis*, Solartron Instrumentation Group Monograph 004-83, The Solartron Electronic group Ltd., Farnborough, England (1984).

221. *A Tutorial on Impedance Spectroscopy*, volume 98-302 (Houston, TX: National Association of Corrosion Engineers, 1998).

222. C. Deslouis, M. M. Musiani, B. Tribollet, and M. A. Vorotyntsev, "Comparison of the AC Impedance of Conducting Polymer Films Studied as Electrode-Supported and Freestanding Membranes," *Journal of the Electrochemical Society*, **142** (1995) 1902–1908.

223. A. Lasia, "Porous Eelectrodes in the Presence of a Concentration Gradient," *Journal of Electroanalytical Chemistry*, **428** (1997) 155–164.

224. T. Ichino, Y. Takeshita, S. Nishi, M. Matsumoto, and K. Naoi, "AC Impedance Analysis on Dual-Phase Polymer Electrolytes Prepared from SBR/NBR Mixed Latices," *Solid State Ionics*, **80** (1995) 119–127.

225. U. Balachandran, B. Ma, P. S. Maiya, R. L. Mieville, J. T. Dusek, J. J. Picciolo, J. Guan, S. E. Dorris, and M. Liu, "Development of Mixed-Conducting Oxides for Gas Separation," *Solid State Ionics*, **108** (1998) 363–370.

226. K. D. Schulze and H. Herrnberger, "Kinetic Analysis of the Transfer of Tetraphenylborate Ions Across Artificial Lipid Membranes," *Zeitschrift fur Physikalische Chemie*, **192** (1995) 33–46.

227. K. D. Schulze and H. Herrnberger, "Impedance Spectroscopic Investigation of Ion Channel Formation in Lipid Membranes," *Zeitschrift fur Physikalische Chemie*, **194** (1996) 243–254.

228. M. I. N. Zhang and J. H. M. Willison, "Electrical Impedance Analysis in Plant Tissues: The Effect of Freeze-Thaw Injury on the Electrical Properties of Potato Tuber and Carrot Root Tissues," *Canadian Journal of Plant Science*, **72** (1992) 545–553.

229. T. J. Vander Noot and M. Levinkind, "AC Impedance Characteristics of Human Dental Enamel and Dentine," *Journal of Electroanalytical Chemistry*, **300** (1991) 191–198.

230. F. X. Hart and W. H. Cole, "Dielectric Properties of Apples in the Range 0.1-100 kHz," *Journal of Materials Science*, **28** (1993) 621–631.

231. T. Repo and M. I. N. Zhang, "Modeling Woody Plant Tissues Using a Distributed Electrical Circuit," *Journal of Experimental Botany*, **44** (1993) 977–982.

232. J. J. Ackmann and M. A. Seitz, "Methods of Complex Impedance Measurements in Biologic Tissue," *Critical Reviews in Biomedical Engineering*, **11** (1984) 281–311.

233. W. Archer, R. Kohli, J. M. C. Roberts, and T. S. Spencer, *Skin Impedance Measurement. Chapter 7 of Methods for Cutaneous Investigation edited by Robert L. Rietschel and Thomas S. Spencer* (New York: Marcel-Dekker, 1990) 121–142.

234. M. E. Orazem, P. Agarwal, and L. H. García-Rubio, "Critical Issues Associated with Interpretation of Impedance Spectra," *Journal of Electroanalytical Chemistry*, **378** (1994) 51–62.

235. P. T. Wojcik, P. Agarwal, and M. E. Orazem, "A Method for Maintaining a Constant Potential Variation During Galvanostatic Regulation of Electrochemical Impedance Measurements," *Electrochimica Acta*, **41** (1996) 977–983.

236. K. I. Reid, R. A. Dionne, L. Sicard-Rosenbaum, D. Lord, and R. A. Dubner, "Evaluation of Iontophoretically Applied Dexamethasone for Painful Pathologic Temporomandibular Joints," *Oral Surgery Oral Medicine Oral Pathology*, **77** (1994) 605–609.

237. P. Agarwal, M. E. Orazem, and L. H. García-Rubio, "Measurement Models for Electrochemical Impedance Spectroscopy I. Demonstration of Applicability," *Journal of the Electrochemical Society*, **139** (1992) 1917–1927.

238. P. Agarwal, O. D. Crisalle, M. E. Orazem, and L. H. García-Rubio, "Application Measurement Models to Impedance Spectroscopy. II. Determination of the Stochastic Contribution to the Error Structure," *Journal of the Electrochemical Society*, **139** (1995) 4149–4158.

239. P. Agarwal, M. E. Orazem, and L. H. García-Rubio, "Measurement Models for Electrochemical Impedance Spectroscopy. III. Evaluation of Consistency with the Kramers-Kronig Relations," *Journal of the Electrochemical Society*, **142** (1995) 4159–4168.

240. M. E. Orazem, *User Manual for the Measurement Model Toolbox for Impedance Spectroscopy*, University of Florida, Gainesville, Florida (2001).

241. M. Durbha, M. E. Orazem, and L. H. García-Rubio, "Spectroscopy Applications of the Kramers-Kronig Transforms: Implications for the Error Structure Identification," *Journal of the Electrochemical Society*, **144** (1997) 48–55.

242. M. Kendig, "Protocol for Removal of Epidermis from Cadavers," (1999). Personal Communication.

243. D. A. Skoog, F. J. Holler, and T. A. Nieman, *Principles of Instrumental Analysis*, 5th edition, Saunders Golden Sunburst Series (Philadelphia, PA: Harcourt Brace College Publishers, 1998).

244. D. A. Skoog and D. M. West, *Analytical Chemistry: an Introduction*, 4th edition (Philadelpia, PA: Saunders College Publishing, 1986).

245. L. E. Schoeff and R. H. Williams, *Principles of Laboratory Instruments* (St. Louis, MO: Mosby Publishers, 1993) 92–123.

246. L. L. Langley, I. R. Telford, and J. B. Christensen, *Dynamic Anatomy and Physiology*, 4th edition (New York: McGraw-Hill Book Company, 1974).

247. J. B. Phipps, R. V. Padmanabhan, and G. A. Lattin, "Iontophoretic Delivery of Model Inorganic and Drug Ions," *Journal of Pharmaceutical Sciences*, **78** (1989) 365–369.

248. H. Inada, A. Ghanem, and W. I. Higuchi, "Studies on the Effects of Applied Voltage and Duration on Human Epidermal Membrane Alteration/Recovery and the Resultant Effects upon Iontophresis," *Pharmaceutical Research*, **11** (1994) 687–697.

249. D. C. Montgomery, *Design and Analysis of Experiments*, 3rd edition (New York: John Wiley and Sons, Inc., 1991).

250. G. A. Milliken and D. E. Johnson, *Analysis of Messy Data. Volume 1 : Designed Experiments*, 1st edition (Chapman and Hall, 1992).

251. R. G. J. Miller, *Beyond ANOVA, Basics of Applied Statistics* (New York: John Wiley and Sons, 1986).

252. R. L. Ott, *An Introduction to Statistical Methods and Data Analysis* (Belmont, California: Wadsworth Publishing Company, 1993) 769–798.

253. P. M. Elias, E. R. Cooper, A. Korc, and B. E. Brown, "Percutaneous Transport in Relation to the Stratum Corneum Structure and Lipid composition," *Journal of Investigative Dermatology*, **76** (1981) 297–301.

254. M. Cormier and B. Johnson, "Skin Reactions Associated with Electrotransport," in *Transdermal Administration, a Case Study, Iontophoresis*, P. Couvreur, D. Duchene, P. Green, and H. E. Junginger, editors, European Symposium, Controlled Release Society (Paris, France: Editions de Sante, 1997) 50–57.

255. R. H. Guy, "Current Status and Future Prospects of Transdermal Drug Delivery," *Pharmaceutical Research*, **13** (1996) 1765–1769.

256. A. L. Bunge, R. H. Guy, and J. Hadgraft, "The Determination of a Diffusional Pathlength Through the Stratum Corneum," *International Journal of Pharmaceutics*, **188** (1999) 121–124.

257. Y. N. Kalia and R. H. Guy, "Modeling Transdermal Drug Release," *Advanced Drug Delivery Reviews*, **48** (2001) 159–172.

258. E. L. Cussler, *Diffusion: Mass Transfer In Fluid Systems* (Cambridge University Press, 1984).

259. R. O. Potts and R. H. Guy, "Predicting Skin Permeability," *Pharmaceutical Research*, **9** (1992) 663–669.

260. R. Reid, J. Prausnitz, and T. Sherwood, *The Properties of Gases and Liquids* (McGraw-Hill Book Company, 1977).

261. J. S. Newman, "Numerical Solution of Coupled, Ordinary Differential Equations," *Industrial and Engineering Chemistry Fundamentals*, **7** (1968) 517–517.

262. R. L. Bronaugh, *Skin permeation: In vitro techniques, Methods for Cutaneous Investigation. Edited by Robert L. Rietschel and Thomas S. Spencer* (New York: Marcel-Dekker, 1990) 171–183.

263. P. T. Wojcik, *The Electrochemical Behavior of Copper and Copper Nickel Alloys in Synthetic Sea Water*, Ph.D. thesis, University of Florida (1997).

264. K. E. Jeffers, *Electrochemical Impedance Spectroscopy for the Characterization of Corrosion and Cathodic Protection of Buried Pipelines*, Master's thesis, University of Florida (1999).

BIOGRAPHICAL SKETCH

Michael A. Membrino received a bachelor of science degree in chemical engineering from Worcester Polytechnic Institute in May 1992. He then accepted a National Science Foundation MEDI fellowship and began his graduate studies at the University of Florida in January 1993. After his arrival in Florida he joined Professor Mark Orazem's electrochemical engineering research group to pursue a doctorate of philosophy degree. Upon completion of degree requirements in May 2002, Mike plans to secure a position for the application of electrochemical engineering principles to industrial research and development.